The role of RNA in antagonizing aberrant phase transitions of RNA-binding proteins in ALS/FTD

by

Jacob Riley Mann

Bachelor of Science, Lafayette College, 2014

Submitted to the Graduate Faculty of the

School of Medicine in partial fulfillment

of the requirements for the degree of

Doctor of Philosophy

University of Pittsburgh

2020

UNIVERSITY OF PITTSBURGH

SCHOOL OF MEDICINE

This dissertation was presented

by

Jacob Riley Mann

It was defended on

May 13, 2020

and approved by

Amantha Thathiah, Ph.D.
Committee Chair
Assistant Professor of Neurobiology, University of Pittsburgh

Elias Aizenman, Ph.D.
Professor of Neurobiology, University of Pittsburgh

Jeffrey Brodsky, Ph.D.
Professor, Avinoff Chair of Biological Sciences, University of Pittsburgh

Udai Pandey, Ph.D.
Associate Professor of Human Genetics, University of Pittsburgh

James Shorter, Ph.D.
Professor of Biochemistry and Biophysics, University of Pennsylvania

Christopher Donnelly, Ph.D.
Dissertation Director
Assistant Professor of Neurobiology, University of Pittsburgh

Copyright © by Jacob Riley Mann

2020

The role of RNA in antagonizing aberrant phase transitions of RNA-binding proteins in ALS/FTD

Jacob Riley Mann, PhD

University of Pittsburgh, 2020

Aberrant aggregation of RNA-binding proteins (RBPs) is a common pathological hallmark of neurodegenerative disorders like amyotrophic lateral sclerosis (ALS) and frontotemporal dementia (FTD). In these diseases, RBPs like TDP-43 and FUS are observed to be both depleted from the nuclear compartment, where they are normally localized, and found within cytoplasmic inclusions in degenerating regions of patient postmortem tissue. The mechanisms responsible for the aggregation of these proteins has remained elusive, largely due to technological limitations, but current hypotheses have proposed that liquid-liquid phase separation (LLPS) might serve as a critical nucleation step in the formation of pathological inclusions. This process of phase separation also seems to underlie the formation of a number of membraneless organelles (MLOs) throughout the cell, some of which have been shown to contain TDP-43, FUS, and other disease-linked RBPs. While various *in vitro* assays have been the predominant method to investigate protein phase behavior, here we describe the development of novel optogenetic-based tools to investigate the endogenous forces regulating phase separation of these proteins in the native intracellular environment. We also demonstrate the application of these tools to selectively induce pathologically-relevant aggregation of these proteins under the spatiotemporal control of light, which has allowed for the first direct testing of neurotoxicity resulting from TDP-43/FUS inclusions. Along with established *in vitro* assays, the use of these models has also led to the discovery of intracellular RNA as a strong modulator of TDP-43 and FUS LLPS and aggregation.

Furthermore, we show here that short, specific RNA oligonucleotides mimicking this endogenous buffer system are capable of preventing and reversing aberrant TDP-43/FUS phase transitions, both *in vitro* and in cells, resulting in a rescue of cellular toxicity associated with pathological aggregation. While the exact mechanisms underlying RNA-mediated antagonization of TDP-43/FUS aggregation are still unclear, in-depth analysis of various RNA inhibitors outlined in this dissertation has begun to identify specific molecular properties, such as length, sequence, and secondary structure, that may mediate these effects. Together, this work may represent the discovery of a new potential therapeutic opportunity to target aberrant RBP aggregation observed in neurodegenerative disease.

Table of Contents

List of Tables

List of Figures

Preface

As is often the case in academic research, the work presented in this dissertation is the product of strong collaborative efforts both within the University of Pittsburgh and abroad. I am incredibly honored and thankful to have had the opportunity to work with such dedicated individuals and research teams and to play this small part in the advancement of our collective knowledge as a scientific community. First and foremost, I would like to thank my dissertation advisor, Dr. Chris Donnelly, for his support and guidance throughout my graduate career. I am eternally grateful for your trust and for all the opportunities you personally afforded me to further my scientific and professional development. I would also like to thank all my colleagues in the Donnelly Lab over these years, Dr. Amanda Gleixner, Joss Mauna, Michael Marks, Katie Copley, Charlie Otte, Ailsa Luce, Bill Tennant, Dr. Joseph Clarke, Noah Pyles, and Jenna Gale, for your continual collaboration and support. I also owe a great deal of appreciation to my fellow graduate student Bryan Hurtle. While our projects have remained distinct, it has often felt as though we were striving towards a common goal. Thank you to Dr. Amantha Thathiah as well, both for graciously serving as my committee chair and for offering so much of your time to advise me on matters big and small. I also wish to thank my fellow collaborators and dissertation committee members Dr. Udai Pandey, Dr. Jeff Brodsky and Dr. Elias Aizenman for providing invaluable guidance and mentorship over the course of my studies here at the University of Pittsburgh. Thank you as well to our collaborators in the lab of Dr. Jim Shorter at the University of Pennsylvania, including Dr. Lin Guo, Dr. Bede Portz and Edward Gomes, without whom this work would never be possible. I would of course be remiss to not acknowledge Suzanne and Neil Alexander, Barbara McCormick, the Phi Delta Theta Fraternity and the Live Like Lou Foundation for their tireless

efforts to raise awareness and much needed funding for ALS patients and research here in Pittsburgh. I also wish to thank the CNUP and Center for Protein Conformational Diseases at the University of Pittsburgh for the generous fellowship support during my graduate research. Additionally, I would like to offer a special thank you to Dr. Lisa Gabel at Lafayette College for taking a chance on a senior student in her Introduction to Neuroscience course. Without your generosity I would have never had the opportunity to work with and learn from all the exceptional individuals listed on this page. Lastly, I would like to sincerely thank my friends and family for their unwavering support. While this time has been one of great personal challenge, I truly would have never persevered without your love and inspiration.

1.0 Introduction

1.1 The amyotrophic lateral sclerosis/frontotemporal dementia (ALS/FTD) spectrum

1.1.1 Clinical definitions of ALS/FTD

Amyotrophic lateral sclerosis (ALS) and frontotemporal dementia (FTD) are two related neurodegenerative disorders characterized primarily by the loss of neurons in the motor cortex and ventral horn of the spinal cord or frontal and temporal lobes of the brain, respectively (Ling et al., 2013). Clinically, these patterns of neurodegeneration produce distinct patient symptomologies. In classical ALS, patients typically present with muscle weakness, fasciculations, and/or cramping (Zarei et al., 2015). Disease onset typically occurs between the ages of 50-65 and is most often is experienced in the limbs (60-70%), but also commonly occurs in bulbar regions (30-40%) of patients (Ferrari et al., 2011; Zarei et al., 2015). In classical FTD, patients usually experience symptoms involving cognitive impairments, frequently associated with sharp changes in social behavior and affect, at ~50-60 years of age (Achi and Rudnicki, 2012; Ferrari et al., 2011). Speech and language dysfunction are also not atypical in these patients, while conversely memory and other cognitive abilities are usually unaffected (Ferrari et al., 2011). Interestingly, while perhaps most cases present with strictly ALS-like symptomologies, up to 50% of patients diagnosed with ALS also experience one or more of the above listed clinical features of FTD (Ferrari et al., 2011). Similarly, it has been reported that up to 30% of diagnosed FTD patients meet some of the diagnostic criteria for ALS (Abramzon et al., 2020; Fay et al., 2017; Ringholz et al., 2005), suggesting a potential overlap in pathogenesis across these two disorders.

1.1.2 Genetics of ALS/FTD

Further evidence for crosstalk between ALS and FTD can be found in recent investigations into the genetics underlying these diseases. Due to modern technological advancements in genome-wide association studies (GWAS) and other genetic assays, mutations in over 50 genes have been identified and linked to the development of ALS and/or FTD over the last 30 years (Mejzini et al., 2019). The proteins encoded by these genes range in terms of functionality, but clusters of affected genes have been identified as being involved in such cellular processes as RNA processing/homeostasis, protein quality control, nucleocytoplasmic trafficking and cytoskeletal dynamics (Abramzon et al., 2020; Ling et al., 2013; Polymenidou et al., 2012). Furthermore, a number of these mutated genes were identified in both ALS and FTD patients, as well as some in patients with a clinical diagnosis of ALS/FTD, including but not limited to: *C9ORF72, TBK1, SQSTM1, TDP-43* and *FUS* (Abramzon et al., 2020). Interestingly, there have also been genes identified in patients diagnosed with only ALS or FTD, such as *SOD1* (ALS) and *MAPT* (FTD), which along with clinical observations has led to the current understanding of these two diseases as existing as an ALS/FTD spectrum rather than two distinct disorders (Ling et al., 2013).

1.1.3 Neuropathology of ALS/FTD

While clues from these genetic studies have certainly drawn a link between these disorders, it is important to note that familial forms of ALS/FTD represent a minority of the entire patient population (~10% of ALS, ~30% of FTD). The remaining majority of patients suffer from sporadic forms of the disease with no known family history or cause of pathogenesis (Ferrari et al., 2011; Greaves and Rohrer, 2019). However, a long history of neuropathological analyses of postmortem

patient tissue of these familial and sporadic patients has drawn further support for the overlap between ALS and FTD. In the 1980's, examination of some of the first recognized cases of ALS with dementia revealed FTD-like degeneration within the temporal and frontal lobes of patient brains, in addition to typical ALS-like degeneration of motor areas (Ferrari et al., 2011). A few years later, another study then reported that a subset of FTLD patients with non-Alzheimer's frontal lobe degeneration (FLD) shared similar neuropathological features to these ALS with dementia cases (Ferrari et al., 2011). In addition to gross morphological changes, subsets of these patients were later identified to also share some histopathological features in the form of ubiquitin-positive, tau-negative inclusions in affected brain and/or spinal cord regions (Leigh et al., 1991; Lippa et al., 2001), further suggesting potential etiological commonalities between these different disorders. It was later discovered that the predominant component of these ubiquitin-positive, tau-negative inclusions was the DNA/RNA-binding protein TDP-43 (Neumann et al., 2006), which we now know is present in ~97% of all ALS cases and ~45-50% of all FTD patients (neuropathologically classified as FTLD-U) regardless of sporadic or familial forms of disease (Ling et al., 2013). Furthermore, this common neuropathological hallmark, termed TDP-43 proteinopathy, has also recently been estimated to be present in up to 75% of Alzheimer's Disease (Amador-Ortiz et al., 2007; Wilson et al., 2011; Youmans and Wolozin, 2012) and ~85% of Chronic Traumatic Encephalopathy (CTE) patients (McKee et al., 2010). Thus, considering that the occurrence and distribution of TDP-43 proteinopathy seems to correlate with regions of the nervous system undergoing neurodegeneration in postmortem patient tissue (Baloh, 2011), these observations may suggest that the aberrant aggregation of TDP-43 may represent a common downstream mechanism driving neurodegeneration across these different diseases.

1.2 TDP-43 proteinopathy and relevance to neurodegeneration in ALS/FTD

1.2.1 TDP-43 in physiological and pathological states

TDP-43, encoded by the *TARDBP* gene, is a ubiquitously expressed DNA/RNA-binding protein that under normal physiological conditions is primarily localized within the nuclear compartment of cells. Structurally, TDP-43 consists of four major domains: 1) an N-terminal domain proposed to mediate functional oligomerization of the protein, as well as its nuclear localization via a bipartite nuclear localization signal (NLS) (Afroz et al., 2017; Mompeán et al., 2017; Wang et al., 2018a); 2) an RNA-recognition motif (RRM1) mediating nucleic acid binding and thought to serve as the primary RNA-binding domain of TDP-43 (Buratti and Baralle, 2001); 3) a second RRM (RRM2) that while displaying weaker binding affinity to target nucleic acids in isolation (Kuo et al., 2009) has been proposed to enhance binding specificity through cooperative binding with RRM1 (Furukawa et al., 2016), potentially mediated by an intramolecular salt bridge formed between the two RRM domains (Flores et al., 2019); and 4) an intrinsically disordered, low-complexity domain (IDR or LCD) that harbors a majority of disease-linked mutations in the protein and is inherently aggregation-prone (Johnson et al., 2009).

Functionally, TDP-43 has been reported to play a role in many different aspects of RNA metabolism in the nuclear compartment, including pre-mRNA splicing, miRNA biogenesis, and regulation of ncRNA and lncRNA expression (Ratti and Buratti, 2016). TDP-43 has also been reported to shuttle out of the nucleus and perform a number of functions related to RNA homeostasis in the cytoplasmic compartment, such as mRNA transport, stability and translational regulation (Ratti and Buratti, 2016). While it was long thought that TDP-43 achieved this cytoplasmic shuttling via a predicted nuclear export sequence (NES) within RRM2, it has now

been established that this predicted NES is non-functional and TDP-43 may conversely travel out to the cytoplasm by passive diffusion independent of major nuclear export proteins (Ederle et al., 2018; Pinarbasi et al., 2018). As mentioned above, TDP-43 returns to the nucleus through active importin α/β-mediated nuclear import, where it remains predominantly localized under normal conditions (Ederle et al., 2018).

However, in TDP-43 proteinopathies, the protein is conversely depleted from the nuclear compartment and can be found to be sequestered within inclusion bodies in the cytoplasm of affected cells (Prasad et al., 2019). These inclusions display a number of immunohistochemical and biochemical hallmarks, including C-terminal hyperphosphorylation, ubiquitin and p62 immunoreactivity, detergent-insolubility, and C-terminal cleavage (Neumann et al., 2006; Prasad et al., 2019). Interestingly, similar to other neurodegenerative disease-linked proteins like Tau in Alzheimer's Disease and other tauopathies (Karikari et al., 2019), TDP-43 has been recently shown to aggregate into different "strains" exhibiting distinct morphological and biochemical properties across different disease subtypes (Laferrière et al., 2019; Porta et al., 2018). It has also been suggested that TDP-43 has the capability to spread via prion-like propagation between regions of the nervous system (Shimonaka et al., 2016; Smethurst et al., 2016), much like other disease-linked protein aggregates, and these distinct TDP-43 strains are hypothesized to exhibit unique spreading patterns that may underlie the different patterns of neurodegeneration observed across various TDP-43 proteinopathies (Porta et al., 2018).

1.2.2 TDP-43 toxicity: gain- and/or loss-of-function mechanisms of neurodegeneration?

While the common occurrence of TDP-43 proteinopathy across various neurodegenerative disorders, as well as its correlation with regional degeneration in postmortem patient tissue, may

suggest that the aggregation of TDP-43 could be driving cellular death, it still is unclear whether TDP-43 pathology is an active pathogenic mechanism or a secondary byproduct of another perturbed pathway in these diseases. Furthermore, questions regarding the precise mechanisms of TDP-43 toxicity, be it gain-of-function via toxic cytoplasmic inclusions, loss-of-function via nuclear TDP-43 depletion/cytoplasmic sequestration, or some combination of the two, remain unanswered. Unfortunately, modelling these specific aspects of TDP-43 proteinopathy *in vitro* and in animal models has been difficult and has produced variable results.

Perhaps the most common experimental strategy has been overexpression of TDP-43, both in its wildtype isoform as well as ALS/FTD-linked mutant versions and disease-linked C-terminal truncations of the protein (Hergesheimer et al., 2019). Overexpression of full-length wildtype TDP-43 has seemed to produce cellular toxicity in a majority of *in vitro* model systems, ranging from yeast to rodent primary cortical and motor neurons (Hergesheimer et al., 2019). Interestingly, investigations into the effects of disease-linked mutant TDP-43 in neuronal overexpression models has yielded inconsistent results, with some groups reporting enhanced toxicity associated with mutant proteins and others showing no difference between overexpression of wildtype and mutant proteins (Hergesheimer et al., 2019). Similar findings have been reported in various *in vivo* models, with the severity of degeneration seemingly being dependent upon the degree of TDP-43 overexpression produced in these organisms (Ling et al., 2013; Vanden Broeck et al., 2014). However, the toxicity observed in these models has not consistently correlated with typical TDP-43 pathology observed in patient tissue, with many groups reporting a lack of aggregation and largely nuclear localization of overexpressed TDP-43 (Hergesheimer et al., 2019). Given the typical adult-onset of TDP-43 proteinopathies in human patients, it is possible that other age-related factors, such as decline in proteostasis (Hipp et al., 2019; Kaushik and Cuervo, 2015) or

nucleocytoplasmic transport (Dormann and Haass, 2011), may be important contributors to TDP-43 mislocalization and aggregation that are not yet experienced by these relatively young transgenic models.

Instead, this overexpression-induced toxicity may alternatively result from a dysregulation of target RNA homeostasis, as widespread changes in RNA expression and splicing profiles have been reported in various wildtype and mutant TDP-43 overexpression models (Flores et al., 2019; Hazelett et al., 2012). Mutation of the TDP-43 RNA-binding regions to reduce RNA-binding efficiency has also been shown to prevent these changes and ameliorate associated overexpression-induced toxicity in multiple model systems (Flores et al., 2019; Loganathan et al., 2019). Additionally, it still remains unclear whether upregulation of TDP-43 can be reliably observed in patient postmortem samples (Cortese et al., 2014), raising the question of whether neurodegeneration produced in these overexpression models may be reflecting pathogenic events experienced by patient cells in disease or producing toxicity through distinct mechanisms.

To begin to address these questions, many groups have begun to utilize recent technological advancements in gene editing and patient-derived iPSC models to investigate the effects of disease-linked TDP-43 mutant proteins expressed by endogenous promoters at physiological expression levels (Guo et al., 2017; Hergesheimer et al., 2019). Unfortunately, a majority of the *in vitro* neuronal models derived from patients harboring ALS/FTD-causing mutations have failed to recapitulate many of the hallmarks of TDP-43 proteinopathies, showing little to no TDP-43 mislocalization or aggregation (Hergesheimer et al., 2019). While this may be limiting from an experimental perspective, it is perhaps not surprising considering the difference in timescales typically utilized in these models (~2-3 months in culture) compared to the adult-onset of these disorders in human patients (Lee and Huang, 2017; Zarei et al., 2015). However,

regardless of the developmental nature of many of these cellular models, various disease-related phenotypes, such as alterations in neuronal activity, transcriptional changes, and susceptibility to cellular stressors, have been observed of these cells and thus may provide some clues into the mechanisms underlying ALS/FTD pathogenesis (Guo et al., 2017; Lee and Huang, 2017). Similar results have also been reported using knock-in rodent models of disease-linked TDP-43 mutations, with most showing no mislocalization/aggregation of TDP-43 and only subtle neurodegenerative and/or motor phenotypes (De Giorgio et al., 2019; Hergesheimer et al., 2019). However, while many of these models did not demonstrate robust TDP-43 proteinopathy, one commonality seen across many of these animals was a disruption in TDP-43 function in the regulation of alternative splicing (De Giorgio et al., 2019). These alterations have been predominantly described in terms of exon inclusion/exclusion and seem to vary depending on the precise mutation(s) in question, but these common observations across individual TDP-43 mutations, as well as some reports from overexpression models and postmortem patient tissue, may suggest that splicing dysregulation as a result of TDP-43 dysfunction may play a vital role in driving neurodegeneration in these disorders (Prasad et al., 2019).

Interestingly, TDP-43 depletion has been shown to recapitulate some of these observations in a variety of model systems, further illustrating the role of proper TDP-43 regulation in the maintenance of RNA homeostasis (Prasad et al., 2019). While ubiquitous homozygous knockout of TDP-43 in mice has been shown to result in embryonic lethality, heterozygous mice have been shown to survive into adulthood and exhibit late-onset motor impairments (Kraemer et al., 2010). Furthermore, conditional knockout of TDP-43 in motor neurons seems to produce similar motor impairments, and a recent conditional depletion model targeting the mouse forebrain has reported FTD-like phenotypes that were associated with widespread RNA expression and processing

changes (Wu et al., 2019; Xu, 2012). Additional transcriptomic studies of human stem-cell derived motor neurons following TDP-43 depletion have shown comparable alterations in RNA expression profiles that interestingly overlapped with some changes observed in iPSC motor neurons derived from patients harboring ALS-linked TDP-43 mutations (Klim et al., 2019; Melamed et al., 2019), further drawing a link between RNA homeostasis and TDP-43 functionality. However, while this relative convergence across gain- and loss-of-function model systems has certainly uncovered important clues into the potential pathogenic mechanisms underlying TDP-43 proteinopathies, it has still remained difficult to specifically model TDP-43 aggregation in order to tease apart the relative contributions of these different toxic mechanisms. Transfection of pre-formed TDP-43 inclusions, either through artificial generation or purified from FTLD patient tissue, has been shown to produce toxicity in cellular models, demonstrating the ability of TDP-43 inclusions to exert gain-of-toxic function (Capitini et al., 2014; Laferrière et al., 2019). However, it is unclear in these studies whether these exogenous inclusions also sequestered endogenous TDP-43, thereby depleting nuclear functionality, to fully recapitulate the disease-state observed in end-stage TDP-43 proteinopathies. Thus, while both loss of TDP-43 function and inclusion-related toxicity have been separately shown to produce cellular toxicity in these models, the precise mechanisms underlying neurodegeneration observed in these diseases remains an open query in the field.

1.3 Liquid-liquid phase separation as a potential nucleator of TDP-43 proteinopathy

1.3.1 Phase transitions in biological systems

While the question of whether TDP-43 aggregation is a key driver of neurodegeneration in various TDP-43 proteinopathies is still unclear, another critical unresolved issue in the field relates to the intrinsic and extrinsic factors that might be responsible for the initiation of TDP-43 aggregation in these pathological conditions. One major hypothesis that has recently emerged from the fields of polymer chemistry and biophysics revolves around the concept of phase separation. In biological terms, phase separation refers to a process by which certain organic molecules dynamically transition from an initially mixed population into separate compartments, or phases. In the same manner that non-biological molecules, such as water, can transition between different states (i.e. liquid water, ice, and water vapor) based upon variables like temperature, it is becoming increasingly recognized that various biological molecules, proteins for example, can be found in different biophysical states within a cell (i.e. soluble proteins or solid-like aggregates) based upon various changes in the intra- and extracellular environment (Hyman et al., 2014). Again using temperature as an example, recent proteomic studies have shown that a large number of proteins in the yeast proteome undergo heat-induced aggregation upon brief heat shock that appears reversible upon return to normal incubation conditions (Wallace et al., 2015). Interestingly, these heat-sensitive proteins were only a small subset of the proteome, potentially suggesting this temperature-induced phase transition as an evolved trait to allow for adaptive function in response to changes in the environment (Wallace et al., 2015). Similar effects also have been reported with stressors such as nutrient starvation and oxidative stress (Ibstedt et al., 2014; Narayanaswamy et al., 2009).

1.3.2 Liquid-liquid phase separation and membraneless organelles

In addition to a response to system-wide changes in the intracellular environment, these kinds of phase transitions can also be utilized to dynamically compartmentalize and organize the cell without the use of lipid membranes (Shin and Brangwynne, 2017). Complementing more canonical lipid-bound organelles like mitochondria and the endoplasmic reticulum, these "membraneless organelles" (MLOs) can be found all over the cell and include such structures as the nucleolus, RNA transport granules, P-bodies and the nuclear pore complex (Gomes and Shorter, 2019). While some of these MLOs, Cajal bodies for example, have been studied for over 100 years, until recently the biological mechanisms underlying the formation and maintenance of these membraneless structures had remained unclear (Shin and Brangwynne, 2017). Following pioneering biophysical investigations into the *C. elegans* germline P granule (Brangwynne et al., 2009) and the *X. laevis* oocyte nucleoli (Brangwynne et al., 2011), it has now been established that the many of these MLOs may arise through a type of phase transition called liquid-liquid phase separation (LLPS). Commonly presented as analogous to the behavior of oil in water, LLPS involves the selective condensation of molecules (i.e. proteins and nucleic acids) from an initially mixed dilute phase into distinct droplets, or a condensed phase, within a surrounding liquid environment (i.e. the cytoplasm) (Hyman et al., 2014). These condensed droplets have been shown to exhibit many properties of "classical" liquids, for example: spherical shape, fission/fusion, dripping, surface wetting, and dynamic molecular exchange both within droplets and with the surrounding environment (Hyman et al., 2014; Shin and Brangwynne, 2017).

Interestingly, the dynamic nature and liquid-like properties of MLOs are proposed to provide unique advantages over membrane-bound organelles, especially for sensing rapid changes in the intra- and extracellular environment (Yoo et al., 2019). One example of this notion can be

found in the behavior of the yeast poly-A binding protein (Pab1) in response to heat stress (Riback et al., 2017). Under normal conditions, Pab1 often functions as a translational repressor through the binding of A-rich regions of target mRNAs (Riback et al., 2017). However, upon brief heat shock Pab1 was shown to release RNA and undergo a rapid, temperature-dependent phase transition into gel-like assemblies, which has been hypothesized to allow for translation of target mRNAs like molecular chaperones to assist with the cellular stress response (Riback et al., 2017; Yoo et al., 2019). A similar mechanism has also been described in the cellular recovery from pH stress involving the yeast translational termination factor Sup35 (Franzmann et al., 2018). Here, a drop in intracellular pH was found to trigger rapid LLPS of Sup35, effectively sequestering the protein in non-fibrillar condensates. Upon return to normal pH conditions, a dissolution of Sup35 assemblies was observed and seemed to coincide with translational restart and cell recovery from stress. Cells that expressed a Sup35 deletion mutant unable to undergo pH-induced LLPS exhibited impaired stress recovery, which together led to the hypothesis that initial condensation functioned to protect the Sup35 catalytic domain from stress-induced damage that would impair its ability to effectively aid in translational restart during recovery (Franzmann et al., 2018).

In addition to "sensing" rapid changes in the intracellular environment, the selective concentration of molecules afforded by these types of phase transitions offer distinct functional benefits over membrane-bound compartments. In the case of the nucleolus, the ability of different nucleolar proteins to assemble into liquid-like condensates with unique biophysical properties has recently been shown to underlie the compartmentalized internal architecture of this MLO (Feric et al., 2016). Interestingly, it seems as though these core nucleolar proteins form distinct, non-coalescing sub-compartments within the greater liquid-like nucleolar environment, producing a "multi-layered droplet" due to differences in surface tension that maintains the internal

organization of the nucleolus and is proposed to aid in the sequential processing reactions of rRNA and ribosome assembly (Feric et al., 2016). Similar advantages can be found in the process of nucleocytoplasmic transport, where it has become increasingly understood that the selectivity of the nuclear pore complex (NPC) can be attributed to the phase behavior of FG-nucleoporins (FG-Nups) residing in the central channel of the NPC (Schmidt and Görlich, 2016). In this sense, it has been shown that these FG-Nups can undergo phase transitions to form liquid- or hydrogel-like droplets that seem to mimic the selective transport permeability observed at the nuclear pore (Celetti et al., 2020; Hülsmann et al., 2012; Labokha et al., 2013; Schmidt and Görlich, 2015, 2016). Whereas specific nuclear import proteins are able to enter and transverse the FG-Nup droplets/gels, other non-specific molecules are impermeable and are largely excluded from these structures (Celetti et al., 2020; Hülsmann et al., 2012; Labokha et al., 2013; Schmidt and Görlich, 2015). Interestingly, both the formation and permeability of these condensates has been proposed to be due to multivalent interactions between highly-conserved FG-repeat domains in specific nucleoporins found along the central channel of the NPC (Terry and Wente, 2009). Similar conserved domains that seem to mediate LLPS have been identified in a number of other proteins (discussed below), thus suggesting that certain proteins and other molecules may have been shaped by evolution to produce specific features to allow for the fine-tuning of phase behavior for a variety of functional outcomes.

1.3.3 Intrinsically-disordered regions (IDRs) as key players in the formation and material properties of phase-separated assemblies

As the number and diversity of proteins reported to utilize phase separation across the proteome has grown, so too has our understanding of the molecular determinants governing the

formation and biophysical properties of these different assemblies. While the precise domain composition and molecular interactions can be varied, one key common feature that has seemed to allow for proteins to drive phase separation is multivalency (Boeynaems et al., 2018). This multivalency can be achieved in a number of ways, but generally involves weak, transient contacts, often through repeated interaction motifs or modules, within and between molecules (Boeynaems et al., 2018; Shin and Brangwynne, 2017). However, while the existence of multiple specific interaction modules, sometimes called "stickers", seems to be imperative for phase separation, the interspersing of these modules by flexible linker, or "spacer", sequences also seems to be a critical determinant of phase behavior in these systems (Posey et al., 2018). This general mode of sticker-spacer organization can be observed in a variety of naturally occurring proteins shown to undergo phase separation, but often seems to involve some combination of folded interaction domains or patches and intrinsically-disordered regions (IDRs) that provide flexibility and/or serve as scaffolds for non-covalent interactions between short linear motifs (SLiMs) embedded within these domains (Boeynaems et al., 2018; Posey et al., 2018).

Due to the enrichment of these regions within phase-separating proteins, as well as their ability to often drive homotypic phase separation in the absence of more-defined interaction domains (Shin and Brangwynne, 2017), IDRs have been the recipient of much research attention in recent years. IDRs are typically defined as regions of a protein sequence that lack a defined, or ordered, secondary structure and thus are capable of adopting a range of three-dimensional conformations (van der Lee et al., 2014). Often times this structural ambiguity is conferred by amino acid compositions of limited sequence complexity, and regions conforming to these characteristics are typically referred to as low-complexity domains (LCDs) or low-complexity IDRs (van der Lee et al., 2014). These domains are also typically enriched in charged (i.e. arginine,

lysine, glutamic acid), polar (i.e. serine, glutamine, asparagine), and/or aromatic (i.e. phenylalanine, tyrosine, tryptophan) amino acids and also generally contain a number of amino acids like glycine and proline that may convey some structural information (Shin and Brangwynne, 2017; Theillet et al., 2013). These sequence compositions in turn allow for a variety of the non-covalent interactions that seem largely responsible for driving phase separation of these domains and the proteins they are part of. While these interaction types can vary both across and within IDRs, they generally involve a combination of charge-based interactions (charge-charge or cation-π), dipole-dipole interactions and π-π stacking of aromatic residues (Brangwynne et al., 2015). Interestingly, recent simulations and mutational studies have predicted that the heterogeneity of both structural conformation and interaction type (via amino acid composition) in IDRs can have profound effects on the formation and biophysical properties of higher-order assemblies (Boeynaems et al., 2018; Tüű-Szabó et al., 2018; Wang et al., 2018b). These material properties in turn likely reflect specific functions that are encoded within the sequence of IDRs and other interaction domains within protein components of various MLOs, and this notion can be seen in some of the examples mentioned above. For instance, the selective permeability barrier formed within the nuclear pore, which seems to be gel-like in nature, is thought to be due to multivalent aromatic interactions between repetitive FG motifs (i.e. FxFG, GLFG, xxFG) within intrinsically-disordered FG-nucleoporins (Li et al., 2016). Conversely, the nucleolar protein FIB-1 has been shown to phase separate into more liquid-like assemblies, both in homotypic *in vitro* reactions and within the nucleolus *in vivo*, which is likely driven by charge-based interactions afforded by its R/G-rich IDR (Feric et al., 2016). In this sense, each of these distinct interaction types encoded within these regions have likely been evolutionarily tuned to allow for the formation of assemblies with specific, functionally-beneficial material properties.

1.3.4 Prion-like domains and their relevance to aberrant RNA-binding protein aggregation in neurodegenerative disease

Another subtype of IDR that has been identified to mediate phase separation of various proteins into assemblies with unique biophysical properties are prion-like domains (PrLDs) (Franzmann and Alberti, 2019). First identified in the yeast proteins Ure2 and Sup35, these PrLDs were shown to drive the assembly of self-propagating, amyloid-like aggregates that were capable of templating their aggregated state to soluble versions of the proteins (Franzmann and Alberti, 2019). Subsequent analysis of these domains revealed that these PrLDs were intrinsically-disordered and contained very limited sequence complexity, skewing towards amino acid compositions of glycine and largely uncharged, polar amino acids like glutamine, asparagine, serine and tyrosine (Verdile et al., 2019). Interestingly, when the human proteome was later scanned for proteins containing PrLD-like amino acid compositions, a heavy enrichment of proteins identified as containing PrLDs was found in RNA-binding proteins (RBPs) (Franzmann and Alberti, 2019). Furthermore, a number of these PrLD-containing RBPs have also been reported to form pathological inclusions in post-mortem patient tissue across several neurodegenerative and muscle-related disorders, including FUS (ALS, FTLD, HD) (Doi et al., 2008; Lagier-Tourenne et al., 2010), TAF15 (FTLD, ALS) (Couthouis et al., 2011; Svetoni et al., 2016), EWSR1 (FTLD) (Neumann et al., 2011), hnRNPA1 (IBM, MSP) (Harrison and Shorter, 2017; Kim et al., 2013), hnRNPA2B1 (IBM, MSP) (Harrison and Shorter, 2017; Kim et al., 2013), and TDP-43 (Gitler and Shorter, 2011), suggesting that this common element may play a role in the aberrant aggregation of these proteins observed in disease.

In addition to prion-like IDRs, all of these proteins also contain multiple RNA-binding domains, either in the form of "canonical" RNA-recognition motifs (RRMs) or RGG/ZnF regions

(Gomes and Shorter, 2019), and have been reported as components of various RNA-containing MLOs in the cell like RNA transport granules (Purice and Taylor, 2018), paraspeckles (An et al., 2019; Modic et al., 2019) and nuclear gems (Cacciottolo et al., 2019). Purified preparations of these proteins have also all been shown to undergo LLPS *in vitro* (Maharana et al., 2018; Ryan et al., 2018), and the PrLDs of these RBPs seem to be necessary and sufficient for phase separation in these systems (Babinchak et al., 2019; Conicella et al., 2016, 2020; Molliex et al., 2015; Patel et al., 2015; Ryan et al., 2018; Schmidt and Rohatgi, 2016). Interestingly, while initial assemblies formed by these proteins, as well as their PrLDs in isolation, display liquid-like biophysical properties, it has recently been shown that extended incubation seems to promote a "maturation" or hardening of these droplets into more gel-like structures or solid-state aggregates that resemble the pathological state of these proteins observed in patient tissue (Patel et al., 2015). These liquid-to-solid transitions seem to occur in a concentration-dependent manner, which has led to the hypothesis that increasing the concentration of these PrLD-containing proteins in the dense phase may alter the molecular dynamics within these assemblies and/or promote interactions that may be responsible for the nucleation of protein fibrillization/aggregation (Patel et al., 2015). Similar preliminary droplet-like states have also been reported to preceded amyloid formation of the previously mentioned yeast prion protein Sup35 (Patel et al., 2015; Serio et al., 2000), which might suggest that PrLDs contain evolutionarily-conserved elements that while allowing for the formation of liquid-like compartments in response to physiological stimuli may also confer a propensity for solid-state aggregation under certain pathological conditions.

In support of this notion, these liquid-to-solid state transitions, also called aberrant phase transitions, have also been reported to be promoted by different disease-linked familial mutations in the PrLDs of these proteins (Gomes and Shorter, 2019; Gopal et al., 2017; Patel et al., 2015).

For example, an ALS-linked mutation in the FUS PrLD (G156E) has recently been shown to gradually increase the viscosity of initially liquid-like FUS droplets *in vitro* and promote emergent fibrillization at incubation times in which wildtype droplets remained dynamic (Patel et al., 2015). Similar results have been observed when examining the effect of an MSP-linked PrLD mutation on the *in vitro* phase behavior of hnRNPA1, which seemed to undergo LLPS indistinguishably from wildtype protein at initial timepoints and co-phase separate into liquid-like droplets with wildtype protein when mixed (Molliex et al., 2015). However, over time fibrillization of the mutant protein was observed to emerge from wildtype droplets and eventually seeded wildtype protein into similar fibril-like assemblies (Molliex et al., 2015). These *in vitro* assays have allowed for the precision required to uncover this mechanism, but it is important to note that these reactions are limited by the conditions that are often required to induce phase separation and aggregation in these cell-free systems (Alberti et al., 2019). For example, many of these proteins require non-physiological buffer conditions (i.e. low salt), enhanced protein concentration, and/or artificial molecular crowding (i.e. Dextran/PEG) to initiate this process that may draw into question the relevance of these findings in the context of human cells (see also Chapter 4). However, recent intracellular models have begun to recapitulate some of these findings (Mackenzie et al., 2017; Ray et al., 2019, see also Chapter 2), suggesting that similar liquid-to-solid transitions may be at work within cellular environments in disease.

Additional work suggests that similar mechanisms can be observed in the phase behavior of TDP-43. Interestingly, over 85% of the 45+ mutations in *TARDBP* that have been identified and linked to the development of ALS and FTLD fall within the protein's PrLD (Prasad et al., 2019). Although many of these mutations have been reported to enhance aggregation and toxicity of TDP-43, until recently the role for TDP-43 LLPS in the formation of pathological inclusions and the

impact of disease-linked PrLD mutations on this behavior had yet to be elucidated (Johnson et al., 2009). Largely due to difficulties associated with purifying full-length TDP-43, many *in vitro* investigations have focused on LLPS of the TDP-43 PrLD in isolation. However, the TDP-43 PrLD alone has been reported by multiple groups to undergo homotypic LLPS *in vitro* (Babinchak et al., 2019; Conicella et al., 2020; Li et al., 2018), and this LLPS has recently been reported to enhance the aggregation rate of the TDP-43 PrLD when compared to incubation conditions in which LLPS is not observed (Babinchak et al., 2019). Furthermore, in a manner analogous to FUS and hnRNPA1 mentioned above, fibril-like assemblies of the TDP-43 PrLD were subsequently shown to emerge from these liquid-like droplets upon extended incubation times, potentially representing a liquid-to-solid transition (Babinchak et al., 2019). Interestingly, other *in vitro* studies of the TDP-43 PrLD in isolation have shown that certain ALS-linked mutations can have varied effects on TDP-43 PrLD self-assembly, with some mutations actually antagonizing LLPS and encouraging direct aggregation of these regions (Conicella et al., 2016). This effect was proposed to result from disruption of a unique α-helical structure that seems to be important for mediating the self-association of these TDP-43 PrLD fragments (Conicella et al., 2016).

Importantly, it has recently been recognized that the N-terminal oligomerization domain of TDP-43 also plays a critical role in mediating full-length TDP-43 LLPS, likely through the enhancement of multivalency and/or promoting PrLD intermolecular interactions (Wang et al., 2018a). Taking this notion into consideration, an artificial model of intracellular TDP-43 phase separation involving this N-terminal oligomerization domain along with the C-terminal PrLD has reported that both wildtype and similar ALS-linked mutant versions of these proteins form droplet-like structures within cells, highlighting the role of the N-terminal domain in phase separation of full-length TDP-43 (Schmidt and Rohatgi, 2016). This observation may suggest that, in an

analogous manner to FUS, full-length TDP-43 and the PrLD alone may undergo phase separation through distinct molecular mechanisms. When next examining the material properties of droplets formed in this system, ALS-linked mutants were shown to exhibit a more static, less dynamic state when compared to wildtype assemblies, possibly representing a solid-state transition promoted by disease-causing mutations (Schmidt and Rohatgi, 2016). Interestingly, this study also showed that replacement of a highly-conserved portion of the TDP-43 PrLD, which included this proposed α-helical structure, with a stretch of PrLD-like amino acids led to the formation of solid, fibril-like structures emerging from a spherical core (Schmidt and Rohatgi, 2016). More recent in-depth investigations into full-length TDP-43 oligomerization and aggregation *in vitro* have also proposed that higher-order oligomerization of TDP-43 is associated with maturation of an initial droplet phase following extended incubation and that this higher-order oligomerization is accelerated by similar ALS-linked mutations within the PrLD (French et al., 2019). From a physiological perspective, RNA transport granules containing mutant TDP-43 have been reported by multiple groups to exhibit diminished dendritic or axonal transport rates (Alami et al., 2014; Gopal et al., 2017; Liu-Yesucevitz et al., 2014), which has been proposed to be due to an increased viscosity and reduced dynamics of these normally liquid-like granules (Gopal et al., 2017). Together, these observations may suggest that this conserved α-helical region important for PrLD self-assembly may assist in the coordination of proper PrLD intermolecular contacts during physiological phase separation to encourage liquid-like behavior of full-length TDP-43 and that enhanced protein concentration or disease-linked mutations in this region may conversely encourage interactions that alter molecular dynamics and/or promote solid-state transitions within these assemblies.

1.3.5 Stress granules as physiological incubators for aberrant phase transitions of disease-linked RBPs

The above-mentioned investigations certainly point to LLPS as an initial nucleation step preceding subsequent solid-state transitions and the deposition of insoluble inclusions of different RBPs implicated in neurodegenerative disease. However, the physiological context(s) in which these initial phase transitions arise, as well as the pathological conditions that promote aberrant solid-state conversion, have remained open questions in the field. One emerging hypothesis has centered around one type of MLO called stress granules. In simplified terms, stress granules are cytoplasmic granules that form in response to the inhibition of translation initiation, due either to cellular stressors or pharmacological/genetic intervention, and contain a large abundance of RBPs, translation initiation factors and nontranslating mRNAs (Buchan and Parker, 2009; Protter and Parker, 2016). These granules exhibit liquid-like properties in cells and are thus presumed to arise through the process of LLPS. Functionally, stress granules have been proposed to function in translational regulation and mRNA homeostasis, given the presence of stalled mRNP complexes and the global translational arrest observed in conditions triggering their formation (Wolozin and Ivanov, 2019). However, these granules also seem to sequester a number of other non-RNA binding proteins involved in various signaling pathways and thus may participate in additional or alternative functions (Wolozin and Ivanov, 2019).

Recently, stress granules have become a major focus in neurodegeneration following the discovery that both TDP-43 and FUS could be observed as components of these structures under certain conditions (Dewey et al., 2012). Additional links have arisen from observations that these proteins may have some regulatory capacity over stress granule formation and that disease-linked mutations in TDP-43 and FUS may lead to enhanced recruitment into stress granules (Li et al.,

2013). Furthermore, familial disease-linked mutations have also been identified in other stress granule components, some of which have been shown to alter stress granule assembly and/or dynamics (Wolozin and Ivanov, 2019). For example, ALS-linked mutations in the stress granule-associated protein TIA-1 have recently been reported to both promote TIA-1 LLPS and delay the dissolution of stress granules following stress removal (Mackenzie et al., 2017).

Together, these observations have led to the hypothesis that during the physiological stress response, proteins like TDP-43 and FUS shuttle out to the cytoplasm and are incorporated into stress granules. In normal conditions, these granules are then disassembled or cleared by autophagy during stress recovery, allowing for translational restart of stalled mRNPs and degradation or return to normal function of other RBP components (Protter and Parker, 2016). Conversely, during pathological conditions in which stress granule clearance or disassembly is delayed, these liquid-like structures could serve as "reaction crucibles" to promote the aggregation of proteins like TDP-43 and FUS in a similar mechanism to that observed *in vitro* (Li et al., 2013). In this sense, the prolonged incubation of these aggregate-prone proteins present at high local concentrations within these assemblies could promote a "maturation" of stress granules and ultimately result in their deposition into insoluble inclusions capable of driving disease (Wolozin and Ivanov, 2019). However, while one might expect other stress granule components to co-aggregate with TDP-43 or FUS in patient inclusions as a result of this process, postmortem analyses of TDP-43 or FUS proteinopathy patient tissue has yielded largely negative results (Hirsch-Reinshagen et al., 2017). Even in ALS patients harboring TIA-1 mutations shown to delay stress granule disassembly in cellular models, no evidence of TIA-1-positive inclusions nor co-localization of TIA-1 with TDP-43 pathology was observed in postmortem tissue (Hirsch-Reinshagen et al., 2017; Mackenzie et al., 2017). Still, the possibility does exist that initial TDP-43 or FUS aggregate formation may

occur within stress granules, which may persist following disassembly of other stress granule components. However, direct evidence for this notion is lacking and thus it is still unclear whether these proposed mechanisms, based on observations in extreme cellular models, may be truly representative of pathogenic processes occurring in human disease.

1.3.6 Other factors modulating physiological and aberrant PrLD-driven phase transitions

While it appears that inherited genetic factors can have a strong effect on the phase behavior of TDP-43 and other PrLD-containing RBPs in various systems, it is important to note that mutations in genes encoding these proteins only represent a small fraction of patients that exhibit RBP pathology in disease. Taking TDP-43 for example, it has been estimated that only 5-10% of familial ALS patients, who themselves only represent ~10% of the entire ALS patient population, exhibit mutations in the *TARDBP* gene (Prasad et al., 2019). However, as mentioned above, ~97% of all ALS patients (both familial and sporadic) present with TDP-43 proteinopathy upon postmortem examination (Prasad et al., 2019). This suggests that other pathways or factors that dynamically regulate the phase behavior of these proteins, as well as various MLOs they are components of, may be altered in disease states and ultimately result in their aberrant deposition within pathological inclusions.

Likely due to certain pathological signatures of protein inclusions in postmortem patient tissue, one of the best characterized regulators of phase separation of various disease-linked proteins, including these PrLD-containing RBPs, has been alterations in post-translational modifications. Furthermore, when considering the typical amino acid composition of IDRs, and the enrichment of typically-modified amino acids like arginine, serine, and tyrosine, it is not hard to imagine that alterations in post-translational modification patterns within these regions could

have profound effects on phase separation and aggregation of these proteins (Hofweber and Dormann, 2019).

Interestingly, certain post-translational modifications, for example phosphorylation, have been shown to have opposing effects on phase separation of different proteins (Hofweber and Dormann, 2019). For instance, DNA-PK-mediated phosphorylation of the FUS PrLD, as well as phosphomimetic substitutions within this region, seem to oppose LLPS and subsequent aggregation (Monahan et al., 2017; Murray et al., 2017). This effect has been proposed to be due to electrostatic repulsion between PrLDs due to the introduction of negatively-charged phosphate groups to the normally uncharged, polar PrLD (Monahan et al., 2017). Similar reports have emerged from investigations of hnRNPA2 phase behavior, where tyrosine phosphorylation was shown to antagonize LLPS and aggregation of both wildtype and disease-linked mutant versions of hnRNPA2 *in vitro* (Ryan et al., 2020). Conversely, phosphorylation of the intrinsically-disordered protein Tau, which is often found within hyperphosphorylated neurofibrillary tangles in Alzheimer's Disease and other tauopathies (Götz et al., 2019), has been shown to enhance LLPS and subsequent fibrillization of both the microtubule-binding repeat regions and full-length Tau protein (Ambadipudi et al., 2017; Wegmann et al., 2018). This enhancement has been hypothesized to be due to similar charge-based mechanisms, involving effects like neutralization of the positively-charged proline-rich regions of tau and/or conformational changes also associated with the introduction of negatively-charged phosphate groups that may lead to Tau phase separation (Wegmann et al., 2018). Promotion of LLPS by phosphorylation may also be at play in the aggregation of Parkinson's Disease-associated protein α-synuclein, as it has been recently reported that a single phosphomimetic substitution at serine 129, a site that is often observed to be

phosphorylated within Lewy bodies in patient tissue (Oueslati, 2016), leads to an enhancement of α-synuclein phase separation and aggregation (Ray et al., 2019).

Another major post-translational modification that can have a striking impact on phase behavior, particularly in proteins with RG-rich domains, is arginine methylation (Hofweber and Dormann, 2019). Considered a relatively more stable modification than other post-translational modifications like phosphorylation, many reports have recently emerged centered upon the suppression of phase separation of FUS (Hofweber and Dormann, 2019). In these studies, arginine methylation within FUS RGG domains was shown to antagonize long-range cation-π interactions between these arginines and the tyrosine-rich PrLD, thereby decreasing FUS LLPS (Qamar et al., 2018). Methylated FUS droplets also were shown to exhibit much more dynamic properties than un-methylated assemblies formed at the same concentration (Hofweber et al., 2018). Furthermore, de-methylation of FUS with the methylation inhibitor AdOx led to a strong enhancement of LLPS that resulted in the formation of assemblies that exhibited some gel- and potentially amyloid-like properties when compared to methylated FUS droplets, suggesting a potential liquid-to-solid state transition in these structures (Qamar et al., 2018). Similar mechanisms have separately been described for the homotypic phase separation of the hnRNPA2 and Ddx4 IDRs, which both rely on cation-π interactions between arginine and aromatic residues and are also suppressed by arginine methylation in these regions (Nott et al., 2015; Ryan et al., 2018). While most observations point to arginine methylation as a general inhibitor of LLPS, particularly in proteins that rely on cation-π interactions for phase separation, it has been shown that arginine methylation within the Lsm4 RGG domain enhances the formation of P-bodies, a type of liquid-like MLO thought to function in mRNA turnover, in mammalian cells (Arribas-Layton et al., 2016). However, this effect could result from altered interactions with other factors important for P-body

assembly, as in-depth investigations into the effect of methylation on the phase behavior of Lsm4 have yet to be reported.

While phosphorylation and arginine-methylation may be the most characterized post-translational modifications in the regulation of RBP LLPS, other modifications like acetylation, PARylation, O-GlcNAcylation, SUMOylation, and ubiquitination have also been reported to affect the phase behavior of various proteins, including TDP-43 (Hofweber and Dormann, 2019). Given the common observations of hyperphosphorylation of the TDP-43 PrLD within inclusions in postmortem patient tissue (Scotter et al., 2015), as well as the enrichment of serine residues in the TDP-43 PrLD, the role of phosphorylation in the regulation of TDP-43 LLPS and aggregation has been the focus of many research investigations in recent years. However, reports have been varied and this question remains relatively unclear. For example, multiple investigations studying the effects of phosphorylation at pathology-linked residues on the aggregation of C-terminal truncations of TDP-43 have proposed phosphorylation as a defense mechanism against pathological aggregation, reporting a reduction in aggregation of these fragments with phosphorylation-mimetic mutations (S>D/E) and an enhancement of aggregation with phosphorylation-dead (S>A) mutations (Brady et al., 2011; Li et al., 2011). Importantly, these effects were not observed when examining aggregation of full-length TDP-43, potentially suggesting a distinct effect of phosphorylation on the self-assembly of C-terminal fragments (Li et al., 2011).

In support of this notion, similar investigations of phospho-dead mutations at these residues have conversely shown a reduction of ALS-linked mutant TDP-43 toxicity associated with insoluble TDP-43 aggregation in *C. elegans* models (Liachko et al., 2010). Furthermore, multiple studies have linked increased phosphorylation by various casein kinases, including CKIε, CKIδ,

and CKII, to enhanced aggregation of TDP-43 in various *in vitro* and *in vivo* systems (Carlomagno et al., 2014; Choksi et al., 2014; Nonaka et al., 2016). One of these investigations additionally reported that phospho-dead mutations at residues not typically associated with TDP-43 proteinopathy (S393/S395) ameliorated this effect, suggesting that the role of phosphorylation at other sites within the PrLD on TDP-43 LLPS and aggregation may be worthy of further study (Nonaka et al., 2016). While it has been shown that a single phospho-mimetic mutation at S48 in the N-terminal oligomerization domain seems to antagonize TDP-43 LLPS (Wang et al., 2018a), surprisingly direct investigations of the effect of PrLD phosphorylation on LLPS of TDP-43 have yet to be reported. However, one potential clue could be found in recently-determined atomic structures of various segments of the TDP-43 PrLD (Guenther et al., 2018a). Here, the authors describe a number of identified LARKS (Low-complexity Aromatic-Rich Kinked Segments), previously proposed to mediate reversible hydrogel-like assembly of low-complexity domains in proteins like FUS and hnRNPA1 (Hughes et al., 2018), within the TDP-43 PrLD and show that disease-associated mutations in one of these LARKS may promote irreversible aggregation through the stabilization of beta-sheet interactions (Guenther et al., 2018a). Interestingly, these specific mutations (A315E/A315T) were hypothesized to have direct relevance to phosphorylation, as the A>E mutation mimics a constitutively-phosphorylated residue and the A>T introduces a novel phosphorylation site that when phosphorylated (A315pT) showed enhanced stability compared to its unphosphorylated counterpart (A315T) (Guenther et al., 2018a).

In addition to post-translational modifications, many other extrinsic factors, such as salt, pH, temperature, and metal ions, have been shown to modulate phase separation and aggregation of PrLD-containing RBPs. In addition to the inclusion of molecular crowding agents, such as polyethylene glycol (PEG) or dextran, many of these *in vitro* experiments have utilized alterations

in salt concentrations to trigger LLPS of these proteins (Alberti et al., 2018). Interestingly, different proteins have displayed varying degrees of salt-dependence in their phase behavior, which likely reflects the particular interaction types responsible for driving phase separation across proteins. For example, LLPS of FUS, which seems to rely on charge-based cation-π interactions, is strongly inhibited by increasing salt (Patel et al., 2015), while TDP-43 LLPS, which has been proposed to utilize aromatic and hydrophobic interactions for phase separation, seems to be stimulated by increased salt concentrations (McGurk et al., 2018). Similar observations have also been reported for alterations in temperature and pH in various systems (Franzmann et al., 2018; Riback et al., 2017). Another often-neglected factor in the regulation of RBP phase behavior is the influence of divalent metal ions, such as Zn^{2+}, and Ca^{2+}. Although the free concentration of these ions are typically low within cells, certain cellular events such as oxidative stress (McCord and Aizenman, 2014) or action potentials (Ross, 2012) can cause dramatic spikes in the intracellular concentration of these ions and thus may serve as rapid signals to induce or antagonize phase separation. Interestingly, Zn^{2+} has been linked to enhanced TDP-43 aggregation, both *in vitro* and intracellularly (Caragounis et al., 2010; Garnier et al., 2017), and has recently been shown to promote the *in vitro* LLPS of the similar PrLD-containing RBP TIA-1 and enhance its recruitment to liquid-like stress granules (Rayman et al., 2018). Unfortunately, little is currently known regarding the direct effects of Ca^{2+} on TDP-43, or other RBP, phase behavior. However, there have been reports of various indirect mechanisms of calcium-induced TDP-43 aggregation, including calpain-mediated c-terminal fragmentation (Berning and Walker, 2019), casein-kinase-induced phosphorylation (Hicks et al., 2019) and alternative splicing driven by hyperexcitability (Weskamp et al., 2020).

Overall, our increasing understanding of the intricate molecular grammar governing the phase behavior of various proteins will be crucial in the effort to elucidate the biological mechanisms underlying membraneless organelle formation/function, as well as in the identification of targetable components within these systems for drug development in disease. Furthermore, determination of the intrinsic and extrinsic factors responsible for the regulation of these processes may provide some additional clues into vulnerable pathways that may be dysregulated upstream of pathological protein aggregation, especially in sporadic forms of disease. Still, while the causal role of aberrant phase transitions in neurodegeneration is a continued subject of debate, the common pathology shown across patients and diseases remains a critical observation. For example, the identification of unmethylated FUS inclusions as a pathological hallmark in sporadic FTLD has led to the subsequent discoveries of dysregulation of various protein arginine methyltransferases (PMRTs) in other neurodegenerative diseases like Alzheimer's Disease, Huntington's Disease, spinobulbar muscular atrophy and other polyglutamine-expansion disorders (Blanc and Richard, 2017). In this sense, even if protein inclusions were a secondary by-product and dispensable for neuronal toxicity, the identification of dysregulated pathways that promote this behavior will still provide invaluable information regarding other potential toxic mechanisms at work in disease outside of protein aggregation.

1.4 RNA as a key regulator of RNA-binding protein phase behavior

1.4.1 RNA as a scaffold for promoting physiological phase transitions and MLO formation

In addition to the above-mentioned intrinsic/extrinsic factors, such as protein sequence, post-translational modifications, and environmental conditions, regulating the phase behavior of various proteins, another critical determinant of these processes is the participation of natural ligands like RNA (Fay and Anderson, 2018). This notion appears to be particularly true for multi-component MLOs, as well as heterotypic phase separation *in vitro*, and has recently been conceptually described in terms of "client-scaffold" relationships (Ditlev et al., 2018). In simplified terms, this framework describes the formation and composition of phase-separated compartments as being dictated by the interactions between multivalent "scaffold molecules", RNA for example, and "client molecules", such as RNA-binding proteins (Banani et al., 2016; Ditlev et al., 2018). The enhanced multivalency afforded by interactions between RNA-binding regions within RBPs and specific binding motifs encoded within RNA nucleotide sequence can thus in theory drive heterotypic phase separation (i.e. through lowering a protein's C_{sat}) in these systems and provide some specificity in the recruitment of particular RBPs to membraneless ribonucleoprotein (RNP) granules (Langdon and Gladfelter, 2018) (Figure 1). Of course, other factors such as relative scaffold/client concentrations, client affinity/valency, and additional multivalent interactions between different scaffold and client molecules play a large role in determining this behavior for naturally occurring MLOs containing a diverse array of protein and/or RNA components (Boeynaems et al., 2018). However, many recent *in vitro* studies have begun to uncover some of the basic mechanisms underlying the variable effects of RNA on RBP phase behavior in more simplified systems. For example, one of the first direct investigations of

RNA's effect on RBP phase separation reported a strong enhancement of LLPS observed of artificial fusion proteins containing RNA-binding elements from the PTB protein along with IDRs from various other RBPs (including FUS, hnRNPA1, TIA-1, and others) upon addition of RNA (Lin et al., 2015). This effect seemed to be strongly dependent upon the presence of IDR regions, as phase separation of PTB alone with RNA only occurred at very high protein concentrations (50μM alone versus 1.25-2.5μM with IDRs) (Lin et al., 2015). Similarly, addition of RNA in these studies did not seem to promote LLPS of IDR regions alone (without PTB RNA-binding regions), suggesting a synergistic effect of PTB:RNA and IDR:IDR interactions in the driving of phase separation in these systems (Lin et al., 2015). Similar results have been reported for full-length RBPs like FUS (Burke et al., 2015; Han et al., 2012) and hnRNPA1 (Lin et al., 2015; Molliex et al., 2015), which has in part led to the hypothesis that this scaffolding characteristic of RNA may encourage a high local concentration of IDR-containing RBPs that, upon binding to RNA, contribute the additional multivalent interactions required to drive phase separation of these RNP structures.

Additional investigations into the formation of naturally-occurring MLOs within intracellular systems has also supported this notion, as the presence of certain RNAs within a cell seems to be required for the assembly of many different cellular RNP compartments like P-bodies (Teixeira et al., 2005), nucleoli (Berry et al., 2015; Falahati et al., 2016), bacterial BR-bodies (Al-Husini et al., 2018), paraspeckles (Clemson et al., 2009) and nuclear A-bodies (Audas et al., 2016). Furthermore, a number of these MLOs, such as stress granules, nuclear speckles, paraspeckles, Cajal bodies and nuclear stress bodies, can be formed *de novo* by the introduction of excess RNA substrates into the cell (Bounedjah et al., 2014; Kaiser et al., 2008; Shevtsov and Dundr, 2011). Binding to RNA has also been reported to be required for the recruitment of certain protein

components to RNP granules. For example, the incorporation of RBPs like FUS and TDP-43 within stress granules, or NPM1 within nucleoli, seems to be dependent upon functional RNA-binding domains, as deletion or mutation of these domains has been shown to antagonize their co-localization with these structures (Bentmann et al., 2012; Colombrita et al., 2009; Daigle et al., 2013; Mitrea et al., 2016). Global RNA degradation has shown a similar effect, with RNase I-treated cells exhibiting significantly reduced enrichment of hnRNPA2B1, FUS, and TDP-43 within stress granules (Fang et al., 2019).

1.4.2 Distinct RNA species differentially regulate RBP phase behavior

Interestingly, while many of these initial studies focused on the effect of total RNA or bulk mRNA samples on LLPS of more promiscuous RNA-binding proteins, recent investigations into RBP phase behavior with specific target RNA molecules have uncovered a more intricate regulatory capacity for RNA. For example, in many cases it seems as though high affinity RNAs can be more efficient in driving condensation of their cognate RBPs (Langdon et al., 2018; Maharana et al., 2018; Zhang et al., 2015a). In the case of Whi3, it has been shown that the endogenous target mRNA *CLN3* can nucleate Whi3 droplets at concentrations at which DNA or total yeast RNA was ineffective (Zhang et al., 2015a). Similar observations have been reported in the phase behavior of TDP-43 and FUS, which have both been separately shown to undergo LLPS upon the addition of the long noncoding RNA *NEAT1* into reactions containing high background concentrations of tRNA incapable of driving phase separation of these proteins (Maharana et al., 2018; Wang et al., 2019). Importantly, while RNA can potentially act as a molecular crowder to drive LLPS in certain *in vitro* reactions involving low-affinity proteins (Nguemaha and Zhou, 2018), these effects seemed to be dependent upon proper RBP:RNA interactions, as deletion of

the Whi3 RRM or TDP-43 RRM1 seemed to abrogate the ability of these specific RNAs to drive phase separation (Wang et al., 2019; Zhang et al., 2015a).

In addition to promiscuous versus specific RNA binding, it is becoming increasingly clear that different properties of RNA molecules can have distinct effects on the formation, as well as material properties, of these RNP assemblies (Zhang et al., 2015a). RNA length is one such variable, and although direct comparisons are limited it has been proposed that longer RNAs may exhibit an enhanced ability to drive protein phase separation, as has been observed with the RBP PGL-3 *in vitro* (Saha et al., 2016). Recent smFRET studies of LAF-1 and FUS interactions with synthetic oligonucleotide sequences of varying lengths have suggested a similar mechanism, with longer oligonucleotides promoting multimerization of these proteins with RNA and dynamic RBP:RNA interactions that may be representative of the initiation of phase separation (Kim and Myong, 2016; Niaki et al., 2020). Observations regarding the RNA content of various intracellular MLOs, such as stress granules and various nuclear bodies, have also supported this notion, albeit indirectly. For example, transcriptomic investigations into the RNA content of cytoplasmic stress granules have revealed CDS/UTR or overall length as one common feature of enriched transcripts across various stressors (Khong et al., 2017; Namkoong et al., 2018). Furthermore, alternative isoforms of the long noncoding RNA *NEAT1* have differing effects in nucleating paraspeckle assembly, with replacement of only the longer of the two isoforms (*NEAT1_2*) shown to recover paraspeckle assembly in *NEAT1* knockout MEF cells (Fox et al., 2018; Naganuma et al., 2012). This unique ability of the longer *NEAT1_2* isoform has been proposed to be driven by the recruitment and resulting phase separation of PrLD-containing RBPs, like FUS and RBM14, through functionally-redundant elements not present in the shorter *NEAT1_1* isoform (Chujo and Hirose, 2017; Yamazaki et al., 2018). A similar mechanism has been proposed to underlie the

formation of nuclear stress bodies, where the heat-induced transcription of highly-repetitive satellite III (*HSATIII*) long noncoding RNA has been linked to the recruitment of various IDR-containing RBPs and nucleation of these droplet-like structures (Biamonti and Vourc'h, 2010; Metz et al., 2004; Ninomiya et al., 2020).

Importantly, while these observations have both directly and indirectly suggested that increased length of RNAs might afford for additional valency between RNAs and various IDR-containing RBPs to drive phase separation, recent investigations into the phase behavior of Whi3 with various target RNAs have suggested that additional characteristics of specific RNA molecules may play a key role in modulating this process (Langdon et al., 2018; Zhang et al., 2015a). Initial studies focusing on two separate target RNAs, *CLN3* and *BNI1*, containing the same number of predicted Whi3 binding sites but differing in overall length (CLN3 = 1596bp; *BNI1* = 6590bp) have shown that while both transcripts could drive phase separation of Whi3 in physiological conditions, presence of the longer *BNI1* mRNA seemed to increase the optimal RNA:protein molar ratio for Whi3 droplet formation, in comparison to the shorter *CLN3* transcript, and shift the phase boundary towards higher RNA concentration (Zhang et al., 2015a). Furthermore, phase separation driven by these different RNAs significantly altered the material properties of Whi3 assemblies, with Whi3/*BNI1* droplets exhibiting increased fusion rates and decreased viscosity when compared to Whi3/*CLN3* condensates formed at the same concentration (Zhang et al., 2015a). Increasing the concentration of *CLN3* RNA in these reactions seemed to exacerbate this hardening, producing droplets with further decreased dynamics and increased viscosity, while increasing Whi3 protein concentration seemed to have the opposite effect. Interestingly, subsequent studies of similar reactions between Whi3 and these target RNAs showed that *BNI1*-driven assemblies incorporated significantly more Whi3 protein into condensates than *CLN3* at equivalent concentrations

(Langdon et al., 2018), which is in agreement with these initial findings that higher protein:RNA ratios promoted fluidity in Whi3/*CLN3* droplets (Zhang et al., 2015a). Given that the effective valency of these RNAs for Whi3 binding were predicted to be equivalent, the authors proposed these effects could be due to factors like binding site density (more clustered for *CLN3*/evenly distributed for *BNI1*) or differing secondary structures formed by these distinct RNA species. Follow-up smFRET studies of these two mRNA targets have supported this notion, with *CLN3* showing a higher baseline FRET signal than *BNI1*, indicative of a more compacted structural conformation, in the absence of Whi3 protein (Langdon et al., 2018). Furthermore, while broadening of FRET peaks was observed with *CLN3* mRNA, FRET fluctuations were much more rapid for the less-compacted *BNI1* mRNA upon addition of Whi3, indicating a much more dynamic nature of Whi3/*BNI1* complexes that could reflect the increased fluidity observed of these droplets in initial studies (Langdon et al., 2018; Zhang et al., 2015a). Certain structural elements of various RNAs have also been reported to promote proper interactions and phase separation with RBPs shown to be important for the formation and function of intracellular MLOs, including low-complexity regions of rIGSRNA for A-bodies (Wang et al., 2018c) and "zipcode" elements encoded within UTR-regions of mRNAs in transport RNP granules (Jambhekar and Derisi, 2007).

Another critical finding that emerged from these studies was that in addition to modulating interactions with Whi3 protein alone, RNA structure seemed to determine heterotypic RNA:RNA interactions and resulting RNA partitioning into Whi3 droplets formed with other RNA species (Langdon et al., 2018). Interestingly, while structurally-intact *CLN3* mRNA was not incorporated into pre-formed *BNI1*/Whi3 assemblies, thermal unfolding or point mutations induced to disrupt *CLN3* structure and expose *BNI1* complementary regions did allow for *CLN3* partitioning into *BNI1*/Whi3 droplets (Langdon et al., 2018). Incorporation into *BNI1*/Whi3 condensates was also

observed for another mRNA, *SPA2*, which contains complementary *BNI1* regions in its native structure and is found to be co-localized with *BNI1* within *Ashbya gossypii* polarity granules *in vivo* (Langdon et al., 2018). These effects were also re-created in the absence of Whi3 protein, with *BNI1* and *SPA2* co-assembling into gel- or liquid-like RNA condensates, highlighting the role for RNA:RNA interactions in the sorting of functionally-related RNAs into specific RNP assemblies (Langdon et al., 2018).

These findings are especially interesting in light of recent work that has demonstrated the role of RNA self-assembly in the formation of other physiological RNA-containing MLOs like stress granules. It has long been known that a variety of RNA species can self-assemble into different higher-order structures (Grabow and Jaeger, 2014; Van Treeck et al., 2018). However, recent work has demonstrated that RNA homopolymers (particularly polyU sequences), as well as total yeast RNA, can self-assemble into liquid-like droplets that are capable of recruiting RNA-binding proteins like hnRNPA1 (Van Treeck et al., 2018). Furthermore, sequencing of RNAs enriched within total RNA assemblies created *in vitro* revealed a striking similarity to the stress granule-enriched transcriptome mentioned above, showing overlaps in both RNA characteristics (longer RNAs enriched) and specific RNA transcripts contained within these assemblies (Van Treeck et al., 2018). In addition to these observations, it has also been noted that alterations in osmotic conditions that favor RNA:RNA interactions (i.e. hyperosmotic stress) (Bounedjah et al., 2012) or the introduction of G-quadruplex-forming RNAs can separately promote stress granule assembly within a cell (Fay et al., 2017), which together has led to the hypothesis that intermolecular interactions between these longer, potentially more-structured, RNAs play an active role in physiological RNP assembly (Van Treeck and Parker, 2018).

Homotypic RNA phase separation has also been recently suggested to participate in the formation of pathological RNA foci in repeat expansion disorders like Huntington's Disease (HD) and *C9ORF72*-ALS/FTD. Specifically, it has been shown that disease-associated repeat RNA (CAG_n for HD/$GGGGCC_n$ for *C9ORF72*-ALS/FTD) can phase separate *in vitro* and in cells to form liquid- or gel-like RNA assemblies in a length-dependent manner (Fay et al., 2017; Jain and Vale, 2017). This effect importantly was proposed to arise from the long GC-rich tracts contained within these repeats that allow for multivalent base-pairing and the formation of structural elements, such as hairpins and/or G-quadruplexes, as foci formation was reversed by interrupting complementary base-pairing interactions with blocking antisense oligonucleotides or the nucleic acid intercalator doxorubicin (Jain and Vale, 2017). Another similar repeat-expansion (CGG_n) in the FMR1 5'UTR linked to Fragile-X associated tremor ataxia syndrome (FXTAS) has also been shown to drive the formation of nuclear RNA foci (Cid-Samper et al., 2018). In a similar manner to CAG/GGGGCC repeats described above, these CGG_n repeats were capable of recruiting RBPs in cellular models that are often observed to be sequestered within foci in patient tissue (Cid-Samper et al., 2018; Jain and Vale, 2017). Disruption of distinct hairpin structures formed by these repeats prevented both nuclear foci formation and RBP recruitment (Cid-Samper et al., 2018; Jain and Vale, 2017), again highlighting the role of RNA structure in mediating homo- and heterotypic RNA/RBP phase separation. Some of this behavior can also be observed in non-disease contexts, as other G-quadruplex-forming nucleic acids, such as regions of the *SHR* mRNA and ssDNA from the *c-myc* promoter region, have similarly been shown to undergo LLPS that is highly sensitive to structural perturbations and can recruit proteins like linker histone H1 to condensates (Mimura et al., 2020; Zhang et al., 2019b).

In addition to features like sequence, length, and secondary structure, post-transcriptional modifications like methylation (i.e. N6-methyladenosine (m6A), 2′-O-methylation, 5-methylcytidine (m5C)) could also have profound effects on RNA-mediated modulation of phase separation and MLO formation/function. While many of these modifications have been reported to modulate RNA structure and protein interactions through a variety of mechanisms (Drino and Schaefer, 2018), m6A is currently the only modification that has been directly investigated in the context of RBP phase transitions (Ries et al., 2019). Specifically, it was shown that LLPS of m6A-binding proteins like YTHDF2, which is a PrLD-containing RBP capable of *in vitro* phase separation in the absence of RNA, can be strikingly enhanced by the addition of m6A-modified RNA oligonucleotides in a valency-dependent manner (Ries et al., 2019; Wang et al., 2020). Incorporation of YTHDF2 into MLOs seems to be similarly dependent upon m6A RNA binding, as knockout of the *Mettle14* methyltransferase or YTHDF2 mutation to reduce m6A binding affinity resulted in reduced localization within p-bodies and stress granules (Ries et al., 2019). Interestingly, subsequent transcriptomic analysis revealed an enrichment of polymethylated RNAs within these structures, leading the authors to propose m6A RNAs as novel multivalent scaffolds that can be utilized to regulate the phase behavior of various RNA-binding proteins (Ries et al., 2019).

Together, these observations suggest that RNA can play a crucial role in tuning the phase behavior of different membraneless organelles, both through interactions with proteins and other RNA components of these structures. In this way, specific characteristics of these RNAs, especially architectural noncoding RNAs like those observed in paraspeckles and other MLOs, have likely evolved along with other regulators of phase separation, such as RBP sequence/structure and post-translational modifications, to dynamically regulate the formation of

specific types of assemblies for various functions. However, these regulatory mechanisms at work during normal physiology can likely also go awry during pathological conditions and thus may provide clues into the dysregulated pathways playing a role in the pathogenesis of diseases characterized by aberrant phase behavior of these RBPs.

1.4.3 RNA can antagonize phase transitions of RBPs at physiological concentrations

In addition to influencing the formation and material properties of various membraneless assemblies, many investigations have made it clear that RNA can certainly promote RBP phase separation and incorporation into these structures both *in vitro* and in cellular environments. This effect has often been recognized as heavily dependent upon RNA:protein molar ratios, with lower RNA concentrations promoting phase separation of excess protein concentrations in most *in vitro* experiments (Maharana et al., 2018; Zhang et al., 2015a). However, in a cellular environment under physiological conditions, many of these RBPs reside in the nuclear compartment where these molar ratios are generally reversed (Maharana et al., 2018). FUS for example, which has been predicted to be endogenously expressed at ~7μM within the nucleus (Maharana et al., 2018), has been shown to readily undergo LLPS at these concentrations *in vitro* (Burke et al., 2015; Monahan et al., 2017), but remains largely soluble within the nuclear compartment in cells (Maharana et al., 2018). While addition of low concentrations of total RNA (~0.4:1 RNA:FUS ratio) have been reported to enhance this *in vitro* LLPS, multiple studies have also noted that increasing RNA concentrations to excess, thus mimicking the native intracellular environment, seemed to reverse this effect and actually prevent FUS phase separation in some of these reactions (Burke et al., 2015; Maharana et al., 2018; Schwartz et al., 2013) (Figure 1). This kind of biphasic effect of RNA on phase separation *in vitro* has also been demonstrated for specific mRNA targets

of RBPs in proteins like Whi3 (Zhang et al., 2015a). However, the precise molar ratios at which phase separation was opposed in these experiments varied across mRNA species (Zhang et al., 2015a), suggesting that specific RNA characteristics such as those described above may also influence RNA-mediated antagonization of RBP phase transitions.

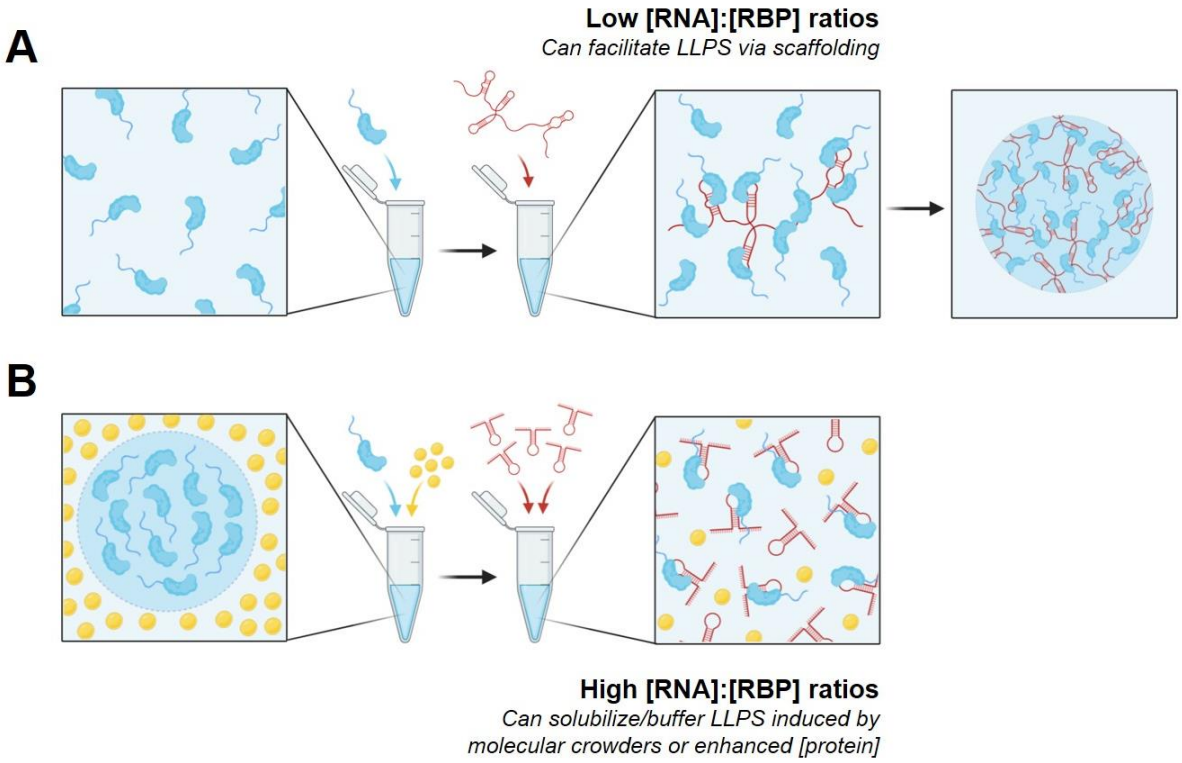

Figure 1. Varying effects of RNA on *in vitro* RBP phase separation.

(A) At protein concentrations and/or reaction conditions in which homotypic phase separation is not observed, addition of low concentrations of longer RNA species may promote RBP LLPS through the facilitation of protein multimerization on single RNA species. (B) In conditions in which homotypic RBP LLPS is observed *in vitro* (i.e. due to enhanced protein concentration or addition of molecular crowders), excess concentrations of RNA (particularly shorter sequences) may act as molecular buffers to antagonize RBP multimerization and phase separation.

1.4.4 Implicated pathways in ALS/FTD may converge on RNA-regulated formation and clearance of aberrant RBP inclusions

Considering the largely soluble nature of these RBPs in the RNA-rich nuclear compartment, it is interesting to note that the aberrant inclusions observed in postmortem tissue are almost exclusively observed to be localized in the cytoplasm where RNA concentrations have been predicted to be ~36.5-fold lower than that of the nucleus (Maharana et al., 2018). Furthermore, a majority of *in vitro* and *in vivo* models utilizing TDP-43 or FUS overexpression to produce aberrant aggregation have shown a similar preferential accumulation of inclusions in the cytoplasmic compartment (Hergesheimer et al., 2019; Nolan et al., 2016), which may reflect a lower saturation concentration (C_{sat}) required for the nucleation of RBP phase transitions in the RNA-depleted cytoplasm. In support of this notion, artificial impairment of the nuclear import of TDP-43 and FUS, through mutation of their respective nuclear localization sequences (NLS), seems to promote the formation of cytoplasmic inclusions (Elden et al., 2010; Shiihashi et al., 2016; Walker et al., 2015; Winton et al., 2008), suggesting that cytoplasmic mislocalization might precede aggregation of these proteins in disease. Clues from studies of various genetic ALS/FTD subtypes associated with TDP-43 proteinopathy have provided further evidence for this idea, as signs of altered nucleocytoplasmic transport, such as irregular nuclear morphology, altered localization of nuclear transport factors, and/or disrupted Ran gradients, have been observed in a number of cellular models and postmortem tissue samples of these patients (Boeynaems et al., 2016; Kim and Taylor, 2017) (Figure 2). Furthermore, other stimuli or cellular events previously associated with ALS/FTD pathogenesis, such as hyperactivity, stress granule assembly, and aging, have been shown to either directly trigger the nuclear egress of TDP-43 and FUS or disrupt nucleocytoplasmic transport in a way that may promote their cytoplasmic mislocalization

(Sugiyama et al., 2017; Tischbein et al., 2019; Weskamp et al., 2020; Zhang et al., 2018). Together, these observations have led to the general hypothesis that redistribution of RBPs like TDP-43 and FUS, due to enhanced export or impaired nuclear import, from the RNA-rich nucleus to the RNA-depleted cytoplasm may precede and promote their eventual aggregation into insoluble inclusions observed in disease.

Another key pathway that has been identified as playing a pivotal role in ALS/FTD pathogenesis and may also converge on this RNA-dependent regulation of TDP-43 and FUS aggregation is RNA processing and homeostasis (Ling et al., 2013; Nussbacher et al., 2019) (Figure 2). In addition to TDP-43 and FUS themselves, disease-linked mutations in several other genes encoding proteins regulating various aspects of RNA splicing and stability have been identified, including *MATR3, SETX, TIA-1, TAF15, EWSR1, hnRNPA1, hnRNPA2B1*, and *ANG* (Nussbacher et al., 2019; Taylor et al., 2016). Interestingly, while several of the proteins encoded by these genes have been shown to undergo LLPS and associate with various MLOs, direct analysis of postmortem tissue of patients harboring some of these mutations, such as *TIA-1*, *SETX*, and *ANG*, has often shown classical TDP-43 proteinopathy in the absence of aggregation of these mutated proteins (Bennett et al., 2018; Hirsch-Reinshagen et al., 2017; Mackenzie et al., 2017; Seilhean et al., 2009). Furthermore, recent Bru-seq analysis has shown widespread alterations of RNA stability and synthesis in fibroblasts and iPSCs derived from sporadic and *C9ORF72*-ALS patients, who typically also exhibit characteristic TDP-43 proteinopathy but not direct mutation of RNA processing proteins (Tank et al., 2018). Unbiased, genome-wide screens have also identified an enrichment of proteins involved in this process of RNA metabolism as modifiers of TDP-43 and FUS toxicity in yeast (Elden et al., 2010; Sun et al., 2011), and together these observations

suggest that dysregulation of RNA homeostasis may be a common pathogenic mechanism upstream of TDP-43 or FUS aggregation in ALS/FTD and other neurodegenerative disorders.

In addition to nucleocytoplasmic transport and RNA processing, another major subset of genes implicated in ALS/FTD pathogenesis have been functionally linked to protein quality control pathways like the ubiquitin/proteasome system (UPS) and autophagy (Taylor et al., 2016) (Figure 2). Both of these systems seem inherently linked to the aggregation of TDP-43 and FUS, as inhibition of proteasomal and/or autophagic protein degradation leads to the accumulation of these proteins in a variety of models (Scotter et al., 2014; Sun et al., 2011; van Eersel et al., 2011). However, a recent investigation has proposed that these systems may display some selectivity in their degradation these proteins, with the UPS being responsible for the turnover of mostly soluble TDP-43 and autophagy conversely handling insoluble, aggregated forms of the protein (Scotter et al., 2014). Other studies have similarly shown that selective activation of the autophagy pathway is capable of promoting the clearance of accumulated TDP-43 and FUS and reducing toxicity associated with these proteins in neuronal models (Barmada et al., 2014; Marrone et al., 2019). These proposals are in agreement with current hypotheses related to the process of "aggrephagy", in which large, insoluble protein aggregates are selectively engulfed by autophagosomes and degraded through the macroautophagy pathway (Lamark and Johansen, 2012). Considering these observations, it is important to note that a majority of the ALS/FTD-linked mutations in proteostasis-related genes, including *PRGN*, *SQSTM1/p62*, *VCP*, *OPTN*, *TBK1*, and *C9ORF72*, have been predominantly connected to disruption of the autophagic system (Shahheydari et al., 2017), which may implicate these causative mutations with a failure to clear aggregated species of TDP-43 and FUS. Interestingly, it has also long been established that this proteostasis network seems to decline during aging (Hipp et al., 2019; Kaushik and Cuervo, 2015), especially in long-

lived/post-mitotic cells like neurons, which has been proposed to play a significant role in the accumulation of insoluble protein inclusions in various other age-related neurodegenerative disorders like Parkinson's Disease, Alzheimer's Disease and Huntington's Disease (Kurtishi et al., 2019).

These genetic studies and observations from sporadic ALS/FTD and other neurodegenerative disorders have provided invaluable clues into the major dysregulated pathways that may underlie the pathogenesis of TDP-43 and FUS proteinopathies. Interestingly, while dysregulation all of these pathways can have numerous detrimental effects on the vulnerable population of cells affected in these disorders, one common convergence point can be found in the accumulation of aggregate-prone RBP inclusions. Of course, it is still possible that these pathological hallmarks are themselves simply a signature of dysregulated RNA homeostasis, nucleocytoplasmic transport and/or proteostasis that drive neurodegeneration independent of protein inclusions. However, evidence connecting disruption of these protein inclusions with reduced toxicity in various models may suggest a viable therapeutic strategy in the direct targeting of RBP aggregation in these diseases (Guo et al., 2018; Tariq et al., 2019). Thus, additional studies into the regulatory mechanisms governing RBP phase behavior will hopefully provide opportunities for the discovery and development of novel therapeutics for neurodegenerative disorders like ALS/FTD.

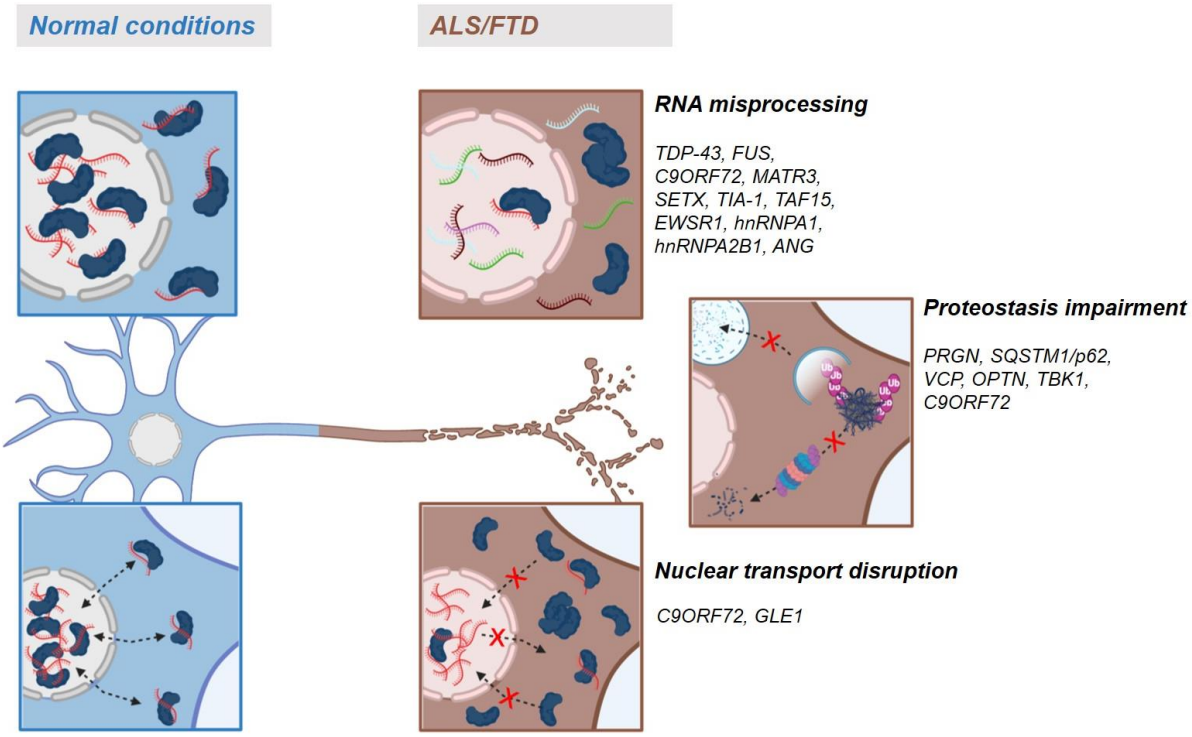

Figure 2. Perturbed pathways in familial ALS/FTD may converge on RBP mislocalization and aggregation. Implicated genes in ALS/FTD have been associated with three major pathways directly related to RNA binding protein aggregation: (1) RNA homeostasis, in which mutations have been linked to global RNA processing/expression changes (i.e. *C9ORF72*) or fall within RNA-binding proteins themselves (i.e. *TIA-1*, *MATR3*, *hnRNPA1*); (2) Nucleocytoplasmic transport, in which mutations have been linked to impaired nuclear import of disease-linked proteins (i.e. *C9ORF72*) or reduced mRNA export (i.e. *GLE1*); and (3) Protein quality control, in which mutations in genes are associated with autophagic (i.e. *SQSTM1/p62*, *VCP*, *OPTN*) and proteosomal (i.e. *UBQLN2*) protein degradation.

1.5 Summary and aims of dissertation

In summary, intracellular aggregation of the RNA-binding proteins (RBPs) TDP-43 or FUS is a common neuropathological feature in ALS and FTD. *In vitro* investigations of these proteins have suggested that prion-like domains (PrLDs) are responsible for the nucleation of TDP-

43/FUS aggregation through the process of liquid-liquid phase separation (LLPS), which is also thought to underlie the physiological assembly and function of membraneless organelles. The phase behavior of TDP-43, FUS and other RBPs have been shown to be modulated by a variety of intrinsic and extrinsic factors, including natural ligands like RNA. Current cellular and animal models of ALS/FTD rely on enhanced expression of wildtype or rare mutant variants of these proteins to initiate pathological aggregation; however, this approach lacks critical spatio-temporal control over the aggregation process required to uncover the precise intra- and inter-molecular interactions regulating intracellular TDP-43/FUS inclusion formation. Furthermore, these strategies are unable to directly test whether aggregation of these proteins are innately neurotoxic devoid of overexpression-related confounds.

This dissertation aims to address these questions by utilizing novel optogenetic models of intracellular TDP-43/FUS phase transitions along with established cellular and *in vitro* assays. In the following chapters, we will first describe the development of these models to directly test the inherent neurotoxicity of RBP inclusions and to investigate the contribution of PrLDs and RNA in regulating these aberrant phase transitions. We will also discuss our efforts to determine the role of RNA in modulating physiological phase transitions of TDP-43 into stress granules and determine whether recruitment to these membraneless organelles may promote insoluble inclusion formation. We will additionally describe the development of short RNA oligonucleotide molecules capable of preventing and reversing aberrant phase transitions of TDP-43 and FUS and explore the molecular mechanisms and properties of these molecules responsible for these effects. Lastly, we will determine whether this RNA oligonucleotide-mediated antagonization of TDP-43 and FUS inclusion formation is capable of rescuing cellular toxicity associated with aberrant phase transitions of these proteins and thus may represent a novel therapeutic strategy for ALS/FTD.

2.0 RNA binding antagonizes neurotoxic phase transitions of TDP-43

This chapter is adapted from: Mann, J. R., Gleixner, A. M., Mauna, J. C., Gomes, E., DeChellis-Marks, M. R., Needham, P. G., Copley, K. E., Hurtle, B., Portz, B., Pyles, N. J., Guo, L., Calder, C. B., Wills, Z. P., Pandey, U. B., Kofler, J. K., Brodsky, J. L., Thathiah, A., Shorter, J., & Donnelly, C. J. (2019). *RNA Binding Antagonizes Neurotoxic Phase Transitions of TDP-43.* Neuron, 102(2), 321–338.e8. https://doi.org/10.1016/j.neuron.2019.01.048.

2.1 Introduction

Amyotrophic Lateral Sclerosis (ALS) and Frontotemporal Dementia (FTD) are fatal neurodegenerative disorders characterized by the progressive loss of motor neurons of the spinal cord and motor cortex or cortical neurons of the frontal and temporal lobes, respectively. No effective treatments currently exist to halt ALS or FTD progression and the cause(s) of these disorders remain unknown. Significant overlap of clinical, genetic, and neuropathological features among patients suggests that ALS and FTD exist on a neurodegenerative disease spectrum (Ling et al., 2013), and a number of familial ALS and/or FTD causing mutations have been identified (Nguyen et al., 2018). Despite this vast genetic heterogeneity, 97% of ALS patients and up to 45% of FTD patients exhibit a common neuropathological feature called TDP-43 proteinopathy. TDP-43 proteinopathy is characterized by the cytoplasmic deposition and nuclear clearance of the transactivation response element DNA-binding protein 43 kDa (TDP-43; *TARDBP*) (Neumann et al., 2006).

TDP-43 is a ubiquitously-expressed, tightly-regulated, and predominantly nuclear DNA/RNA-binding protein that contains two RNA-Recognition Motifs (RRMs) and a C-terminal

glycine-rich, low complexity domain (LCD) (Scotter et al., 2015). TDP-43 preferentially binds UG-rich RNA intronic sequences or 3′UTR stem loop structures and influences a variety of RNA processing events including alternative splicing, RNA trafficking, and RNA stability (Ling et al., 2013). In ALS and FTD, the protein is found in cytoplasmic inclusions that are detergent-insoluble, hyperphosphorylated, p62-positive, and ubiquitinated (Scotter et al., 2015). Cytoplasmic inclusions also contain truncated TDP-43 species resulting from its N-terminal cleavage (Neumann et al., 2007). This neuropathological hallmark correlates well with regions of neurodegeneration in ALS/FTD patient tissue (Baloh, 2011) and is found in postmortem tissue from patients diagnosed with Alzheimer's Disease (60%) (Youmans and Wolozin, 2012), and Chronic Traumatic Encephalopathy (80%) (McKee et al., 2010). Thus, TDP-43 proteinopathy might serve as a convergence point of pathogenesis despite the diverse upstream mechanisms responsible for disease etiology across several neurodegenerative disorders.

Over 50 ALS/FTD-causing missense mutations have been identified in the *TARDBP* gene (Harrison and Shorter, 2017). While rare in the total patient population, these mutations occur more frequently in fALS patients (5%) as compared to patients with familial FTD (Ling et al., 2013). The majority of known ALS/FTD-causing *TARDBP* mutations cluster within the TDP-43 LCD, although others have been identified within the RRMs (Harrison and Shorter, 2017). The location and functional impact of these mutations likely reflects the importance of these regions in disease pathogenesis. LCDs are common in RNA-binding proteins (RBPs) and mediate protein and RNA interactions through a process termed liquid-liquid phase separation (LLPS). LLPS involves the condensation of molecules into liquid-like compartments and is driven by weak, transient interactions between LCD regions and other multivalent protein/nucleic acid interaction domains (Harrison and Shorter, 2017). Following specific protein:protein, protein:RNA and/or

RNA:RNA nucleating interactions, this de-mixing process allows for intracellular compartmentalization, as observed with membraneless organelles such as nucleoli, P-bodies, and stress granules (SGs) (Shin and Brangwynne, 2017). Many of these biological condensates contain high local concentrations of LCD-containing proteins, which contribute to the properties of these structures through a combination of specific and non-specific heterotypic protein/nucleic acid interactions (Harrison and Shorter, 2017; Shin and Brangwynne, 2017). Interestingly, ALS-associated mutations in the TDP-43 LCD alter LLPS behavior and enhance aggregation of the protein (Conicella et al., 2016; Johnson et al., 2009; Schmidt and Rohatgi, 2016). Similar observations have been reported of other RBPs implicated in neurodegeneration, where disease-linked LCD mutations or aging of droplets promotes the maturation and fibrillization of initially reversible protein assemblies (Harrison and Shorter, 2017). While the physical processes underlying droplet solidification is unknown, these findings suggest that aberrant phase transitions drive the formation of pathological inclusions of RNA-binding proteins observed in neurodegenerative disease.

The cellular pathway(s) that promote aberrant TDP-43 phase transitions remain unclear, but evidence suggests that altered SG homeostasis contributes to the seeding of pathological inclusions. SGs are membraneless organelles that assemble in the cytoplasm via LLPS during periods of cellular stress and may reversibly inhibit non-essential protein synthesis (Anderson and Kedersha, 2008; Harrison and Shorter, 2017). In addition to mRNA, ribosomal subunits, and translation initiation factors, SGs sequester a number of RBPs mutated in fALS, including TDP-43 (Boeynaems et al., 2016). The nucleation and phase separation of these various proteins and RNAs into liquid-like droplets is required for cellular compartmentalization of SGs and alterations of intermolecular dynamics may promote an irreversible gel-like state or fibrillization of prion-

like protein components of these structures. The high local concentration of aggregate-prone proteins, like TDP-43, within SGs is thought to enhance protein self-interactions that subsequently mature into pathological inclusions (Harrison and Shorter, 2017). Supporting the role of SGs in seeding TDP-43 proteinopathy, recent work has also revealed that antisense oligonucleotide-mediated depletion of SG components ameliorates neurotoxicity in a TDP-43 rodent model (Becker et al., 2017).

Modeling TDP-43 proteinopathy has proven challenging. Current cellular and animal models rely on enhanced expression of wildtype or rare mutant variants of TDP-43 to initiate pathological aggregation; however, this approach is unreliable and many models fail to develop inclusions that recapitulate ALS/FTD phenotypes (Philips and Rothstein, 2015). Furthermore, the lack of control over intracellular TDP-43 interactions impedes the ability to test whether cytoplasmic phase separation precedes inclusion formation and whether this process, or these inclusions themselves, are neurotoxic. A mechanistic understanding of the molecular processes that drive the formation of TDP-43 inclusions may reveal avenues for therapeutic intervention and uncover the underlying pathobiology of ALS/FTD and related neurodegenerative disorders. To this end, we developed an optogenetic method to induce TDP-43 proteinopathy with blue light and examine the mechanisms that drive the formation of intracellular inclusions. We found that homo-oligomerization of the TDP-43 LCD mediates light-induced phase separation (LIPS) capable of driving the formation of pathologically-relevant inclusions. We also show that RNA-binding regulates these aberrant phase transitions and TDP-43 residence in SGs. Finally, we demonstrate that aberrant TDP-43 phase transitions drive neurodegeneration, and that treatment of neurons with oligonucleotides comprised of TDP-43 binding sequences inhibits inclusion formation and are neuroprotective.

2.2 Materials and methods

2.2.1 Cell culture

HEK293 cells were maintained in DMEM (Thermo Fisher Scientific) supplemented with 10% HyClone Bovine Growth Serum (GE Healthcare Life Sciences) and 1X GlutaMAX (Thermo Fisher Scientific) at 37 °C and 5% CO_2. Cells were seeded onto coverslips or plates coated with collagen (50 μg/mL, Gibco) and allowed to incubate overnight prior to transfections (Lipofectamine 3000, Thermo Fisher Scientific) with 100 ng of DNA performed according to manufacturer's instructions. Cells were plated on collagen-coated glass bottom plates for live-cell imaging, high throughput screening, and FRAP analysis. All manipulations of cells expressing optogenetic constructs were performed under red lamp illumination to avoid ambient light exposure.

2.2.2 Neuronal progenitor maintenance and differentiation

ReNcell VM (Millipore) were maintained and differentiated according to previously described protocols but with minor modifications (Donato et al., 2007). In brief, cells were maintained in proliferation media (DMEM/F-12, 1x GlutaMAX™ supplemented with 1x B27 (Gibco), 2 ng/mL heparin (Sigma), 20 μg/mL bFGF (Millipore) and 20 ug/mL hEGF (Millipore). Differentiation was initiated by plating ReNcell VM onto low attachment plates in proliferation media in order to establish neurosphere production. Neurospheres were then mechanically dissociated and grown to full confluency. Cells were further differentiated in DMEM/F-12, supplemented with 1x GlutaMAX™, 1x B27, 2 ng/mL GDNF (PeproTech) and 1 mM diburtyrl-

cAMP (Tocris) for one week and then maintained in DMEM/F-12 supplemented with 1x GlutaMAX™, 1x B27, and 2 ng/mL GDNF.

2.2.3 Lentiviral production and transduction

Lentiviral transfer vectors encoding optoTDP43, Cry2-mCh or iRFP670 were co-transfected with packaging plasmids (OriGene) into HEK293T cells using the Turbofectin transfection reagent (OriGene) according to manufacturer's instructions. Following an initial media change, lentiviral supernatant was collected at 24 and 48 hr post-transfection prior to filtration and overnight incubation at 4℃ with 1X Lentivirus concentration solution (OriGene). The following day, concentrated lentiviral supernatant was centrifuged at 3,500 *x g* for 25 min at 4℃. The resulting pellet was recentrifuged at 3,500 *x g* for 5 min prior to re-suspension in ice-cold, sterile PBS. Pellets were then allowed to dissolve for 1-2 days at 4℃. Resuspended lentiviral particles were then aliquoted and titers were determined utilizing the One-Wash Lentivirus Titer Kit, HIV-1 p24 ELISA (OriGene). Neuron transductions were performed by diluting lentiviral particles at an MOI of 5 in neuronal differentiation media. Media changes were performed after 48 hr of incubation and all experiments were initiated at 96 hr post-transduction.

2.2.4 Stress treatments

Sodium arsenite (0.5 mM, 30 min) and heat shock (43 °C, 45 min) treatment were used to induce stress granule formation where indicated.

2.2.5 Blue light treatments

Blue light stimulation was performed in 24-well or 6-well plates using custom-built LED arrays designed to fit plate dimensions and withstand common temperature/humidity requirements of cell culture incubators. Individual LED diodes were positioned ~3.0 cm above the culture surface to provide a range of ~0.1-0.3 mW/cm^2 of 465 nm light stimulation to the cultured cells.

2.2.6 RNA and oligonucleotide treatments

Total HEK293 RNA was extracted utilizing the miRNeasy RNA isolation kit (Qiagen) according to manufacturer's instructions. RNA oligonucleotides with 2'OMe modifications were synthesized by GenScript. For experiments utilizing HEK293 cells, total RNA (2.5μg) or RNA oligonucleotides (200nM-1μM as indicated) were transfected into cells using the Lipofectamine RNAiMAX reagent (Thermo Fisher) according to manufacturer's instructions. For ReNcell neuron experiments, oligonucleotides were diluted into normal differentiation medium at the indicated concentrations prior to direct addition to cells.

2.2.7 Bacterial growth and protein expression

For purification of MBP-tagged TDP-43 WT and 5FL proteins, BL21 (DE3) E. coli cell cultures were grown at 37°C to an OD600 of 0.6–0.9 as previously reported (Wang et al., 2018a). Protein expression was induced by IPTG (1mM) prior to overnight incubation at 16°C. Cells were then harvested by centrifugation.

2.2.8 Cloning

All full-length and truncated optoTDP43 plasmids were constructed by inserting PCR-generated fragments at the SmaI restriction enzyme site by Gibson Assembly (HiFi DNA Assembly Master Mix, NEB) of Cry2olig-mCh and Cry2PHR-mCh base vectors (Plasmids 60032 and 26866, Addgene). TDP43-mCh was generated by inserting full-length TDP-43 CDS (synthesized by Genecopoeia) between the NheI and SmaI restriction enzyme sites of the Cry2olig-mCh backbone. All wild-type optoTDP43 vectors were constructed using the same TDP-43 insert. optoTDP43 constructs containing the TDP43cyto, 5FL and/or M337V point mutations were generated from mutant TDP43 plasmids (Plasmids 84912, 84914, 98674, Addgene). Constructs containing the fusRRM (WT or 4FL) were generated by three-fragment Gibson Assembly, inserting the fusRRM fragment and TDP-43 LCD simultaneously into the Cry2olig-mCh backbone at the SmaI restriction site. The plasmid encoding TDP as a C-terminal MBP-tagged protein (TDP43-MBP-His6) was purchased from Addgene (Plasmid 104480) and the 5FL mutant was generated via QuikChange Multi Site-directed Mutatagenesis (Agilent). EGFP-TDP43 constructs were generated by inserting the wild-type or mutant TDP-43 fragments between the HindIII and KpnI restriction enzyme sites of EGFP-alpha-synuclein vector (Plasmid 40822, Addgene). G3BP1-mCh was generated through the insertion of the full-length G3BP1 CDS (synthesized by Genecopoeia) into the mCherry2-C1 backbone (Plasmid 54563, Addgene) at the SmaI restriction site.

2.2.9 Detergent solubility assay

Solubility of TDP-43 was assessed as previously described with minor modifications (van Eersel et al., 2011). In brief, cells were washed once with ice-cold PBS, lysed with modified RIPA buffer (25mM Tris-HCl pH 7.6 (Sigma-Aldrich), 150 mM NaCl (Millipore Sigma), 5 mM EDTA (Sigma-Aldrich), 1% Triton X-100 (Sigma-Aldrich), 1% sodium deoxycholate (Sigma-Aldrich), 0.1% SDS (Fisher Scientific), protease inhibitor cocktail (Sigma-Aldrich), 1 mM PMSF (Thermo Fisher Scientific), phosphatase inhibitor cocktails 2 and 3 (Sigma-Aldrich)) and incubated on ice for 10 min. Following brief sonication on ice, lysates or homogenates were centrifuged for 1 hr at 100,000 *x g* at 4 °C. Supernatants were collected as the detergent-soluble fraction. Protein concentrations were determined using the RC DC protein assay (Bio-Rad). Pellets were then resuspended in RIPA buffer and re-sonicated and re-centrifuged. The resulting supernatant was discarded and pellets were resuspended in urea buffer (30 mM Tris pH 8.5 (Sigma-Aldrich), 7 M urea (Sigma-Aldrich), 2 M thiourea (Sigma-Aldrich), 4% CHAPS (Thermo Fisher Scientific), protease inhibitor cocktail (Sigma-Aldrich), 1 mM PMSF (Thermo Fisher Scientific), phosphatase inhibitor cocktails 2 and 3 (Sigma-Aldrich)). Following brief sonication on ice, lysates were centrifuged for 1 hr at 100,000 *x g* at 22°C. This final supernatant was then collected as the detergent-insoluble, urea-soluble fraction. Proteins from each fraction were then separated by SDS-PAGE and analyzed by western blot analysis.

2.2.10 Nuclear/cytoplasmic fractionation

Nuclear/cytoplasmic subcellular fractionation was performed utilizing NE-PER Nuclear and Cytoplasmic Extraction Reagents (Thermo Fisher Scientific) according to manufacturer's

instructions. Protein concentrations for individual fractions were determined using the Pierce BCA Protein Assay Kit (Thermo Fisher Scientific) and subsequently analyzed by western blot.

2.2.11 Size-exclusion chromatography

A 90 mL Sephacryl S-300 column equilibrated in 25 mM Tris pH 7.8, 150 mM NaCl, 5 mM EDTA, 0.5% Triton X-100, 0.5% deoxycholate was calibrated with the size standards Blue Dextran (2000 kDa), Catalase (232 kDa), and Hemoglobin (60 kDa). Lysates from cells expressing optoTDP43 which had been subjected to blue light stimulation or darkness were loaded in a 0.5 mL volume and the column was run at a flow rate of 0.3 mL/min at 4°C. An initial volume of 30 mL was passed through the column, which corresponded to the column void volume, then 2.5 mL fractions were collected. A sample from each fraction was mixed with SDS sample buffer and subjected to SDS-PAGE, followed by western blotting as described below.

2.2.12 SDS-PAGE/Western blotting

Prior to SDS-PAGE, protein concentrations were determined using the Pierce BCA Protein Assay (Thermo Fisher Scientific) or RC DC Protein Assay (Bio-Rad). Samples were separated by SDS-PAGE (4-20% Mini-PROTEAN TGX Precast Gels, Bio-Rad) and transferred to PVDF membranes (Immobilon-FL, EMD Millipore) using the Trans-Blot Turbo Transfer System (Bio-Rad). Following water and TBS washes, membranes were blocked in Odyssey Blocking Buffer (Li-Cor) for 1 hr at room temperature. Membranes were then washed and incubated with primary antibodies in TBS-T (0.1% Tween) supplemented with 50% blocking buffer overnight at 4 °C. Primary antibody dilutions used were as follows: rabbit anti-TDP43 (Proteintech, 1:1000), mouse

anti-α-tubulin (Sigma-Aldrich, 1:10000), rabbit anti-Lamin B1 (Abcam, 1:5000), rabbit anti-GAPDH (Sigma-Aldrich, 1:10000), mouse anti-mCherry (Novus Biologicals, 1:1000). Following TBS-T washes, membranes were incubated with secondary antibodies (Li-Cor, IRDye 680/800, 1:10000) for 1 hr at room temperature. Membranes were then washed with TBS-T and bands were visualized using the Odyssey CLx imaging system.

2.2.13 Immunofluorescence

For standard immunofluorescence analysis, cells were then fixed with 4% PFA for 15 min at room temperature following one PBS wash. Following three additional PBS washes, cells were blocked with 5% normal donkey serum (NDS) in 0.3% Triton X-100 for 1 hr at room temperature. Primary antibodies were prepared in 1X PBS supplemented with 0.3% Triton X-100/5% NDS and cells were incubated in antibody solution overnight at 4°C. Primary antibody dilutions used were as follows: mouse anti-SQSTM1/p62 (Abcam, 1:100), rabbit anti-SQSTM1/p62 (Abcam, 1:500), rat anti-phospho TDP-43 (S409/410), Clone 1D3 (EMD Millipore, 1:200), rabbit anti-G3BP1 (Proteintech, 1:500), mouse anti-eIF4G (Santa Cruz, 1:300), rabbit anti-ATXN2 (Proteintech, 1:400), rabbit anti-TIAR (Santa Cruz, 1:300), mouse anti-digoxin (Jackson ImmunoResearch, 1:200), mouse anti-ubiquitin (Santa Cruz, 1:200). Following three PBS washes, secondary antibodies were diluted in 0.3% Triton X-100/5% NDS and incubated with cells for 1-2 hrs at room temperature. Cells were then washed and coverslips were mounted onto slides (ProLong Diamond Antifade Mounting Media with DAPI, Invitrogen) to be visualized by confocal microscopy.

For total RNA staining, cells were fixed in 100% methanol for 15 min at -20°C. Following three PBS washes, cells were incubated in SYTO® RNASelect™ Green Fluorescent Cell Stain

(Thermo Fisher Scientific) staining solution (500 nM in PBS) for 20 min at room temperature. Cells were then washed three additional times in PBS prior to blocking and counterstaining as described above.

2.2.14 Immunohistochemistry

Formalin-fixed, paraffin-embedded human hippocampus and cervical spinal cord sections of ALS/FTLD subjects retrieved from the Neurodegenerative Brain Bank at the University of Pittsburgh, following protocols approved by the University of Pittsburgh Committee for Oversight of Research and Clinical Training Involving Decedents (CORID). Following antigen retrieval with Target Retrieval Solution, pH 9 (Dako Agilent), immunofluorescence staining was performed using the following primary antibodies: TIA1 (1:1000, Abcam), Ataxin 2 (1:50, Proteintech), G3BP1 (1:100, Proteintech) and pTDP-43 (1D3, 1:500, kindly provided by Manuela Neumann, Helmholtz Zentrum, Munich, Germany). Immunofluorescence signal was visualized using Alexa Fluor 488 and Cy3 labeled secondary antibodies (both 1:200, Jackson ImmunoResearch) and DAPI nuclear counterstain (1:1000, Thermo Scientific).

2.2.15 RNA Fluorescent In Situ Hybridization (RNA FISH)

RNA-FISH using PolyT (TTTTTTTTTTTTTTTTTTTTTTTTTTVN/3Dig_N) (Exiqon) or scramble control (5DigN/GTGTAACACGTCTATACGCCCA) (Batch 233334, Exiqon) probes was conducted as previously described but with minor modifications (Zhang et al., 2015b). In short, cells were fixed in 3.2% PFA (Electron Microscopy Science), permeabilized for 10 min in 0.3% Triton X-100 (Sigma-Aldrich), equilibrated for 10 min in 1X SSC (Thermo Fisher Scientific)

and then incubated in 40% formamide (Sigma-Aldrich) at 55°C for 10 min. Hybridization buffer (100% formamide, 1 mg/mL BSA Fraction V (Fisher Scientific), 20 mM ribonucleoside vanadyl complex (Sigma-Aldrich), 0.1M $NaPO_4$, 20X SSC) and then probe mixture (10 g/L salmon sperm (Thermo Fisher Scientific), 20 mg/mL E. Coli tRNA (Thermo Fisher Scientific), 80% formamide, 25 µM RNA-Probe preheated to 85 °C) were added to the cells for 2 hrs at 55°C. Next, the cells were washed with 40% formamide, 1X SSC, TBS-50 pH 7.4, 5M NaCl (Thermo Fisher Scientific Scientific) 1M Tris pH 7 (Thermo Fisher Scientific), 1M Tris, pH 8 (Thermo Fisher Scientific Scientific)), and then 1X PBS. Following a cross-linking step with 3.2% PFA and 0.3% Triton X-100, the cells were immunostained and washed with IF Buffer (TBS-50, 0.5 g BSA Fraction V, Protease-free BSA (Fisher Scientific)) and then incubated in blocking buffer (TBS-50, BSA Fraction V, 5% Normal Donkey Serum). Finally, the cells were incubated with primary antibodies at 4°C overnight, and the following day were washed with IF buffer and incubated with secondary antibodies for 1 hr at room temperature. Additional washes with IF Buffer, TBS-50, $MgCl_2$, and 1X PBS were performed prior to mounting coverslips with ProLong Diamond Antifade Mounting Media and visualized by confocal microscopy.

2.2.16 Cell viability assays

Analysis of cell viability was performed utilizing the CellTiter Glo Luminescent Cell Viability Assay (Promega) according to manufacturer's instructions. Treatment of cells with 0.1% Triton X-100 for 1 hr served as negative viability controls. Raw luminescence values were normalized to control group means and compared across experimental conditions.

2.2.17 Live-cell imaging

All live-cell imaging experiments were performed on a Nikon A1 laser-scanning confocal microscope system outfitted with a Tokai HIT stagetop incubator utilizing 40X and/or 60X oil immersion objectives (CFI Plan Apo Lambda 60X Oil, Nikon; CFI Plan Fluor 40X Oil, Nikon). Following transfections and/or treatments, medium was changed to phenol red-free growth medium (Gibco) and cells were allowed to equilibrate on the preheated (37°C and 5% CO_2) stagetop incubator for 10 min prior to imaging. Acute blue light stimulation was achieved by utilizing the 488nm laser line and the stimulation module within Nikon Elements imaging software. Activation duration varied from 1-8 sec and laser power ranged from 1-20% as indicated in different experiments. Stimulation regions of interest (ROIs) were drawn over fields of view prior to image acquisition. Following 2-5 baseline images, laser stimulation was performed and cells were imaged for up to 1 hr post-activation.

2.2.18 Fluorescence Recovery After Photo-bleaching (FRAP) Imaging

Initially, granules or inclusions were identified using a 60X oil immersion objective by confocal microscopy and a 2x2 μm^2 bleaching ROIs were drawn over objects of interest. Reference ROIs of the same size were drawn in adjacent, non-bleached cells to control for photo-bleaching. Following 2-5 baseline images, objects were bleached for 500 ms using 50% laser power (488nm or 594 nm laser lines) and cells were imaged for up to 5 min post-bleaching without delay.

2.2.19 High-throughput LED Screening

Following transfection or transduction, plates were placed into a pre-warmed Tokai HIT stage-top incubator and allowed to equilibrate for 30 min prior to imaging. Custom 96-well LED arrays were positioned above wells to provide blue light stimulation (~0.3 mW, 465 nm) and were interfaced with Nikon Elements imaging software to cooperate with imaging protocols. Communication between the LED array and microscope occurred through a 5 V analog output transmitted from a Texas Instruments BNC-2110 triggering device. Voltage signals were interpreted by a microcontroller by taking real-time voltage measurements corresponding to a specific light group combination. Through the use of a map function, the software was able to assign a value to each light group and turn the group on or off following the reading of the corresponding value by the microcontroller. Automated imaging protocols were designed and executed utilizing the Jobs module within Nikon Elements imaging software. In brief, the microscope was first programmed to perform three sequential baseline plate scans prior to light exposure. Epifluorescent images were acquired with a Prime 95B CMOS camera (Photometrics) using the ET-dsRED filter set (Chroma). Nine fields of view were imaged over time per well in duplicate per experiment per condition. Baseline images were acquired every 10 min for 30 min in total. This was followed by simultaneous blue light stimulation and image acquisition for up to 24 hrs. Every 10 min during the stimulation period, LED diodes were programmed to sequentially switch off and allow for image acquisition. Following completion of imaging within wells, LED diodes were programmed to switch back on to resume light stimulation and a subsequent set of diodes was programmed to turn off to allow for imaging. This pattern was repeated throughout the remainder of the imaged wells to complete the plate scan.

2.2.20 Recombinant protein purification

MBP-tagged TDP-43 WT and 5FL proteins were purified as previously reported (Wang et al., 2018a). In brief, cells were harvested by centrifugation, resuspended in TDP-43 binding buffer (20mM Tris–Cl pH 8.0, 1 M NaCl, 10mM imidazole, 10% (v/v) glycerol, 1mM DTT), supplemented with complete EDTA-free protease inhibitor cocktail, and lysed via sonication. The protein was purified over Ni-NTA agarose beads (Qiagen) and eluted from the beads using 20mM Tris–Cl pH 8.0, 1 M NaCl, 300mM imidazole, 10% (v/v) glycerol, 1mM DTT. The eluate was further purified over amylose resin (NEB) and eluted using 20mM Tris–Cl pH 8.0, 1 M NaCl, 10mM maltose, 10% (v/v) glycerol, 1mM DTT. The protein was concentrated, flash frozen in liquid N_2, and stored as aliquots in -80°C until further use.

2.2.21 In vitro phase separation and aggregation assays

To induce formation of droplets, the proteins were first buffer exchanged into 20mM HEPES (pH 7.4), 150mM NaCl, and 1mM DTT using a Micro Bio-Spin P-6 Gel column (Bio-Rad). The protein was then centrifuged at 16,000 rpm for 10 min to remove any preformed aggregates and the protein concentration was measured via a Bradford assay. LLPS was initiated with the addition of 10% dextran (final buffer conditions of 5μM TDP43, 15mM Hepes (pH 7.4), 150mM NaCl, and 1mM DTT with the indicated amounts of total yeast RNA) and droplets were imaged using DIC microscopy.

To measure aggregation kinetics, TDP-43 was thawed and centrifuged at 16,000 rpm for 10 min. Protein concentration was measured via Bradford and TDP-43 WT or 5FL were diluted to a final concentration of 5μM (in 20mM Hepes (pH 7.0), 150mM NaCl, 1mM DTT, with indicated

quantities of RNA). Aggregation was initiated by cleavage of the MBP tag using 5μg/mL TEV protease and monitored via turbidity measurements using a TECAN M1000 plate reader.

2.2.22 Electron Microscopy

Transmission electron microscopy (TEM) of purified TDP-43 WT and 5FL aggregates was performed as described previously (Guo et al., 2018). In brief, following the aggregation assays described above, 10μL of each sample was adsorbed onto 300-mesh Formvar/carbon-coated copper grids (Electron Microscopy Sciences, Hatfield, PA) and stained with 2% (w/v) uranyl acetate. Excess uranyl acetate solution was removed prior to drying of the grids. Samples were then imaged using a JEOL-1010T12 transmission electron microscope.

2.2.23 Image quantification and analysis

All image visualization and quantification was performed utilizing Nikon Elements Imaging Software and analyses were performed in a double-blind fashion. For fixed-cell image quantification of stress granule co-localization and granule size, 4-5 fields of view were analyzed per condition. EGFP-TDP43 granules were examined and percentages of granules co-localizing with stress granule markers (G3BP1, eIF4G) were calculated. Maximum intensity projections for each field of view were generated and granule area was determined using automated object detection.

For FRAP imaging experiments, mean fluorescence intensity was tracked within bleaching ROIs over time. Intensity values were corrected for photo-bleaching utilizing reference ROIs drawn within adjacent, non-bleached cells in the imaging field. Fluorescence intensity values were

converted to percentages of baseline (pre-bleach) fluorescence intensity means, with minimum fluorescence intensity values collected throughout the imaging period set to 0%, and percentage fluorescence recovery to baseline values was plotted over time.

Time-lapse image sequences acquired during high-throughput LED screening were analyzed utilizing automated object recognition to identify intracellular optoTDP43 particles and inclusions. Objects were defined by fluorescence intensity and object area thresholding. The number of cells containing detected objects were tracked over time and divided by the total number of cells within the imaging field to generate percentage of cells with inclusions for each timepoint within the imaging sequence. Analysis of neuronal survival in longitudinal imaging datasets was performed through monitoring of the far-red iRFP670 fluorescent reporter. Cell death was defined by somatic rounding, neurite retraction/blebbing and loss of fluorescence signal. Times-of-death were recorded as the last timepoint at which neurons were observed to be alive and were used to generate Kaplan-Meier survival curves.

Quantification of light-induced granule formation and dissociation was performed using the spot detection function within Nikon Elements imaging software. Granules were identified according to size and contrast thresholding. Granule number per cell was monitored over time in pre-identified cells that were labeled by an ROI. Raw granule number per cell values were first normalized to baseline values per cell over time. In order to calculate normalized granule number per cell over time, a weighted baseline intensity and cell area was determined. Baseline cell fluorescence intensity and area were determined from the image acquired prior to light stimulation and from this means were calculated across all experimental groups to control for differences in protein concentration and cell size. Total group baseline mean fluorescence intensity and cell area were then used to weight granule number values per cell by dividing individual cell values by total

group means. For granule dissociation rate quantification, raw granule number per cell values were first normalized to baseline values. Normalized granule number values were then converted to percentages of each individual cell's maximum granule number per stimulation cycle. Mean percentages of cell maximum granule number were then plotted over time for each stimulation cycle.

2.2.24 Statistics

Statistical significance was calculated by Graphpad Prism software (Version 7.03) and resulting P values less than or equal to 0.05 were deemed to be significant. Unpaired Student's t-tests were used to determine statistical significance in data sets comparing two variables. Two-way ANOVAs with Sidak Post-hoc analysis was used for comparisons of FRAP and granule formation/intracellular inclusion screening curves. Pearson's correlations were performed to determine r^2 values between data sets. Exponential decay nonlinear regression analysis was performed to compare optoLCD dissociation curves across groups. For survival analysis, Kaplan-Meier estimates were used to generate survival curves and Gehan-Breslow-Wilcoxon tests were used to compare across groups. Cumulative risk-of-death curves were generated as described previously (Malik et al., 2018) using custom scripts in RStudio.

2.3 Results

2.3.1 Optogenetic modulation of TDP-43 inclusions

We generated an optogenetic Cry2olig-TDP-43-mCherry expression construct (optoTDP43) to selectively induce TDP-43 proteinopathy under the spatiotemporal control of light stimulation. Cry2olig is a variant of the Photolyase-Homologous Region (PHR) of the Cryptochrome 2 protein from *Arabidopsis thaliana* that undergoes reversible homo-oligomerization (~5 min) in response to blue light (Taslimi et al., 2014) (Figure 3A, top). Due to recent findings, suggesting the importance of N-terminal oligomerization in promoting higher-order assembly and LLPS of TDP-43 (Afroz et al., 2017; Chang et al., 2012; Mompeán et al., 2017; Wang et al., 2018a), we positioned the Cry2olig domain on the N-terminus of the full-length TDP-43 protein. We first tested whether Cry2olig-mediated increases in focal concentrations of optoTDP43 protein leads to intracellular TDP-43 proteinopathy upon light exposure (Figure 3A, bottom). To monitor this event, we performed automated epifluorescence imaging of live HEK293 cells expressing the mCherry-tagged optoTDP43 protein (Figure 3B, top). Cells were intermittently imaged during a persistent blue light treatment using a 96-well LED array positioned within a stage-top incubator. optoTDP43-expressing cells exposed to blue light showed a progressive depletion of nuclear optoTDP43 signal and developed significantly more cytoplasmic inclusions relative to optoTDP43-expressing cells kept in the dark over a 24 hr live-imaging session (Figure 3B-C, Appendix Video 1). TDP-43 was not mislocalized in cells expressing Cry2olig-mCh alone with or without light exposure, as assessed by immunofluorescence and subcellular fractionation/western blotting (Figure 3A-B). TDP-43 inclusions were absent from TDP-43-mCh-expressing cells with or without light exposure during the imaging period indicating

that optoTDP43 inclusion formation is selectively driven by light-induced oligomerization of TDP-43 and not TDP-43 overexpression (Figure 3C). Consistent with this observation, size-exclusion chromatography confirmed that light treatment induced the formation of higher-order optoTDP43 protein oligomers (Figure 5A-B, top bands). Together, these data indicate that light treatment initiates intracellular oligomerization of the optoTDP43 protein independent of overexpression-induced aggregation.

We next evaluated whether the features of optoTDP43 inclusions recapitulate the biochemical and neuropathological hallmarks of TDP-43 proteinopathy seen in patient tissue, including detergent-insolubility, N-terminal cleavage, C-terminal hyperphosphorylation, p62 co-localization, and the formation of ubiquitin-enriched inclusions (Al-Sarraj et al., 2011; Scotter et al., 2015). We first performed fluorescence recovery after photo-bleaching (FRAP) analysis of light-induced optoTDP43 inclusions to first assess the material state of light-induced optoTDP43 inclusions. While the Cry2-mCh signal recovered immediately, the optoTDP43 inclusions exhibited minimal signal recovery following photobleaching, indicating the formation of immobile intracellular protein assemblies (Figure 3D-E; Appendix Video 2). In addition, detergent-solubility fractionation and immunoblotting for TDP-43 and mCherry proteins showed that light induced a dramatic shift in optoTDP43 to the insoluble fraction and promoted N-terminal cleavage (Figure 3F, Figure 5C), mimicking the biochemical profile observed in ALS/FTLD patient tissue (Figure 5D). TDP-43-mCh-expressing cells did not display a similar shift in solubility or cleavage in the presence or absence of light when examined at the same timepoint (Figure 3F). Endogenous TDP-43 was also detected in the insoluble fraction and exhibited enhanced N-terminal cleavage in optoTDP43-expressing cells exposed to light (Figure 3F). Size-exclusion chromatography similarly revealed a shift of endogenous TDP-43 species to heavier fractions relative to cells in the

dark (Figure 5A). These combined data suggest that optoTDP43 sequesters non-optogenetic TDP-43 proteins into light-induced insoluble fraction. This phenomenon is likely due to TDP-43-specific interactions, as Cry2olig-mCh expression did not affect endogenous TDP-43 solubility or cleavage regardless of light exposure (Figure 5E).

We next confirmed the ability of optoTDP43 to directly recruit other non-optogenetic TDP-43 species into light-induced inclusions by co-expressing an EGFP-tagged TDP-43 construct along with optoTDP43 or Cry2-mCh alone. We found that EGFP-TDP-43 co-localized with the light activated optoTDP43 inclusions, while no such co-localization was observed with Cry2-mCh (Figure 5F). Furthermore, optoTDP43 inclusions are p62-positive (Figure 3G, 82.9%), hyperphosphorylated in the C-terminal domain (Figure 3H, 85.7%), and colocalize with ubiquitin (Figure 5G) as seen in patient tissue (see for example Figure 3I-J). Together, these data indicate that light-activated optoTDP43 inclusions exhibit the biochemical and pathological hallmarks of TDP-43 proteinopathy and may seed endogenous TDP-43 aggregation.

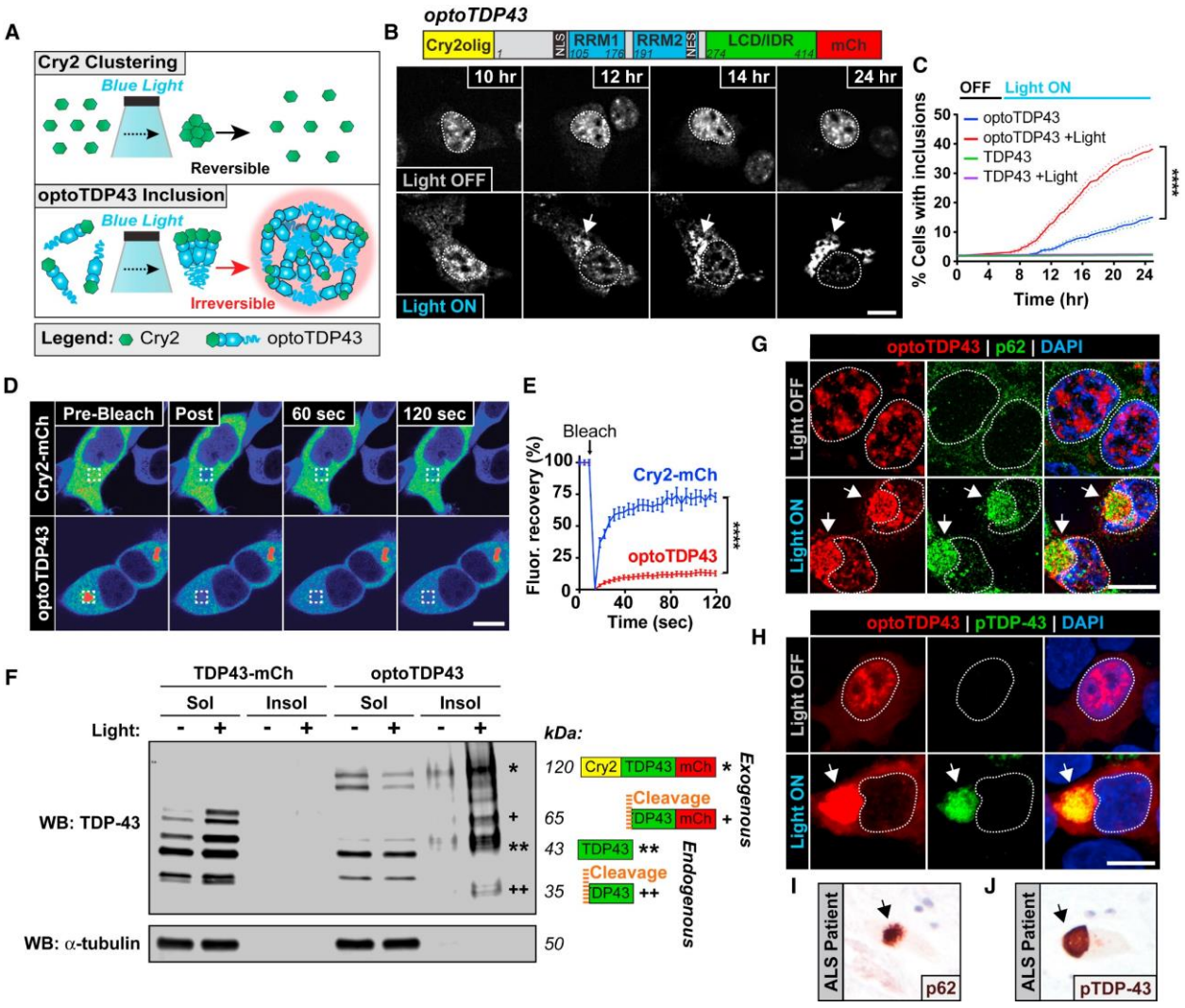

Figure 3. optoTDP43 is a light-inducible model of TDP-43 proteinopathy.

(A) Schematic of light-inducible TDP-43 proteinopathy approach using the Cry2olig photoreceptor and TDP-43 protein. (B) optoTDP43 fusion protein and representative images of HEK293 cells expressing optoTDP43 exposed to blue light stimulation (bottom; ~0.3 mW/cm2; 465 nm) or darkness (top). Cell nuclei are circled. Arrow indicates optoTDP43 inclusion formation with light treatment. (C) Percentage of cells exhibiting optoTDP43 inclusions over time using automated longitudinal live-imaging. n = 494–791 cells. (D) Representative images of FRAP analysis images of Cry2-mCh or light-induced optoTDP43 inclusions. (E) Quantification of FRAP analysis shows lack of signal recovery for optoTDP43 inclusions. n = 18–22 cells. (F) Detergent-solubility fractionation and western blotting for TDP-43 of optoTDP43-expressing cells with and without light stimulation. ∗ indicates full-length exogenous optoTDP43; + indicates optoTDP43 cleavage product; ∗∗ indicates full-length endogenous TDP-43; ++ indicates

endogenous TDP-43 cleavage product. (G–J) Immunofluorescence analysis of optoTDP43 inclusions (G and H) and ALS patient spinal cord (I and J) for pathological hallmarks p62 (G and I) and C-terminal hyperphosphorylated TDP-43 (H and J). Data shown are mean ± SEM. **** $p < 0.0001$. Scale bars represent 10 μm.

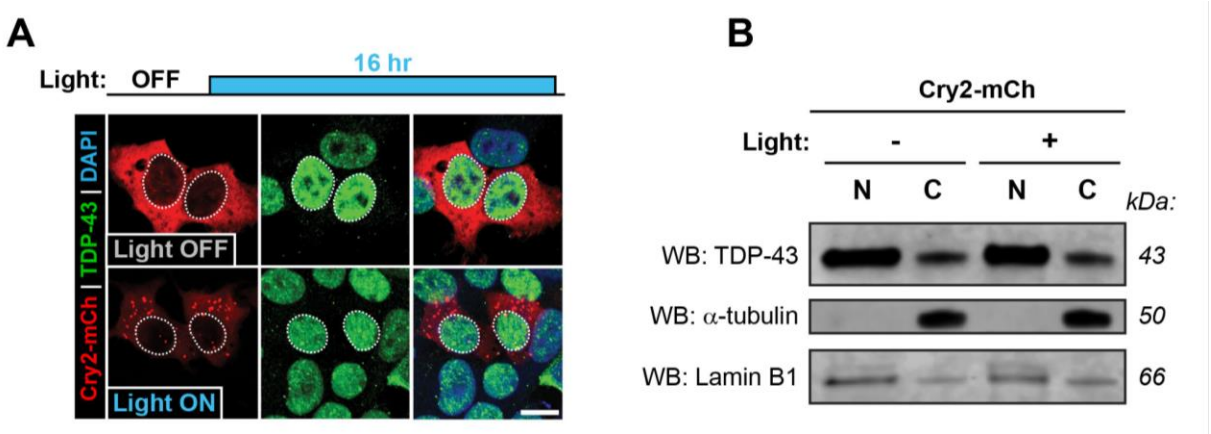

Figure 4. Chronic blue light stimulation alone does not induce mislocalization or aggregation of endogenous TDP-43.

(A-B) HEK293 cells expressing Cry2olig-mCh were exposed to chronic blue light stimulation (16h, ~0.3 mW/cm2, 465 nm) and analyzed for mislocalization of endogenous TDP-43. (A) Cells exposed to chronic blue light stimulation (bottom) or darkness (top) both show no cytoplasmic mislocalization of endogenous TDP-43 (green) by immunofluorescence. Cell nuclei are circled. (B) Cell lysates were collected following chronic blue light stimulation (lanes 3-4) or darkness (lanes 1-2) and separated into nuclear (N; lanes 1, 3) and cytoplasmic (C; lanes 2, 4) fractions. Western blot analysis of endogenous TDP-43 shows no cytoplasmic mislocalization of TDP-43 with or without blue light stimulation. Scale bar = 10 μm.

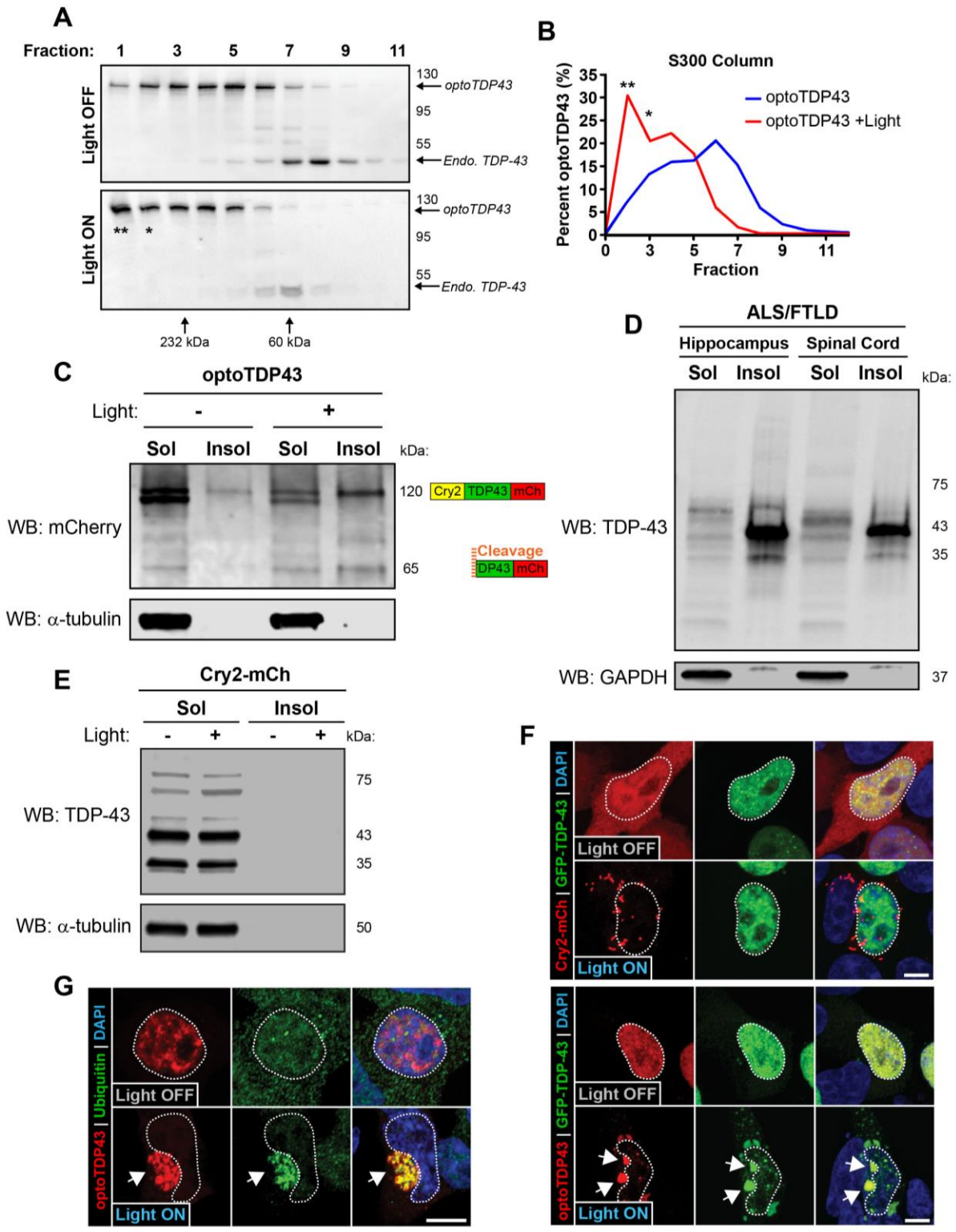

Figure 5. Chronic blue light stimulation promotes the formation of high-molecular-weight optoTDP43 oligomers and recruitment of non-optogenetic TDP-43 to inclusions.

(A-B) Cell lysates from HEK293 cells expressing optoTDP43 were collected and analyzed by size exclusion chromatography. Samples were collected from cells either exposed to stimulation with blue light (16h, ~0.3mW/cm2, 465 nm, bottom) or kept in darkness (top). The void volume of the column was determined with blue dextran (2000 kDa). Column fractions were subjected to SDS-PAGE and western blot analysis for TDP-43. The molecular weight standards are indicated to the right of the representative blots. The elution peak of column size standards (232 kDa and 60 kDa) are indicated by arrows at the bottom of the gel. (B) optoTDP43 proteins exposed to blue light stimulation demonstrate a shift towards higher-molecular weight species (fractions 1-3, indicated by asterisks), indicating light-induced oligomerization. (C) Lysates from optoTDP43-expressing cells exposed to chronic blue light treatment (16h, ~0.3mW/cm2, 465 nm) or darkness were collected and separated into detergent-soluble (lanes 1, 3) and RIPA-insoluble, urea-soluble (lanes 2, 4) fractions. Western blot analysis of mCherry proteins shows an enhanced shift of full-length and N-terminal cleaved optoTDP43 products in the detergent-insoluble fraction. (D) ALS/FTLD patient tissue from the hippocampus and spinal cord was separated into detergent-soluble (lanes 1, 3) and RIPA-insoluble, urea-soluble (lanes 2, 4) fractions prior to western blot analysis of TDP-43. (E) Cell lysates collected from Cry2-mCh-expressing cells following chronic blue light stimulation (lanes 2, 4) or darkness (lanes 1, 3) were separated into detergent-soluble (lanes 1, 2) and RIPA-insoluble, urea-soluble (lanes 3, 4) fractions. Western blot analysis probing for endogenous TDP-43 shows no recruitment of TDP-43 to the insoluble fraction with or without chronic blue light stimulation. (F) To confirm the ability of optoTDP43 to recruit non-optogenetic TDP-43 species into light-induced inclusions, HEK293 cells were co-transfected with either optoTDP43 (bottom) or the photoreceptor-only control Cry2olig-mCh (top) and EGFP-TDP43. optoTDP43-expressing cells exposed to chronic blue light stimulation (16h, ~0.3mW/cm2, 465 nm) show co-localization of light-induced inclusions with EGFP-TDP43 (indicated by arrows). Light-induced Cry2olig-mCh clusters show no co-localization with EGFP-TDP43 signal, indicating a TDP-43:TDP-43 interaction-dependence of recruitment to induced optoTDP43 inclusions. Cell nuclei are circled. Scale bar = 10 µm. (G) Cells expressing optoTDP43 were exposed to chronic blue light stimulation (16h, ~0.3mW/cm2, 465 nm, bottom) or darkness (top) and immunostained for ubiquitin (green). Light-induced optoTDP43 inclusions strongly co-localize with ubiquitin signal (indicated by arrows). Cell nuclei are circled. Scale bar = 10 µm.

2.3.2 Aberrant LCD interactions drive the formation of TDP-43 inclusions

Recent studies indicate that LCDs mediate the homo- and hetero-oligomerization of LCD-containing proteins through LLPS (Elbaum-Garfinkle et al., 2015; Molliex et al., 2015; Nott et al., 2015) and aberrant interactions between these low-complexity regions are hypothesized to promote the maturation/fibrillization of phase-separated droplets (Harrison and Shorter, 2017). To determine whether the TDP-43 LCD mediates the formation of optoTDP43 inclusions, we employed the optoDroplet approach (Shin et al., 2017) to study intracellular TDP-43 LCD phase separation behavior using the WT Cry2 PHR domain (Cry2PHR). This photoreceptor has a higher saturation concentration as compared to the lower-threshold, and more potent, Cry2olig photoreceptor used to produce optoTDP43 inclusions, and allows us to detect subtle changes in droplet properties. We first generated an optogenetic construct containing the Cry2PHR photoreceptor fused to the TDP-43 LCD (optoLCD) and found that optoLCD proteins readily underwent reversible light-induced phase separation (LIPS) in response to brief pulses of blue light in HEK293 cells (Figure 6A-B, Appendix Video 3). These findings are consistent with studies reporting that purified TDP-43 LCD protein undergoes LLPS *in vitro* (Conicella et al., 2016; Sun and Chakrabartty, 2017). Light-induced clustering of the Cry2PHR photoreceptor alone did not induce droplet formation, indicating that the TDP-43 LCD drives LIPS (Figure 6A-B). Light-activated optoLCD granules also displayed classical properties of phase-separated liquid-like protein droplets (Brangwynne et al., 2015, 2009), undergoing fusion upon granule contact (Figure 7A) and exhibiting concentration- (Figure 6C, Figure 7B) and light-dependent droplet formation (Figure 7C). These data are consistent with light-activated optoDroplet formation of the LCDs of other RNA-binding proteins, including FUS, HNRNPA1 and DDX4 (Shin et al., 2017).

To determine whether aberrant LCD interactions promote the formation of intracellular inclusions, we next examined the effects of repetitive and chronic LIPS on optoLCD droplet dynamics in live cells. We tested the wildtype TDP-43 LCD and optoLCD proteins containing three ALS-causing mutations (M337V, Q331K, A321V), which alter LLPS properties and promote aggregation of TDP-43 in diverse *in vitro* and cellular models (Gopal et al., 2017; Johnson et al., 2009; Schmidt and Rohatgi, 2016). Using a 10-minute cycling blue light stimulation protocol to induce repetitive LIPS of the LCD, we observed gradual maturation of optoLCD granules over successive cycles of droplet formation (Figure 6D-E; Appendix Video 4). optoLCD droplets exhibited a progressive increase in the number of persistent, irreversible optoLCD granules with each successive cycle, an effect that was exacerbated by ALS-linked mutations (Figure 6E-F). Mutant optoLCD proteins displayed more rapid conversion to stable droplets upon successive LIPS, as determined by an increased number (Figure 6F) and size (Figure 6G) of persistent granules, compared to WT optoLCD droplets despite similar protein level as determined by Western blot analysis (Figure 7D). We next employed a chronic blue light stimulation paradigm to investigate whether the WT optoLCD droplets matured into pathologically-relevant inclusions with prolonged LCD oligomerization. Interestingly, a 4 hr chronic blue light stimulation resulted in hyperphosphorylated and p62-positive optoLCD inclusions (Figure 6H) that were immobile as evaluated by quantitative FRAP analysis (Figure 6I). These results indicate that TDP-43 LCD undergoes intracellular phase separation upon self-oligomerization and that maturation of LCD droplets, either through repetitive/chronic phase transitions or ALS-linked mutations, drives LCD inclusion formation.

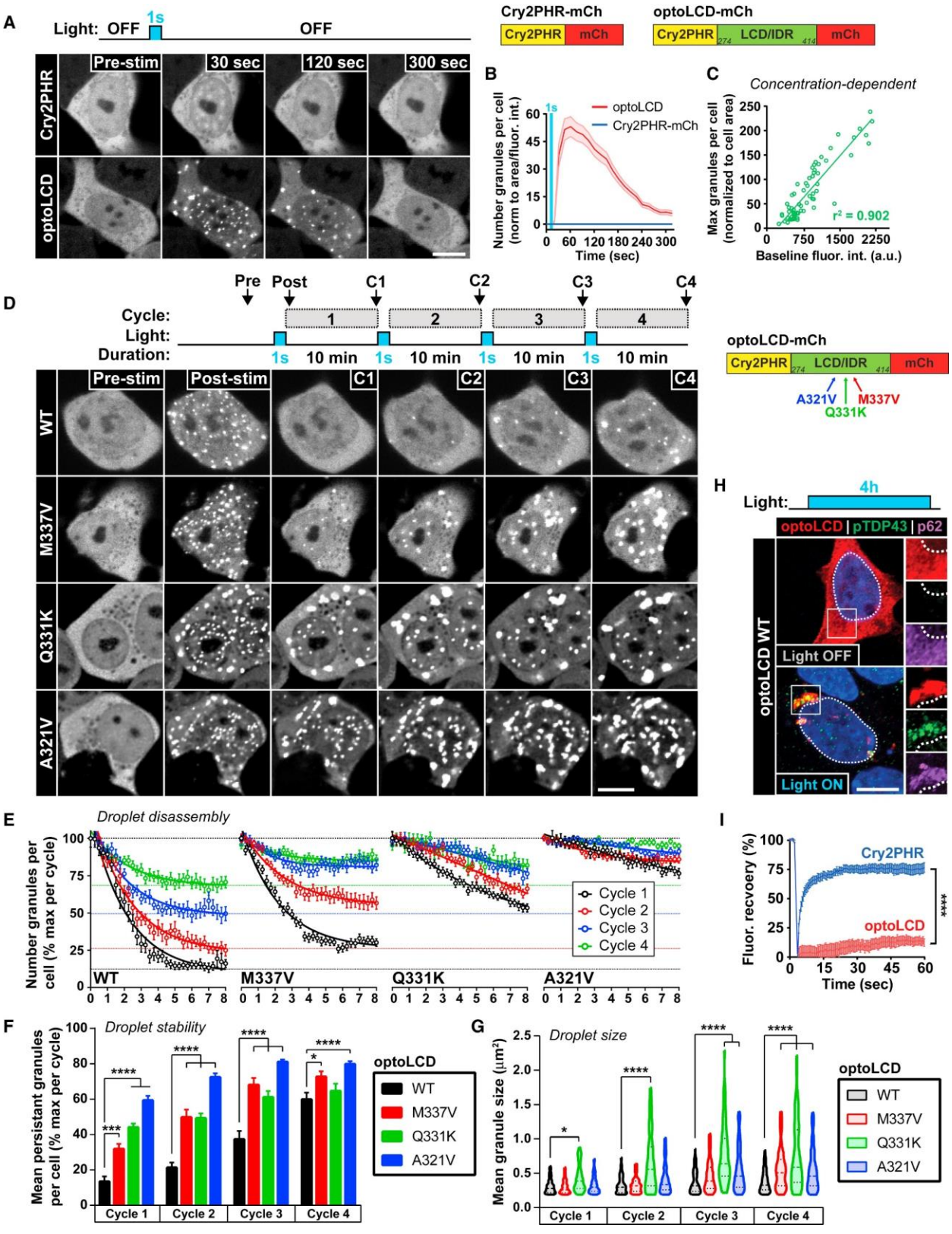

Figure 6. Optogenetic phase transitions of the TDP-43 LCD drives inclusion formation.

(A) Representative images of HEK293 cells expressing Cry2PHR-mCh (top) or optoLCD (bottom) exposed to acute blue light stimulation (1 sec, 1% laser power, 488 nm). (B) Quantification of normalized granule number per cell in response to acute stimulation. n = 26-48 cells. (C) Quantification of protein concentration-dependence of optoLCD phase transitions. r^2 was determined by Pearson's correlation. Data points represent individual cells. n = 66 cells. (D) Representative images of repetitive light-induced phase transitions of WT and ALS-linked mutant (M337V, Q331K, A321V) optoLCD proteins during a cycling light stimulation protocol consisting of a single blue light pulse (1 sec, 1% laser power) every 10 min for 40 min. Images shown are the final images acquired per cycle prior to subsequent light stimulation. (E) Quantification of granule disassembly dynamics following cycling stimulation protocol shown in (D). n = 21-31 cells per construct. (F-G) Quantification of irreversible optoLCD number (F) and area (G) per cycle with repeated phase transitions. (H) Immunofluorescence analysis of optoLCD inclusions formed following chronic blue light stimulation (4 hrs, ~0.3mW/cm2, 465 nm) for hyperphosphorylated TDP-43 (green) p62 (purple). (I) Quantification of fluorescence recovery after photobleaching of optoLCD inclusions formed by chronic light stimulation. n = 16 cells per construct. Data points shown are mean +/- S.E.M. ****, $p < 0.0001$. Scale bars = 10 µm.

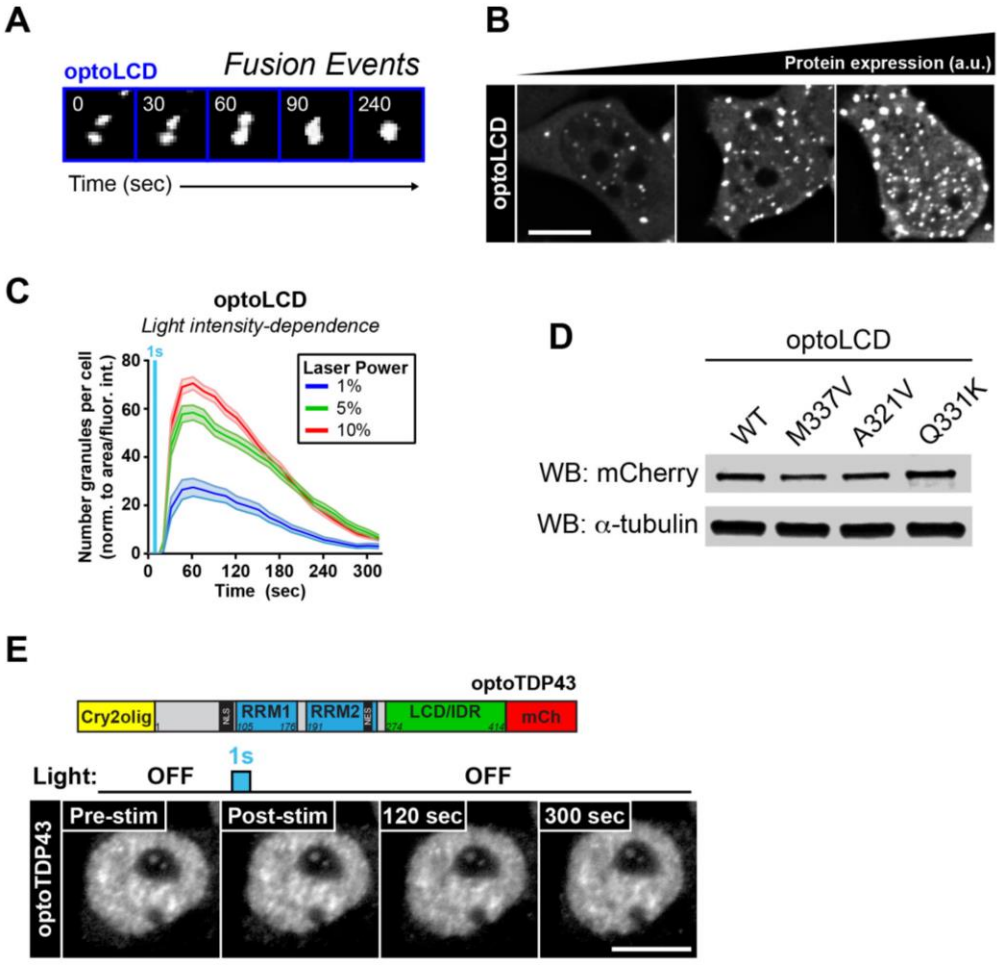

Figure 7. optoLCD granules display properties of phase-separated droplets and full-length optoTDP43 does not form optoDroplets.

(A) Representative images of individual optoLCD granules showing fusion events following acute blue light stimulation (1 sec, 1% laser power, 488 nm). optoLCD granules underwent fusion and subsequent relaxation upon granule:granule contact, suggesting a liquid-like state of light-induced LCD granules. (B) Representative images of optoLCD particle formation following acute blue light stimulation (1 sec, 1% laser power, 488 nm) in cells expressing increasing concentrations of optoLCD proteins (as determined by relative fluorescence intensity). (C) Cells expressing optoLCD were exposed to acute blue light stimulation of increasing laser intensity (1 sec, 1-10% as indicated, 488 nm) and normalized granule number per cell was tracked over time. optoLCD proteins displayed enhanced phase transition responses following acute blue light stimulation of increasing light input, indicating a tunable property of light-induced LCD phase transitions as a function of activated photoreceptor molecules. *n* = 25-67 cells per laser setting. (D) Western blot analysis of WT and mutant optoLCD protein expression levels. (E) Full-length optoTDP43

was expressed in HEK293 cells exposed to acute blue light stimulation (1 sec, 10% laser power, 488 nm) to determine whether full-length TDP-43 could undergo LIPS. No optoTDP43 granule formation was observed in response to acute blue light stimulation. Data shown are mean +/- S.E.M. Scale bars = 10 μm.

2.3.3 RNA-binding inhibits homotypic phase separation and pathological aggregation of the TDP-43 LCD

While the TDP-43 LCD undergoes intracellular LIPS with acute blue light treatment (Figure 6A), the same light stimulation paradigm did not induce a phase transition of full-length optoTDP43 (Figure 7E; Appendix Video 5), even when fused to the more potent homo-oligomerizing Cry2 photoreceptor domain (Cry2olig) (Taslimi et al., 2014). Given the ability of full-length purified TDP-43 to undergo rapid LLPS (McGurk et al., 2018; Molliex et al., 2015; Wang et al., 2018a), we suspected there may be components within the intracellular environment which oppose TDP-43 LLPS in our model. The presence of the prominent TDP-43 RNA-binding domains (or RNA-recognition motifs, RRMs), along with reports of an increased aggregation propensity of C-terminal cleavage products lacking these domains (Zhang et al., 2009), led us to hypothesize that RNA-binding inhibits the ability of the full-length optoTDP43 protein to homo-oligomerize via its LCD.

To test this notion, we fused the Cry2olig photoreceptor domain to the TDP-43 RRMs and evaluated the ability of the RRM domains to oligomerize in response to light. The enhanced homo-oligomerization of the Cry2olig photoreceptor domain allowed us to ensure that any observed inhibition of LIPS was likely a result of endogenous TDP-43 properties and not due to insufficient Cry2 activation. While the TDP-43 LCD fused to Cry2olig domain (Cry2olig-LCD) underwent LIPS in response to blue light and mimicked the droplet-like properties seen with optoLCD

assemblies (Figure 8A-B, top row; Figure 9A-E; Appendix Video 6), light treatment did not stimulate TDP-43 RRM phase separation (Figure 8A-B, bottom row; Appendix Video 6). We next generated fusion proteins containing both the TDP-43 RRMs and Cry2olig-LCD (RRMs + LCD WT) to test whether the RRM domains affect TDP-43 LCD LIPS. Strikingly, the RRMs completely inhibited LIPS of the LCD, even when the potent Cry2olig photoreceptor was employed (Figure 8C-D, top row; Appendix Video 6). To test whether RNA binding to the RRMs inhibits TDP-43 LCD oligomerization, we introduced five point phenylalanine to leucine mutations within the RRM domains (5FL), which were previously shown to significantly impair, but not abolish, TDP-43 RNA-binding (RRMs + LCD 5FL) (Elden et al., 2010). Remarkably, robust induction of LIPS is observed following light stimulation (Figure 8C-D, bottom row; Appendix Video 6). Since Cry2olig fusion proteins containing mutated RRMs alone (RRMs 5FL) did not show any light-induced droplet formation (Figure 9F), the recovery of LIPS in the RNA-binding deficient construct is mediated by the LCD. To ensure that RNA-binding activity, and not a conformational change in the construct, inhibited LIPS, we assessed whether the TDP-43 LCD can drive phase separation of the FUS RRM (fusRRM WT + LCD). Like the TDP-43 RRMs, the FUS RRM fusion to the TDP-43 LCD failed to undergo LIPS (Figure 8E-F, top row; Appendix Video 6). However, when similar phenylalanine to leucine point mutations that compromise the RNA-binding ability of the FUS RRM were introduced (Daigle et al., 2013) (fusRRM 4FL + LCD), the FUS RRM + TDP-43 LCD fusion protein underwent rapid LIPS (Figure 8E-F, bottom row; Appendix Video 6). These data indicate that RNA-binding dictates the ability of the TDP-43 LCD to homo-oligomerize and drive LIPS.

To determine whether RNA-binding also plays a role in the formation of pathological inclusions of full-length TDP-43, we performed RNA fluorescent *in situ* hybridization (FISH) and

used an RNA dye to assess whether RNA resides within the light-induced optoTDP43 inclusions. Interestingly, RNA was absent in light-induced optoTDP43 inclusions (Figure 8G; Figure 10A). Supporting the notion that RNA-binding dictates the ability of the LCD to drive pathological oligomerization of TDP-43, longitudinal imaging also revealed that RNA-deficient optoTDP43 5FL formed inclusions at a significantly enhanced rate and frequency than the RNA-binding competent optoTDP43 in live cells (Figure 10B).

Since our data suggest that RNA-binding inhibits LCD-driven phase-transitions of TDP-43, we hypothesized that addition of exogenous RNA substrates might inhibit optoTDP43 inclusion formation. To test this hypothesis, we treated optoTDP43-expressing HEK293 cells with blue light for 16 hr to induce inclusions and transfected cells with total HEK293 cell RNA 4 hr after illumination. Surprisingly, there was a measurable reduction (28%) of optoTDP43 inclusion formation in cells treated with purified RNA, as compared to mock-treated cells, following light stimulation (Figure 8H-I). To determine whether mRNA colocalizes with TDP-43 inclusions in patients, we performed RNA FISH using a poly-T probe in ALS/FTLD patient tissue and examined TDP-43/mRNA colocalization. TDP-43 inclusions lacked mRNA signal in both sporadic ALS (sALS) spinal cord (Figure 8J, Figure 10C) and FTLD hippocampus (Figure 8K, Figure 10C). Taken together, we propose that RNA-binding to the TDP-43 RRM domains inhibits LCD:LCD interactions, thus blocking aberrant TDP-43 phase transitions and the formation of pathological inclusions.

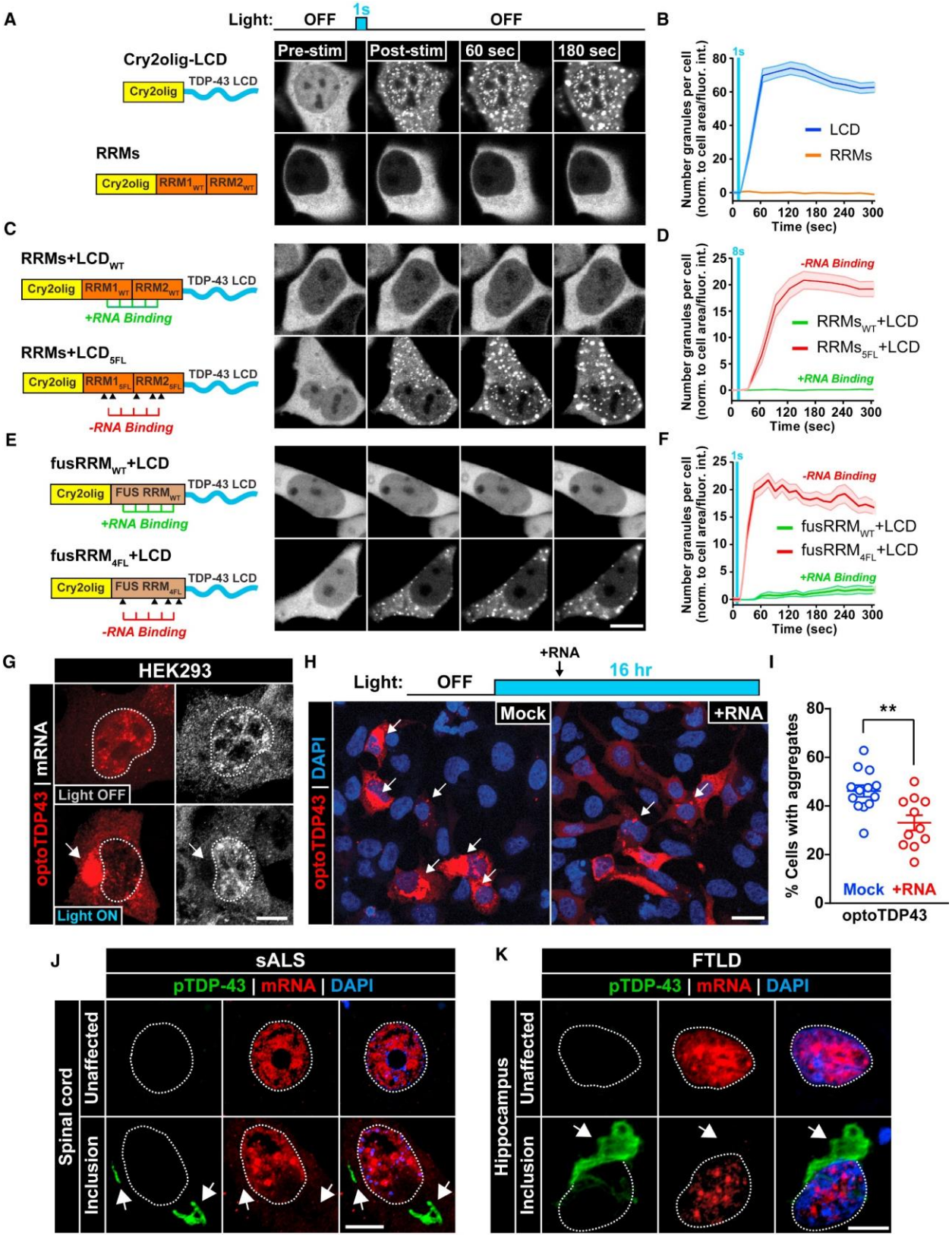

Figure 8. RNA-binding prevents light-induced phase separation and aggregation of TDP-43.

(A-F) HEK293 cells expressing the Cry2olig photoreceptor fused to the TDP-43 LCD (A), TDP-43 RNA-binding regions (RRMs) (A), TDP-43 LCD and functional (WT) RRMs (C), TDP-43 LCD and RNA-binding deficient (5FL) RRMs (C), TDP-43 LCD fused to the functional (WT) FUS RRM (E), or TDP-43 LCD fused to FUS RNA-binding deficient (4FL) RRM (E) were exposed to acute light stimulation (1-8 sec, 10% laser power, 488 nm) and normalized granule number per cell quantification is shown in right hand column (B, D, F). n = 33-59 (A-B), 24-36 (C-D) and 31-45 cells (E-F). Data shown are mean +/- S.E.M. (G) mRNA within full-length optoTDP43 inclusions was assessed by RNA fluorescence *in situ* hybridization (FISH) for Poly-A tails. Arrow indicates absence of mRNA signal within inclusion. (H) Representative images of HEK293 cells expressing optoTDP43 that received mock or RNA (2.5 μg HEK293 total mRNA) treatment 4 hours into a 16 hour chronic blue light treatment. (I) Quantification of optoTDP43-expressing cells with cytoplasmic inclusions. Data points correspond to individual fields of view. n = 662-673 cells. (J-K) RNA FISH analysis of ALS/FTLD patient tissue targeting Poly-A mRNA. TDP-43 inclusions (green, bottom rows) in spinal cord (J, sALS) and hippocampal (K, FTLD) sections both show no co-localization with mRNA signal (red). Data shown are mean +/- S.E.M. **, $p < 0.01$. Scale bars = 10 μm.

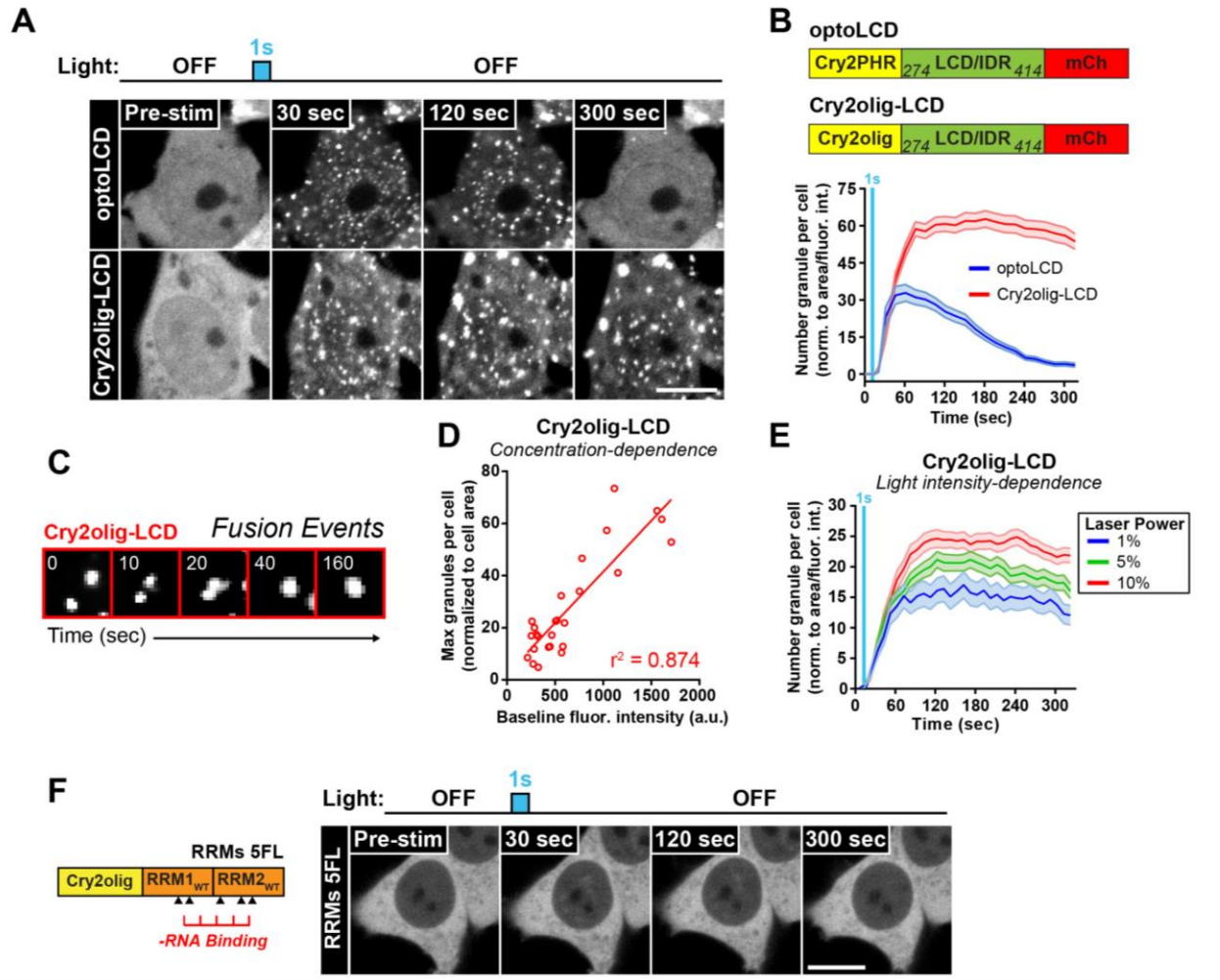

Figure 9. Cry2olig-LCD confers an enhanced phase separation response to light.

(A-B) HEK293 cells expressing either optoLCD (top) or the Cry2olig modified photoreceptive domain fused to the TDP-43 LCD (Cry2olig-LCD, bottom) were subjected to acute blue light stimulation (1 sec, 1% laser power, 488 nm) and granule formation was tracked over time. (B) Quantification of normalized granules per cell over time shows an enhanced phase transition response to light when the TDP-43 LCD is fused to the Cry2olig domain versus the WT Cry2PHR domain. *n* = 25-48 cells per construct. Data shown are mean +/- S.E.M. (C) Representative images of individual Cry2olig-LCD granules undergoing fusion events following acute blue light stimulation (1 sec, 1% laser power, 488 nm). As was observed with optoLCD droplets, Cry2olig-LCD granules underwent fusion and relaxation upon granule:granule contact. (D) A Pearson's correlation was executed to analyze the protein concentration-dependence of Cry2olig-LCD phase transitions in response to acute blue light stimulation (1 sec, 10% laser power, 488 nm). Baseline fluorescence intensity was plotted against maximum granule number per cell during the imaging

period. Data points shown are representative of individual cells. *n* = 26 cells. (E) Cry2olig-LCD-expressing cells were exposed to acute blue light stimulation of increasing laser intensity (1 sec, 1-10% as indicated, 488 nm) and normalized granule number per cell was quantified post-stimulation. Again, an enhanced phase separation response was observed following blue light stimulation of increasing intensity. *n* = 50-81 cells per laser setting. (F) Cells expressing a protein containing the TDP-43 RRMs with RNA-binding mutations fused to the Cry2olig photoreceptor (RRMs 5FL) were exposed to acute blue light stimulation (1 sec, 10% laser power, 488nm). No droplet formation is observed following light stimulation, suggesting the TDP-43 LCD is necessary for LIPS behavior. Data shown are mean +/- S.E.M. Scale bars = 10 μm.

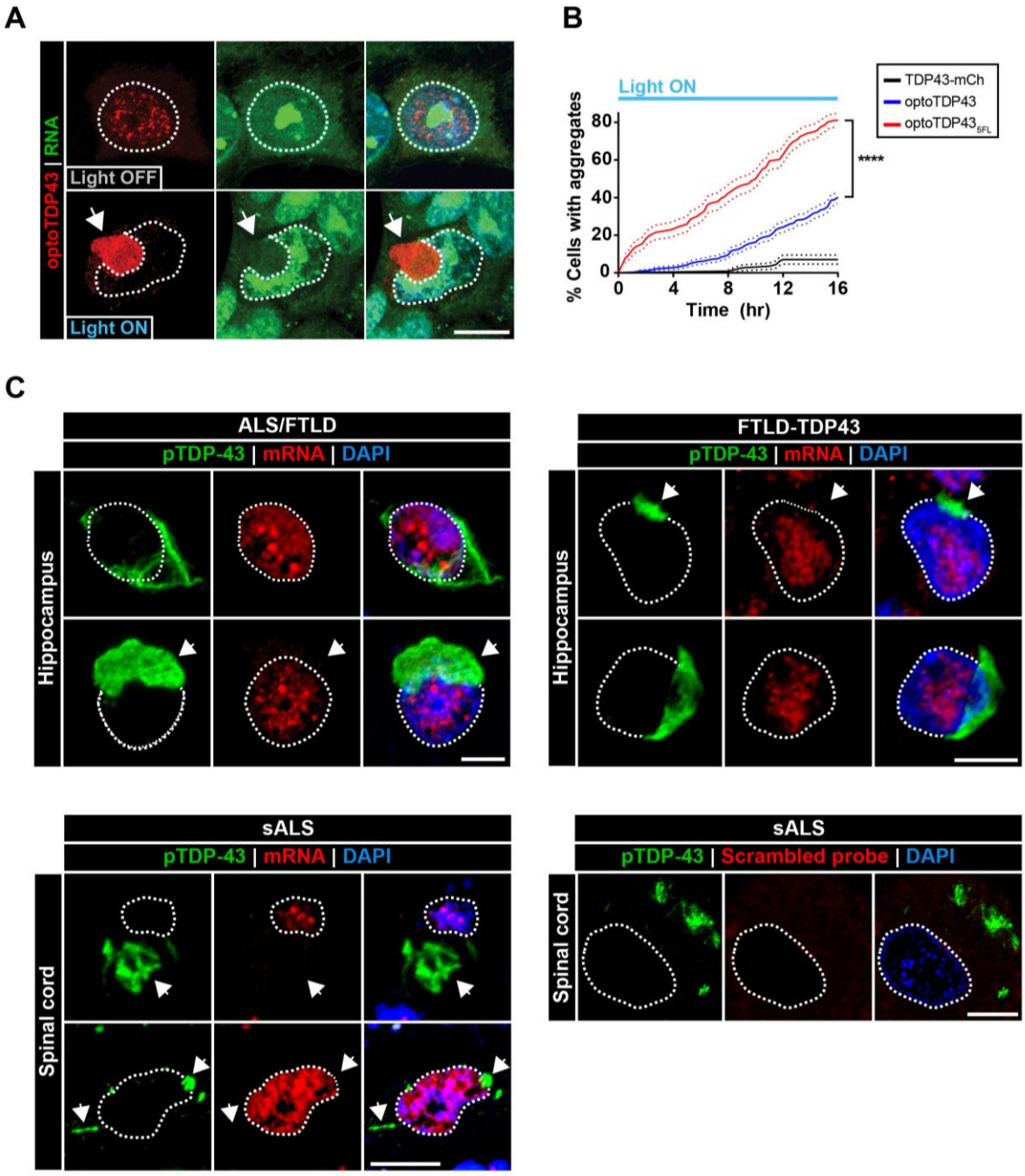

Figure 10. TDP-43 inclusions in patient tissue and optoTDP43 system show an absence of RNA.

(A) optoTDP43 was expressed in HEK293 cells that were exposed to chronic blue light stimulation (16h, ~0.3mW/cm^2, 465 nm) to induce optoTDP43 inclusion formation. Cells were then fixed in ice-cold methanol and stained with SYTO RNAselect non-selective RNA dye to determine whether optoTDP43 inclusions contained any RNA species, in addition to mRNA. optoTDP43 inclusions do not appear to co-stain with SYTO RNAselect dye,

suggesting there are no RNA species contained within inclusions. (B) HEK293 cells expressing WT optoTDP43 (blue), RNA-binding-deficient optoTDP43 5FL (red), or non-optogenetic TDP43-mCh (black) were chronically stimulated with blue light (~0.3mW/cm^2, 465 nm) and simultaneously imaged over time in an automated microscopy screen to assess whether RNA-binding affects full-length TDP-43 inclusion formation. Quantification of percentage of cells with inclusions over time shows a significantly increased rate of light-induced inclusion formation with reduced RNA-binding efficiency (optoTDP43 5FL, red). *n* = 113-239 cells per construct. (C) Additional representative images of mRNA FISH analysis of ALS/FTLD patient tissue. Hippocampal and spinal cord sections from two FTLD cases (*C9ORF72*-FTLD, top left; FTLD-TDP43, top right) and one ALS case (sporadic ALS, bottom left) were examined by immunohistochemistry and RNA FISH. In all cases, no co-localization was observed between mRNA and pTDP-43 signal. Data shown are mean +/- S.E.M. ****, $p < .0001$. Cell nuclei are circled. Scale bars = 10 μm.

2.3.4 RNA antagonizes TDP-43 phase transitions *in vitro* and in cells

We next utilized purified WT TDP-43 and a TDP-43 protein with identical RRM point mutations (TDP-43 5FL, henceforth referred to as RNA-binding deficient TDP-43) to examine whether RNA-binding alters TDP-43 LLPS and aggregation *in vitro*. In the absence of RNA, C-terminal MBP-tagged TDP-43 WT and 5FL formed liquid-like droplets at physiological salt concentrations that did not form in the presence of 1,6 hexanediol, which disrupts weak contacts between LCDs that drive LLPS (Gopal et al., 2017; Patel et al., 2007) (Figure 11A). However, in the presence of increasing concentrations of total RNA, WT TDP-43 LLPS was inhibited in a dose-dependent manner (Figure 11B). In contrast, the RNA-binding deficient TDP-43 5FL species was unaffected by exogenous RNA (Figure 11B). Upon selective cleavage of the MBP tag with TEV protease, TDP-43 WT and 5FL form solid-phase aggregates (Figure 11C). While WT and RNA-binding-deficient TDP-43 displayed similar aggregation kinetics in the absence of RNA, the addition of RNA completely inhibited WT TDP-43 aggregation (Figure 11C-D). The aggregation

kinetics of TDP-43 5FL was initially delayed in the presence of RNA, likely due to residual RNA-binding (Figure 11D), but the final extent of aggregation was identical to TDP-43 in the absence of RNA upon further incubation (Figure 11C-D). Moreover, the addition of RNase A (2.5μg) 90 min after TEV cleavage reversed the initial inhibition of WT TDP-43 aggregation conferred by RNA addition (Figure 11E).

If RNA-binding prevents aberrant phase separation and TDP-43 inclusion formation, then RNA-binding deficient protein expression should generate TDP-43 proteinopathy. We therefore expressed (non-optogenetic) EGFP-tagged TDP-43 constructs containing wildtype or RNA-binding-reduced RRM domains in HEK293 cells (Figure 11F). Surprisingly, mere expression of the RNA-binding-deficient TDP-43 protein (EGFP-TDP43 5FL) generated large nuclear inclusions that were hyperphosphorylated and p62-positive (Figure 11G). When the protein's NLS was mutated (EGFP-TDP43cyto 5FL), the RNA-binding-deficient protein localized to the cytoplasm and formed hyperphosphorylated and p62-positive inclusions that resembled the neuropathology observed in ALS/FTLD (Figure 11H). This finding suggests that cytoplasmic mislocalization is an upstream event preceding formation of RNA-deficient cytoplasmic inclusions. FRAP analysis revealed that RNA-deficient TDP-43 inclusions in both the nucleus and cytoplasm did not recover from photo-bleaching (Figure 11I-J). Nuclear RNA-binding deficient TDP-43 inclusions also exhibited slightly enhanced fluorescence recovery after photo-bleaching compared to the cytoplasmic RNA-deficient TDP-43. This may be due to the abundance of accessible RNA species in the nucleus whereas RNAs destined for the cytoplasm are pre-assemblied into heterogenous RNP complexes (Köhler and Hurt, 2007). Overall, these findings indicate that RNA-binding dictates the propensity for TDP-43 to form pathologically-relevant inclusions.

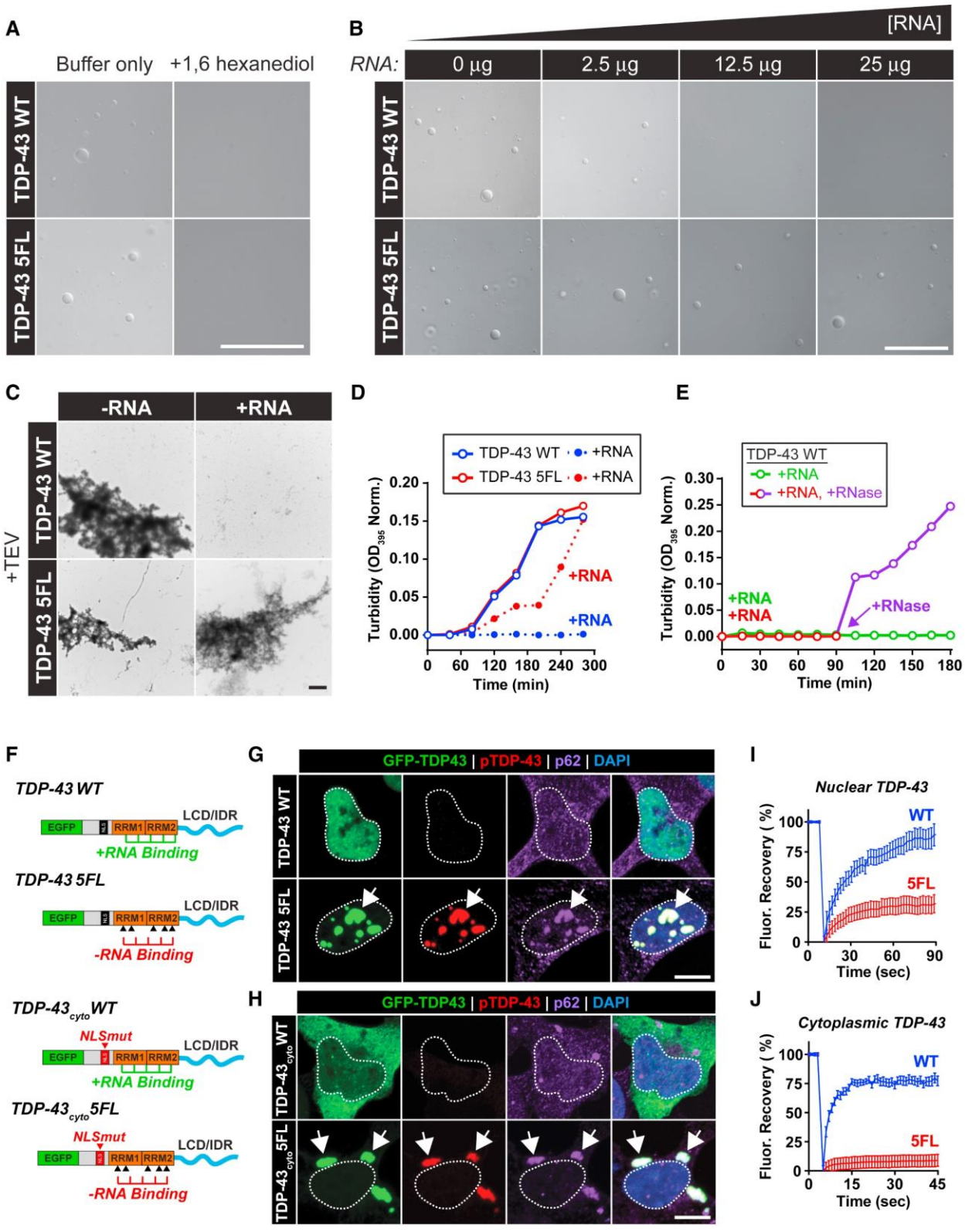

Figure 11. TDP-43 LLPS and aggregation is inhibited by RNA-binding.

(A) Purified TDP43-MBP WT or 5FL (5μM) were incubated for 2 hours (10% dextran buffer, 150 mM NaCl) in the absence or presence of 1,6 hexanediol (10% w/v). Scale bar = 50 μm. (B) Representative DIC images of purified TDP43-MBP WT or 5FL following incubation with increasing concentrations of yeast total RNA. Scale bar = 50 μm. (C) Representative electron micrographs of TDP-43 WT and 5FL following TEV cleavage in the absence (left) or presence (right) of yeast total RNA (15 μg). Scale bars = 4 μm. (D) Turbidity changes (normalized OD_{395} readings) of TDP-43 WT (blue) and 5FL (red) following TEV cleavage in the absence (open circles) or presence (solid circles) of yeast total RNA (15 μg). (E) Turbidity changes (normalized OD_{395} readings) of TDP-43 WT proteins following TEV cleavage in the presence of yeast total RNA-only (25 μg) (green) or yeast total RNA (25μg) followed by RNase A addition (2.5μg) at 90 min post-TEV cleavage (red prior to/purple following RNase A). (F) Construct designs for non-optogenetic TDP-43 vectors containing functional (WT) or RNA-binding deficient (5FL) RRMs. TDP-43cyto constructs contain point mutations in the nuclear localization sequence to mimic cytoplasmic mislocalization. (G-H) Immunofluorescence analysis of cells expressing EGFP-TDP-43 constructs (G) or EGFP-TDP43cyto constructs (H) with/without functional RRMs (WT/5FL) for hyperphosphorylated TDP-43 (red) and p62 (purple). Scale bars = 10 μm. (I-J) FRAP analysis of EGFP-TDP43 5FL (G) and EGFP-TDP43cyto 5FL (H) inclusions. *n* = 14-23 (I) and 20-24 cells (J). Data shown are mean +/- S.E.M. Scale bars = 10 μm.

2.3.5 RNA-deficient phase separation relies upon aromatic residues in the TDP-43 low-complexity domain

Given the contribution of aromatic interactions to the phase separation of related RBPs like FUS (Lin et al., 2017; Murthy et al., 2019; Wang et al., 2018b), we next sought to determine whether LLPS of RNA-deficient TDP-43 might arise through similar mechanisms. To first test the contribution of these amino acids in the phase behavior of the TDP-43 LCD, we performed serine substitutions at all 8 phenylalanine residues within our optoLCD construct (F>S) (Figure 12A), a strategy that has been used successfully to mitigate the contribution of tyrosine-driven cation-pi interactions in the LLPS of FUS (Lin et al., 2017; Wang et al., 2018b). While the WT optoLCD

readily undergoes light-induced phase separation (LIPS), phenylalanine substitutions result in a complete inhibition of droplet formation in response to light stimulation (Figure 12B). To next determine whether these phenylalanine residues play a similar role in LLPS of full-length TDP-43, we performed the same F>S substitutions within the LCD of EGFP-tagged TDP-43 constructs with RNA-binding mutations (5FL) shown to promote intracellular droplet formation (Figure 11G-H). As expected, expression of EGFP-TDP43 5FL resulted in enhanced nuclear droplet formation compared to WT TDP-43 proteins (Figure 12C-D). However, F>S mutations in the LCD of EGFP-TDP43 5FL reduces droplet formation back to levels of EGFP-TDP43 WT, as measured by mean fluorescence intensity variation (Figure 12C-D). FRAP analysis was then performed on EGFP-TDP43 5FL and EGFP-TDP43 5FL F>S droplets to determine whether phenylalanine substitutions may also alter the biophysical properties of these TDP-43 condensates. Both whole (Figure 12E) and partial bleach (Figure 12F) experiments showed an increased fluorescence recovery of EGFP-TDP43 5FL proteins with F>S mutations, possibly suggesting a role for interactions involving these phenylalanine residues in driving maturation of TDP-43 droplets.

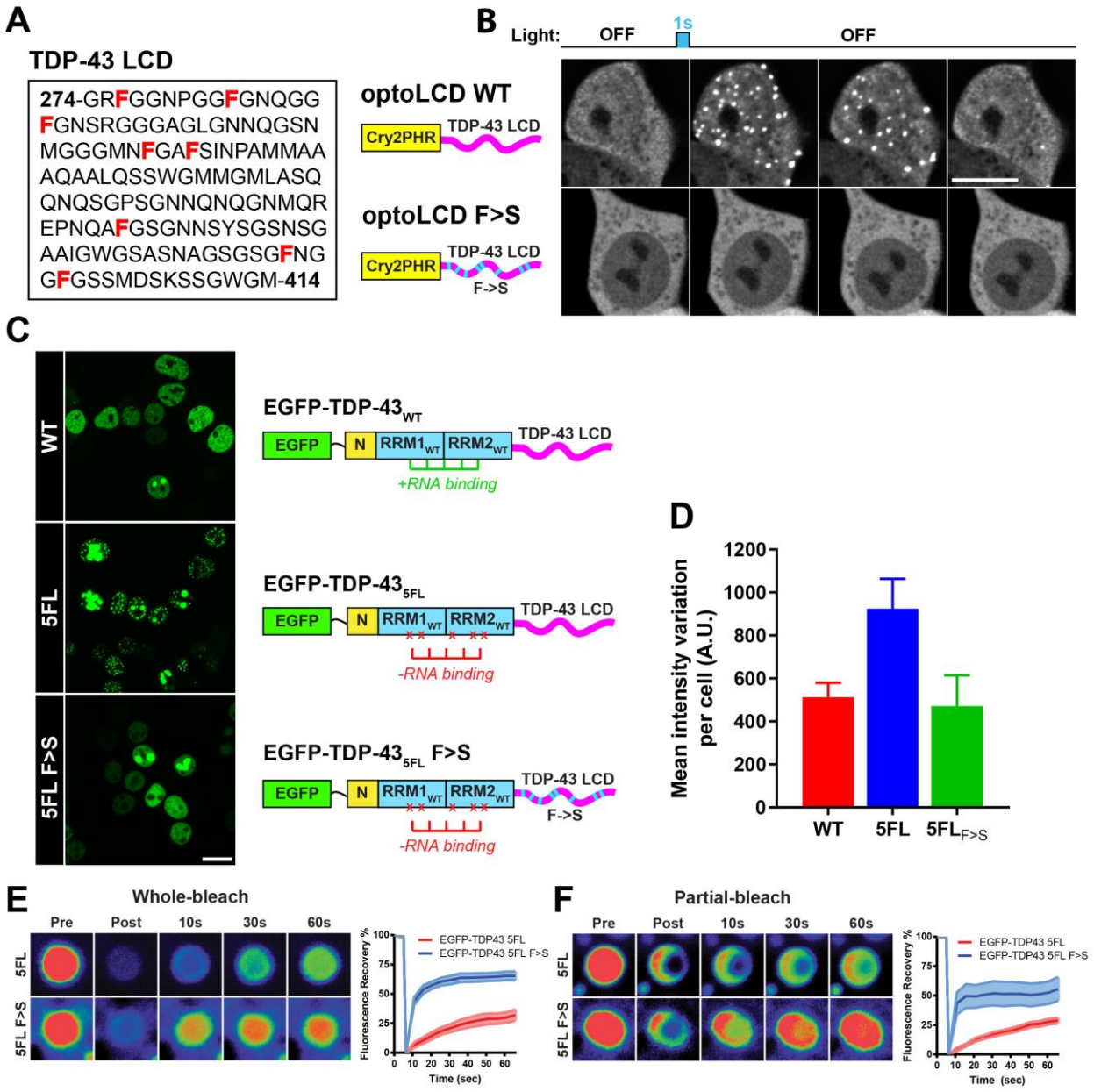

Figure 12. Phenylalanine residues in the LCD may contribute to TDP-43 droplet formation and maturation.

(A) Amino acid composition of the TDP-43 LCD (a.a. 274-414). The most abundant aromatic residue within this region is phenylalanine (highlighted in red). (B) Representative images of HEK293 cells expressing optoLCD WT (top) or optoLCD F>S (bottom) exposed to acute blue light stimulation (1 sec, 1% laser power, 488 nm). (C) Representative images of HEK293 cells expressing EGFP-tagged full-length TDP-43 WT (top), TDP-43 5FL (middle), or TDP-43 5FL F>S (bottom). (D) Quantification of mean intensity variation within the nucleus of cells expressing the indicated constructs. (E) Whole-bleach FRAP analysis of EGFP-TDP-43 5FL (top) or EGFP-TDP-43

5FL F>S nuclear droplets. (F) Partial-bleach FRAP analysis of EGFP-TDP-43 5FL (top) or EGFP-TDP-43 5FL F>S nuclear droplets. Data points shown are mean +/- S.E.M. Scale bars = 10 µm.

2.3.6 Impaired SG recruitment promotes aberrant TDP-43 phase transitions

SG components are modifiers of toxicity and pathological aggregation associated with TDP-43-overexpression in yeast, fly, and mouse models (Becker et al., 2017; Elden et al., 2010; Kim et al., 2014). SGs are composed of high concentrations of LCD-containing proteins and form through LLPS (Shin and Brangwynne, 2017), and maturation of TDP-43-containing SGs may seed pathological inclusions (Harrison and Shorter, 2017). Since RNA-binding dictates the ability of TDP-43 to undergo LLPS and inclusion formation, we asked whether reducing the RNA-binding ability of TDP-43 would confer enhanced SG recruitment and subsequent maturation into insoluble inclusions. Because cytoplasmic mislocalization is required for TDP-43 recruitment to SGs (Bentmann et al., 2012), we first induced SG formation in cells expressing cytoplasmic TDP-43 (EGFP-TDP43cyto) with functional (WT) or RNA-binding deficient (5FL) RRMs and examined co-localization with known SG markers. Notably, RNA-binding-deficient TDP-43 (TDP43cyto 5FL) was excluded from endogenous SGs upon heat shock or sodium arsenite-induced cell stress, whereas RNA-binding-competent TDP-43 was recruited to SGs (TDP-43cyto WT; SG+ granules) (Figure 13A-C). However, during our analysis we discovered a subset of cytoplasmic WT TDP-43 granules that formed under stress conditions did not co-localize with SG markers (SG- granules) (Figure 13A-B). Further investigation revealed that these TDP-43 granules (SG- granules) lacked mRNA (Figure 13D) and were enlarged (Figure 13E). In contrast, cytoplasmic TDP-43 recruited to SGs (SG+) co-localized with mRNA signal (Figure 13D). FRAP analysis of these two subsets of cytoplasmic TDP-43 granules in live cells similarly revealed that

TDP-43 recruited to RNA-containing stress granules (SG+) remained dynamic, whereas the excluded TDP-43 species (SG-) were static (Figure 13F-G, Appendix Video 7). Furthermore, TDP-43 residing in SG- inclusions were hyperphosphorylated and p62-positive (Figure 14A), thus exhibiting pathological hallmarks of TDP-43 proteinopathy. This result suggests that TDP-43 recruitment to SGs requires RNA binding and that localization to acutely-formed, RNA-rich SGs promotes TDP-43 solubility, whereas TDP-43 outside of these RNA-containing assemblies are insoluble.

In support of this notion, TDP-43 5FL inclusions due to RNA-binding deficiencies did not co-localize with SG proteins in the nucleus or in the cytoplasm in HEK293 cells (Figure 14B). Furthermore, although optoTDP43 proteins were recruited to SGs upon sodium arsenite treatment, optoTDP43 inclusions of all sizes were devoid of key stress granule components (Figure 14C-D) (Boeynaems et al., 2016) after illumination. Neuropathological analysis of ALS/FTLD patient tissue similarly revealed an absence of co-localization between TDP-43 inclusions and G3BP1/ATXN2 (Figure 13H, Figure 14E).

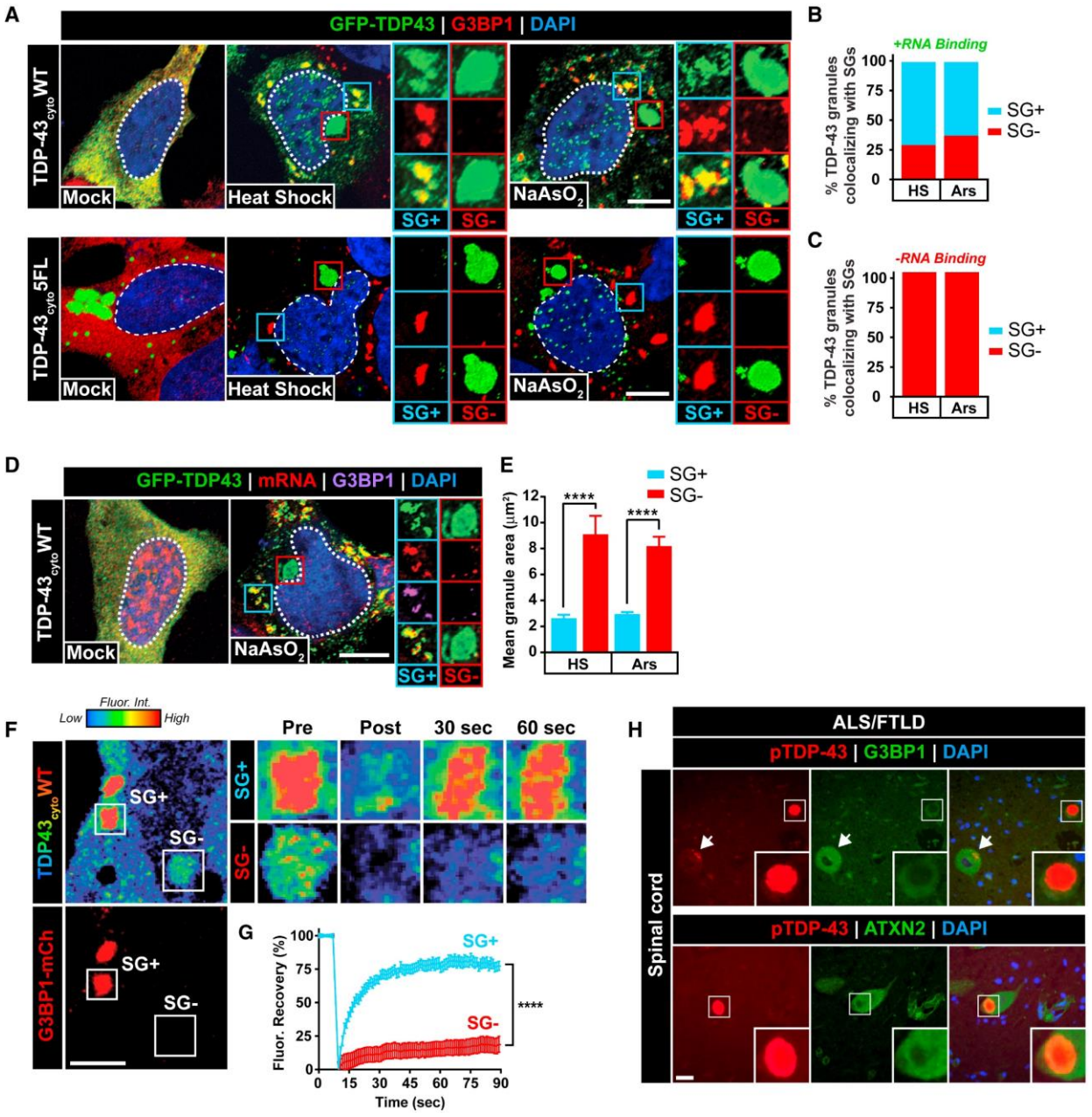

Figure 13. RNA-binding and stress granule localization prevents TDP-43 inclusions.

(A) Cytoplasmic EGFP-TDP43 constructs were expressed with functional (WT, top) or RNA-binding deficient (5FL, bottom) RRMs in HEK293 cells prior to heat shock or sodium arsenite treatment and immunostaining for G3BP1 (red) and eIF4G (not shown). (B-C) Percentage of EGFP-TDP43 granules that co-localized with G3BP1/eIF4G were calculated (SG+/-). *n* = 99-316 granules. (D) RNA FISH targeting Poly-A tails was performed to assess mRNA presence in SG+/- TDP-43 granules following sodium arsenite treatment. Scale bar = 10 μm. (E) Mean granule area for SG+ and SG- TDP-43 granules following heat shock and sodium arsenite treatment was determined by

immunofluorescence. *n* = 24-68 granules per condition. (F-G) HEK293 cells were co-transfected with cytoplasmic EGFP-TDP43cyto and G3BP1-mCh and exposed to sodium arsenite treatment to induce stress granule formation. FRAP analysis of TDP-43 granules that co-localized (SG+) or did not co-localize (SG-) with G3BP-mCh was performed to assess material state of SG+/- granules. *n* = 17-27 cells. (H) Immunohistochemical analysis of ALS/FTLD spinal cord tissue was performed to determine whether patient TDP-43 inclusions contain SG proteins. Arrows or insets indicate a lack of co-localization between TDP-43 inclusions (red) and the SG components G3BP1 (top) and ATXN2 (bottom) (green). Scale bar = 20 µm. Data shown are mean +/- S.E.M. ****, $p < 0.0001$.

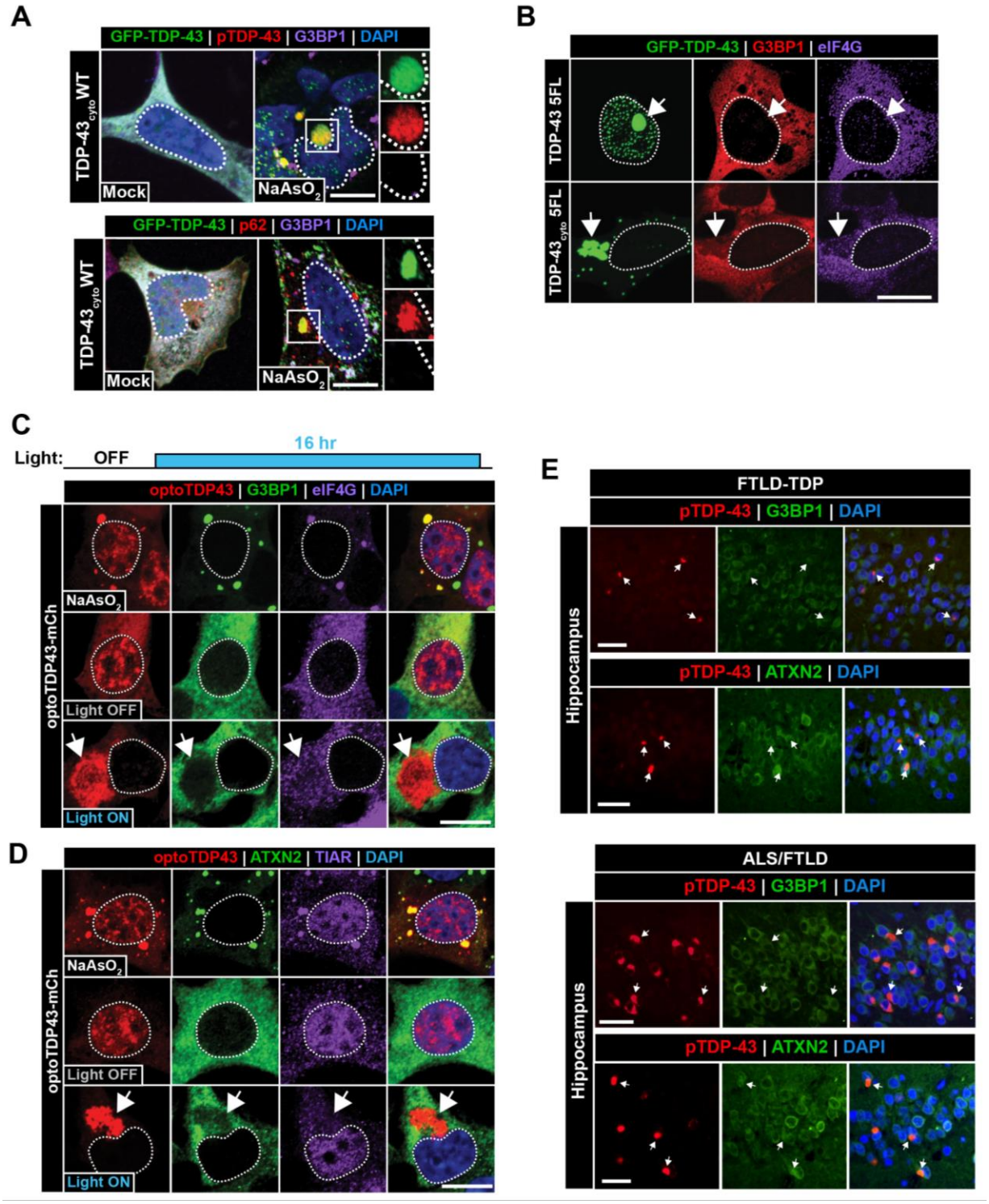

Figure 14. RNA-deficient TDP-43 inclusions do not co-localize with stress granule components.

(A) HEK293 cells expressing EGFP-TDP43cyto were immunostained for hyperphosphorylated TDP-43 (top row, red) or p62 (bottom row, red) and G3BP1 (purple) following sodium arsenite treatment. (B) Representative images of cells

containing TDP-43 5FL and TDP-43cyto 5FL inclusions immunostained for stress granule proteins G3BP1 (red) and eIF4G (purple). (C-D) HEK293 cells expressing optoTDP43 were subjected to sodium arsenite treatment (top row), chronic blue light stimulation (16 hr, ~0.3 mW/cm^2, 465 nm) (bottom row), or darkness (middle row) and immunostained for known stress granule components G3BP1 (green) and eIF4G (purple) (C) or ATXN2 (green) and TIAR (purple) (D). Cells treated with sodium arsenite (top row) show that optoTDP43 can be recruited to stress granules through the activation of endogenous cellular stress pathways. However, optoTDP43 inclusions (indicated by arrows) induced with blue light stimulation do not co-localize with any of the tested stress granule markers. Scale bars = 10 μm. Cell nuclei are circled. (E) Representative images of neuropathological examination of TDP-43 inclusions and SG component proteins (G3BP1, top rows; ATXN2, bottom rows) in FTLD-TDP and ALS/FTLD hippocampal sections. Arrows indicate lack of co-localization between SG components and TDP-43 inclusions. Scale bars = 50 μm.

2.3.7 Optogenetic induction of aberrant TDP-43 phase transitions is neurotoxic

TDP-43 proteinopathy correlates with regions of neurodegeneration in ALS/FTD patients (Mackenzie et al., 2013). To determine whether the formation of TDP-43 inclusions is toxic to human neurons, we differentiated human ReNcell VM neural progenitor cells into cortical-like neurons and obtained highly-enriched neuronal cultures (Figure 16A-C) (Donato et al., 2007). We then utilized a lentiviral expression system to selectively express optoTDP43 and a far-red fluorescent reporter (iRFP670) in human ReNcell cortical neuron cultures under the control of the human synapsin promoter (hSyn) (Figure 15A) prior to induction of optoTDP43 inclusion formation with chronic light stimulation. Longitudinal live-imaging at 30 min intervals revealed no significant neuronal loss in optoTDP43-expressing neurons kept in the dark (Figure 15B-C, Appendix Video 8). However, optoTDP43 neurons exposed to blue light exhibited progressive blebbing and loss of iRFP670 fluorescent signal in the soma after ~28 hr of light exposure

(determined by Chi-Square analysis) (Figure 15B-C, Appendix Video 8). At the final 90 hr timepoint, we observed a 4.3-fold increase in cell death in optoTDP43-expressing neurons exposed to light in comparison to those maintained in darkness (Figure 15B-C). No significant decrease in cell survival was recorded in neurons expressing the Cry2-mCh photoreceptor alone regardless of light treatment (Figure 15C, Appendix Video 9). Light stimulation alone also failed to induce alterations in neuron morphology (Figure 16D) or cell viability (Figure 16E), indicating no phototoxicity due to the light exposure. Subsequent analyses revealed a striking cytoplasmic shift of optoTDP43 signal in dying cells ~1 hr before cell death (Figure 15D) that was followed by formation of either large optoTDP43 inclusions (inclusions) or smaller, more circular assemblies (particles) (Figure 15B). No significant differences were observed in either the overall survival patterns (Figure 15E) or the time-to-death following detection of either of these assembly types in individual neurons (Event-Death) (Figure 15F). Importantly, neurons harboring either optoTDP43 assemblies exhibited reduced survival as compared to those with diffuse nuclear signal throughout the imaging period (Figure 15E). Immunofluorescence analysis of neurons at the 48 hr timepoint confirmed the presence of hyperphosphorylated and p62-positive optoTDP43 inclusions in the cytoplasm of ReNcell neurons exposed to light (Figure 15G). However, examination of the smaller and equally toxic optoTDP43 particles revealed no co-localization with these markers (Figure 15G). These observations suggest that aberrant cytoplasmic phase transitions drive neurodegeneration and exert toxic downstream effects independent of S409/S410 phosphorylation or p62-colocalization status.

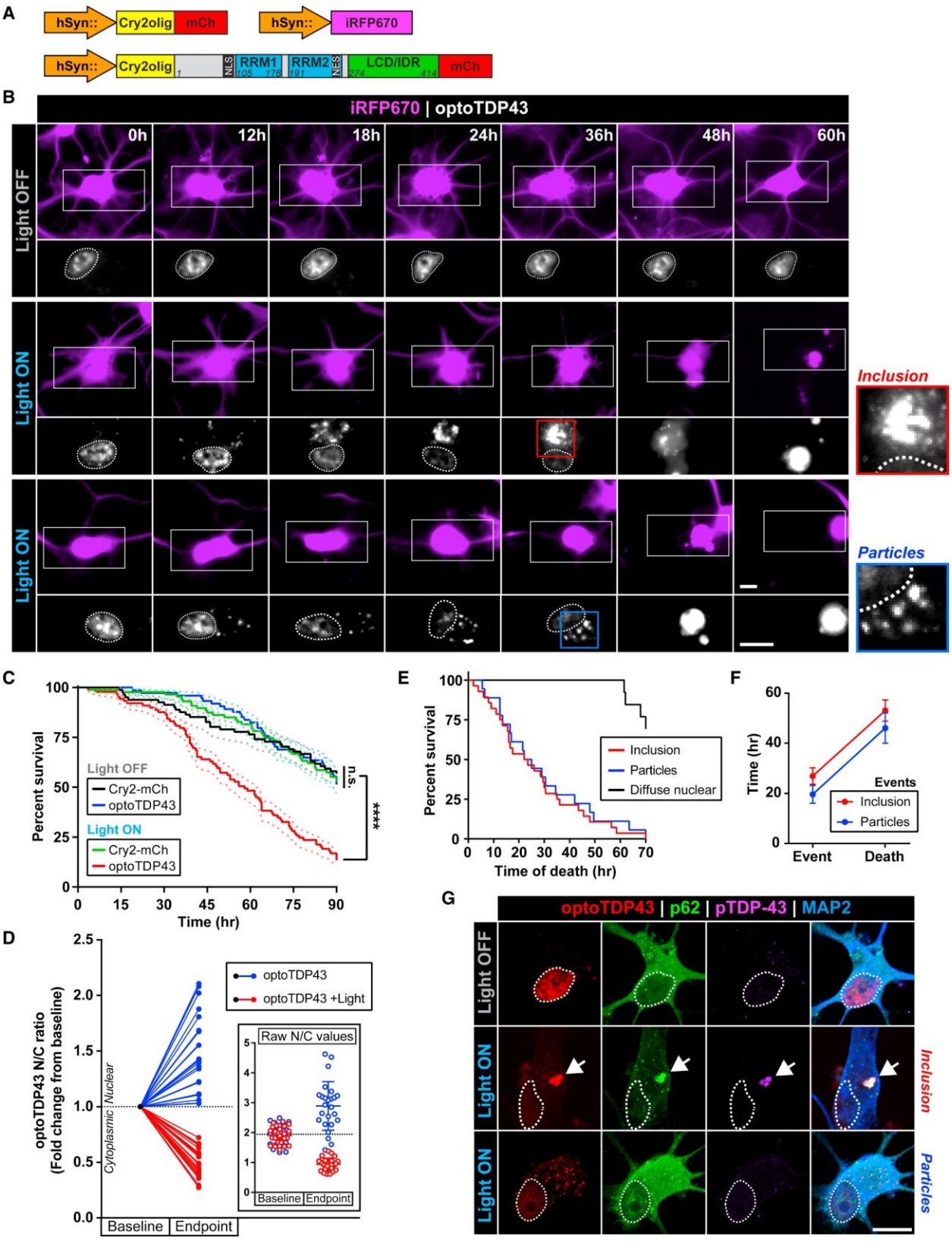

Figure 15. Light-induced optoTDP43 phase transitions are neurotoxic.

(A) Diagrams of lentiviral expression vectors used in neuronal survival experiments. optoTDP43 or the Cry2-mCh photoreceptor alone were expressed along with a far-red fluorescent reporter (iRFP670) under the control of the human synapsin promoter (hSyn). (B) Representative images of ReNcell cortical neurons expressing optoTDP43 kept in darkness (top row) or exposed to blue light (bottom two rows) (~0.3 mW/cm^2, 465 nm) during longitudinal toxicity screening. The iRFP670 reporter is shown (purple) to visualize cell bodies and neurites. Insets show optoTDP43 signal (white) in the same neurons. Cell nuclei are circled. Loss of signal and neurite blebbing indicates cell death (bottom rows, 48-60 hr). (C) Survival curves of ReNcell neurons during longitudinal toxicity screening. n = 74-89 cells. Data are presented as mean percent survival. (D) Nuclear-cytoplasmic (N/C) ratios of optoTDP43 signal were analyzed at baseline (prior to light exposure) and endpoints (last frame prior to cell death or conclusion of imaging session) in neurons exposed to light (red) or maintained in darkness (blue). n = 25 cells per light condition. Data is presented as fold-changes in N/C ratios normalized to baseline values. Inset shows raw N/C values and data points represent individual neurons. Dotted lines indicate population mean at baseline. (E) Survival curves of optoTDP43-expressing neurons exposed to light stimulation stratified by optoTDP43 assembly phenotype. n = 13-28 cells. (F) Time-to-death between event onset (particle or inclusion formation) and cell death were analyzed between neurons showing either optoTDP43 assembly subtype. n = 17-28 cells. (G) Immunofluorescence analysis of light-induced optoTDP43 assemblies in ReNcell neurons for pathological hallmarks p62 (green) and hyperphosphorylated TDP-43 (purple). Data shown are mean +/- S.E.M. ****, $p < 0.0001$. Scale bar = 10 µm.

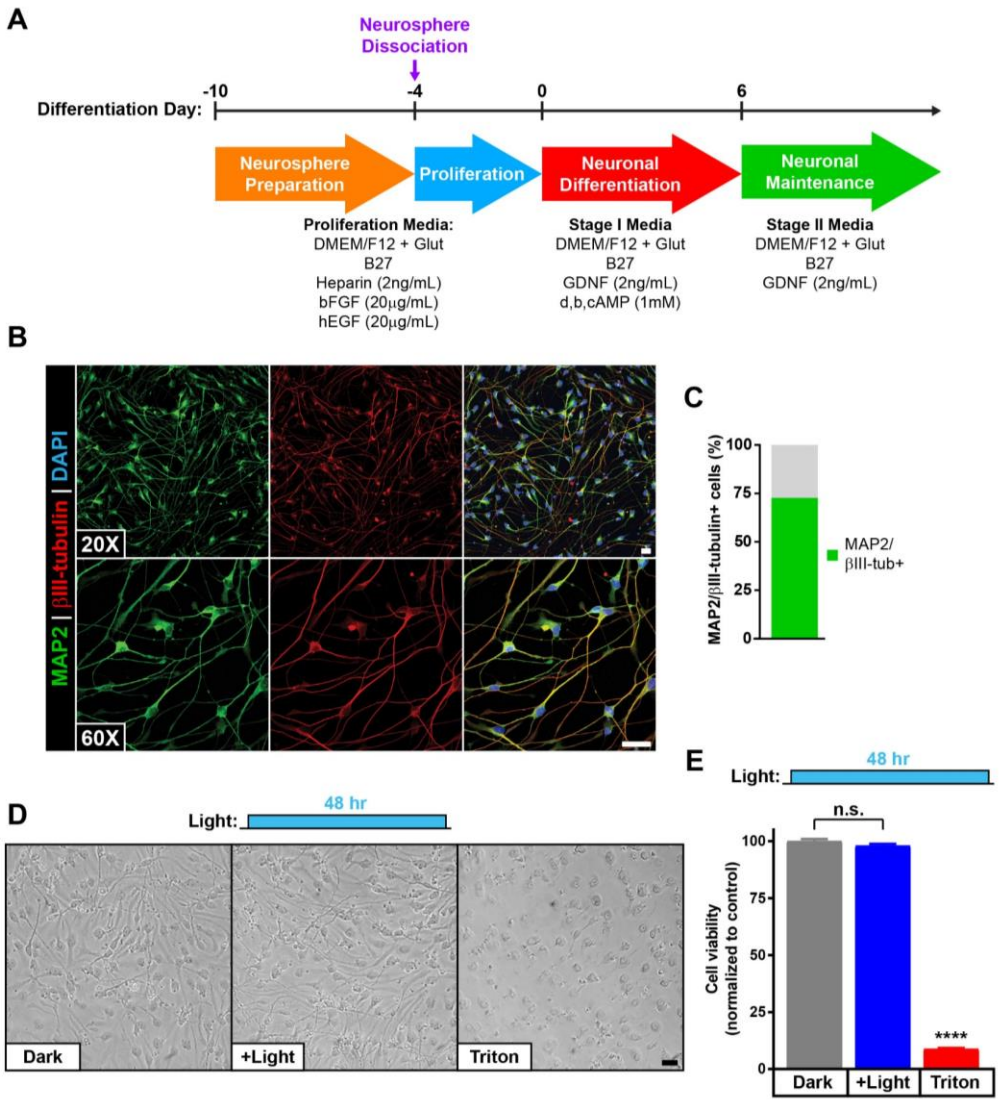

Figure 16. ReNcell VM differentiation yields a highly neuronally-enriched culture.

(A) ReNcell VM neuronal differentiation protocol schematic. (B) Representative immunofluorescence images of ReNcell VM neurons (differentiation day 18) following the differentiation protocol outlined in (A). MAP2 (green) and βIII-tubulin (red) are shown at 20X (top) and 60X (bottom) magnification. (C) Quantification of the percentage of MAP2/BIII-tubulin double-labeled cells shows a highly enriched neuronal population following the outlined differentiation protocol. *n* = 260 cells. (D-E) ReNcell neurons were exposed to chronic blue light stimulation (48 hr, ~0.3 mW/cm^2, 465 nm) or darkness prior to examination of neuronal morphology (D) and cell viability, as assessed by measurements of ATP levels (E) (CellTiter-Glo, Promega). No differences in morphology (D) or cell viability (E)

were observed between neurons in blue light or darkness conditions. Treatment with 0.1% Triton X-100 served as a positive death control. Scale bars = 20 μm.

2.3.8 Bait oligonucleotides rescue aberrant TDP-43 phase transitions and neurotoxicity

To investigate whether the neurotoxicity associated with aberrant optoTDP43 phase transitions could be mitigated through enhanced RNA binding, we designed a 2'OMe-modified RNA oligonucleotide based on a well-characterized TDP-43 binding sequence (Clip_34nt) previously shown to exhibit a high affinity for TDP-43 RRMs and a Kd of 112 nM (Ayala et al., 2011; Bhardwaj et al., 2013). We next employed the Clip_34nt to assess the ability of these bait oligonucleotides (bONs) to prevent light-induced optoTDP43 phase transitions in HEK293 cells. Cells expressing optoTDP43 were treated with either Clip_34nt or a scrambled oligonucleotide of equal length and nucleic acid composition prior to an 8 hr light stimulation protocol (Figure 17A). Similar to the effect produced by total HEK293 RNA, treatment with the bONs resulted in a dose-dependent reduction in cytoplasmic optoTDP43 assemblies (Figure 17B) in contrast to the non-targeting scrambled control. To test whether preventing light-induced optoTDP43 phase transitions enhanced neuronal survival, we next performed automated longitudinal imaging of optoTDP43-expressing ReNcell cortical neurons following a 4 hr pre-treatment with either Clip_34nt or the control oligonucleotide (Figure 17C). While no significant differences were observed in cumulative risk-of-death, we observed a significant and dose-dependent reduction in neurotoxicity during light treatment following treatment with the bONs (Figure 17D-E). Decreased toxicity was associated with similar dose-dependent reductions in light-induced optoTDP43 phase transitions, both inclusions and particles (Figure 17F), and nuclear-cytoplasmic redistribution of the optoTDP43 protein (Figure 17G). Consistent with results presented above, these studies

suggest that the neuroprotective effect of a TDP-43-binding oligonucleotide occurs through the prevention of aberrant and neurotoxic cytoplasmic TDP-43 phase transitions.

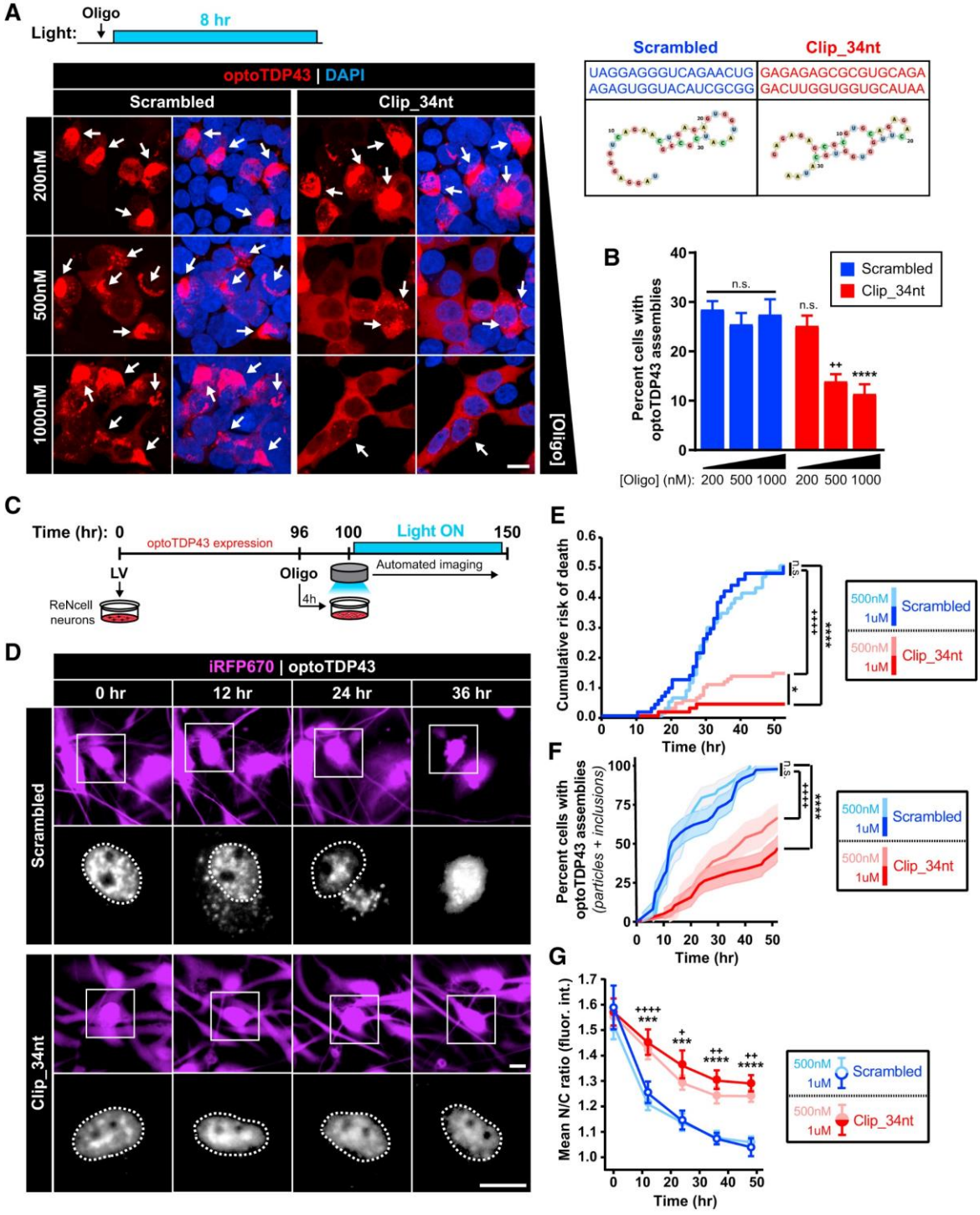

Figure 17. Bait oligonucleotides inhibit aberrant phase transitions of TDP-43 and rescue associated neurotoxicity.

(A-B) HEK293 cells expressing optoTDP43 were pre-treated with non-targeting scrambled or targeting Clip_34nt RNA oligonucleotides for 30 min prior to chronic blue light stimulation (8 hr, ~0.3 mW/cm^2, 465 nm). Arrows indicate cytoplasmic optoTDP43 assemblies. (B) Quantification of percentage of cells showing light-induced cytoplasmic optoTDP43 assemblies following indicated oligonucleotide treatments. *n* = 578 – 943 cells. (C) Diagram representing timeline of oligonucleotide treatments and neuronal survival screening. optoTDP43-expressing ReNcell neurons were treated with indicated oligonucleotides 4 hr prior to blue light exposure and automated longitudinal imaging. (D) Representative images of neurons treated with 1μM scrambled or Clip_34nt oligonucleotides prior to light exposure. Insets show optoTDP43 signal. Cell nuclei are circled. (E) Cumulative risk-of-death plots generated from Kaplan-Meier survival curves of ReNcell neurons over time following treatment with increasing doses of scrambled (blue) or targeting Clip_34nt (red) oligonucleotides. Shades of traces indicate treatment concentration (light = 500nM; dark = 1μM). *n* = 78-121 cells. (F) Automated object detection was utilized to determine percentage of ReNcell neurons showing optoTDP43 assemblies over time following the indicated oligonucleotide treatments. *n* = 37-39 cells. (G) Nuclear-cytoplasmic (N/C) ratios of optoTDP43 signal were calculated over time in neurons exposed to the indicated oligonucleotide treatments. n = 34-45 cells. *, $p < 0.05$; **, $p < 0.01$; ***, $p < .001$; ****, $p < 0.0001$. + indicate comparisons between 500nM treatment groups; * indicate comparisons between 1000nM treatment groups. Data shown are mean +/- S.E.M. Scale bars = 10 μm.

2.4 Discussion

TDP-43 proteinopathy is a pathological hallmark in several neurodegenerative disorders. Modeling this pathology has proven challenging and no standard currently exists to reliably reproduce TDP-43 inclusions in live cells. To address this problem, we developed a photokinetic system to selectively induce TDP-43 proteinopathy that recapitulates pathological features observed in ALS/FTD and other neurodegenerative diseases. This system allowed us to study the intracellular mechanisms driving pathological phase separation. We show that the intracellular

phase transitions of TDP-43 are mediated by the LCD, and events which promote homo-oligomerization of the TDP-43 LCD seed neuropathological inclusions. RNA-binding status dictates TDP-43 LCD-mediated oligomerization and RNA treatment blunts LLPS, aggregation of purified TDP-43, and light-induced optoTDP43 inclusion formation in live cells. Given recent evidence suggesting a role for SGs in seeding TDP-43 inclusions (Fernandes et al., 2018), we hypothesized that the heightened ability of RNA-binding deficient TDP-43 to undergo LLPS and aggregation confers enhanced recruitment to phase-separated SGs. Surprisingly, RNA-binding deficient TDP-43 is excluded from acutely-induced SGs and instead found in inclusions devoid of SG components. In contrast, TDP-43 recruited to SGs remained dynamic within these RNA-rich, liquid-like compartments. Since RNA binding inhibits aberrant phase transition of TDP-43, we tested whether a TDP-43-binding oligonucleotide sequence inhibits a pathogenic event. Remarkably, treatment with the oligonucleotide mitigated the cytoplasmic mislocalization and aberrant phase transition of optoTDP43 in response to light and rescued neurotoxicity.

Therefore, we propose that RNA-binding dictates the ability of optoTDP43 to form light-induced inclusions. In this model, LCD oligomerization of RNA-bound optoTDP-43 is blocked upon Cry2-mediated increases in local protein concentration while RNA-binding deficient optoTDP43 LCDs associate, thereby promoting inclusion formation (Figure 18A). This phenomenon could arise from a conformational change associated with nucleic acid binding, as shown for other RNA-binding proteins (Williamson, 2000). Nucleic acid binding also maintains the TDP-43 dimer and promotes solubility, potentially through an allosteric prevention of LCD:LCD interactions (Afroz et al., 2017; Sun et al., 2014). It is also possible that RNA-binding impedes TDP-43 homo-oligomerization through competitive inhibition. While the LCD appears to be dispensable for RNA binding (Buratti and Baralle, 2001), it contains an RGG motif that can

mediate RNA interactions (Conicella et al., 2016). Consistent with this, RNA depletion results in the *in vitro* oligomerization and aggregation of a C-terminal TDP-43 cleavage product lacking RRM1 and a portion of RRM2 (TDP-25) (Kitamura et al., 2016). Contacts within the TDP-43 RRMs themselves may also cooperate and play a distinct role in the TDP-43 aggregation process, as both RRM1 and RRM2 can form tetrameric assemblies *in vitro* (Kuo et al., 2009), and the RRM2 contains various segments capable of forming amyloid-like conformations (Guenther et al., 2018b). Overall, interactions between these domains and RNA may block regions that mediate aberrant TDP-43 phase transitions. Similarly, FUS LLPS is inhibited by the nuclear import receptor Karyopherin-β2 due to competitive interactions within domains that drive self-association (Guo et al., 2018; Yoshizawa et al., 2018).

Our work and other observations suggest that an altered TDP-43:RNA ratio creates an aggregation-prone environment for TDP-43 and serves as an upstream event in TDP-43 proteinopathy. This may occur due to disease causing mutations such as C9orf72 ALS/FTD that disrupt nuclear transport dynamics resulting in elevated cytoplasmic TDP-43 protein (Zhang et al., 2015b) and retention of RNA in the nucleus (Freibaum et al., 2015). Disease-causing mutations in the TDP-43 RRMs that abolish RNA binding have not yet been described. However, disease associated mutations within the TDP-43 LCD likely promote aberrant phase transitions of RNA-deficient TDP-43 proteins. This RNA-dependent model explains the aggregation of TDP-43 observed in overexpression models, in which insoluble inclusions may result from concentration-dependent phase transitions of cytoplasmic TDP-43 due to a lack of RNA substrates, as well as the cytoplasmic localization of TDP-43 inclusions observed in patient tissue (Scotter et al., 2015). Furthermore, this phenomenon likely serves as the convergence point for a number of pathways proposed to contribute to ALS/FTD including: altered TDP-43 expression, half-life and clearance;

disrupted nucleocytoplasmic transport; and abnormal RNP assembly and trafficking (Boeynaems et al., 2016; Gopal et al., 2017; Ling et al., 2013). A TDP-43:RNA imbalance is further supported by a recent study indicating that RNAs are buffers to inhibit LLPS of nuclear RNA binding proteins (Maharana et al., 2018).

SG-mediated seeding may underly the formation of TDP-43 inclusions. For example, the modulation of SG components alleviates TDP-43 inclusion formation and toxicity in overexpression models (Becker et al., 2017; Elden et al., 2010; Kim et al., 2014). While previous studies show that both the TDP-43 RRMs and LCD are necessary for SG targeting (Colombrita et al., 2009), we show that TDP-43 RNA binding is required for SG localization. This is consistent with previous reports describing the RNA-dependent recruitment of ALS/FTD-linked FUS protein to SGs (Daigle et al., 2013). Furthermore, we observed that cytoplasmic TDP-43 excluded from acute SGs forms pathological inclusions lacking mRNA, whereas TDP-43 recruited to SGs is dynamic and mobile. This is likely due to the abundance of RNA and other LCD-containing RBPs within SGs. RNA itself has been shown to alter the properties of protein-rich droplets (Zhang et al., 2015a) and reduces droplet viscosity through dynamic protein:RNA interactions within LAF-1 droplets (Elbaum-Garfinkle et al., 2015). These dynamic protein:protein, protein:RNA, and RNA:RNA interactions within SGs likely contribute to the liquid-like properties of these structures and may convey a diminished propensity to initiate pathological maturation/fibrillization as compared to a more homogenous, protein-rich granule. Therefore, our findings may delineate between normal, physiological LLPS interactions, specifically in the formation of heterogeneously-composed membraneless organelles, and pathological homogeneous LLPS interactions prone to seed disease-associated protein inclusions (Figure 18B). However, this does not eliminate the possibility that altered SG dynamics contribute to the aggregation of TDP-43.

For example, whereas RNA-containing SGs may initially inhibit TDP-43 proteinopathy, shifts in the SG composition to a more protein-saturated state might be capable of directly promoting TDP-43 LCD:LCD interactions. Consistent with this, prolonged stress was recently observed to elicit TDP-43-positive SGs that dissolve leaving phosphorylated TDP-43 (McGurk et al., 2018). Thus, there may be many roads to TDP-43 aggregation only some of which involve SGs (Boeynaems and Gitler, 2018).

It is unclear whether aberrant phase transitions or inclusions themselves are inherently neurotoxic and/or capable of driving neurodegeneration. ALS-linked mutations in TDP-43 that increase aggregation propensity result in enhanced toxicity in a variety of *in vitro* and *in vivo* models (Janssens and Van Broeckhoven, 2013). In contrast, neurodegeneration has also been characterized prior to significant accumulation of detergent-insoluble TDP-43 species in other systems (Arnold et al., 2013). TDP-43 sequestration within artificial inclusions recapitulates loss-of-function phenotypes (Prpar Mihevc et al., 2016) and TDP-43 knockout is embryonic lethal while conditional knockdown models produce ALS-like phenotypes *in vivo* (Xu and Yang, 2014). This suggests that perturbations in TDP-43 function, such as RNA processing, may also drive neurotoxicity. Our data indicate that cytoplasmic mislocalization precedes light-induced TDP-43 particle or inclusion formation and neuronal death, while neuroprotective oligonucleotide treatment delays/prevents these events. Thus, it is possible that cytoplasmic sequestration in the form of aberrant TDP-43 assemblies may produce neurodegeneration through both gain- and loss-of-function mechanisms.

In sum, we describe an optogenetic-based method to induce controlled TDP-43 proteinopathy in live cells and establish that RNA regulates the formation of TDP-43 inclusions. Our studies indicate that aberrant phase transitions are toxic to human cortical-like neuronal cells

and future work will dissect the properties of toxic TDP-43 assemblies and the downstream processes that contribute to neurodegeneration. Finally, our data suggest bONs or bait nucleic acid (bNA) strategies can inhibit aberrant phase transitions of TDP-43, providing a potential therapeutic approach for future study.

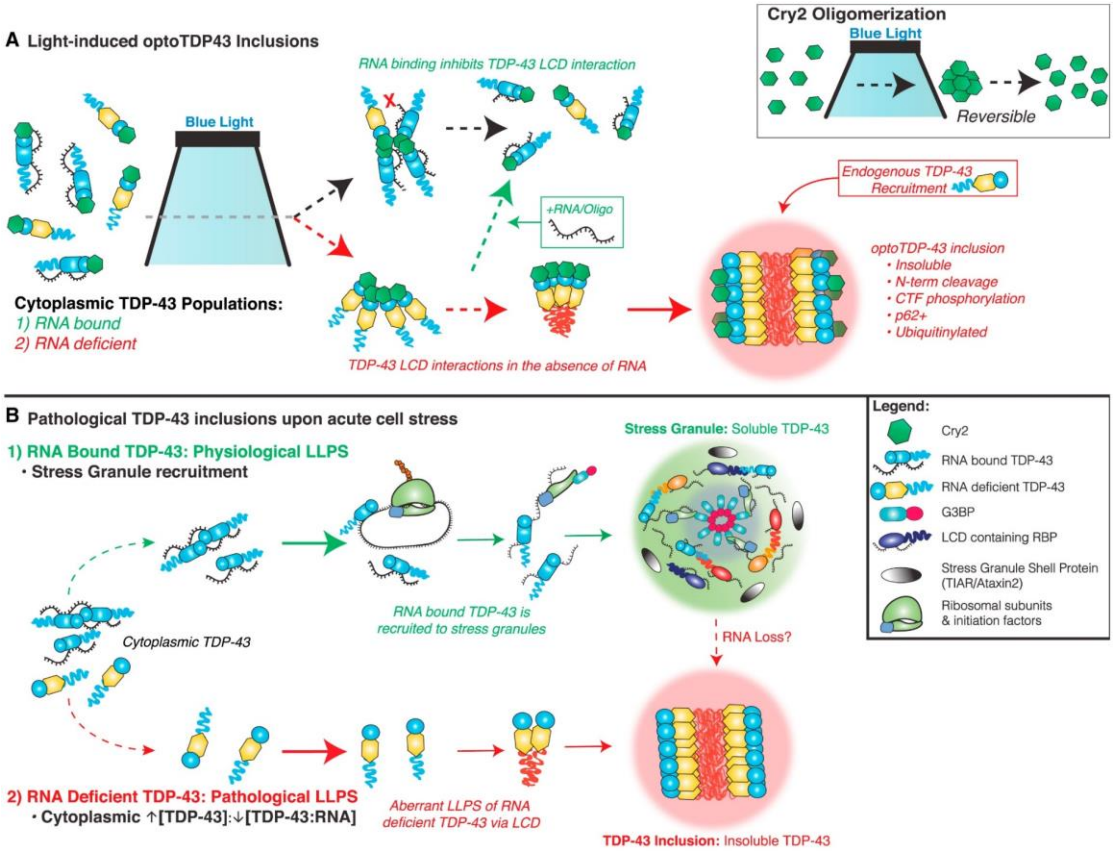

Figure 18. RNA dependent model of TDP-43 proteinopathy.

(A) Schematic of light-induced optoTDP43 inclusion formation. Cry2 photoreceptor reversibly homo-oligomerizes upon illumination (upper right corner). In the cytoplasm, light-induced increases in the focal concentration of RNA-unbound optoTDP43 (yellow) result in aberrant phase transitions that mature into insoluble inclusions capable of recruiting endogenous TDP-43 protein. LCD interactions of RNA-bound optoTDP43 (blue) are blocked upon illumination, maintaining optoTDP43 solubility and inhibiting inclusion formation. Addition of TDP-43 target RNA binding sequences and bNAs inhibit aberrant phase transitions of optoTDP43. (B) Proposed role of SG localization and intracellular TDP-43 LLPS. Physiological LLPS: RNA-bound TDP-43 localizes to SGs and the LCD promotes physiological phase separation into a heterogeneous RNP environment. The abundance of additional LCD-containing RBPs and RNA species promotes transient hetero-molecular interactions and rapid exchange of molecules, which maintains the liquid-like state and solubility of the granule. Pathological LLPS: An altered stoichiometric balance of TDP-43:RNA substrates promote RNA-deficient TDP-43 interactions. These aberrant homo-molecular interactions through the LCD may initiate aberrant TDP-43 phase transitions into insoluble inclusions. Loss of SG RNA may also promote the liquid-to-solid transition of TDP-43.

3.0 Diverse short RNA species inhibit, reverse, and remodel aberrant FUS self-assemblies

This chapter is adapted from: Guo, L.*, Mann, J.*, Gomes, E., Portz, B., Gleixner, A., Mauna, J., Gale, J., Donnelly, C.#, Shorter, J# (2020). *Diverse short RNA species inhibit, reverse and remodel aberrant FUS self-assemblies.* In preparation.

(*Authors shared equal contribution*) (# Co-corresponding authors #)

3.1 Introduction

Protein aggregates and inclusion body formations are common characteristics of many neurodegenerative diseases and are suggested to cause neuronal damage (Taylor et al., 2002). Numerous RNA binding proteins (RBPs) with Prion-like Domains (PrLD) including TDP-43, FUS, TAF15, EWSR1, TIA1, hnRNPA1, and hnRNPA2, have been found to be mislocalized and aggregated in several neurodegenerative diseases, including amyotrophic lateral sclerosis (ALS), frontotemporal dementia (FTD), and multisystem proteinopathy (MS) (Andersen and Al-Chalabi, 2011; Couthouis et al., 2011; Kim et al., 2013; King et al., 2012; Lagier-Tourenne et al., 2010; Mackenzie et al., 2017). Further studies showed these disease-linked proteins are intrinsically aggregation-prone and are highly toxic upon accumulation in cytoplasmic inclusions (Fang et al., 2014; Gitler and Shorter, 2011; Johnson et al., 2008, 2009). Although it is not yet clear how cytoplasmic accumulation induces toxicity, a link between accumulation of pathological inclusions formed by these RBPs and persistent stress granules has been indicated (Dewey et al., 2012; Molliex et al., 2015; Monahan et al., 2016). Indeed, all of the RBPs implicated in ALS are components of RNP granules (Alberti et al., 2017). Emerging evidence suggests that the RNP

granules are membrane-less organelles that behave like dynamic liquid droplets that rapidly assemble through liquid-liquid phase separation (LLPS) (Boeynaems et al., 2018; Shin and Brangwynne, 2017). *In vitro*, purified RBPs with PrLDs form liquid droplets that resemble biophysical properties of RNP granules and upon incubation these droplets mature into irreversible, solid-like hydrogel and fibrillar aggregates (Lin et al., 2015; Molliex et al., 2015; Murakami et al., 2015; Patel et al., 2015). In a cellular context, it has been hypothesized that persistence of RNP granules, caused by either failure of granule removal or disease-causing mutation in RBPs, can lead to similar aberrant phase transitions, which may induce neurotoxicity by sequestering RNP cargo and impairing RNP granule function (Elbaum-Garfinkle and Brangwynne, 2015; Lin et al., 2015; Molliex et al., 2015; Murakami et al., 2015; Patel et al., 2015).

Previously, we and others have shown that toxicity associated with aberrant FUS phase transitions can be rescued by overexpression of the nuclear import receptor Kapβ2, which can function as a protein chaperone and disaggregase to prevent and reverse FUS aberrant phase transitions (Guo et al., 2018; Hofweber et al., 2018; Qamar et al., 2018; Yoshizawa et al., 2018). However, since the major binding site for Kapβ2 is the PY-NLS of FUS, its activity is reduced when there is a disruption in the PY-NLS, which harbors most of the disease-causing mutations that impair Kapβ2-FUS interactions (Da Cruz and Cleveland, 2011; Dormann and Haass, 2011; Dormann et al., 2010; Guo et al., 2018; Ito et al., 2011; Mackenzie et al., 2011). Therefore, disaggregating agents targeting areas outside of the PY-NLS are needed for these mutants. Although the PrLD may be the major driving force of LLPS and aggregation, the RNA-binding domains provide additional regulation of FUS LLPS as RNAs can modulate the biophysical properties of liquid-like RBP droplets and modulate their aging process (Burke et al., 2015; Lin et al., 2015; Monahan et al., 2017; Zhang et al., 2015a). Therefore, here we have focused on

developing FUS-binding RNA molecules that can stabilize the liquid phase of the RBP assembly or reverse the aberrant phase transition process.

RNA binding is essential for FUS function, cellular localization, cytotoxicity and incorporation into stress granules (Bentmann et al., 2012; Daigle et al., 2013; Liu et al., 2013; Shelkovnikova et al., 2013a; Sun et al., 2011; Vance et al., 2013; Yu et al., 2015). FUS binds RNA through its RNA Recognition Motif (RRM), Zinc Finger Motif (ZnF), and 2 RGG domains (Burd and Dreyfuss, 1994; Ito et al., 2011; Ozdilek et al., 2017; Prasad et al., 1994; Schwartz et al., 2013). FUS is a promiscuous binder of RNA whose aggregation can be prevented by recruitment into RNP granules (Hoell et al., 2011; Nakaya et al., 2013; Shelkovnikova et al., 2013b; Wang et al., 2015). Consistent with these in vivo results, *in vitro* studies show that RNA binding can affect RBP liquid droplet formation, viscoelasticity and molecular dynamics in a variety of ways, suggesting it may be possible to regulate RBP phase behavior with RNA (Lin et al., 2015; Molliex et al., 2015; Murakami et al., 2015). For example, while initial addition of low concentrations of RNA can promote the formation of liquid droplets of proteins like FUS, higher concentrations of RNA seem to conversely inhibit liquid droplet formation (Burke et al., 2015). RNA has also been shown to differentially tune the material properties of RBP condensates, with some RNA species enhancing and some decreasing droplet fluidity in different protein/RNA contexts (Elbaum-Garfinkle et al., 2015; Zhang et al., 2015a). However, these earlier studies did not provide in-depth characterization of how individual RNA motifs or species may regulate the formation and biophysical properties of their cognate RBPs in different ways. Moreover, it was not clear whether RNA can reverse pre-formed RBP aggregates, which is more relevant in disease contexts where patient cells likely already contain inclusion bodies prior to disease presentation. Therefore, in

order to develop agents with therapeutic potential, it is important to define short RNA motifs that can both prevent and reverse FUS aberrant phase transitions and aggregation.

There are several identified FUS-binding RNA motifs. For example, the first published preferred FUS-binding motif (GGUG) was identified via *in vitro* SELEX analysis (Lerga et al., 2001). More recently, high throughput sequencing has discovered many RNA targets of FUS in the mouse and human genome (Hoell et al., 2011; Ishigaki et al., 2012; Lagier-Tourenne et al., 2012; Qiu et al., 2014). Included within these sequences are the GUGGU motif, U1 snRNA, and several regions in the *BDNF* (brain-derived neurotrophic factor) pre-mRNA. Most of these RNA targets contain G/U rich segments; however, not all FUS-binding RNAs contain these motifs. For example, the 48-nucleotide RNA prD from the *DNMT3b* promoter contains none of these G/U motifs but has been shown to interact with FUS and seed its aggregation (Schwartz et al., 2013). In addition to sequence-specificity, FUS also recognizes RNA through specific secondary structures such as AU-rich stem-loop structures (Hoell et al., 2011). Although it is widely accepted that FUS binds many different RNA targets to perform its function, it is not clear whether these FUS-binding RNA motifs can modulate the phase behavior of FUS and reverse aberrant FUS assemblies, and how this process might regulate FUS function.

Here we identify multiple FUS-binding short RNA sequences, several of which appear to be strong inhibitors of FUS aggregation and LLPS, while others exist as weak inhibitors that only inhibit FUS aggregation and not LLPS. Moreover, two of the FUS-binding RNA oligonucleotides, one from the 3'UTR of BDNF and one from *Escherichia coli*, can completely solubilize aberrant phase transitions of FUS. Conversely, other identified strong inhibitor oligonucleotides can reverse the formation of large FUS aggregation by remodeling them into smaller solid-like assemblies. The varying function of these inhibitors was found to be dependent upon RNA oligonucleotide

length, sequence and structure, as well where and how they interacted with the FUS protein. The RRM and RGG domains of FUS have been identified to be the regions that are particularly important for FUS-RNA interaction, but the ZnF domain also binds weakly to RNAs and might provide important cooperativity upon RNA binding. Interestingly, here we show a strong interaction between strong RNA inhibitors and the RRM/RGG regions, in addition to weak contacts within the ZnF domain. We also show that mutation of the RRM seemingly mitigates strong inhibitors' ability to prevent/reverse aberrant FUS assemblies *in vitro* and furthermore seems to promote FUS LLPS in mammalian cells using the optogenetic Corelets system (Bracha et al., 2018). While binding of the ZnF domain appears to be nonessential for the ability of strong inhibitors to prevent/reverse FUS aggregation, mutation of this domain did effect the function of weak inhibitors *in vitro* and seemed to further promote FUS LLPS in mammalian cells when combined with RRM mutations.

To test the efficacy of these inhibitors in mammalian cells, we also generated a novel optogenetic model of full-length FUS proteinopathy (optoFUS) based on previous methods used to control aggregation of TDP-43 (Chapter 2). Based on the strongest inhibitor identified *in vitro* from the BDNF 3'UTR, we designed an RNA analogue able to prevent and reverse light-induced FUS aggregation in this system that seems to reduce cellular toxicity upon inclusion disassembly. We further show that this therapeutic strategy could potentially be expanded to other RBP proteinopathies, such as TDP-43, using similar small RNA oligonucleotides to reduce the burden of pre-formed optogenetic TDP-43 inclusions (ssTDP43) and achieve a similar cytoprotective effect. Thus, it is possible that individual or a combination of RNAs defined in this study could be important therapeutic agents to restore RBP homeostasis in several fatal neurodegenerative disorders.

3.2 Materials and methods

3.2.1 Protein purification

GST-TEV-FUS, GST-TEV-FUS$^{1-214}$, GST-TEV-FUS$^{C428A:C433A:C444A:C447A}$, GST-TEV-FUS$^{F305L:F341L:F359L:F368L}$, GST-TEV-FUS^{371X} were purified as described (Sun et al., 2011). Briefly, N-terminally tagged GST-TEV-FUS was overexpressed in BL21(DE3)-RIL *E. coli*. The *E.coli* cells were then lysed by sonication on ice in PBS and protease inhibitors (cOmplete, EDTA-free, Roche Applied Science). The protein was purified over Glutathione Sepharose 4 Fast Flow beads (GE Healthcare) and eluted from the beads using FUS assembly buffer (50mM Tris-HCl pH 8, 200mM trehalose, 1mM DTT, and 20mM reduced glutathione). RNA and fluorescein labeled RNA were purchased from Dharmacon (GE).

3.2.2 RNA-Seq

RNA that was bound to GST-TEV-FUS during protein purification was extracted by adding DNase I and then Protease K to the sample followed by phenol-chloroform extractions, and precipitation in 100% ethanol with 70% ethanol wash. For preparing cDNA libraries for high-throughput sequencing, we used the NEBNext® Small RNA Library Prep Set for Illumina® and followed manufacturers' instructions. Library quality was checked with the Agilent 2100 BioAnalyzer. The sample was sequenced on the Illumina HiSeq2000 platform. The resulting sequences were aligned to human and *E. coli* genome using Bowtie and the annotated peaks were analyzed by a program HOMER for motif finding (Heinz et al., 2010; Langmead et al., 2009).

3.2.3 Fibril assembly

For GST-TEV-FUS, GST-TEV-FUS$^{C428A:C433A:C444A:C447A}$, and GST-TEV-FUS$^{F305L:F341L:F359L:F368L}$, fibrillization was initiated by addition of TEV protease to GST-TEV-FUS (5μM) in FUS assembly buffer (50mM Tris-HCl pH 8, 200mM trehalose, 1mM DTT, and 20mM glutathione) in the presence or absence of RNasin and 20μM RNA (Couthouis et al., 2011, 2012; Sun et al., 2011). Fibrillization reactions were incubated at 25°C for 90min without agitation. FUS^{371X} took longer to fibrillize, and its fibrillization was initiated by addition of TEV protease to GST-TEV-FUS^{371X} (10μM) in the presence or absence of RNasin and 40μM RNA at 25°C for 20h with agitation at 1200rpm.

Turbidity was used to assess fibrillization by measuring absorbance at 395nm. The absorbance was then normalized to that of FUS plus buffer control to determine the relative extent of aggregation. For sedimentation analysis, reactions were centrifuged at 16,100g for 10 min at 4°C. Supernatant and pellet fractions were then resolved by sodium dodecyl sulfate polyacrylamide gel electrophoresis (SDS–PAGE) and stained with Coomassie Brilliant Blue, and the amount in either fraction (% total) determined by densitometry in comparison to known quantities of the RBP in question. For electron microscopy, fibrillization reactions (10μl) were adsorbed onto glow-discharged 300-mesh Formvar/carbon coated copper grids (Electron Microscopy Sciences) and stained with 2% (w/v) aqueous uranyl acetate. Excess liquid was removed, and grids were allowed to air dry. Samples were viewed by a JEOL 1010 transmission electron microscope.

3.2.4 Fibril disassembly

Fibrils were assembled as above and used for disassembly reactions. 20μM RNA were added to preformed GST-TEV-FUS, GST-TEV-FUS$^{C428A:C433A:C444A:C447A}$, and GST-TEV-FUS$^{F305L:F341L:F359L:F368L}$ fibrils and 40μM RNA were added to preformed GST-TEV-FUS^{371X} fibrils to disassemble fibrils. Turbidity, sedimentation, and EM were used to monitor the progress of disaggregation. For turbidity, the absorbance was normalized to that of the fully assembled FUS fibrils before addition of RNA to determine the relative extent of disaggregation. Sedimentation analysis, and EM were performed as described above.

3.2.5 Droplet formation

FUS droplets were formed by incubating GST-TEV-FUS at indicated concentration in FUS assembly buffer (50mM Tris-HCl pH 8, 200mM trehalose, 1mM DTT, and 20mM glutathione) for 2 to 4 hours. Protein samples were then spotted onto a coverslip and imaged by Differential interference contrast (DIC) microscopy.

3.2.6 Anisotropy assay

8nM fluorescein labeled RNA were added into GST-TEV-FUS, GST-TEV-FUS$^{C428A:C433A:C444A:C447A}$, GST-TEV-FUS$^{F305L:F341L:F359L:F368L}$, or GST-TEV-FUS^{371X} at indicated concentration in FUS assembly buffer (50mM Tris-HCl pH 8, 200mM trehalose, 1mM DTT, and 20mM glutathione) in the presence of RNasin.

3.2.7 Cell culture and treatments

HEK293 cells (purchased from ATCC) were maintained at 37°C and 5% CO_2 in DMEM (high glucose, pyruvate) (Thermo Fisher Scientific) supplemented with GlutaMAX (Thermo Fisher Scientific) and 10% FBS. Transfections were performed using Lipofectamine 3000 (Thermo Fisher Scientific) according to manufacturer's instructions following cell seeding onto coverslips or culture plates coated with 50mg/mL collagen (Gibco) and overnight incubation at 37°C/5% CO_2. ReNcell VM (purchased from Millipore) cells were maintained at 37°C and 5% CO_2 in DMEM/F12 (Thermo Fisher Scientific) supplemented with GlutaMAX, B27 (Gibco), 2ng/mL heparin (Sigma), 20ng/mL bFGF (Millipore) and 20ng/mL hEGF (Millipore). Neuronal differentiation was performed as previously described (Chapter 2) and differentiated neurons were maintained at 37°C and 5% CO_2/5% O_2 prior to lentiviral transduction.

3.2.8 Cloning

All doxycycline-inducible expression constructs, including FUS-SspB mutants, optoFUS and ssTDP43, were generated through Gibson Assembly (HiFi DNA Assembly Master Mix, NEB) of PCR-generated fragments inserted at the NotI/EcoRI restriction enzyme sites of a Tet3G base vector (synthesized by GeneWiz). Synthesized gBlocks (IDT) containing 4FL and 4CA point mutations were used as templates for PCR of fragments used to assembly FUS-SspB mutants. Plasmids containing MBP-tagged FUS (Plasmid #98651, Addgene) were used as templates to generate WT FUS-SspB and optoFUS constructs. Previous-generation optoTDP43 constructs containing TDP-43 coding sequences were used as PCR templates to generate ssTDP43 constructs. For generation of lentiviral transfer vectors, PCR-generated fragments were inserted at the

BsrGI/BamHI restriction enzyme sites by Gibson Assembly of a third-generation base lentiviral vector described previously (Chapter 2) for human synapsin promoter-driven expression of target proteins.

3.2.9 Detergent solubility fractionation

For assessment of relative optoFUS and ssTDP43 detergent solubility, cell lysate fractionation was performed as described in Chapter 2 with minor modifications. Briefly, cells were first lysed with RIPA buffer (25mM Tris-HCl pH 7.6, 150mM NaCl, 2mM EDTA, 1% NP-40, 1% sodium deoxycholate, 0.1% SDS) supplemented with cOmplete Protease Inhibitor Cocktail (Roche) and phosphatase inhibitor cocktails 2/3 (Sigma-Aldrich) following one wash in ice-cold 1X PBS. After brief sonication (five 3 second pulses at 30% amplitude), lysates were then centrifuged at 17,000 *x g* at 4°C for 45 minutes and the resulting supernatant was collected as the RIPA-soluble fraction. Protein concentration was determined using the Pierce BCA assay (Thermo Fisher Scientific). Pellets were then washed in RIPA buffer prior to re-centrifugation at 17,000 *x g* at 4°C for 45 minutes. The resulting supernatants were then discarded and pellets were re-suspended in urea buffer (30 mM Tris pH 8.5, 7 M urea, 2 M thiourea, 4% CHAPS) supplemented with cOmplete Protease Inhibitor Cocktail (Roche) and phosphatase inhibitor cocktails 2/3 (Sigma-Aldrich) and sonicated briefly prior to centrifugation at 17,000 *x g* at room temperature. The resulting supernatant was then collected as the RIPA-insoluble, urea soluble fraction and samples were separated by SDS-PAGE prior to western blot analysis.

3.2.10 SDS-PAGE/Western blotting

Prior to SDS-PAGE, samples were first diluted in 4X Laemmli sample buffer (Bio-Rad) supplemented with 2-mercaptoethanol (Bio-Rad) and heated at 70°C for 10-15 minutes. Samples were then loaded into 12% or 4-20% Mini-PROTEAN TGX Precast gels (Bio-Rad) and separated by SDS-PAGE. Separated samples were next transferred to PVDF membranes (Bio-Rad) prior to washing (1X TBS) and blocking with 1X Odyssey Blocking Buffer (Li-Cor). Membranes were then incubated with primary antibodies diluted in 1X Odyssey Blocking Buffer supplemented with 0.2% Tween-20 overnight at 4°C. Primary antibody dilutions consisted of: mouse anti-mCherry (Novus Biologicals, 1:1000), rabbit anti-mCherry (Abcam, 1:1000), rabbit anti-FUS (Proteintech, 1:1000), rabbit anti-TDP43 (Proteintech, 1:1000), mouse anti-a-tubulin (Sigma, 1:10000). The next day, membranes were washed with TBS-T (0.1% Tween-20) and incubated with secondary antibodies (Li-Cor, IRDye 680/800, 1:10000) for 1 hour at room temperature prior to TBS-T washes and imaging (Odyssey CLx imaging system).

3.2.11 Immunofluorescence

For immunofluorescent characterization of optoFUS and ssTDP43 inclusions, cells seeded onto collagen-coated coverslips (Thermo Fisher, 50 μg/mL) were first fixed for 15 minutes at room temperature in 4% PFA following one 1X PBS wash. Three additional PBS washes were then performed prior to a 1-hour incubation in blocking buffer (0.3% Triton-X100/5% NDS in PBS) at room temperature. Cells were then incubated overnight at 4°C with primary antibodies diluted in blocking buffer at the following concentrations: rabbit anti-TAF15/TAFII68 (Bethyl Labs, 1:500), mouse anti-EWSR1 (Santa Cruz, 1:200), rat anti-methylated TLS/FUS (Clone 9G6, Sigma-

Aldrich, 1:100), guinea pig anti-MAP2 (Synaptic Systems, 1:1000), rabbit anti-G3BP1 (Proteintech, 1:500), rat anti-phospho-TDP43 (S409/410) (Clone 1D3, Biolegend, 1:200), rabbit anti-SQSTM1/p62 (Abcam, 1:500). The following day, primary antibodies were removed and cells were exposed to three 1X PBS washes prior to a 1-hour incubation with secondary antibodies (AlexaFluor 488/594/647, 1:1000) diluted in blocking buffer at room temperature. Three additional PBS washes were then performed prior to mounting coverslips onto slides using ProLong Diamond Antifade Mountant with DAPI (Invitrogen). Slides were allowed to cure overnight prior to visualization by confocal microscopy.

3.2.12 Live-cell imaging

Live-cell imaging experiments were performed on a Nikon Eclipse Ti2 inverted microscope equipped with an X-Light V2 (CrestOptics) spinning disk unit using CFI Plan Apo Lambda 40X dry or CFI Plan Apo VC 60X water immersion objectives (Nikon) and a Prime 95B CMOS camera (Photometrics). Cells were maintained at 37°C and 5% CO_2 in a Tokai HIT STX stagetop incubator throughout the imaging process. For chronic stimulation paradigms, wells were illuminated using custom-built 96-well LED panels (~0.3mW, 465nm) in between image acquisition periods using a 5V analog output from a Texas Instruments BNC-2110 triggering device as described in Chapter 2. For acute LIPS experiments, cells expressing iLID cores along with FUS-mCh-SspB mutants were first imaged using only the 594nm laser line to establish baseline FUS-SspB fluorescence intensity and spontaneous condensate assembly. Acute activation sequences (30 sec or less) were then achieved through dual-channel imaging with the 594nm and 488nm (75% power) laser lines, followed by post-activation image sequences for up to 10 minutes acquired using only 594nm lasers to avoid further activation.

3.2.13 Fluorescence recovery after photo-bleaching (FRAP)

For FRAP analysis of optoFUS and ssTDP43 assemblies, cells expressing these constructs were first imaged prior to light activation of optogenetic proteins to acquire baseline fluorescence recovery rates due to diffusion. Cells were then exposed to light activation for the indicated times and relative dynamics of light-induced condensates/inclusions were determined by FRAP. All imaging was performed on a Nikon A1 laser-scanning confocal microscope utilizing a 60X oil immersion objective (Nikon, CFI Plan Apo Lambda 60X Oil) and Tokai HIT stagetop incubator to maintain cells at 37°C and 5% CO_2. In brief, 2μm diameter bleaching regions-of-interest (ROIs) were drawn within nuclear compartments (for dark or pre-activation conditions) or around light-induced assemblies. 2-3 baseline images were then acquired prior to photo-bleaching within bleaching ROIs using the 488nm laser line (500ms, 50% power). Post-bleaching image sequences were then acquired for up to five minutes and fluorescence recovery within bleaching ROIs was measured over time. Fluorescence intensity values were normalized to intensities within reference ROIs of the same size drawn in non-bleached cells to control for fluorescence loss resulting from post-bleach imaging. These values were then normalized to each ROI's minimum and maximum intensities and were plotted as mean recovery rates per condition.

3.2.14 Automated image analysis

All automated image analysis was performed in NIS-Elements Advanced Research software (Nikon) using built-in analysis packages. For analysis of FUS-SspB condensate formation following acute light activation protocols, individual regions-of-interest (ROIs) were first drawn around all cells expressing both iLID cores and FUS-SspB mutant constructs in each

field-of-view. Baseline FUS-SspB fluorescence intensity was determined in frames prior to light activation. Automated Spot Detection was then used to identify and quantify the number of FUS-SspB droplets within each ROI during and following light activation sequences and the Time Measurement tool was used to export the number of objects per cell over time to Microsoft Excel. Object number values were then normalized to baseline values (prior to light activation), weighted based on baseline FUS-SspB fluorescence intensity (compared to population mean), and plotted over time. For graphs comparing threshold FUS-SspB concentrations required for LIPS, baseline fluorescence values were plotted against the maximum number of objects observed in each individual cell over the time-course of the experiment. C_{thresh} values were determined by calculating the mean baseline fluorescence intensity of the five lowest-expressing cells in each mutant condition that underwent LIPS (defined as the formation of >10 condensates in response to light activation). For quantification of granule dissociation kinetics, the number of objects identified in each individual cell in the first frame following light removal (T_0) was set at 100% and values in each successive frame were normalized as a percentage of initial T_0 values and mean dissociation values were plotted over time. One-phase exponential decay curves were then fit and T½ values for each FUS-SspB mutant were determined using Graphpad Prism 8 software.

For automated analysis of optoFUS normalized aggregation area, individual z-stacks were acquired in 9-16 randomized fields-of-view and maximum intensity projections were generated for analysis. First, binaries for cell nuclei and optoFUS inclusions were generated through fluorescence intensity thresholding of DAPI and mCherry signals respectively (see Appendix Figure 1 for example). Binary subtraction operations were then performed to generate a new binary layer consisting of mCherry signal with nuclear signal subtracted to remove confounding nuclear optoFUS signal from analysis. The total area of this resulting binary layer (optoFUS inclusions

only) was then calculated and normalized to total optoFUS cell area (determined by cell masks based upon mCherry fluorescence) and was presented as normalized aggregation area. Mean aggregation area values were then determined across fields-of-view and plotted as fold-change from control.

For automated quantification of light-induced formation of ssTDP43 inclusions, maximum intensity projections were first generated from z-stacks acquired over at least 6 individual fields-of-view per condition. Automated Spot Detection was then utilized to identify and quantify the number of light-induced granules per field-of-view over time. These values were then normalized to baseline (prior to light activation) values and plotted as mean increase from baseline over the course of light stimulation. For quantification of ssTDP43 and optoFUS inclusion disassembly, individual inclusions from 6-8 fields-of-view were identified and tracked over time. Here, baseline inclusion area was first determined through automatically or manually-drawn ROIs in the first frame acquired following RNA treatments (T_0). ROI areas were then determined for subsequent frames every two hours for up to 10 hours, normalized to baseline values and presented as fold change from T_0 over time. Survival of these inclusion-bearing cells was also manually tracked and Graphpad Prism 8 was used to generate and compare Kaplan–Meier survival curves between treatment groups. All above analyses were performed blinded.

3.2.15 Minigene and splicing assays

For monitoring of TDP-43 splicing function, the CFTR exon 9 minigene assay was performed as previously described (Pagani et al., 2000) with minor modifications. In brief, HEK293 cells transfected with the CFTR minigene plasmid were treated with siRNA (25nM) or RNA inhibitor oligonucleotides (2.5μM) for 72 hours prior to cell lysis and RNA extraction using

the miRNA Easy Kit (Qiagen). The iScript cDNA Synthesis Kit (Bio-Rad) was then used to generate cDNA from RNA samples and PCR reactions were then performed using cDNA templates and primers flanking exon 9 of the CFTR minigene prior to separation on a 1% agarose gel. Primer sequences are as follows: Fwd: 5'-CAACTTCAAGCTCGTAAGCCACTGC-3'; Rev: 5'-TAGGATCCGGTCACCAGGAAGTTGGTTAAATCA-3'. Bands were then visualized and imaged using the Chemidoc MP Imaging System (Bio-Rad).

3.3 Results

3.3.1 Identification of RNA sequence motifs that inhibit and reverse FUS phase transitions

We first aimed to identify RNA sequence motifs that can inhibit and reverse FUS aberrant phase transitions. We found that while extracting recombinant GST-FUS from *E. coli*, purified GST-FUS was RNA-bound (Figure 19A) and RNA removal by RNase A strongly promoted FUS aggregation, suggesting that these FUS-bound RNAs can inhibit FUS from forming aberrant assemblies *in vitro* (Figure 19B). Therefore, we first sought to identify enriched RNA motifs in this FUS-bound RNA population. The A_{260}/A_{280} ratio of the GST-FUS purified from *E. Coli* was 1.8, indicating 38% (w/w) nucleic acid in the sample. Gel electrophoresis and bioanalyzer showed an RNA population with size ranging from 50-100bp (Figure 19C). A cDNA library was constructed from this RNA population and was sequenced on Illumina's HiSeq system. We identified 42 enriched motifs between 8-12nt in our RNA library. 16 RNA motifs were then selected for testing based on the ranking of enrichment and diversity of these sequences. RNA oligonucleotides containing 2 or 4 repeats of individual enriched motifs were synthesized (Table

1) and first tested in *in vitro* FUS aggregation assays. An RNA oligo (RNA C2) that does not interact with FUS was used as a negative control. Remarkably, one of the RNAs tested (RNA S2) completely inhibited FUS aggregation (Figure 20A-C). Moreover, for 10 other tested RNAs, when 20 μM RNA was added to 5 μM FUS in the presence of TEV protease, we observed an elongated lag time to aggregation and reduction in final turbidity measurements to different extents when compared to control RNA (Figure 21A). 5 other tested RNAs did not show activity compared to the control RNA in these assays (Figure 21B).

Since these results indicate that FUS-bound RNA oligonucleotides have the ability to inhibit and delay FUS aggregation, we decided to test other published FUS-binding RNAs in our *in vitro* assays. 11 additional short RNA sequences that promote FUS binding, as well as a $(UG)_6$ RNA that binds TDP-43, were tested[61]. Within this group of RNAs, 7 showed strong inhibition activity where FUS was completely prevented from aggregating (Figure 20A-C). Conversely, addition of other RNAs, such as $(UG)_6$ (RNA W2) and the GGUG containing RNA (RNA W3), resulted in only modest reduction of FUS aggregation (Figure 21A). Depending on the extent of aggregation inhibition, we then divided the RNAs into two groups: strong inhibitors (Figure 20A-C), and weak inhibitors (Figure 21A).

It is curious what differences between strong and weak inhibitors underlie the different degrees of turbidity changes upon the cleavage of the protective GST tag in this assay. One possibility is that strong inhibitors prevent the assembly of all FUS protein and weak inhibitors antagonize only a fraction of FUS from aggregating. However, sedimentation analysis showed that nearly 100% of FUS was pelleted in reactions including weak RNA inhibitors, indicating the higher-order assembly of all FUS protein (Figure 21C-D). It thus may be the case that in the presence of weak inhibitors, FUS assembles into unique structures that scatter light differently

than fibrous aggregates formed in the absence of RNA when performing our turbidity measurements. Due to evidence that FUS aggregation begins with initial phase transition to form liquid-like droplets (liquid-liquid phase separation, LLPS) that subsequently mature into solid-state aggregates (Elbaum-Garfinkle and Brangwynne, 2015; Lin et al., 2015; Molliex et al., 2015; Murakami et al., 2015; Patel et al., 2015), we hypothesized that these different RNA oligonucleotide inhibitors may antagonize different stages of this process. Since turbidity measurements and sedimentation assays were not able to distinguish liquid droplet formation from solid-state aggregation, we next used electron microscopy (EM) to visualize FUS assemblies formed with/without strong and weak RNA oligonucleotides. Here we observed that FUS forms large aggregates in the absence of RNA, but addition of strong inhibitors completely blocked the formation of both droplet-like structures and solid aggregates (Figures 20C, 21E). Interestingly, while the assembly of large aggregates was prevented upon addition of weak inhibitors, we were able to detect numerous spherical assemblies exhibiting high-density stain representative of distinct phases with high protein concentration (Figure 20C). We hypothesized that these spheres were in fact liquid-like droplets whose formation via LLPS could not be prevented by weak RNA inhibitors. To test this idea, we next used DIC imaging to more closely investigate the formation and dynamics of FUS droplets in the presence of strong and weak RNA inhibitors. In the absence of RNA oligonucleotides, GST-FUS formed dynamic droplets that exhibited classic liquid-like behavior such as fusion and surface wetting (Figure 20D). Consistent with our aggregation assays and EM images, RNA oligonucleotides that strongly inhibited FUS aggregation also completely inhibited initial FUS droplet formation (Figures 20D, 21F). Conversely, weak inhibitors did not prevent the formation of FUS liquid droplets (Figure 20D), suggesting that strong and weak inhibitors selectively antagonize different stages of aberrant FUS phase transitions. While strong

inhibitors prevent both initial FUS LLPS and aggregation, weak inhibitors appear to allow for liquid droplet formation but inhibit subsequent solid-state aggregation.

In order to be developed as effective therapeutic agents, it is advantageous that these molecules not only prevent FUS aggregation, but also disassemble any aberrant protein assembly that has already formed. Therefore, we next tested whether the identified RNA inhibitors able to prevent aberrant FUS phase transitions could also reverse pre-formed FUS assemblies (Figure 20E). Remarkably, following FUS fibrillization upon incubation with TEV protease, addition of all strong inhibitors to pre-formed FUS aggregates resulted in the complete disassembly of FUS aggregates within 20 minutes of addition (Figure 20E-F). Similar effects of these RNAs were observed when added following the formation of GST-TEV-FUS droplets, where strong inhibitors completely and quickly disassembled these pre-formed FUS droplets and weak inhibitors had little effect on droplet persistence in these reactions (Figure 20G). The rate of disassembly in these assays was also seemingly dependent upon RNA concentration and motif, with RNA S2 being the fastest-acting and RNA S1 showing the most complete disaggregation activity (Figure 20E-G). Interestingly, when other strong inhibitors were added to pre-formed FUS aggregates, we observed a slow recovery of turbidity upon further incubation (120 min) after an initial rapid decrease (20 min post-addition) corresponding with the disassembly of FUS aggregates (Figure 20F). We attributed this slow increase in turbidity to remodeling of FUS aggregates by RNA and thus monitored the morphology change by EM and DIC at these time points. EM images showed that 20 minutes after addition of RNAs, when turbidity is at the lowest point, all strong inhibitors completely disassembled large aggregates (Figures 20F, 22A). However, 2 hours after addition of RNAs, when turbidity increases recovered, dense protein phases were observed by EM for samples including RNA S3, RNA S7 and RNA S8 (Figures 20F, 22A). Moreover, these dense phases

showed porous structures that resembled a hydrogel state (Figure 22A). DIC imaging confirmed the remodeling of FUS aggregates into smaller hydrogel phases, with observation of small FUS droplets that did not fuse (Figure 22B). Combining these observations, our data indicate that RNA S1 and RNA S2 are the most potent FUS inhibitors among all strong inhibitors. They completely reversed the aggregation and phase transition of FUS, while other strong inhibitors only reverse the formation of large aggregates but could not prevent aberrant phase transitions to a hydrogel state.

Surprisingly, identified weak RNA inhibitors also showed various disaggregation activity. For example, RNA W8 and RNA W9 showed disaggregating activity comparable to some of the strong inhibitors (Figure 22C). Other weak RNA inhibitors (RNA W2 and RNA W2) alternatively showed an initial disaggregation phase followed by a delayed increase in turbidity, indicating their inefficiency in preventing FUS from undergoing aberrant phase transitions. Several additional weak inhibitors did not show any disaggregating activity compared to that of control RNA (Figure 22D), while intriguingly 3 other RNAs that did not show inhibiting activity in initial assays were observed here to disaggregate pre-formed FUS aggregates to an extent that is stronger than control RNA (Figure 22D). These results thus indicate that while strong inhibitory activity may be sufficient to disaggregate FUS aggregates, inhibitory characteristics do not appear to be necessarily required for certain RNAs to be able to disassemble pre-formed FUS aggregates. A closer comparison of the weak inhibitors that did show disaggregating activity to those that did not revealed that longer RNAs have stronger disaggregating activity (Table 1). Together, these observations of varying inhibiting and disaggregating activities of RNA inhibitors may reflect their unique interaction patterns with FUS protein that result in these differential effects.

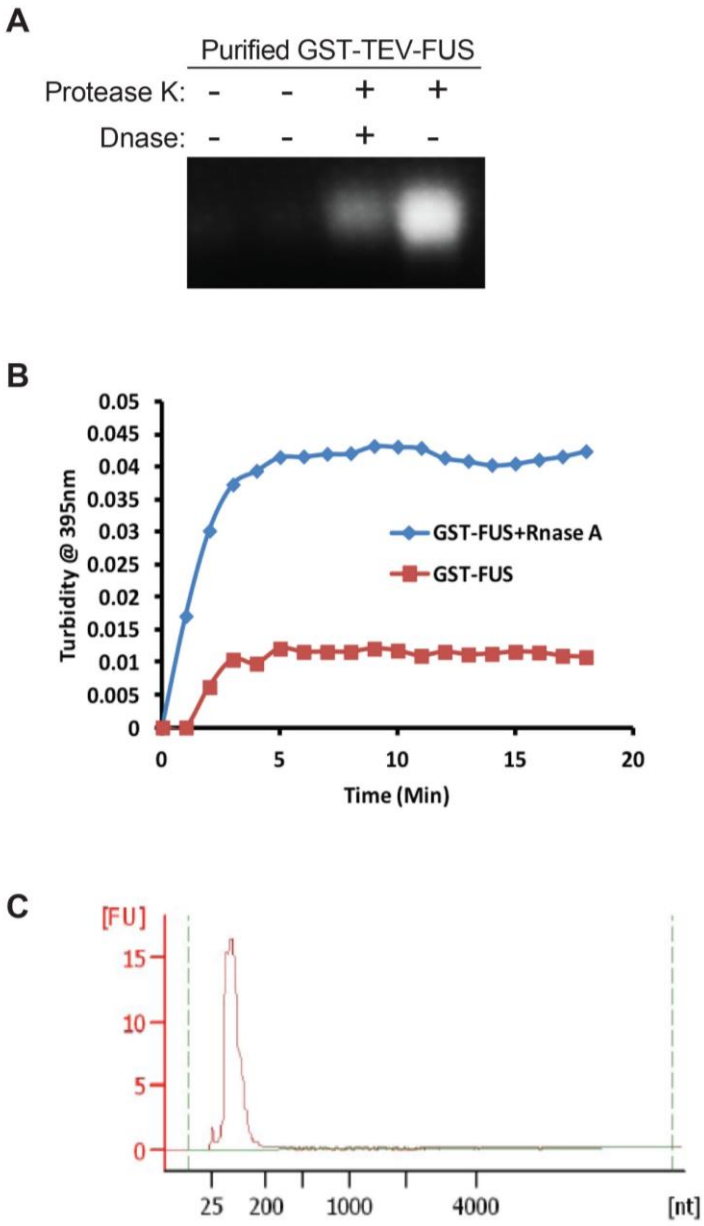

Figure 19. Preparation of RNA-seq sample.

(A) Agarose gel shows the RNA in GST-TEV-FUS purified from E. Coli. (B) GST-TEV-FUS (5μM) was incubated without TEV protease in the presence or absence of RNase A. Turbidity measurement was used to monitor the aggregation kinetics. (C) Bioanalyzer was used to determine the size of the extracted RNA. Experiments were performed by Guo, L., Shorter, J., et al. at the University of Pennsylvania.

RNA	Sequence	Length (nt)	Inhibit aggregation?	Reverse aggregation?
C2	UGUAUUUUGAGCUAGUUUGCUGAU	24	No	No
S1	CUAGGAUGGAGGUGGGGAAUGGUAC	25	Total	Total
S2	GAGGUGGCUAUGGAGGUGGCUAUGG AGGUGGCUAUGGAGGUGGCUAUG	48	Total	Total
S3	AUUGAGGAGCAGCAGAGAAGUUGGA GUGAAGGCAGAGAGGGGUUAAGG	48	Total	Partial
S4	GACUGAAAAAGGUGGGUUUCUUUU	24	Total	Partial
S5	AUUGAGGAGCAGCAGAGAAGUUGGA AAAAAAAAAAAAAAAAAAAAAA	48	Total	Partial
S6	AAAAAAAAAAAAAAAAAAAAAAAAA GUGAAGGCAGAGAGGGGUUAAGG	48	Total	Partial
S7	ACCAUGAUCACGAAGGUGGUUUUCC CAGGGCGAGGCUUA	39	Total	Partial
S8	CUCCGGAUGUGCUGACCCCUGCGAU UUCCCCAAAUGUGGGAAA	43	Total	Partial
W1	GAAAAUUAAUGUGUGUGUGGAAA AUU	28	Partial	No
W2	UUGUAUUUUGAGCUAGUUUGGUGAU	25	Partial	No
W3	UCAGAGACAUCAUCAGAGACAUCA	24	Partial	No
W4	GGUGAGCACAGAGGUGAGCACAGA	24	Partial	No
W5	CCAAUCUUCCUUCCAAUCUUCCUU	24	Partial	No
W6	GAUGGAUUCCAGGAUGGAUUCCAG	24	Partial	No
W7	AAACGGUCUGAUAAACGGUCUGAU	24	Partial	No
W8	AUGUCGCAGAAUGUCGCAGAAUGUC GCAGAAUGUCGCAGA	40	Partial	Partial
W9	AACCUUCGUAAACCUUCGUAAACCU UCGUAAACCUUCGUA	40	Partial	Partial
W10	CGCUGGCAUCCACGCUGGCAUCCA	24	Partial	No
W11	AAAGCGGCGAUGAAAGCGGCGAUG	24	Partial	No
W12	UAUUGAUCCGGUUAUUGAUCCGGU	24	Partial	No

Table 1. List of tested RNA oligonucleotides.

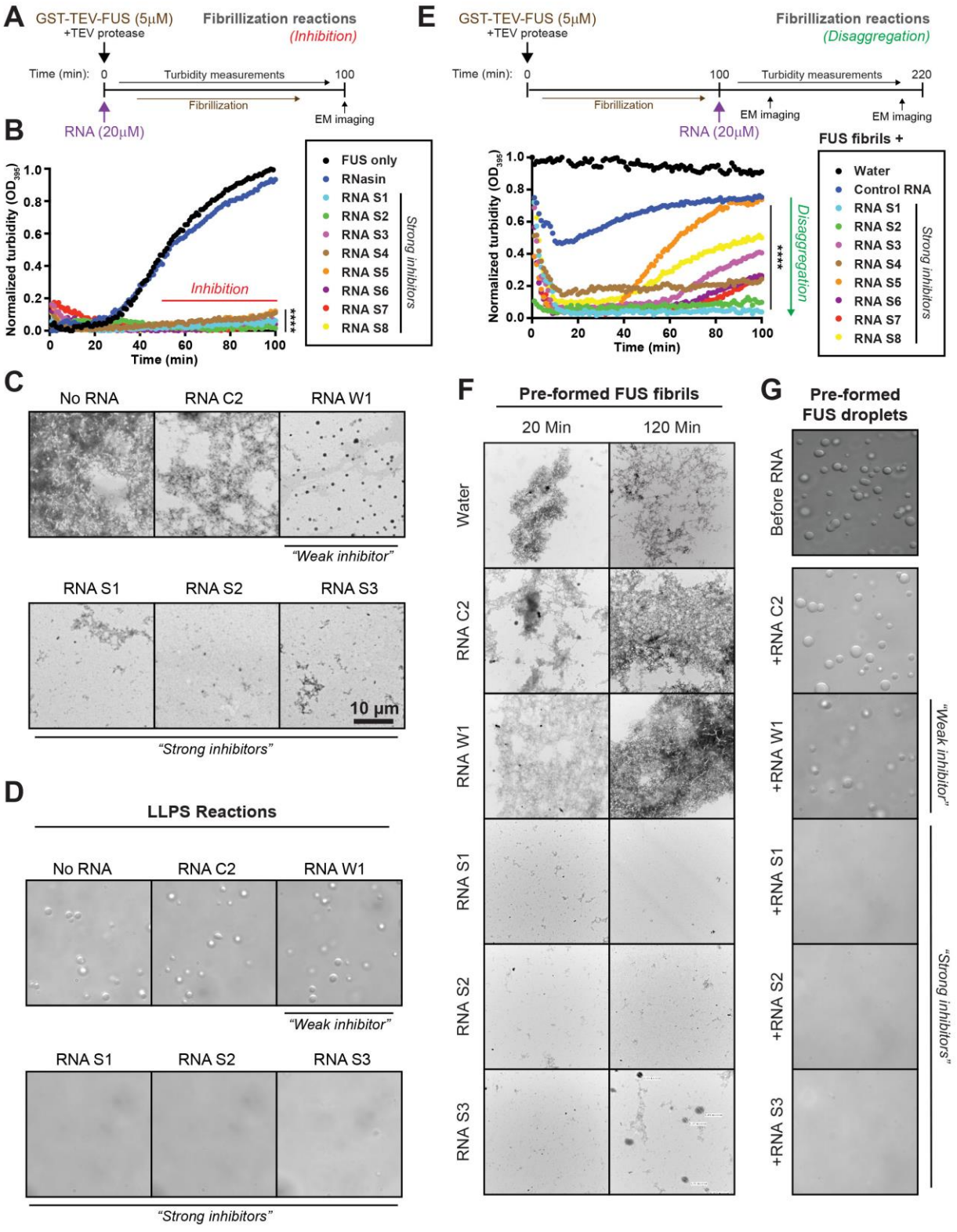

Figure 20. Strong RNA inhibitors inhibit and reverse FUS aggregation and liquid-liquid phase separation.

(A) Schematic of *in vitro* aggregation inhibition assay. GST-TEV-FUS (5μM) was incubated with TEV protease in the presence or absence of strong inhibitor (20μM) for 0–100 min. (B) Turbidity measurements were taken every minute to assess the extent of aggregation. Shown is the representative results of at least three repeats. (C) Fibrillization reactions were performed as in (A-B) and processed for EM at the end of the reaction. Arrows points to spheres with high-density stain that indicates formation of protein phases that have high protein concentration. Bar, 10μm. (D) DIC images of GST-TEV-FUS (5μM) droplets formed in the presence and absence of indicated RNAs (20μM). Bar, 20μm. (E) Schematic of *in vitro* aggregation reversal assay. Fibrillization reactions were performed as in (A-B) and at the end of the reaction, water or strong RNA inhibitor (20μM) were added to the reaction. Turbidity measurements were taken every minute to assess the extent of disaggregation. Shown is the representative results of at least three repeats. (F) Disaggregation reactions were performed as in (E) and processed for EM at indicated time. (G) DIC images of GST-TEV-FUS (5μM) droplets before and after addition of RNA (20μM). Bar, 10μm. Two-way ANOVA with Dunnett's correction were used to compare all groups to control RNA treatments. **** $p < 0.0001$. Experiments were performed by Guo, L., Shorter, J., et al. at the University of Pennsylvania.

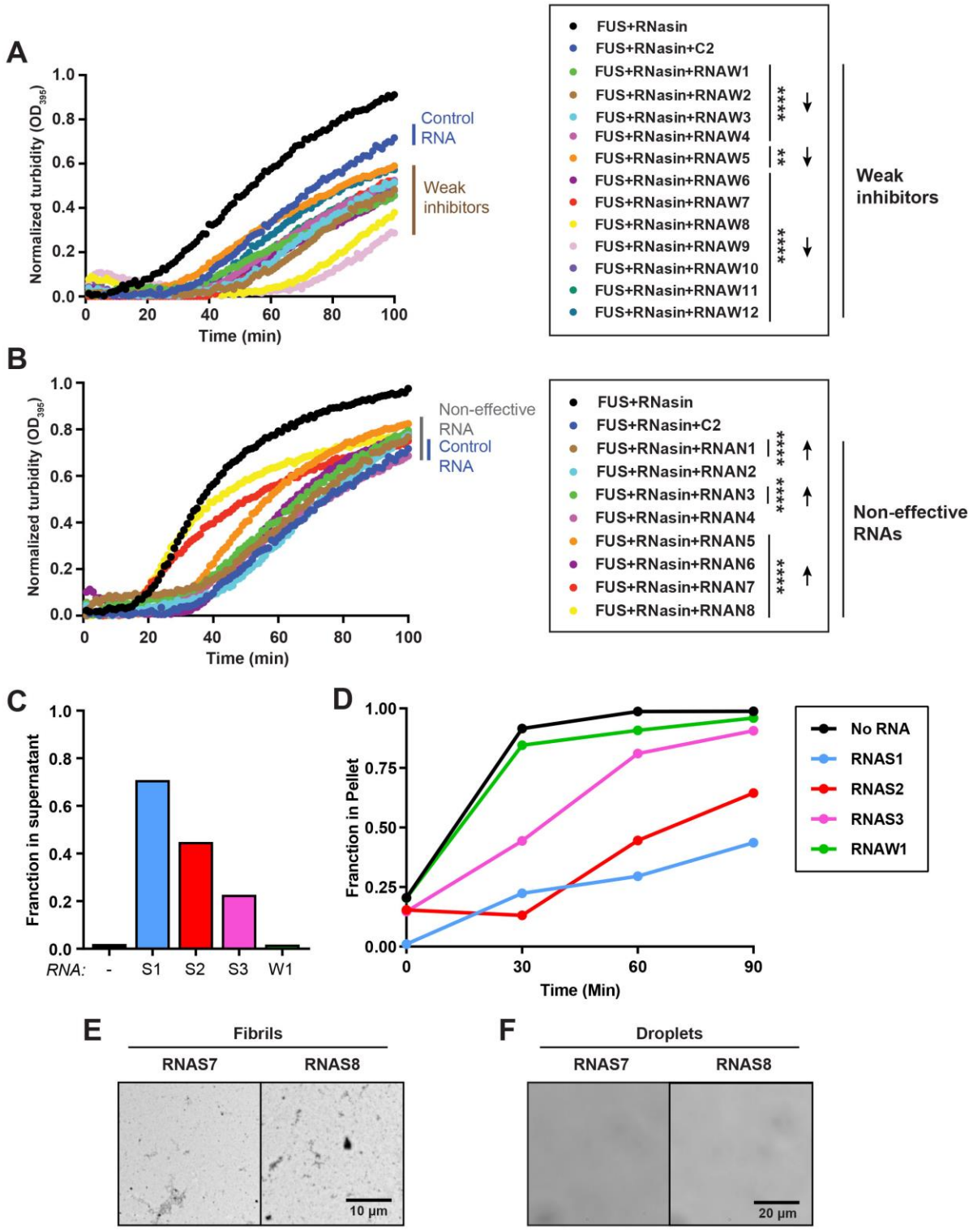

Figure 21. Weak inhibitors prevent FUS aggregation but not liquid-droplet formation.

(A) 12 weak inhibitors: GST-TEV-FUS (5µM) was incubated with TEV protease in the presence or absence of weak inhibitor (20µM) for 0–100 min. Turbidity measurements were taken every minute to assess the extent of aggregation.

Shown is the representative results of at least three repeats. (B) RNA that did not inhibit FUS aggregation: GST-TEV-FUS (5μM) was incubated with TEV protease in the presence or absence of indicated RNA (20μM) for 0–100 min. Turbidity measurements were taken every minute to assess the extent of aggregation. Shown is the representative results of at least three repeats. (C) GST-TEV-FUS (5 μM) was incubated with TEV protease in the presence or absence of with indicated RNA (20μM) for 0–90 min. At 90 minutes, reactions were processed for sedimentation analysis. Pellet and supernatant fractions were resolved by SDS-PAGE and stained with Coomassie Brilliant Blue. The amount of FUS in the pellet fraction was determined by densitometry in comparison to known quantities of FUS and the result are shown. (D) GST-TEV-FUS (5 μM) was incubated with TEV protease in the presence or absence of with indicated RNA (20μM) for 0–90 min. At the indicated times, reactions were processed for sedimentation analysis. Pellet and supernatant fractions were resolved by SDS-PAGE and stained with Coomassie Brilliant Blue. The amount of FUS in the pellet fraction was determined by densitometry in comparison to known quantities of FUS. (E) Fibrillization reactions were performed as in (A) and processed for EM at the end of the reaction. Bar, 10μm. (F) DIC images of GST-TEV-FUS (5μM) droplets formed in the presence and absence of indicated RNAs (20μM). Bar, 20μm. Two-way ANOVA with Dunnett's correction were used to compare all groups to control RNA treatments. ** $p < 0.01$, **** $p < 0.0001$. Arrows indicate direction of relative change in turbidity compared to control RNA. Experiments were performed by Guo, L., Shorter, J., et al. at the University of Pennsylvania.

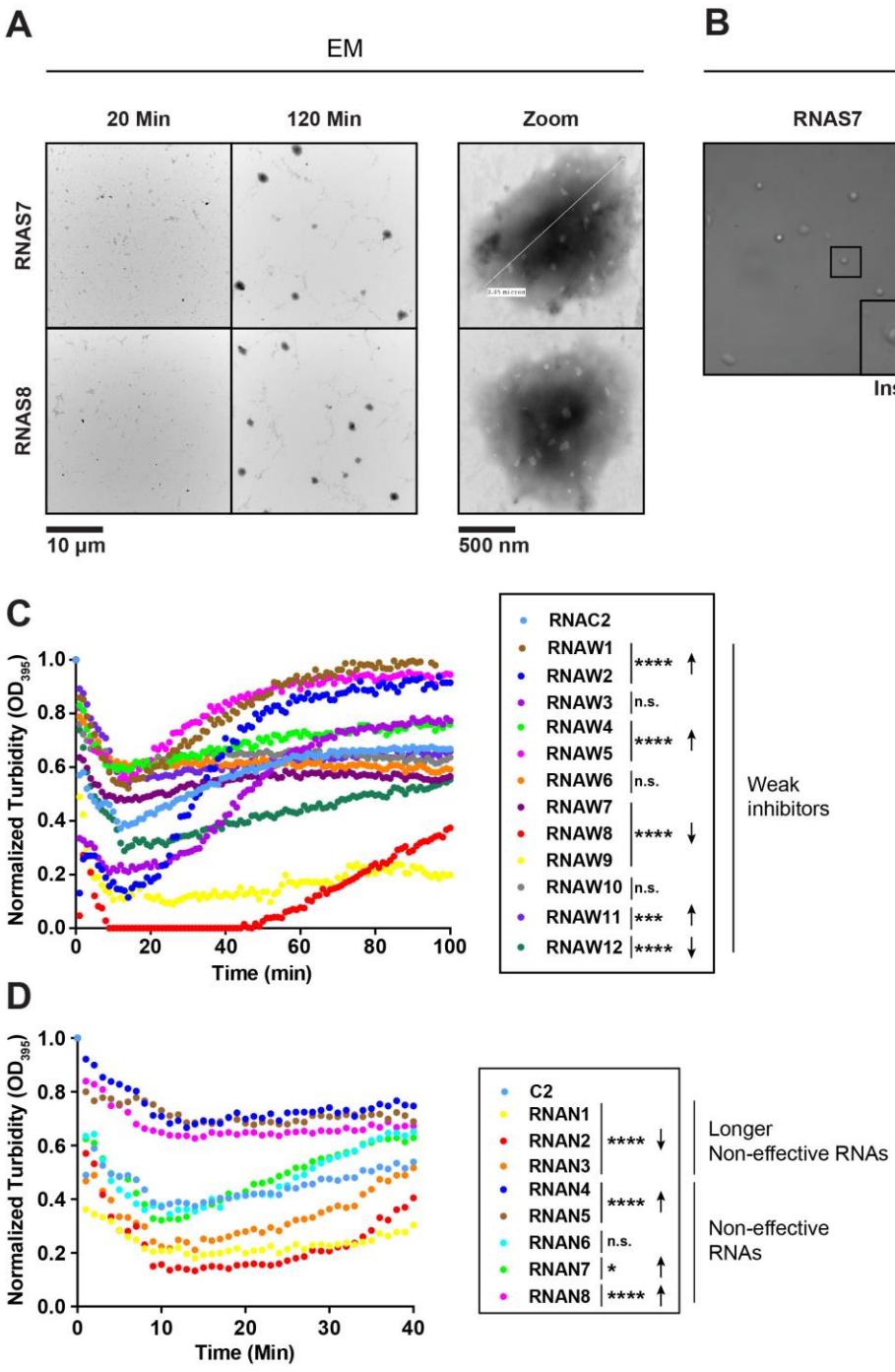

Figure 22. Reversing and remodeling of FUS aggregation by RNA.

(A) Fibrillization reactions were performed as in Figure 20A and at the end of the reaction, water or indicated RNA (20µM) were added to the reaction. At indicated time, samples were processed for EM. The right images show higher magnification of the dense protein phase observed in the middle panel, where the porous structure is indicative hydrogel formation. (B) DIC images of the hydrogel sample observed in (A) indicating they are small solid-like drops

that do not fuse. (C) Weak inhibitor does not reverse FUS aggregation in general. Fibrillization reactions were performed as in (A) and at the end of the reaction, water or indicated RNA (20μM) were added to the reaction. Turbidity measurements were taken every minute to assess the extent of disaggregation. (D) Long RNAs have some activity in reversing FUS aggregation. Fibrillization reactions were performed as in (A) and at the end of the reaction, water or indicated RNA (20μM) were added to the reaction. Turbidity measurements were taken every minute to assess the extent of disaggregation. Two-way ANOVA with Dunnett's correction were used to compare all groups to control RNA treatments. * $p < 0.05$, *** $p < 0.001$, **** $p < 0.0001$. Arrows indicate direction of relative change in turbidity compared to control RNA. Experiments were performed by Guo, L., Shorter, J., et al. at the University of Pennsylvania.

3.3.2 Activity of RNA inhibitors depends on length, sequence, and structure

In order to design RNA-based oligonucleotides with enhanced activity in mitigating FUS toxicity and aberrant phase transitions, it is important to elucidate the mechanism(s) of action underlying these effects. To begin to investigate how these various RNA inhibitors differ in their interaction with FUS, we first tried to identify the intrinsic characteristics of these various RNA inhibitors that may determine their inhibitory and disaggregation activities. We hypothesized that the length, sequence, and secondary structure are potential determinants in this regard. To examine how RNA length may effect oligonucleotides' ability to disrupt aberrant FUS assembly, we selected a strong inhibitor (RNA S2), which consists of 4 repeats of an enriched motif identified in our RNA-seq studies (G.A.G.G.U.G.G.C.U.A.U.G), and synthesized RNA S2/2, which only contains 2 repeats of the same enriched motif (Figure 23A). We also selected a weak inhibitor RNA W1, which contains two repeats of another identified motif (U.C.A.G.A.G.A.C.A.U.C.A.), and synthesized RNA W1*2, which doubles the length and valency of RNA W1 (Figure 23B). As we expected, shortening the length of strong inhibitor RNA S2 (RNA S2/2) reduces its ability to

prevent FUS phase transitions following TEV cleavage *in vitro* (Figure 23C), while doubling the length and valency of weak inhibitor RNA W1 (RNA W1*2) strengthens its inhibition activity (Figure 23D). We next performed assays involving addition of these RNAs after the formation of FUS aggregates to examine how RNA length effects disaggregation activity (Figure 23E-F). Here again we observed that while RNA S2 can completely disaggregate pre-formed FUS aggregates, the shortened RNA S2/2 does not show significant disaggregation activity compared to control RNA C2 (Figure 23E). Similarly, doubling the length of the weak inhibitor RNA W1 that previously did not show disaggregation activity renders it able to disaggregate pre-formed FUS aggregates (Figure 23F).

Although RNA S2 and RNA W1*2 have the same length (48nt), they have markedly different inhibition/disaggregation activity (Figure 23A-F). Therefore, we hypothesized that the sequence of the RNA is also important for its inhibition activity. To test this hypothesis, we introduced a single A to U mutation in RNA S2/2 in order to introduce a known FUS binding motif (G.U.G.G.U) into the sequence (RNA S2/2 (A-U)) (Figure 23A). Surprisingly, while seemingly increasing the valency of this RNA inhibitor, this single mutation significantly weakened the inhibition and disaggregation activity of RNA S2/2 (Figure 23C, E). This result indicates that containing FUS-binding motifs alone does not guarantee RNA inhibition activity and suggests that other effects of RNA sequence, such as RNA secondary structure, may also play a role in determining inhibitory efficacy.

We have used single molecule Förster Resonance Energy Transfer (smFRET) to study the effect of RNA structure on protein LLPS as well as the interaction between FUS and RNA (Niaki et al., 2020). Here, we chose to examine both an unstructured polyU50 RNA and a strong RNA inhibitor with similar length (RNA S2) to investigate how RNA oligonucleotides with varying

structural content interact with FUS differently. Indeed, as predicted by M-Fold, polyU50 is unstructured and the strong inhibitor RNA S2 can fold to a stem loop structure with folding energy of -16.40 kcal/mol (Figure 23G). As expected, unstructured polyU50 RNA showed weak inhibition activity in our turbidity assay (Figure 23H) and, much like other weak RNA inhibitors, did not appear to inhibit FUS LLPS when droplet formation was examined in the presence of polyU50 or RNA S2 by DIC imaging (Figure 23I). To next characterize how these differently-structured RNAs interacted with FUS to promote or inhibit LLPS by smFRET, we prepared FRET pair-labeled RNA substrates such that the FRET pair dyes (Cy3 and Cy5) were separated by the sequence of polyU50 or RNA S2 (Figure 23J-K). The resulting FRET value of labeled polyU50 is approximately 0.2 (Figure 23J), shown as a single FRET peak, consistent with an unstructured RNA oligonucleotide. Conversely, the resulting FRET value of labeled RNA S2 is distributed around a single peak centered at 0.8, indicating a rigid structured RNA (Figure 23K) and consistent with M-Fold predictions.

We then added FUS to labeled RNA substrates to examine how increasing concentrations of FUS would alter FRET efficiency. For polyU50, addition of low FUS concentration (5nM) immediately shifted the low FRET (0.2) to a single high FRET peak (0.8) with single molecule traces displaying stable high FRET signal (Figure 23J), reflecting that FUS induced a tight compaction of the long, unstructured ssRNA. As FUS concentration increased (50-500nM), the high FRET population diminished, while a broad mid FRET peak (~0.5) emerged (Fig. 21J, left panel) with smFRET traces showing increasing level of fluctuations (Fig 21J, middle panel). The mid FRET peak indicates an extended RNA structure allowing dynamic interaction between multimeric FUS and a single RNA oligo (Fig 23J, right panel), consistent with the fact that this weak RNA inhibitor allows FUS droplets to form. Removal of the excess protein by a buffer wash

brought the RNA to the stable high FRET state observed at lower (5nM) concentration (Figure 23J, bottom row), suggesting that the dynamic state (50-500nM FUS) is a weakly engaged, transient state of FUS-RNA complex, consistent with the dynamic nature of liquid-like FUS droplets. In contrast, for strong inhibitor RNA S2, which has a compact structure with a FRET efficiency of 0.8 in the absence of FUS, addition of low FUS concentration (5nM) does not result in shift in FRET efficiency (Figure 23K). Even with increased FUS concentration (50-500nM), only modest decreases of FRET efficiency to 0.6-0.7 were observed and the smFRET traces are highly static without dynamic fluctuation (Figure 23K). This static FRET signal suggests that, in contrast to the unstructured polyU50 RNA, the structured nature of the strong inhibitor RNA S2 may render it unable to expand upon binding of FUS, thus inhibiting the formation of dynamic multiple FUS:RNA complexes and resulting in inhibited LLPS (Figure 23K, right panel). In summary, it appears that longer, unstructured RNA oligonucleotides can allow for remodeling upon interaction with FUS that promotes the additional multimerization of FUS and RNA within dynamic, potentially liquid-like complexes. Conversely, more structured RNA oligonucleotides may inhibit multimerization and phase separation through binding to monomeric FUS molecules and resisting this remodeling that would allow for the binding of additional FUS proteins.

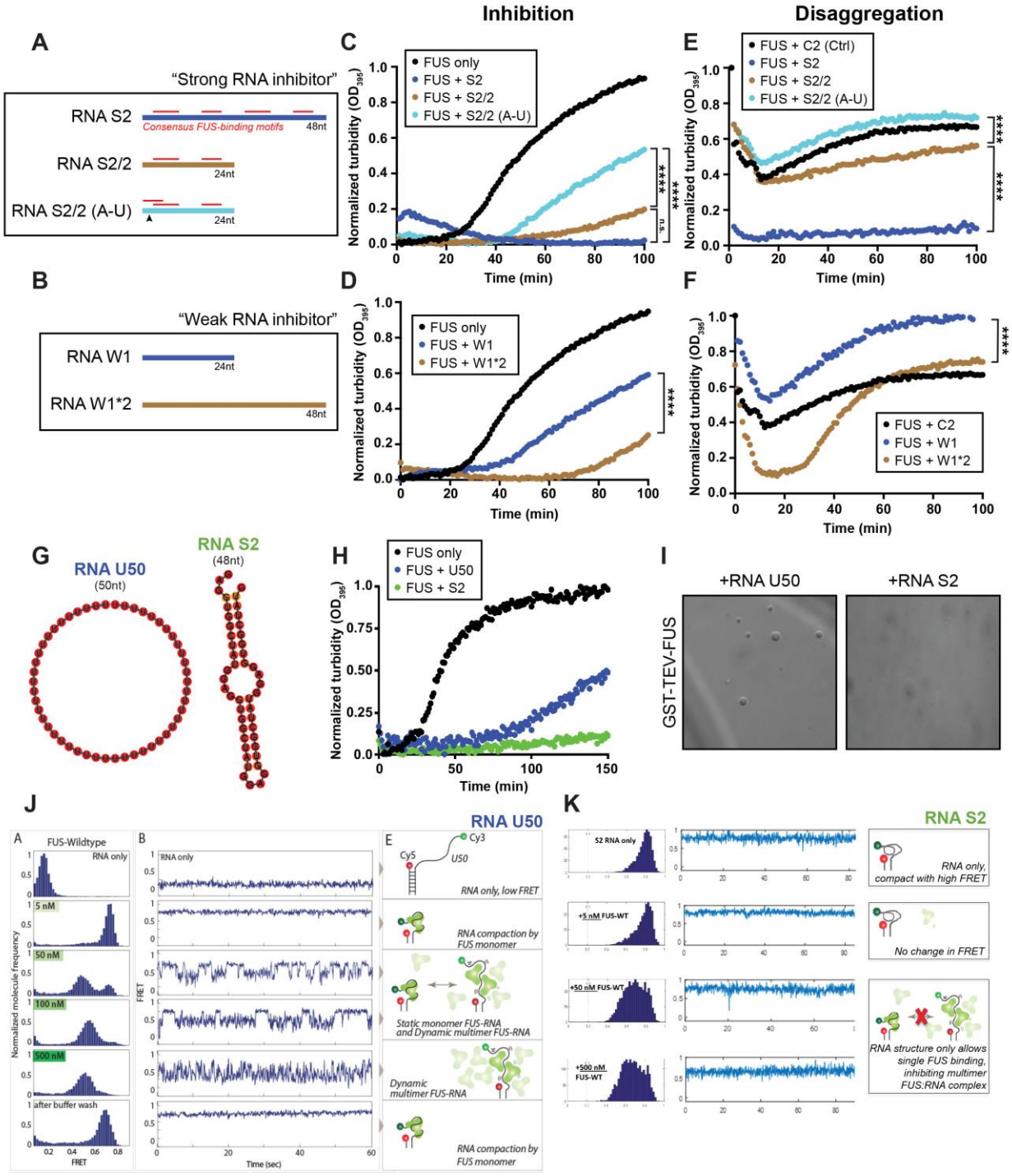

Figure 23. RNA length, sequence, and structure determine activity in preventing/reversing FUS aggregation.

(A-B) Schematics of RNA molecules used in these experiments. Red bars indicate predicted FUS binding sites. (C-D) GST-TEV-FUS (5μM) was incubated with TEV protease in the presence or absence of indicated RNA (20μM) for 0–100 min. Turbidity measurements were taken every minute to assess the extent of aggregation. Shown is the

representative results of at least three repeats. (E-F) Fibrillization reactions were performed as in (C-D) and at the end of the reaction, indicated RNA (20μM) were added to the reaction. Turbidity measurements were taken every minute to assess the extent of disaggregation. (G) Predicted secondary structure of polyU50 and RNA S2 by RNA-Fold. (H) GST-TEV-FUS (5μM) was incubated with TEV protease in the presence or absence of polyU50 (blue) or RNA S2 (green) (20μM) for 0–150 min. Turbidity measurements were taken every minute to assess the extent of aggregation. Shown is the representative results of at least three repeats. (I) DIC images of GST-TEV-FUS (5μM) droplets formed in the presence and absence of indicated RNAs (20μM). (J) FRET representative traces of polyU50 and histograms for varying FUS concentrations (5-500nM) and after wash. (K) FRET representative traces of RNA S2 and histograms for varying FUS concentrations (5-500nM). Two-way ANOVA with Tukey's correction were used to compare across all groups. **** $p < 0.0001$. Experiments were performed by Guo, L., Shorter, J., et al. at the University of Pennsylvania.

3.3.3 Strong and weak RNA inhibitors have different interacting patterns with the FUS RRM, RGG and ZnF domains

While our data suggest that certain characteristics of RNA oligonucleotides, including sequence, length and structure, can be strong determinants of their ability to buffer aberrant FUS phase transitions, we next sought to further define the mechanism of RNA-based aggregate inhibition based upon RNA engagement with specific domains of the FUS protein. We selected three RNAs with the strongest *in vitro* activities (RNA S1, RNA S2, and RNA S3) and one weak inhibitor (RNA W1) for the following studies. Previously, we showed that Kapβ2 couples binding energy to the PY-NLS of FUS to disaggregate FUS aggregates (Guo et al., 2018). We hypothesize that RNA binding is also is important for its function in inhibiting/reversing aberrant FUS phase transitions. Consistent with this hypothesis, strong inhibitors bind to FUS tightly (RNA S1: Kd = 40.82 nM; RNA S2: Kd = 104.7 nM; RNA S3: Kd = 101.5 nM) and weak inhibitor RNA W1 binds

to FUS with a *Kd* that is not detectable by fluorescence anisotropy (Figure 24A-D). We and others have shown that mutating four conserved phenylalanines (F) in FUS RRM to leucine (L) rescues FUS toxicity by abolishing RNA binding (Daigle et al., 2013; Sun et al., 2011). Therefore, we hypothesize that the FUS RRM is the primary site of interaction for the function of RNA inhibitors. Fluorescence anisotropy experiments confirmed that four F to L mutations (FUS 4FL) significantly reduced binding affinity between FUS and strong RNA inhibitors (Figure 24A-C). Upon addition of TEV protease, this mutant protein interestingly aggregated slower than WT FUS, suggesting these mutations in the RRM also may disrupt self-interaction between FUS molecules (data not shown) and is consistent with our previous observation that the RRM is important for FUS aggregation (Daigle et al., 2013; Sun et al., 2011).

Thus, we next tested whether disrupting the interaction between RNA inhibitors and the FUS RRM would abolish the ability of RNA to inhibit and reverse FUS phase transitions. Although aggregating slower, FUS 4FL formed aggregates with similar morphology compared to WT FUS upon extended incubation (Figure 24F). Interestingly, when we next examined aggregation of FUS 4FL in the presence of RNA inhibitors, we found that strong RNA inhibitors effective in buffering WT FUS phase transitions could no longer prevent (Figures 24G, 23A), or reverse pre-formed FUS 4FL aggregates (Figures 24H, 23B). Combining these results with the reduced binding affinity of FUS 4FL to RNA (Figure 24A-C), our data could suggest a model in which RNA binding to the RRM results in the steric hinderance of intermolecular contacts between FUS RRM regions that are required for FUS aggregation. Surprisingly, some strong RNA inhibitors not only lost the ability to inhibit FUS 4FL fibrillization, but actually promoted the aggregation of FUS 4FL (Figure 25A). This observation could indicate that there are additional binding sites where strong inhibitors can interact with and facilitate aggregation of FUS, which is

consistent with the result that even with 4F-L mutation, RNAs bind to FUS 4FL with *Kd* in the nM range.

To next identify other potential domains in FUS that may be playing a role in RNA-mediated antagonization of aberrant phase transitions, we used nuclear magnetic resonance (NMR) to determine the interaction patterns of various RNA inhibitors with the FUS protein (Figure 25C). Since the PrLD domain does not bind to RNA, here we used a construct consisting of known RNA-interaction domains (RRM, RGG and Zinc Finger (ZnF) domains) without the PrLD ($FUS_{269-494}$) that has been used previously to investigate FUS/RNA interactions. NMR spectrum of $FUS_{269-494}$ with and without RNA oligonucleotides was determined. As expected, most strong chemical shift perturbations are observed in the RRM region, suggesting that this is the major binding site of RNA inhibitors (Figure 25C). RNA S1 (bottom panels) induces much higher chemical shifts overall and the most intensity decrease of the signal, indicating that it binds very tightly compared to the other RNAs and is consistent with our *Kd* measurement (Figures 22A-D, 23C). Interesting, chemical shift perturbations are also present in the ZnF and RGG domain, indicating weak interaction throughout these regions (Figure 25C), prompting us to next investigate how the ZnF and RGG domains effect the activity of RNA oligonucleotides in inhibiting and disaggregating FUS assemblies.

To test this, we next generated a $FUS^{C428A:C433A:C444A:C447A}$ (FUS 4CA) mutant which disrupts the C4 type Zinc coordination scheme (Figure 25D-E). FUS 4CA aggregation kinetics and morphology are similar to that of WT-FUS, reflecting the fact that FUS_{1-422} is the region that is particularly important for FUS aggregation (Figure 25D). Surprisingly, when we next tested this FUS 4CA mutant in our turbidity assays, it appeared that disrupting the ZnF domain did not interrupt the inhibition (Figure 25D) and disaggregation (Figure 26A) activity of strong RNA

inhibitors. Consistent with this result, the binding affinities of strong RNA inhibitors to FUS 4CA did not show measurable decreases when compared to their binding to WT FUS (Figure 24A-C). In comparison, these ZnF mutations seemed to have much more pronounced effect on the activity of weak RNA inhibitors, which could neither inhibit nor reverse the aggregation of FUS 4CA (Figures 23E, 24B) compared to reactions with FUS 4CA alone. These alternative effects of ZnF mutations on the activity of strong and weak RNA inhibitors could be due to different interacting patterns with FUS, as NMR data showed strong RRM binding and weak ZnF binding for strong RNA inhibitors (RNA S1) and weak binding between the weak RNA inhibitor (RNA W1) and both the RRM and ZnF domains (Figure 25C). Together, these observations suggest that the activity of weak inhibitors rely more heavily upon interaction with the ZnF domain, while strong RNA inhibitors may be more dependent upon interaction with the RRM region.

In addition to the RRM and ZnF regions, our NMR data suggested that FUS RGG domains also interacted with various RNA inhibitors (Figure 25C). Therefore, to begin to investigate the relative contribution of RNA:RGG domain interactions to inhibition and reversal of FUS aggregation, we created another FUS mutant construct consisting of the N-terminal FUS PrLD and RRM regions with C-terminal deletions of the RGG-ZFN-RGG domains (FUS 371X) (Figure 25F-G). As expected, after deleting the RGGs that are important for FUS assembly (Hofweber et al., 2018; Qamar et al., 2018; Wang et al., 2018b), FUS 371X aggregated much slower than WT FUS, taking up to 24 hours to fully assemble into fibrous aggregates (Figure 26C). Moreover, when the C-terminal RGG domains are deleted, we observed that binding of various RNAs to the protein was interrupted to different degrees depending on the individual inhibitor (Figure 24A-C). For example, the most significant change was observed for RNA S2, where *Kd* increased from 104.7±9.2 nM to N/A. Deleting the C-terminal RGG domains induced moderate changes in

binding of RNA S1 to FUS, with *Kd* increasing from 40.82±8.32 nM to 106.5±58.92 nM. On the other hand, the we found that binding of RNA S3 to FUS without the C-terminal RGG domains was comparable to proteins with C-terminal RGG domains included. Consistent with these trends in binding affinity, deleting the two RGG domains completely abolished the activity of all RNAs to inhibit and reverse the aggregation of FUS (Figure 25F-G) except for RNA S3, which inhibited the aggregation of FUS 371X by ~50%. These results thus suggest that that while RGG domains seem to be important for RNA S2 binding and activity, they appear to be nonessential for the binding of RNA S3 to FUS protein and resulting inhibitory activity, indicating different binding specificity and functional mechanisms for individual RNA oligonucleotides.

Our analysis on the FUS RRM mutant (4FL), FUS ZnF mutant (4CA), and FUS RGG deletion mutant (371X) indicates that RNA binding to different FUS domains is important for its ability to inhibit and reverse FUS phase transition and aggregation. In general, stronger binding indicates stronger activity. However, even with tight binding (K*d* in the nM range), strong RNA inhibitors were not able to inhibit the aggregation of FUS 4FL nor FUS 371X (Figures 23A-B, 23F-G). This result indicates that in addition to binding, other factors, such as interaction between FUS domains, also play important roles in RNA inhibitors' activity. For example, binding to the RRM by RNA may elicit a long-range allosteric conformational change in the RGGs that breaks intermolecular contacts responsible for maintaining the fibril. Alternatively, initial binding to the RRM may enable RNA to engage secondary binding sites in the RGGs that rapidly break intermolecular contacts directly. In both cases, we would expect to observe cooperativity in RNA function. Indeed, both strong inhibitors and weak inhibitors showed strong cooperativities with H-coefficient range from 2 to 4.5 (Figure 25H). Specifically, the inhibiting activity of weak inhibitor RNA W1 showed stronger cooperativity (H-coefficient of 4.5) than strong inhibitors (H-

coefficient of ~2). This is consistent with our results that all three regions (i.e. RRM, ZnF, and RGGs) are important for the activity of weak RNA inhibitors and that mutating any one of them would abolish the ability of weak RNA inhibitors to prevent/reverse FUS aggregation. Alternatively, only two regions (RRM and RGGs) seem to participate in the activity of strong inhibitors. Therefore, in addition to RNA binding to individual domains, the cooperativity between FUS domains seems to also be important for RNA inhibitor function. This cooperativity is most important for weak RNA inhibitors because they bind weakly across the three regions. Support for this notion could be drawn from a recently proposed bipartite model of FUS:RNA binding (Loughlin et al., 2019) involving both structure- and sequence-specific binding of RNA by the FUS RRM and ZnF domains with additional sequence-independent cooperativity from RGG domains.

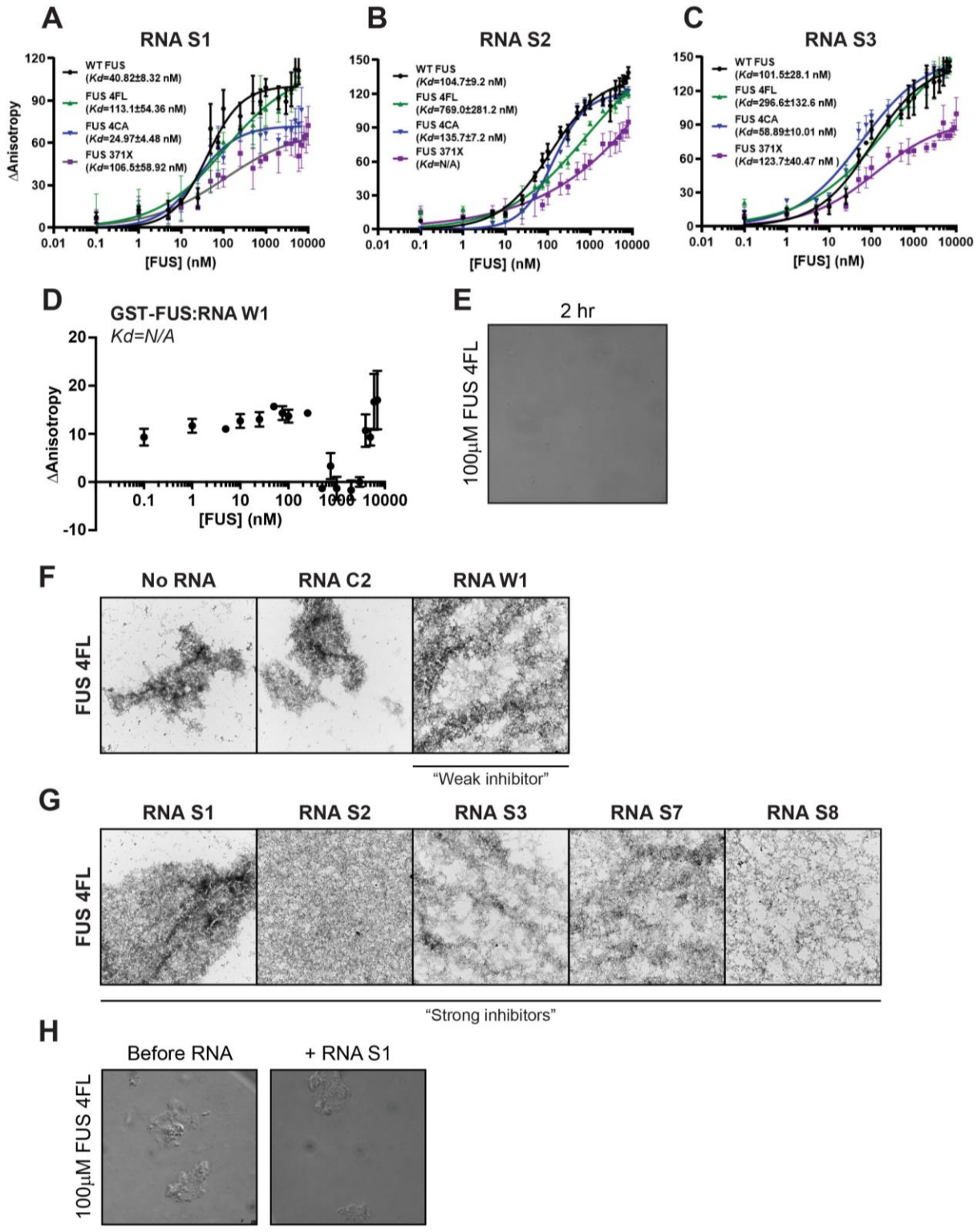

Figure 24. Mutation of FUS RRM affects RNA affinity and inhibitory activity.

(A-D) Anisotropy of 8nM fluorescein-labeled RNA binding to GST-TEV-FUS WT, 4FL, 4CA or 371X at indicated concentration. Values represent means ± SEM (n=3). Binding curve was fitted by Prism. Solid line represents the fit

and the fitted *Kd* was reported on the figure. (E) GST-TEV-FUS 4FL does not form droplets even at 100μM after 2 hours of incubation. (F-G) GST-TEV-FUS 4FL fibrillization reactions were performed in the presence of the indicated RNAs and were processed for EM at the end of the reaction. (H) 100μM GST-TEV-FUS 4FL aggregates were formed by 24 hours of incubation and addition of strong inhibitor RNA S1 does not reverse the formation of the aggregates. Experiments were performed by Guo, L., Shorter, J., et al. at the University of Pennsylvania.

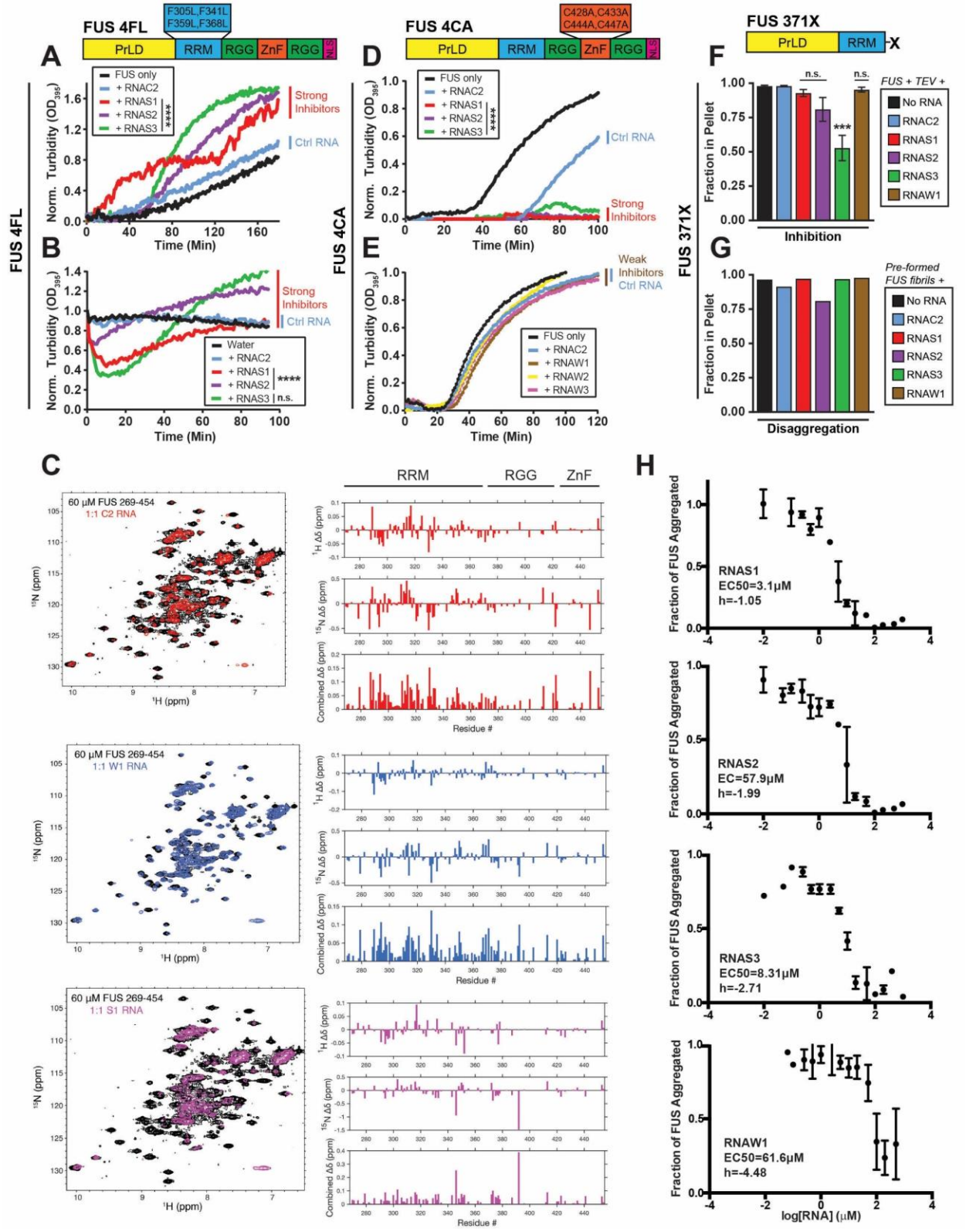

Figure 25. FUS RRM and RGG domains affect cooperative RNA binding and inhibition of FUS aggregation.

(A) GST-TEV-FUS FUS 4FL (5μM) was incubated with TEV protease in the presence or absence of strong inhibitor (20μM) for 0–180 min. Turbidity measurements were taken every minute to assess the extent of aggregation. Shown is the representative results of at least three repeats. (B) Fibrillization reactions were performed as in (A) and at the end of the reaction, water or indicated RNA (20μM) were added to the reaction. Turbidity measurements were taken every minute to assess the extent of disaggregation. (C) NMR spectrum and chemical shift perturbation of FUS (269-494) with and without the addition of the indicated RNA. (D) GST-TEV-FUS 4CA (5μM) was incubated with TEV protease in the presence or absence of strong inhibitors (20μM) for 0–180 min. Turbidity measurements were taken every minute to assess the extent of aggregation. Shown is the representative results of at least three repeats. (E) GST-TEV-FUS 4CA (5μM) was incubated with TEV protease in the presence or absence of weak inhibitors (20μM) for 0–180 min. Turbidity measurements were taken every minute to assess the extent of aggregation. Shown is the representative results of at least three repeats. (F) GST-TEV-FUS 371X (10μM) was incubated with TEV protease in the presence or absence of strong inhibitor (40μM) at 25°C for 20h with agitation at 1200rpm. Aggregated protein was quantified by sedimentation assay. Values represent means ± SEM (n=3). (G) Fibrillization reactions were performed as in (F) and at the end of the reaction, water or indicated RNA (40μM) were added to the reaction. Sedimentation assays were performed at 24 hours after addition of RNA to monitor the progress of disaggregation. (H) GST-TEV-FUS (5μM) was incubated with TEV protease in the presence or absence of strong (RNA S1-S3) or weak (RNA W1) inhibitors at indicated concentration for 0–100 min. Turbidity measurements (absorbance at 395nm) were taken every minute to assess the extent of aggregation. At the end of the fibrilization reaction, the absorbance was then normalized to that of FUS plus buffer control to determine the relative extent of aggregation. Values represent means ± SEM (n=3). Two-way ANOVA with Dunnett's correction were used to compare all groups to control RNA treatments in turbidity assays. One-way ANOVA with Tukey's correction was used to compare pellet fractions across all treatment groups. *** $p < 0.001$, **** $p < 0.0001$. Experiments were performed by Guo, L., Shorter, J., et al. at the University of Pennsylvania.

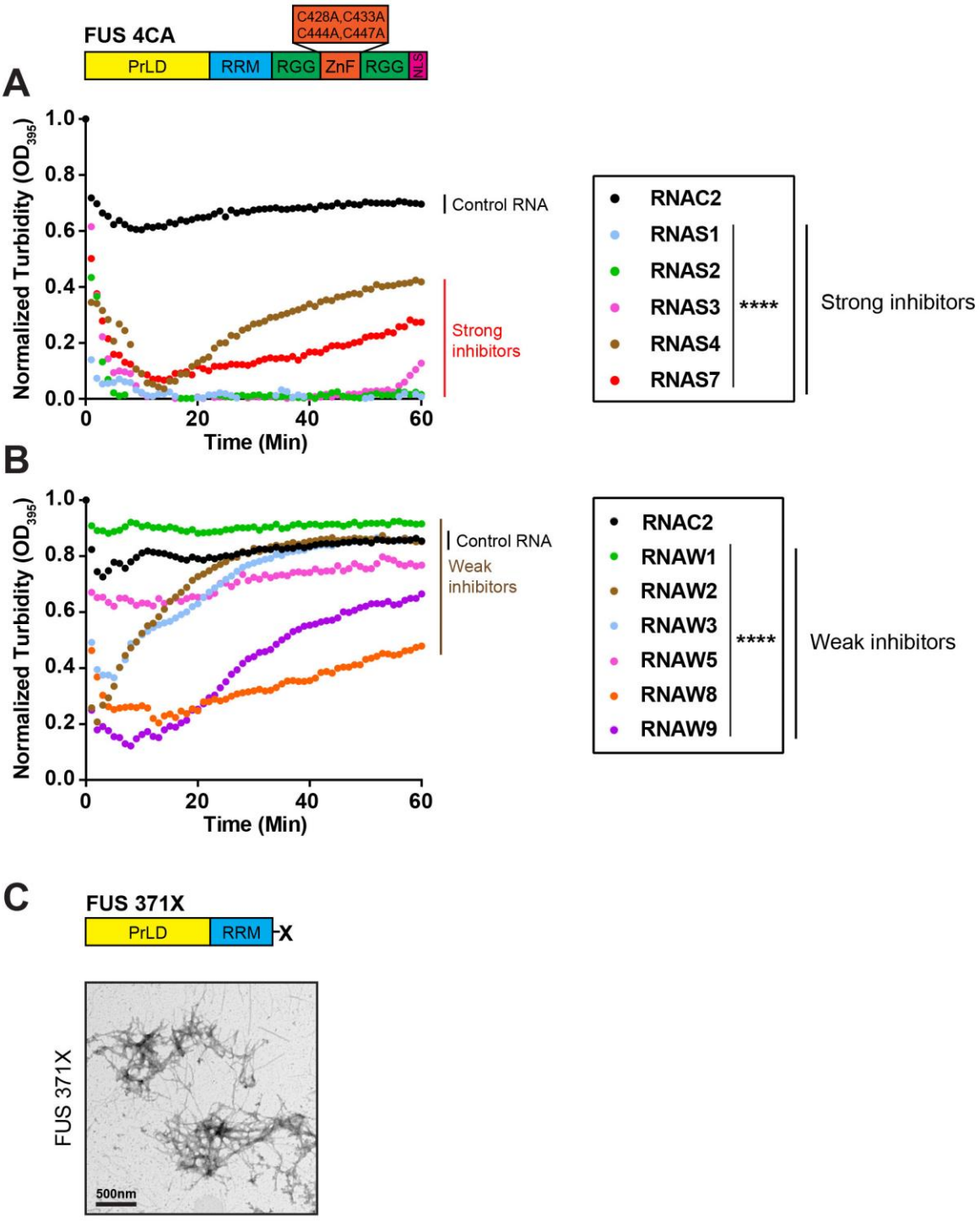

Figure 26. Mutation in FUS ZnF domain affect the activities of weak, but not strong, RNA inhibitors.

(A-B) Fibrillization reactions were performed as in Figure 25D for GST-TEV-FUS 4CA and at the end of the reaction, water or strong inhibitors (20μM) were added to the reaction. Turbidity measurements were taken every minute to assess the extent of disaggregation. Shown are representative traces of at least three replicates. (C) Fibrillization

reactions were performed for FUS 371X as in Figure 25F and at the end of the reaction, sample was processed for EM. FUS 371X forms fibrils similar to WT FUS, although the kinetics are much slower. Two-way ANOVA with Dunnett's correction were used to compare all groups to control RNA treatments. **** $p < 0.0001$. Experiments were performed by Guo, L., Shorter, J., et al. at the University of Pennsylvania.

3.3.4 The RRM and ZnF domains mediate endogenous RNA buffering of intracellular FUS phase transitions

As it has recently been demonstrated that endogenous intracellular RNAs, particularly within the nuclear compartment, have the ability to buffer aberrant phase transitions of FUS within physiological environments (Maharana et al., 2018), we next sought to determine whether the short RNA oligonucleotide inhibitors identified here function in a similar manner to endogenous RNA inhibitors within a cell. To test this hypothesis, we adapted the recently developed Corelet system used to map intracellular phase behavior of the FUS PrLD and other intrinsically disordered regions (IDRs) under the tight control of blue light (Bracha et al., 2018) (see Chapter 4.1.2 for description). Here, we first generated constructs consisting of FUS coding sequences (amino acids 1-453) containing wildtype RNA-binding regions, mutated RRM (4FL), mutated ZnF domain (4CA), or double RRM/ZnF mutants (4FL/4CA) with C-terminal SspB peptide tags (Figure 27A). RGG3 and PY-NLS regions were omitted to prevent spontaneous phase separation of full-length FUS proteins with mutated RNA-binding regions (Daigle et al., 2013), as well as to avoid potential confounds associated with endogenous buffering of FUS phase separation by nuclear import receptors (Guo et al., 2018; Hofweber et al., 2018; Qamar et al., 2018; Yoshizawa et al., 2018). Cells co-expressing these FUS-SspB constructs along with photo-activatable seeds (iLID-EGFP-

FTH1, described in (Bracha et al., 2018)) were then exposed to acute (30 second) blue light activation sequences and condensate formation/dissolution were examined across these mutants (Figure 27B). Interestingly, mutations within the RRM region (4FL, red trace) led to a significantly enhanced formation of light-induced FUS-SspB condensates compared to WT (black trace), while mutations within the ZnF domain (4CA, blue trace) had only a modest effect on LIPS (Figure 27B-C). However, when ZnF mutations were combined with RRM mutations (4FL/4CA, purple trace), a further enhancement of FUS-SspB condensate formation was observed when compared to either RRM or ZnF mutations alone (Figure 27B-C). A similar pattern was observed when we next examined light-induced phase behavior as a function of relative FUS-SspB protein expression levels (Figure 27D-E). Here, ZnF mutations (4CA) again only slightly lowered the threshold protein concentration (C_{thresh}) required within a cell to allow for observable condensate formation, while RRM (4FL) and dual RRM/ZnF (4FL/4CA) mutations greatly reduced C_{thresh} under these light activation conditions (Figure 27D-E). RRM (4FL) and dual RRM/ZnF (4FL/4CA) mutations also led to a slowed dissolution of light-induced condensates when compared to WT and ZnF-only (4CA) mutants following light removal (Figure 27F), potentially indicating an increased stability of these membraneless structures. Together, these results suggest that while endogenous RNA contacts within the RRM may be most important for the buffering of aberrant phase transitions within an intracellular environment, weak or cooperative binding by the ZnF domain likely also plays a role in preventing intracellular aggregation of FUS under physiological conditions.

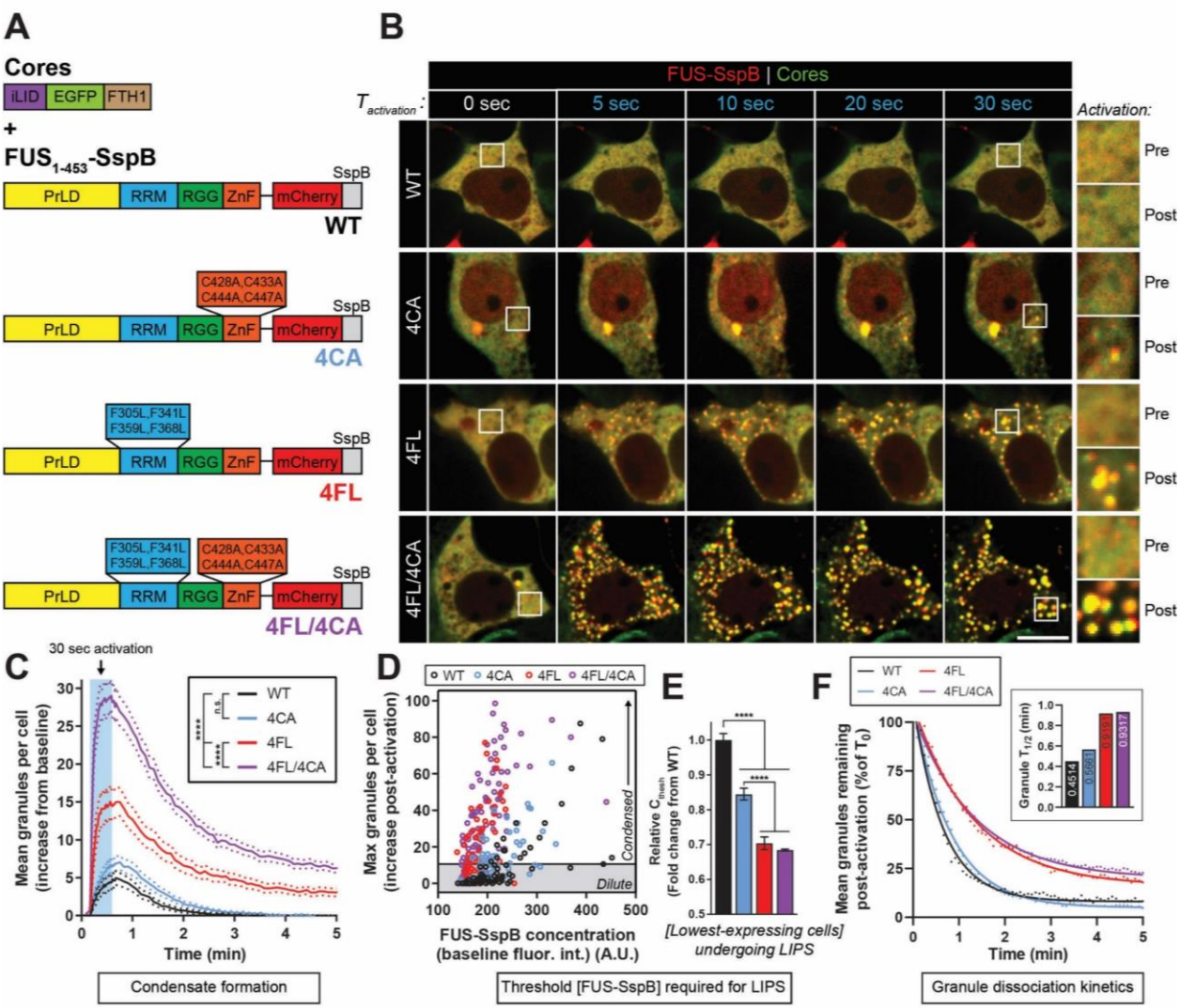

Figure 27. The RRM and ZnF domains cooperate in mediating intracellular RNA buffering of FUS phase separation

(A) Schematic of iLID cores and FUS-SspB mutant constructs used in (B-F). (B) **Representative images of HEK293 cells co-expressing iLID cores (green) and the indicated mutant FUS-SspB protein (red) prior to and during a 30 second light activation protocol (488nm, 75% laser power). Insets show cytoplasmic area at baseline and following 30 second activation. Scale bar = 10μm.** (C) **Quantification of the average number of FUS-SspB assemblies formed per cell during and following a 30 second light activation period. *n* = 68-91 cells per condition. Two-way ANOVA with Tukey's post-hoc test was used to compare across groups.** (D) **Diagram of maximal light response (number of condensates during the activation period) in (C) plotted against baseline FUS-SspB concentration. Data points represent individual cells.** (E) **Quantification of representative threshold**

concentrations required for cells to undergo LIPS. *n* = the lowest-expressing 5 cells with >10 granules post-activation per condition. Fluorescence intensity values are normalized to WT and shown as fold-change. One-way ANOVA with Tukey's post-hoc test was used to compare across groups. (F) **Quantification of granule dissociation kinetics following conclusion of light activation. Number of granules per cell were plotted over time as a percentage of granules in the first frame following light removal (T0). One-phase exponential decay curves were fit and T½ was calculated for each condition and plotted in the inset (top right). *n* = 20-76 cells per group. Data shown are mean +/- S.E.M. **** p < 0.0001.**

3.3.5 Generation of a light-inducible model of FUS-ALS proteinopathy

To next test whether these RNA oligonucleotides can also prevent and reverse FUS aberrant phase transitions and aggregation in mammalian cells, we developed a light-inducible model of FUS proteinopathy based on a previous model developed to control the aggregation of TDP-43 (Chapter 2). To this end, we generated a doxycycline-inducible optogenetic Cry2-FUS (optoFUS) construct to selectively induce FUS proteinopathy under the spatiotemporal control of light stimulation (Figure 28A). Cry2olig is a variant of the Photolyase-Homologous Region (PHR) of the Cryptochrome 2 protein from *Arabidopsis thaliana* that undergoes reversible homo-oligomerization (~5 min) in response to blue light (Taslimi et al., 2014). We first tested whether Cry2olig-mediated increases in focal intracellular concentrations of optoFUS protein can seed intracellular FUS proteinopathy upon chronic light exposure. HEK293 cells treated with 10 ng/mL doxycycline to express optoFUS protein were exposed to 8 hours of blue light (~0.1-0.3 mW/cm^2, 465 nm) or darkness and were first examined by immunofluorescence. Interestingly, cells expressing optoFUS that were exposed to blue light stimulation exhibited a significant depletion of nuclear optoFUS signal and enhanced formation of cytoplasmic inclusions relative to optoFUS-expressing cells kept in the dark (Figure 28C-E). Fluorescence recovery after photo-bleaching

(FRAP) analysis of light-induced optoFUS inclusions revealed minimal recovery after photo-bleaching, indicating limited dynamics and solid-like property of the optoFUS inclusions resulting from aberrant phase transition (Fig. 28F). Sedimentation assay also confirmed that light-induced optoFUS inclusions were detergent-insoluble and seemed to slightly increase the amount of insoluble endogenous FUS relative to cells kept in darkness (Figure 28G). To next determine whether optoFUS inclusions more closely resembled FUS-ALS or FTLD-FUS pathology observed in postmortem patient tissue, we performed immunofluorescence analysis of co-localization between light-induced inclusions and common pathological hallmarks seen in these diseases. While optoFUS inclusions did co-stain positively with the methylated FUS antibody 9G6, we did not observe co-localization with fellow FET family proteins EWSR1 and TAF15 (Figure 26H-I), two proteins that typically co-deposit with FUS inclusions in FTLD but not in ALS patients (Mackenzie et al., 2010; Neumann et al., 2011, 2012). In addition, optoFUS inclusions do not co-localize with stress granule marker G3BP1 (Figure 29A) or TDP-43 (Figure 29B). This immunocytochemical profile was also observed when optoFUS inclusions were induced in human ReNcell VM neurons (Figure 29C-D), suggesting a consistency across human cell line and neuronal models. Taken together, these data indicate that light-activated optoFUS inclusions exhibit the hallmarks of FUS pathology observed in ALS.

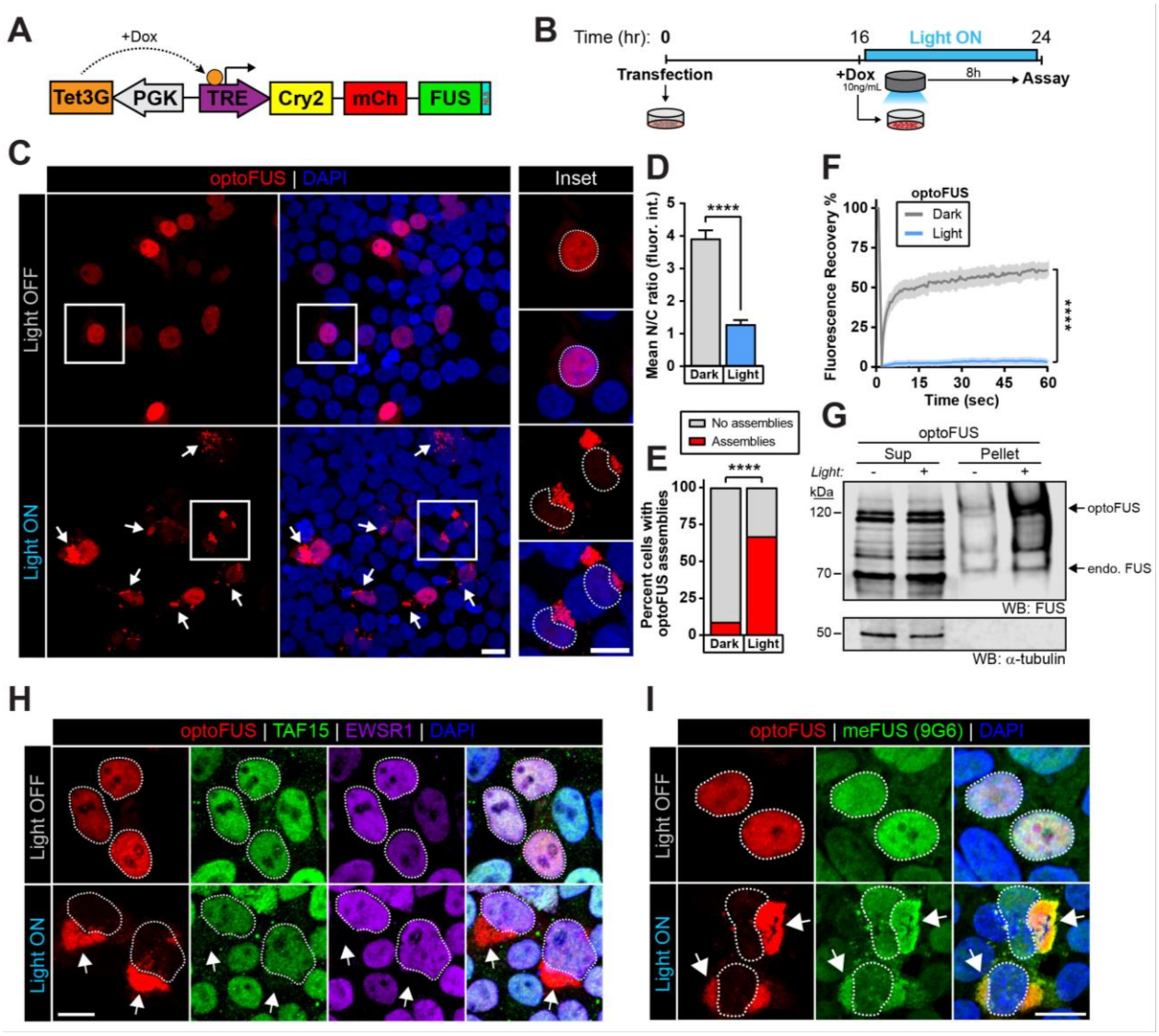

Figure 28. optoFUS is a novel light-inducible model of FUS-ALS pathology.

(A) Schematic of the optoFUS construct used in these experiments, where an N-terminal Cry2olig-mCherry fusion to the full-length FUS protein is expressed under the control of the doxycycline-inducible pTRE3G promoter. (B) Light-induction paradigm used to induce optoFUS inclusion formation. (C) Representative images of cells optoFUS-expressing cells exposed to 8 hours of darkness or light. Cell nuclei are circled. Scale bar = 10μm. (D) Immunofluorescence analysis of optoFUS nuclear/cytoplasmic signal following light induction protocol. *n* = 45 cells per group. (E) Quantification of the percentage of cells containing cytoplasmic optoFUS inclusions following 8 hours of darkness or light. *n* = 128-147 cells per group. (F) Fluorescence recovery after photobleaching (FRAP) analysis of light-induced inclusions or nuclear optoFUS signal in cells kept in darkness. *n* = 15-23 cells. (G) Detergent-solubility

fractionation of optoFUS cell lysates collected following 16 hours of darkness or light. (H-I) Immunofluorescence analysis of optoFUS inclusions for co-localization with (H) FTLD-FUS pathological hallmarks TAF15 (green) and EWSR1 (purple) or (I) the ALS-FUS-associated methylated FUS antibody 9G6 (green). Cell nuclei are circled. Scale bars = 10μm. Data shown are mean +/- S.E.M. Unpaired Student's t-tests were used to compare across groups. **** $p < 0.0001$.

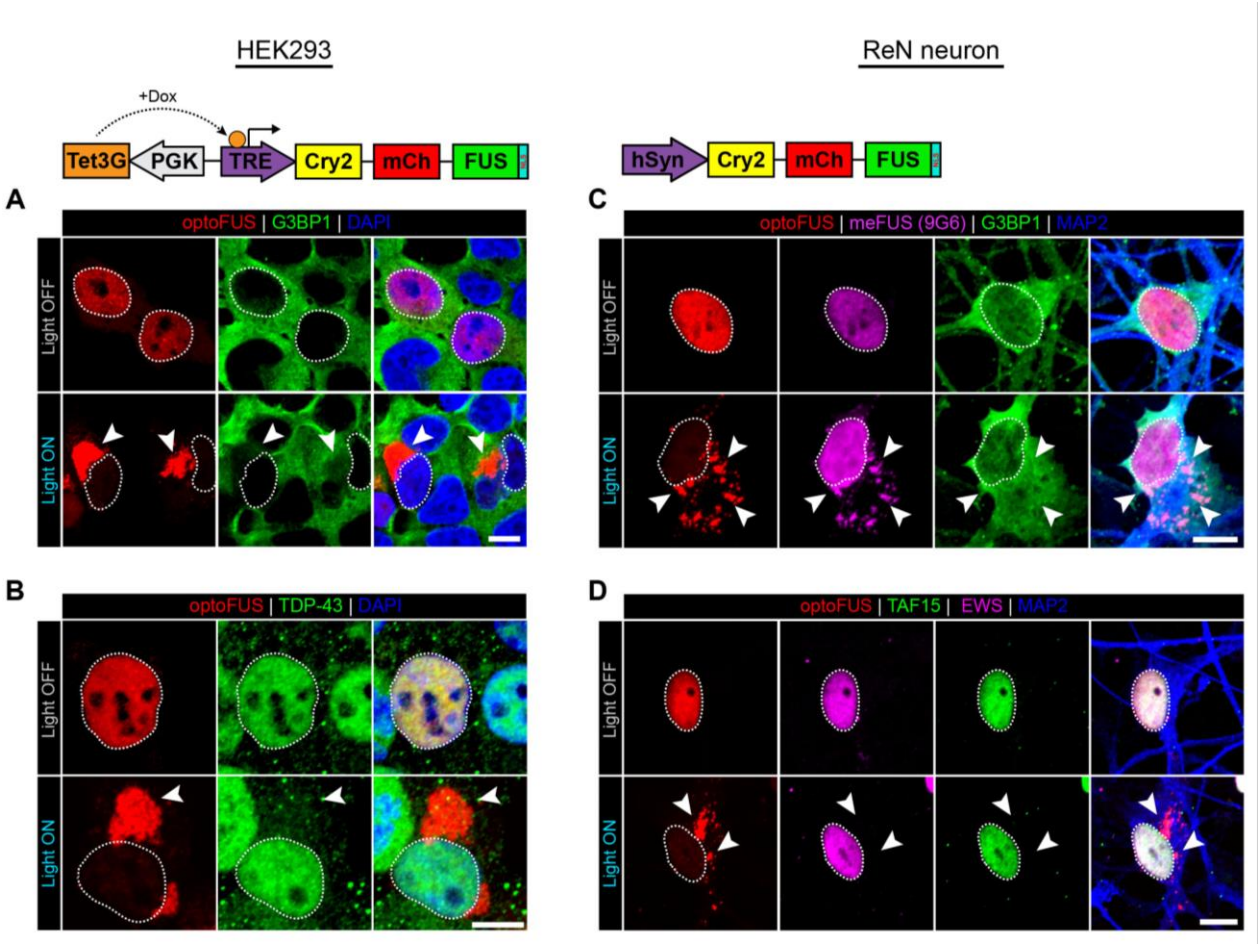

Figure 29. optoFUS inclusions in human neurons also resemble FUS-ALS pathology.

(A-B) HEK293 cells expressing optoFUS were exposed to 8 hours of blue light stimulation prior to fixation and immunofluorescence analysis of stress granule marker G3BP1 (A) and ALS-related protein TDP-43. Arrows indicate optoFUS inclusions. Cell nuclei are circled. Scale bars = 10μm. (C-D) Human ReN neurons expressing optoFUS under the control of the human synapsin promoter (hSyn) were exposed to 72 hours of blue light stimulation prior to immunofluorescence analysis of FUS pathological hallmarks. Similar to inclusions formed in HEK293 cells, optoFUS inclusions in human neurons are positive for methylated FUS (9G6), negative for stress granule protein G3BP1 (C) and negative for fellow FET family proteins TAF15 and EWSR1 (D), suggesting a closer resemblance to FUS-ALS than FTLD-FUS pathology. Arrows indicate optoFUS inclusions. Cell nuclei are circled. Scale bars = 10μm.

3.3.6 FUS-binding RNA oligonucleotides can mitigate aberrant phase transitions of FUS in mammalian cells

We then tested whether the RNA motifs that we discovered *in vitro* can prevent the formation of intracellular FUS inclusions in our optoFUS system (Figure 30A). Experiments using a 6-FAM-labeled RNA S1 oligonucleotide revealed that short RNA inhibitors seemed to accumulate predominantly in the cytoplasm of HEK293 cells ~2 hours after transfection (Figure 31A-C). We thus first pre-treated optoFUS-expressing HEK293 cells with the oligonucleotide that showed strongest activities in our *in vitro* assays (RNA S1), in addition to a control oligonucleotide (RNA C2), for two hours prior to light induction of optoFUS inclusions (Figure 30A). optoFUS inclusion burden was then quantified by automated immunofluorescence analysis of cells fixed following RNA treatment and a 6-hour light stimulation protocol (see Appendix Figure 1 for details). Remarkably, pre-treatment with RNA S1 resulted in a dose-dependent reduction in optoFUS inclusion formation when compared to treatment with control oligonucleotides (Figure 30B-C). Interestingly, while two strong inhibitors RNA S1 and RNA S2 seemed to show similar efficacies *in vitro*, the longer of the two (RNA S2) seem to be less effective in preventing optoFUS inclusions within an intracellular environment (Figure 31D). Because RNA oligonucleotides are relatively quickly digested by ribonucleases in cell, we also designed RNA analogues with higher stability to test in our intracellular optoFUS model. Using RNA S1 as a template, we designed RNA analogues with different combinations of 2'O-Me and PS bond modifications (Figure 31E-G) to test both *in vitro* and in cells. Both RNA analogues show similar inhibition and disaggregation activity compared to the template RNA S1 in our *in vitro* turbidity assays (Figure 31E-F). However, while the 2'OMe-modified RNA oligonucleotide showed slightly enhanced inhibition of optoFUS inclusion formation (Figure 30D), the RNA analogue with both 2'O-Me

and PS bond modifications did not show any activity in inhibiting optoFUS inclusion formation in HEK293 cells relative to unmodified oligonucleotides (Figure 31G). This disparity could potentially be attributed to changes in RNA secondary structure or non-specific protein binding associated with phosphorothioate substitutions (Smith and Nikonowicz, 2000) that may be sufficient to significantly alter FUS interaction patterns within the crowded cellular environment, but have less of an effect within purified *in vitro* reactions. Detergent-solubility fractionation of optoFUS cell lysates exposed to the same light stimulation conditions also confirmed a reduction in the amount of detergent-insoluble optoFUS protein in cells pre-treated with unmodified and 2'OMe-modified S1 relative to control oligonucleotides (Figure 30E-F).

We next sought to determine whether treatment with RNA inhibitors following the formation of optoFUS aggregates could be similarly effective in reducing inclusion burden, as this may represent a more therapeutically-relevant time course of intervention in patients at later stages of disease progression. Thus, here we designed a paradigm in which optoFUS-expressing cells were first subjected to chronic light stimulation to induce the formation of optoFUS aggregates prior to RNA treatments and doxycycline washout to eliminate further optoFUS expression during a 6-hour dark "disassembly" period (Figure 30G). Remarkably, while a small decrease in optoFUS aggregation was observed in control oligonucleotide-treated cells during the disassembly period, treatment with unmodified and 2'OMe-modified RNA S1 oligonucleotides resulted in a significant reduction in optoFUS inclusion burden towards levels observed in optoFUS-expressing cells kept in darkness throughout the experiment (Figure 30H-I). This effect was confirmed by sedimentation analysis of optoFUS cell lysates collected following the same light induction and treatment paradigm (Figure 30J-K). Together, these data suggest that these RNA inhibitors identified through *in vitro* assays can be utilized to aid in the prevention and reversal of aberrant FUS phase

transitions in human cells. Furthermore, common modifications used in antisense oligonucleotide therapies can have differing effects on target engagement in cellular contexts when focusing on RNA-binding protein rather than nucleic acid targets, perhaps due to effects on specific secondary RNA structures that seem to be important for the inhibitory effects of these short RNA oligonucleotides.

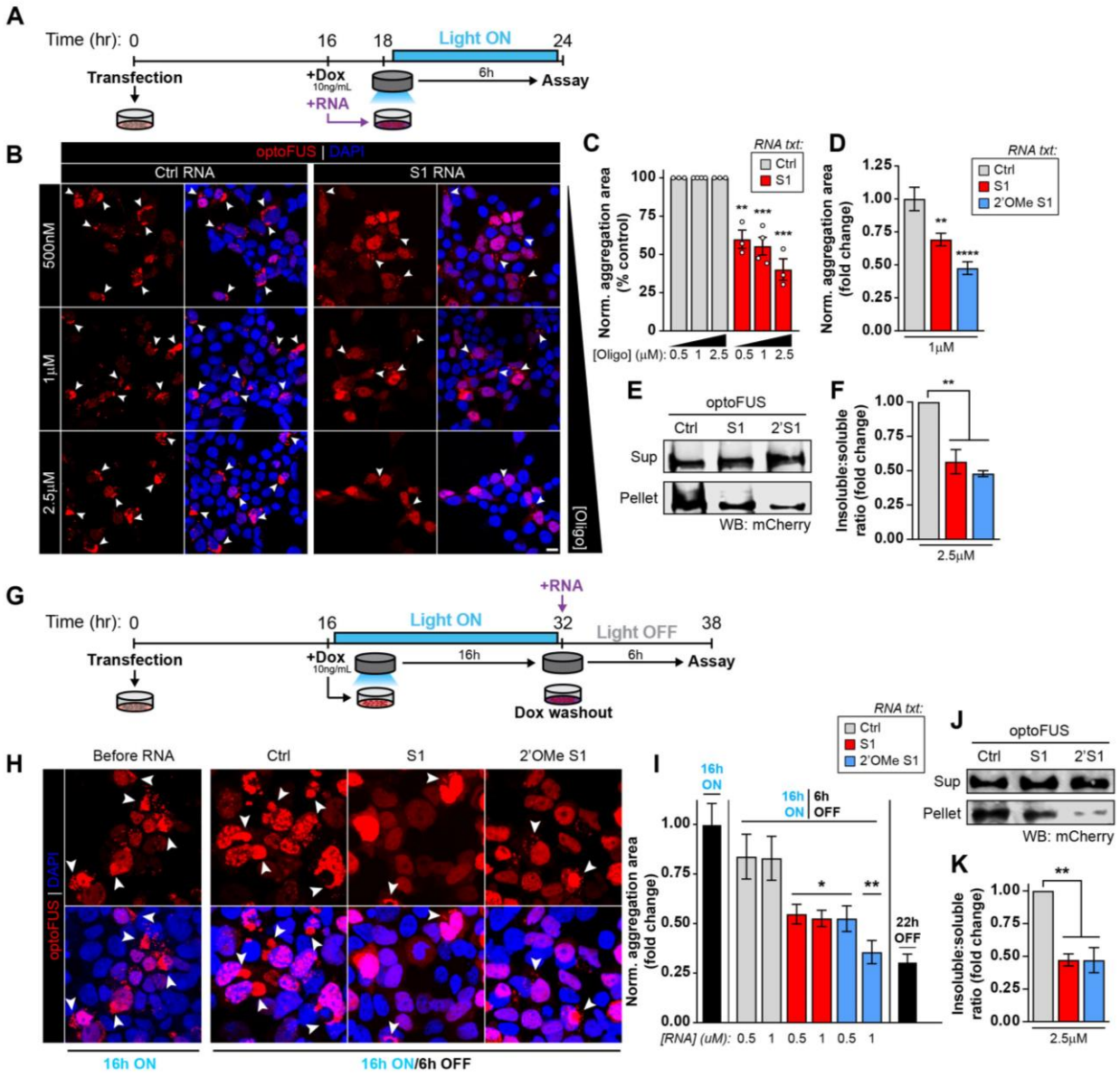

Figure 30. Strong RNA inhibitors can prevent aberrant phase transitions and reduce inclusion burden of pre-formed optoFUS aggregates in mammalian cells.

(A) Schematic of preventative RNA pre-treatment and light-induction protocol used in (B-F). (B) Representative images of optoFUS-expressing HEK293 cells pre-treated with control (Ctrl) or strong RNA inhibitor (S1) at concentrations ranging from 500nM-2.5μM for 2 hours prior to exposure to 6 hours of light activation. Scale bar = 10μm. Arrows indicate cytoplasmic optoFUS assemblies. (C) Automated immunofluorescence analysis of optoFUS aggregation area (see Appendix Figure 1 for details) in light-activated cells pre-treated with Ctrl or S1 RNA at the indicated concentrations. Data points represent individual experiments, *n* = 3-4 individual experiments, 620-904 cells

across 9 randomized fields-of-view per experiment. Values are normalized to control treatments within each treatment concentration group and presented as percentage of control per experiment. (D) Automated immunofluorescence analysis of optoFUS-expressing cells pre-treated with 1μM Ctrl, S1 and a 2'OMe-modified S1 oligonucleotide prior to the light-induction protocol outlined in (A). *n* = 9 randomized fields-of-view, 144-323 cells per field. Values are normalized to control treatments and presented as fold-change from control. (E) Detergent-solubility fractionation of cells pre-treated with 2.5μM Ctrl, S1 and 2'OMe-modifed S1 oligonucleotides prior to light-activation. (F) Quantification of ratios of detergent-insoluble to detergent-soluble band intensities in each treatment group described in (E). *n* = 3 biological replicates per condition. (G) Schematic of light-activation paradigm used for pre-formation of optoFUS inclusions and post-inclusion RNA treatment used in (H-K). (H) Representative images of optoFUS-expressing cells exposed to the light-induction protocol outlined in (G) before addition of RNA (left panel) and following a 6-hour treatment with 1μM Ctrl, S1 or 2'OMe-modified S1 oligonucleotides (right panels) in the absence of further light stimulation. Scale bar = 10μm. Arrows indicate cytoplasmic optoFUS assemblies. (I) Automated immunofluorescence analysis of optoFUS aggregation area prior to (left bar) and following RNA treatment (middle bars) with the indicated oligonucleotides. Aggregation values from cells kept in darkness throughout the experiment (22h OFF) are included for reference. Values are normalized to groups fixed immediately following light activation and prior to RNA treatment. *n* = 9 randomized fields-of-view, 79-275 cells per field. Comparisons shown are between control and targeting RNA treatments. (J) Detergent-solubility fractionation of cells treated with 2.5μM of the indicated oligonucleotides for 6 hours in the absence of light following pre-formation of light-induced optoFUS aggregates as in (G). (K) Quantification of ratios of detergent-insoluble to detergent-soluble band intensities in each treatment group described in (J). *n* = 3 biological replicates per condition. Data shown are mean +/- S.E.M. Unpaired Student's t-tests were used to compare between control and experimental groups. *$p < 0.05$, ** $p < .01$, *** $p < .001$, **** $p < 0.0001$.

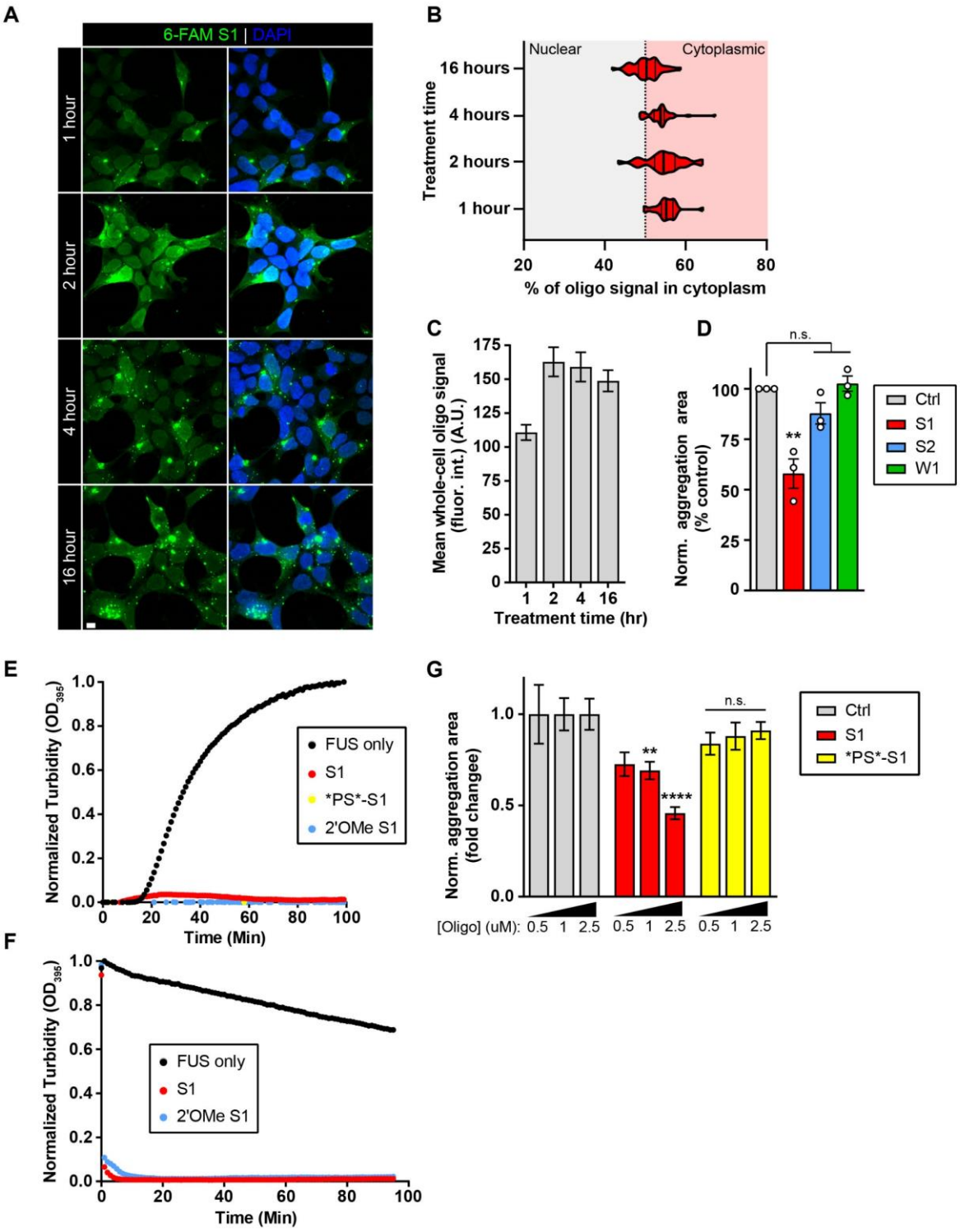

Figure 31. RNA sequence and modifications affect inhibitory activity within an intracellular environment.

(A) Representative images of HEK293 cells treated with 2.5μM of a 6-FAM-labeled S1 oligonucleotide for the indicated time periods. Scale bar = 10μm. (B) Quantification of percentage of 6-FAM S1 oligonucleotide signal

present in the cytoplasm of cells treated for the indicated time periods. *n* = 50-86 cells per treatment time. (C) Quantification of mean whole-cell fluorescence intensity of 6-FAM S1 oligonucleotide present within cells treated for the indicated time periods. *n* = 34-47 cells per treatment time. (D) Normalized aggregation area of optoFUS-expressing HEK293 cells pre-treated with 1μM of the indicated oligonucleotides for two hours prior to a 6-hour light activation period. Data points represent individual experiments. *n* = 3 individual experiments, 1236-2835 cells across 9 randomized fields-of-view per experiment. One-way ANOVA with Tukey's post hoc test was used to compare across groups. (E) *In vitro* fibrillization assay with GST-TEV-FUS was performed as in Figure 20B in the presence of the indicated RNA S1 analogues and turbidity measurements were taken over time. (F) GST-TEV-FUS fibrillization was induced as prior to addition of the indicated RNA S1 analogues, as in Figure 20E, and turbidity measurements. (G) Normalized aggregation area of optoFUS-expressing HEK293 cells pre-treated with 0.5-2.5μM of control, unmodified S1 and PS/2'OMe-modified S1 (*PS*-S1) oligonucleotides for two hours prior to a 6-hour light activation period. Values are normalized to control treatments within each treatment concentration group and presented as percentage of control per experiment. *n* = 9 randomized fields-of-view, 138-381 cells per field. Data shown are mean +/- S.E.M. ** $p < .01$, **** $p < 0.0001$.

3.3.7 Short RNA-based buffering of aberrant phase transitions can extend to other RNA-binding proteins and enhance cellular survival

In addition to FUS, aggregation of other RNA-binding proteins has been reported in patient postmortem tissue in a variety of neurodegenerative diseases, including proteins like TAF15, EWSR1 (Neumann et al., 2011), hnRNP R, hnRNP Q (Gittings et al., 2019), and perhaps most notably TDP-43. While we have previously shown that short RNA sequences can prevent aberrant phase transitions of TDP-43 and rescue associated neurotoxicity (Chapter 2), here we sought to determine whether delayed RNA intervention could assist in the reduction of pre-formed TDP-43 inclusions in a similar manner to FUS and reduce cellular toxicity.

To test this hypothesis, we developed a new optogenetic model of full-length TDP-43 aggregation again based upon the Corelets system described above (Bracha et al., 2018). In this system, cytoplasmic iLID-FTH1 cores were co-expressed with full-length TDP-43 proteins N-terminally tagged with mCherry-SspB (ssTDP43) in HEK293 cells under the control of the doxycycline-inducible Tet3G promoter (Figure 32A). HEK293 cells expressing these constructs were then exposed to 10ng/mL doxycycline treatment and chronic blue light activation (Figure 32B-C) to induce condensation and aggregation of TDP-43. Automated light activation and live-cell imaging of these cells revealed a significant enhancement of ssTDP43 assembly formation in cells exposed to chronic blue light when compared to cells kept in the darkness throughout the experiment (Figure 32B-C). Interestingly, cells expressing ssTDP43 alone (without iLID cores) exposed to the same light activation conditions showed a similar lack of ssTDP43 phase transitions, indicating a specific effect of light-induced Corelet association on TDP-43 assembly rather confounds associated with light exposure itself (Figure 32B-C).

Due to increases in assembly number and size in response to light activation over time (Figure 32B-C), we next sought to determine the effect of increased light exposure on the material state of induced ssTDP43 condensates. FRAP analysis was performed on HEK293 cells expressing iLID cores and ssTDP43 both before light exposure and on ssTDP43 assemblies in response to increasing lengths of blue light activation (Figure 32D). Remarkably, initial assemblies of ssTDP43 formed in response to 30 minutes of blue light displayed nearly full fluorescence recovery following bleaching, suggesting a dynamic or liquid-like material state of these droplets (Figure 32D). However, a progressive decrease in recovery was observed of condensates exposed to increasing lengths of blue light activation, indicating arrested dynamics of these structures over time that seemed to remain stable for at least 12 hours following light removal (Figure 32D). Thus

it appears that much like *in vitro* reactions (Elbaum-Garfinkle and Brangwynne, 2015; Lin et al., 2015; Molliex et al., 2015; Murakami et al., 2015; Patel et al., 2015), light-induced ssTDP43 aggregate formation in a cellular context begins with an initial LLPS stage followed by maturation of these droplets into more solid-state gels and/or inclusions over time. Furthermore, these more solid-state assemblies formed after chronic (8 hour) blue light activation seemed to co-stain with the pathological hallmarks phospho-TDP43 (Figure 32E) and p62 (Figure 32F) commonly observed with TDP-43 inclusions in ALS/FTD postmortem patient tissue (Kawakami et al., 2019; Neumann et al., 2006), suggesting a similar cellular response to light-induced aggregation as endogenous TDP-43 aggregation during disease.

To next determine whether short RNA-based treatment could similarly be utilized to aid in the disassembly of pre-formed TDP-43 inclusions in mammalian cells, we next designed a paradigm in which HEK293 cells transfected with both iLID cores and ssTDP43 subjected to chronic light stimulation to induce the formation of ssTDP43 inclusions were treated with control (Ctrl) and TDP-43-specific RNA oligonucleotides shown in Chapter 2 to reduce TDP-43 aggregation in neuronal models (Clip34) prior to live-cell tracking of ssTDP43 inclusion persistence and cellular survival (Figure 32G). Remarkably, we observed that treatment with Clip34 oligonucleotides resulted in a significant decrease in inclusion size over time when compared to control oligonucleotide treated cells (Figure 32H-I). Furthermore, treatment with Clip34 oligonucleotides seemed to significantly extend cellular survival in cells containing ssTDP43 inclusions at the onset of imaging (Figure 32J). This cytoprotective effect was also observed in cells expressing optoFUS subjected to identical paradigms, where treatment with the strong RNA inhibitor RNA S1 both reduced inclusion size (Figure 32K-L) and resulted in

enhanced cellular survival (Figure 32M) in cells containing optoFUS aggregates when compared to control oligonucleotide-treated cells.

Importantly, treatment of HEK293 cells with either of these short RNA inhibitors did not alter the localization of endogenous FUS (Figure 33A-B) or TDP-43 (Figure 33C-D) and did not disrupt endogenous TDP-43 splicing function (Figure 33E-G) as assessed by the *CFTR* minigene assay described previously (Ayala et al., 2006; Buratti and Baralle, 2001; Flores et al., 2019). These results thus suggest that RNA-based aggregate disruption may be a broadly applicable and viable therapeutic strategy across a number of disorders associated with aberrant RNA-binding protein assemblies.

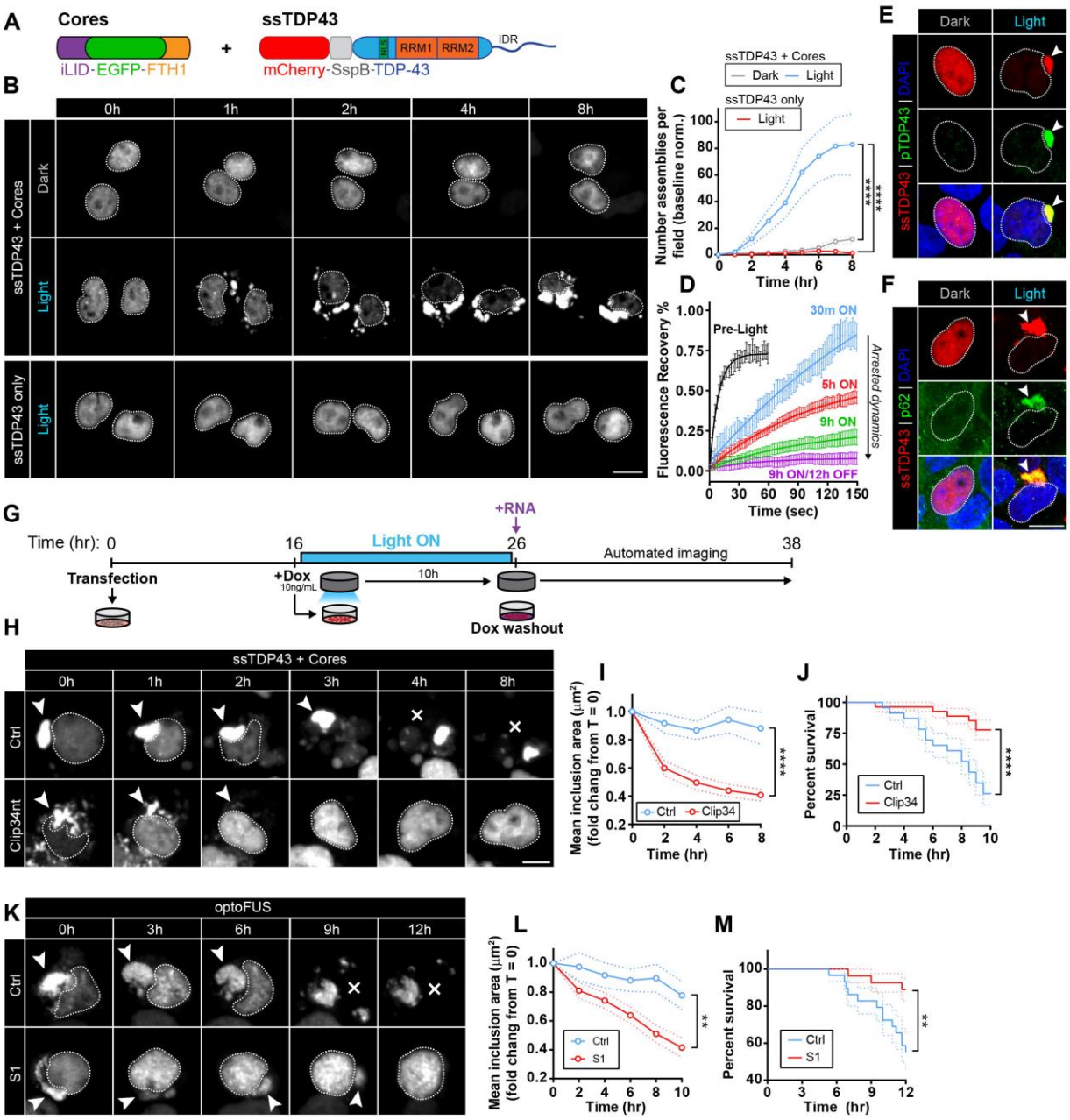

Figure 32. Short RNA oligonucleotides can reduce burden of pre-formed TDP-43 inclusions and promote cellular survival.

(A) Schematic of Corelet-based ssTDP43 system. (B) Representative images of HEK293 cells co-expressing iLID cores and ssTDP43 (top panels) or ssTDP43 alone (bottom panel) during simultaneous live imaging and light stimulation. Scale bar = 10μm. Cell nuclei are circled. (C) Automated quantification of number of ssTDP43 assemblies per field-of-view during time course of live imaging. *n* = 6 fields-of-view, 171-408 cells per field. Two-way ANOVA

with Tukey's post hoc test was used to compare across groups. (D) FRAP analysis of ssTDP43 assemblies formed in HEK293 cells co-expressing iLID cores over increasing lengths of blue light stimulation (0.1-0.3mW/cm^2, 465 nm). (E-F) Immunofluorescence analysis of co-localization between ssTDP43 inclusions formed following 8 hours of blue light stimulation and the pathological hallmarks phospho-TDP43 (E) and p62 (F). Cell nuclei are circled. Arrows indicate light-induced inclusions. Scale bars = 10μm. (G) Schematic of light-activation paradigm used for pre-formation of ssTDP43 and FUS inclusions prior to RNA treatments and live imaging used in (H-M). (H) Representative live images of HEK293 cells co-expressing iLID cores and ssTDP43 pre-exposed to 10 hours of blue light stimulation following treatment with 2μM of the indicated oligonucleotides. Arrows indicate inclusions and X's indicate cell death. Cell nuclei are circled. Scale bar = 10μm. (I) Quantification of mean inclusion size over time following treatment with the indicated oligonucleotides. Values shown are normalized to areas of individual inclusions at the onset of imaging and are presented as fold-change from T_0. *n* = 25-37 inclusions per treatment. (J) Survival curves of cells containing ssTDP43 inclusions at the onset of imaging treated with the indicated oligonucleotides. *n* = 23-26 cells. (K) Representative live images of HEK293 cells expressing optoFUS pre-exposed to 10 hours of blue light stimulation following 2μM treatment with the indicated oligonucleotides as in (G-J). Arrows indicate inclusions and X's indicate cell death. Cell nuclei are circled. Scale bar = 10μm. (K) Quantification of mean optoFUS inclusion size over time following treatment with the indicated oligonucleotides. Data are presented as in (I). *n* = 26-29 inclusions per treatment. (M) Survival curves of cells containing optoFUS inclusions at the onset of imaging treated with the indicated oligonucleotides. *n* = 27-29 cells per treatment. Data shown are mean +/- S.E.M. ** $p < .01$, **** $p < 0.0001$.

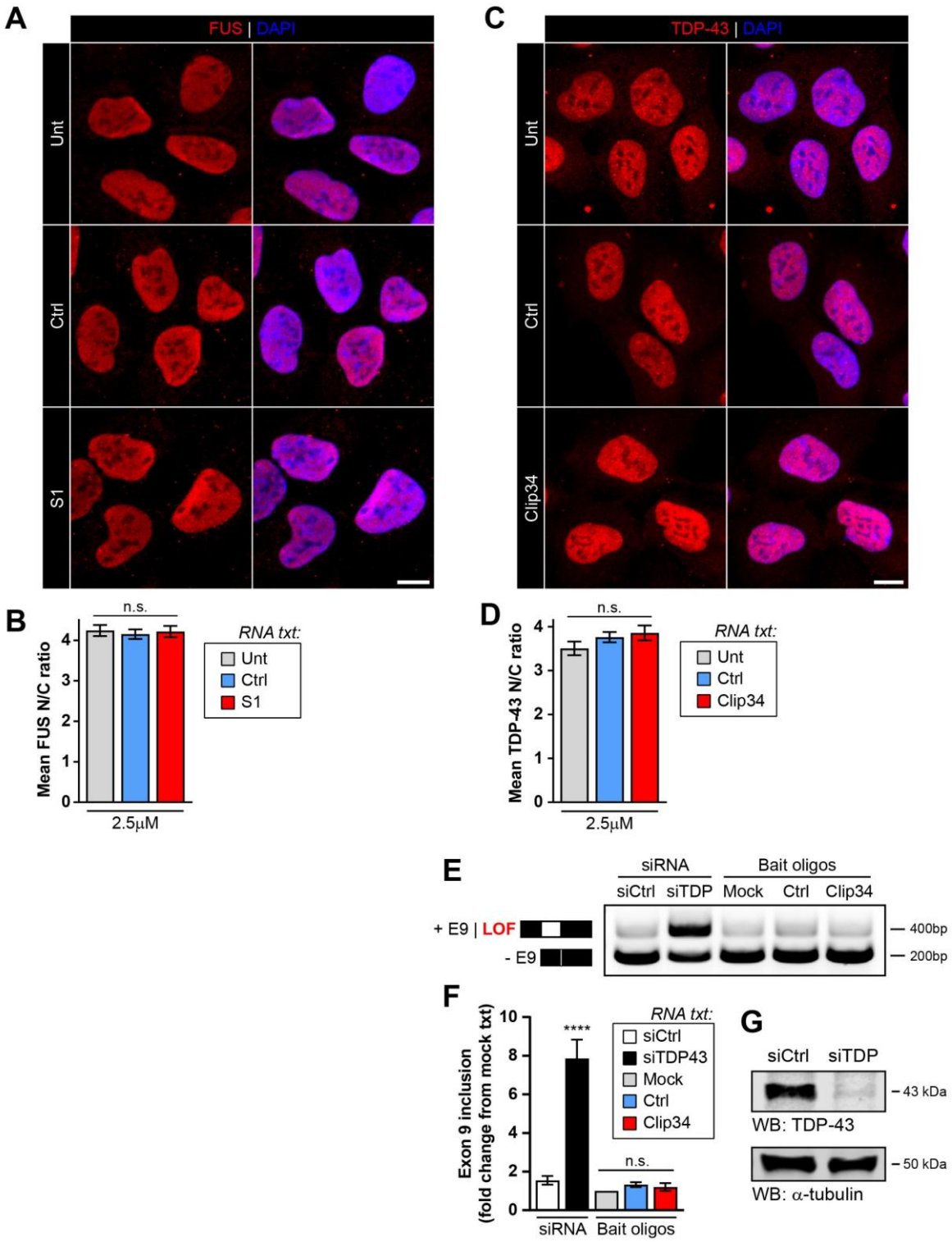

Figure 33. RNA oligonucleotides do not effect endogenous FUS or TDP-43 localization and splicing function.

(A-B) HEK293 cells were treated with 2.5μM of the indicated oligonucleotides for 24 hours prior to immunofluorescence analysis of endogenous FUS localization. Scale bar = 10μm. (B) Mean nuclear/cytoplasmic

ratios of FUS fluorescence intensity in cells treated with the indicated oligonucleotides. *n* = 41-66 cells per group. (C-D) HEK293 cells were treated with 2.5μM of the indicated oligonucleotides for 24 hours prior to immunofluorescence analysis of endogenous TDP-43 localization. Scale bar = 10μm. (D) Mean nuclear/cytoplasmic ratios of TDP-43 fluorescence intensity in cells treated with the indicated oligonucleotides. *n* = 25-39 cells per group. (E) The CFTR minigene assay was used to assess endogenous TDP-43 splicing function in cells treated with the indicated siRNA (25nM) or RNA oligonucleotides (2.5μM) for 72 hours. Top bands indicate loss of TDP-43 splicing function (exon 9 inclusion). TDP-43 knockdown (siTDP43) was used as a positive control in these assays. (F) Western blot analysis of HEK293 cells treated with 25nM of non-targeting (siCtrl) or TDP-43-targeting (siTDP) siRNA to confirm efficient TDP-43 knockdown at the time points of these experiments.

3.4 Discussion

In this study, we identify a variety of short RNAs that modulate FUS phase transitions in different ways. Specifically, we identified two strong inhibitors (RNA S1 and RNA S2) that completely inhibit and reverse FUS phase transition and aggregation. We also identified other strong inhibitors that completely prevent FUS phase separation and fibrillization, but seem to remodel pre-formed large FUS aggregates into smaller hydrogel states when added after initial formation. In addition, we also identified weak RNA inhibitors that inhibit FUS aggregation but not LLPS and droplet formation. We showed that the function of RNA inhibitors in this regard is dependent upon their concentration, sequence, length, and secondary structure. We also determined that the FUS RRM and RGG domains seem to be the major binding sites for strong inhibitors, and that reducing RNA binding efficiency within the RRM impairs RNA's ability to prevent and reverse aberrant FUS assembly. In addition to individual domain binding, cooperativity between FUS domains also appeared to be crucial for proper function of RNAs to

inhibit FUS phase transitions, especially for weak inhibitors. Finally, through the utilization of novel light-inducible models of FUS and TDP-43 proteinopathies, we demonstrated that RNA inhibitors can modulate both FUS and TDP-43 phase transitions and rescue the toxicity induced by aberrant assemblies of these proteins in cellular models of ALS/FTD.

3.4.1 Factors affecting RNA's modulation of FUS LLPS and aggregation

While several of the RNAs identified in the present study were observed to have the ability to prevent FUS phase transitions, only a subset of these RNAs were able to effectively reverse pre-formed FUS aggregates. Interestingly, several of these RNAs instead remodeled these FUS aggregates into solid-like hydrogels. We propose that these RNAs were not able to revert aggregated FUS back to a monomeric state, but they may alternatively disassemble FUS into smaller oligomers, not detectable by turbidity and EM, which proceed to form a gel-like phase phase. In this regard, it is not clear what factors underlie these differing effects of RNA on FUS phase behavior. In the case of another RNA-binding protein Whi3, it was recently shown that low concentrations of two distinct mRNA targets, varying in length but containing the same number of Whi3 binding sites, could differentially promote the formation and tune the biophysical properties of Whi3:RNA coacervates (Zhang et al., 2015a). Interestingly, the same study also showed that higher concentrations of these RNAs conversely inhibited Whi3 phase separation and differed in the molar ratio at which this change was observed (Zhang et al., 2015a). Here we showed that for FUS, diverse RNA sequences can inhibit phase transitions and aggregation of the protein, which is consistent with the fact that FUS is a promiscuous RNA binder and binds to a wide range of RNA partners to function (Wang et al., 2015). However, we found that the factors affecting RNA affinity, such as sequence specificity, are not entirely the same as the factors

affecting RNA's ability to inhibit and reverse FUS aggregation. For example, although the two strongest RNA inhibitors we observed (RNA S1 and RNA S2) both contain the FUS binding motif GGUG, some of the strong RNA inhibitors, such as prD RNA (RNA S3), do not contain any known FUS binding motif. Furthermore, when we generated single point mutations to introduce an additional GUGGU FUS binding motif into a weak inhibitor (RNA S2/2), we paradoxically observed reduced inhibition and disaggregation activity. This result demonstrates that there are likely other effects of the sequences of strong inhibitors that are very specific and simply inserting a FUS binding motif is not sufficient for inhibition function alone. Indeed, a recent NMR study identified ZnF as the major binding site for GGU motif (Loughlin et al., 2019). However, for our strong inhibitors with the GGU motif, ZnF mutations do not affect their binding or activity, indicating the binding motifs are not sole determinants of these RNA's activity.

Secondary structure of RNA targets is another recognition mechanism for FUS binding, and our results demonstrate that the structure of RNA can be important for its regulation of FUS phase transitions. For example, while both polyU50 RNA and RNA S2 are strongly bound by FUS, we only observed complete inhibition of LLPS and aggregation by the more structured RNA S2 that prevented scaffolding and multimerization of FUS on single RNA molecules. The unstructured nature of polyU50 RNA conversely allowed for multiple FUS binding and subsequent LLPS at low RNA:protein molar ratios, highlighting the importance of secondary structure on short RNA regulation of RBP phase separation. However, with high enough RNA:protein ratios, weak RNA inhibitors like polyU50 can also completely inhibit FUS LLPS, which may partially explain the solubility of FUS and other RBPs in the nuclear compartment with an abundance of different RNA species (Maharana et al., 2018). In the case of polyU50, our results suggest this is likely due to the compaction of RNA induced by interacting with a single FUS molecule when

present at excess concentrations. This biphasic effect of RNA on FUS LLPS has also been reported before for total yeast RNA, prD RNA, and the GGUG RNA, where lower concentrations of RNA can promote self-assembly while higher concentrations of RNA instead antagonize FUS phase separation (Burke et al., 2015; Kang et al., 2019; Schwartz et al., 2013). Our smFRET study suggests a model where RNA adopts different structures at different RNA:FUS ratios, thus resulting in differing effects in the regulation of FUS LLPS. Therefore, it would be interesting to determine the optimal structure and concentration of RNA that can inhibit FUS aggregation. One example can be found with the SON RNA, where it has been shown that FUS binds through recognition of its distinct stem-loop structure (Loughlin et al., 2019). However, in our assays the SON RNA did not show inhibition or disaggregation activity, again pointing to a differing molecular language governing FUS:RNA binding and RNA's activity as inhibitor and/or disaggregase.

3.4.2 Mechanisms underlying RNA-mediated antagonization of FUS phase transitions

In order to design specific RNA inhibitors for therapeutic purposes, it is important to determine the mechanism by which RNAs inhibit and reverse FUS aberrant phase transitions. FUS phase transitions and aggregation seem to be in part mediated by the PrLD, as it has been shown that interrupting intermolecular interaction between FUS PrLDs disrupts phase separation (Lin et al., 2017; Monahan et al., 2017; Murakami et al., 2015; Murray et al., 2017; Patel et al., 2015). However, we have found that RNAs do not interact with the PrLD and our NMR studies indicate that RNA inhibitors identified here seem to interact with FUS in the RRM, ZnF, and RGG region, consistent with previous studies (Burd and Dreyfuss, 1994; Ito et al., 2011; Loughlin et al., 2019; Ozdilek et al., 2017; Prasad et al., 1994; Schwartz et al., 2013). Long-range contacts between the

tyrosine-rich PrLD and arginine-rich RGG domains have also been recently proposed to strongly contribute to full-length FUS phase separation, as disruption of these interactions by truncation, mutagenesis or arginine methylation have been shown to disrupt self-assembly of the protein (Hofweber et al., 2018; Qamar et al., 2018; Wang et al., 2018b). Thus, it is possible that RNA may act through competitive inhibition by binding to these regions and limiting accessibility for the inter- and intramolecular interactions between these regions that are important for promoting LLPS.

In general, we found that RNA activity is correlated with its affinity to FUS. In support of this notion, 4FL mutations within the FUS RRM that most significantly decreased FUS binding affinity to strong RNA inhibitors also seemed to completely eliminate their ability to prevent and reverse FUS aggregation. Interrupting RNA binding to RGG regions by C-terminal truncation also seemed to abolish RNA activity in this regard. Consistent with these results, we also observed a strong enhancement of light-induced FUS phase separation resulting from mutation of the RRM in our cellular Corelet-based optogenetic model. Together, these results suggest that the RRM may be the primary engagement site mediating the inhibitory effects of short RNA inhibitors and endogenous RNA buffering of aberrant FUS phase transitions within a cellular environment. However, even with mutations in RRM and RGG, RNA:FUS binding is still relatively strong in the absence of inhibitory activity, suggesting additional factors may contribute to certain RNA's antagonization of FUS phase transitions.

We also found that mutations in the ZnF domain did not reduce RNA binding affinity or activity for strong inhibitors, indicating the interaction between the ZnF domain and RNA is weak and transient. However, disrupting the ZnF fold did seem to disrupt the activity of weak inhibitors, eliminating their ability to inhibit FUS aggregation. A similar pattern emerged when we examined

the phase behavior of ZnF mutants within a cellular environment. While ZnF mutations alone did not produce a significant increase of FUS-SspB phase separation in response to light activation, we did observe a further enhancement of FUS-SspB LIPS when ZnF mutations were added to the RRM mutants. This again provides evidence for the hypothesis that ZnF domain binding cooperativity may be a crucial component of RNA-mediated buffering of FUS phase transitions. For example, while the engagement of the RRM still may remain the primary source of inhibition, additional weak or transient contacts between the ZnF domain and a number of diverse RNA species within the cell may still provide some additional modulation of FUS phase behavior. Additionally, cooperativity provided by the intact ZnF region may allow for enhanced binding of RNAs by the mutated RRM and/or RGG domains, with corresponding enhanced inhibition, that is abolished upon mutation of the ZnF domain.

Combining these mutation analyses with observations from NMR experiments, we propose that strong inhibitors and weak inhibitors engage FUS with different patterns and thus function through distinct mechanisms. For stronger inhibitors, which are also strongly bound by FUS, the binding energy to RRM and RGG is sufficient to break the intra-molecular interactions involved in forming and stabilizing FUS aggregates. For weak inhibitors, binding to RRM and RGGs may not provide enough energy to prevent or break fibril formation, where additional cooperative binding involving the ZnF is then required to disrupt FUS:FUS interactions. This notion is further supported by the finding that the activity of weak inhibitor RNA W1 exhibits increased cooperativity when compared to strong RNA inhibitors. Furthermore, the ZnF domain might provide important cooperativity for weak RNA inhibitors' function via long-range allosteric communication, as it has been shown that RNA can accelerate the folding of a variety of nucleic acid binding proteins up to 30-fold upon binding (Rentzeperis et al., 1999).

3.4.3 Short RNA oligonucleotides as therapeutic agents to mitigate neurotoxicity by regulating RBP phase separation

Our *in vitro* studies determined that unique RNA species have the capacity to inhibit and reverse aberrant FUS phase transitions to varying degrees. Considering these differing effects of RNAs on FUS phase behavior and the diversity of endogenous FUS-binding RNA molecules found within a cell (Lagier-Tourenne et al., 2012; Qiu et al., 2014; Wang et al., 2015), it is quite plausible that RNA, in addition to other factors like nuclear import receptors and post-translational modifications (Monahan et al., 2017; Murray et al., 2017), could serve as an essential factor regulating RNP granule dynamics during normal physiology and in response to changes in the intra- and extracellular environment. For example, in the case of osmotic stress, FUS has been reported by multiple groups to redistribute from the nuclear compartment out to the cytoplasm where it incorporates into stress granules (SGs) along with numerous other RNA-binding proteins (Hock et al., 2018; Sama et al., 2013). However, we and others have shown that RNA binding may be a pre-requisite for FUS, as well as TDP-43, to be incorporated into these membraneless organelles (Daigle et al., 2013; Fang et al., 2019; Shelkovnikova et al., 2013b) (see also Chapter 2). As a result, during pathological conditions in which RNA homeostasis is disturbed, proteins like FUS or TDP-43 could go through aberrant phase transitions into solid gels that induce cytotoxicity by sequestering other RNP components and further disturbing RNP homeostasis (Murakami et al., 2015). This notion could also draw support from a recent study indicating that RNAs often act as buffers within the nucleus to inhibit aberrant LLPS of nuclear RNA-binding proteins (Maharana et al., 2018). In fact, our results are in agreement with a proposed model in which RNA and RBP quality control are inextricably linked during normal cellular physiology, requiring balanced RNA/RBP crosstalk to maintain RBP homeostasis (Ishiguro et al., 2017). Thus,

perturbation in either RNP component could lead to an imbalance between RNAs and RBPs resulting in neurodegeneration. Interestingly, dysregulation of RNA processing and metabolism has long been considered a potential common pathological mechanism across both ALS and FTD, largely due to observations from genetics and various disease models (Butti and Patten, 2018; Mandrioli et al., 2020). It has also been well established that overexpression of RNA-binding proteins like TDP-43 and FUS can produce toxic effects in a number of different *in vitro* and in vivo model systems (Hergesheimer et al., 2019; Prasad et al., 2019; Wegorzewska and Baloh, 2011), again suggesting that disrupting this delicate RNA/RBP balance may serve as a crucial step in ALS/FTD pathogenesis.

Importantly, our results suggest that restoring RNA homeostasis could be a potential therapeutic strategy for ALS/FTD and other RBP proteinopathies. Along these lines, it has been shown that increased expression of TDP-43-binding intronic lariat RNAs can suppress TDP-43 overexpression toxicity by inhibiting its sequestration of essential endogenous RNAs (Armakola et al., 2012). Moreover, while $UGGAA_{exp}$ repeat expansion RNA associated with Spinocerebellar ataxia type 31 (SCA31) co-aggregates with TDP-43 in the disease, the short non-toxic $UGGAA_{22}$ exerts protective effects against TDP-43 toxicity through a proposed mechanism of suppressing TDP-43 aggregation in disease models (Ishiguro et al., 2017). Our group has also recently shown that pre-treatment of neurons with short RNA oligonucleotides comprised of TDP-43 binding sequences can antagonize inclusion formation and rescue associated neurodegeneration driven by aberrant TDP-43 phase transitions in an optogenetic model of TDP-43 proteinopathy (Chapter 2), suggesting that oligonucleotide-based inhibition of aberrant phase transitions could be a viable therapeutic strategy in disease. In the current study, we discovered similar FUS-binding RNA oligonucleotides that could not only prevent, but also promoted the disassembly of pre-formed

optogenetic FUS inclusions in mammalian cells. This RNA-based disassembly further proved able to effectively mitigate the toxicity associated with initial inclusion formation of both FUS and TDP-43 in our optogenetic models. We thus propose the RNA-based oligonucleotides could be capable of mitigating neurodegeneration by eliminating: (1) any toxic gain of function of the misfolded form; and (2) any loss of function due to sequestration in cytoplasmic aggregates. In an ideal scenario, disaggregated FUS and TDP-43 would then be allowed to be transported back to the nucleus by their corresponding nuclear import receptors and perform their normal nuclear function. It would be important to test combinations of nuclear import receptors and these RNAs to determine how they might synergize to modulate the properties of FUS/TDP-43 droplets and corresponding toxicity. Interestingly, the most effective RNA oligonucleotide in reversing optoFUS inclusions in our cellular model is derived from the 3'UTR of *BDNF*. We propose that the 3'UTR region might harbor other RNA sequences that mitigate FUS neurotoxicity. In fact, we searched in a FUS CLIP-seq data set obtained using human brain and mouse neurons differentiated from embryonic stem cells (Lagier-Tourenne et al., 2012) and found that 65% of the total peaks are located on 3'UTR. Interestingly, the RNA oligonucleotide used to disrupt optogenetic TDP-43 inclusions here was also derived from a 3'UTR sequence (from the *TARDBP* gene) (Bhardwaj et al., 2013) and similar datasets have shown an enrichment of 3'UTR targets of TDP-43 in cortical neurons (Sephton et al., 2011).

For further development of oligonucleotides capable of disrupting RBP inclusions in patient cells, RNA analogues with increased cellular stability are desired from a therapeutic perspective. The 2'O-Methyl (2'-OMe) modification is best characterized as an RNA analogue that offers stability against general base hydrolysis and nucleases, as well as increased T_m (Khvorova and Watts, 2017; Majlessi et al., 1998). Another common modification used in current

oligonucleotide-based therapies is the phosphorothioate (PS) bond. The PS modification substitutes a sulfur atom for a non-bridging oxygen in the phosphate backbone of an oligo, which renders the internucleotide linkage resistant to nuclease degradation (Wan et al., 2014). In the present study, we tested different combinations of 2'O-Me and PS modifications in our *in vitro* assays and cellular models. Although RNA oligos with either or both modifications showed similar activity compared to the template in the *in vitro* assays, RNA oligos with the PS modifications lost their activity to prevent and reverse optoFUS inclusion formation in the cellular model. As we have shown that structure is important for inhibitory activity of RNA oligonucleotides, it is possible structural alterations associated with excessive PS modification could alter their interaction with RBP targets in a cellular context (Chen et al., 2015), leading to a reduction in efficiency. It is also plausible that while irrelevant in a purified *in vitro* reaction, PS modifications may increase off-target binding in the crowded cellular milieu, as they have been shown to enhance non-specific protein binding (Brown et al., 1994). In future studies, it will be important to explore other RNA modifications and their effect on RNA's stability and activity.

Here, we established that distinct short RNA species regulate FUS phase transition in different ways. We propose disturbed RNA homeostasis might contribute to RNP dysregulation in ALS/FTD pathogenesis and have demonstrated RNA-based oligonucleotide can be designed to fine tune FUS phase behavior and mitigate FUS toxicity. Therefore, it would be important to test if RNAs that are up- or down- regulated in ALS can modify FUS LLPS. Special focus should be on the 3'UTR region. It would also be important to determine if RNA can also regulate the phase transition of other RNP proteins that aggregated in ALS including TDP-43, hnRNPA1, hnRNPA2, TAF15, EWSR1, and TIA1.

4.0 Conclusions

The work described in this dissertation aimed to further elucidate the intrinsic and extrinsic factors responsible for the initiation and regulation of aberrant aggregation of the ALS/FTD-linked RNA-binding proteins TDP-43 and FUS. Earlier *in vitro* investigations into these and similar RBPs had suggested that the process of liquid-liquid phase separation (LLPS) could represent an initial nucleation event in this process, utilized during normal physiology to allow for self-assembly and partitioning of these proteins into membraneless compartments for a variety of functions (Alberti and Hyman, 2016). These experiments have also highlighted the role of both intrinsically disordered and/or PrLD domains and RNA in promoting initial LLPS of RBPs, which has been proposed to subsequently lead to the formation of solid-state inclusions upon extended incubation (Verdile et al., 2019). Such aberrant liquid-to-solid phase transitions seem to be promoted by enhanced protein concentration, as well as disease-linked mutant proteins, within *in vitro* assemblies and have led to the presumption that excess or untimely phase separation of these proteins in patient cells, such as within chronic or persistent stress granules, ultimately underlie the deposition of insoluble inclusions seen in neurodegenerative disease (Patel et al., 2015). While these *in vitro* studies have revolutionized the field of cell biology and provided invaluable insight into the phase behavior of molecules found all over the cell, it will be imperative moving forward to complement these approaches with unique intracellular models of these events in order to deepen our knowledge of the prevalence and regulation of phase separation in physiology and disease.

Experiments outlined in Chapter 2 represent initial efforts towards this end, where we first describe the development of novel optogenetic methods to selectively induce the phase separation

of TDP-43 under the spatiotemporal control of light stimulation. Using these systems, we highlight the role of the TDP-43 low-complexity PrLD in mediating phase separation in an intracellular environment, demonstrating the importance of aromatic interactions and ALS-linked mutations within this region for driving LLPS and subsequent liquid-to-solid state transitions. This study also describes the first model able to selectively induce the formation of pathologically-relevant TDP-43 inclusions in neuronal cultures and to directly connect aberrant intracellular phase transitions of the protein to cellular toxicity. Furthermore, experiments in this chapter utilize these systems to uncover the importance of intracellular RNA in the buffering of aberrant phase transitions of TDP-43, as well as in promoting recruitment of TDP-43 to stress granules that maintain its solubility during cellular stress. Lastly, this study describes a novel potential therapeutic strategy for targeting aberrant phase transitions of TDP-43, in which short RNA "bait" oligonucleotides were shown to both antagonize optogenetic TDP-43 aggregation and rescue associated neurotoxicity.

In Chapter 3, we move on to demonstrate that this short RNA-mediated inhibition of aberrant phase transitions can also be observed with the related ALS/FTD-linked RNA binding protein FUS and describe the specific properties of RNAs that may be mediating this effect. Interestingly, this study shows that in addition to preventing aberrant phase transitions, certain RNAs are also capable of reversing LLPS and fibrillization of these proteins. Properties such as sequence, length and secondary structure seem particularly important in mediating the prevention and disaggregation activity of these RNAs, and RNAs that engage the FUS RRM regions seem to be particularly potent inhibitors in this regard. We also describe improved optogenetic systems to induce aberrant intracellular FUS and TDP-43 phase transitions in this study and show that these short RNAs are able to reverse pre-formed inclusions in cells and rescue resulting cellular toxicity.

Together, the work included in this dissertation provides evidence that in addition to promoting the phase separation and assembly of various proteins and membraneless organelles, various RNA species, particularly within the cellular environment, can also play an important physiological role in the buffering or prevention of aberrant phase transitions of ALS/FTD-linked RNA binding proteins. These studies additionally suggest that from a therapeutic perspective, we may be able to harness this evolved trait of certain RNAs to design novel RNA-based molecules aimed at the direct disruption of aberrant RBP assemblies to counter neurodegeneration in these diseases. Furthermore, future studies utilizing the novel optogenetic methods developed in these experiments may provide invaluable insight into additional intracellular modifiers of RBP and other protein phase behavior and might similarly uncover new therapeutic approaches to target aberrant protein aggregation observed in other neurodegenerative disorders.

The following discussion will address: (1) the advantages and limitations of these new optogenetic approaches and comparisons with existing/future models, (2) the mechanisms, implications and potential breakdown of RNA-mediated buffering of aggregation-prone RBPs in physiological and pathological states, and (3) the therapeutic potential of RNA-based antagonization of RBP inclusions in the context of existing strategies to treat ALS/FTD and other disorders.

4.1 Novel optogenetic models of intracellular phase transitions

4.1.1 Current models of phase separation in molecular biology

Following initial demonstrations of phase separation at work in biological systems, a majority of studies investigating the phase behavior of various proteins and other biological molecules have relied upon various *in vitro* assays to assess the formation and material properties of biomolecular condensates (Alberti et al., 2019). In general, this *in vitro* reconstitution usually involves the dilution of proteins-of-interest, first purified from bacterial or insect expression systems, at a range of concentrations into physiological buffer solutions of varying ionic strength (Alberti et al., 2018). Often times, these solutions are incubated for certain lengths of time at differing temperatures prior to measurement of turbidity changes or microscopic analysis of droplet assembly in these different conditions (Alberti et al., 2018). This kind of reductionist approach offers many benefits in the assessment of modulators of phase separation. In contrast to the intracellular environment, these simplified systems allow for the direct testing of single components or variables within these reactions, such as protein/salt concentration, molecular crowding reagents, and/or the presence of RNA or other ligands (Alberti et al., 2018). Furthermore, a number of very sophisticated methods have been developed to thoroughly interrogate the material properties of these assemblies that are not possible to execute in cellular systems (Bracha et al., 2019). Overexpression of fluorescently-tagged proteins has also been commonly used to complement these in-depth *in vitro* analyses, allowing for the assessment of the assembly and dynamics of phase separated compartments in the intracellular environment. However, these overexpression approaches do not provide the tight control over these events that may be required to test specific hypotheses related to the phase behavior of proteins in certain conditions. Recently

developed chemically-inducible systems, such as the rapamycin-dependent iPOLYMER dimerization system (Nakamura et al., 2018), have started to move towards inducible assembly of various synthetic condensates, but these systems generally require the use of global pharmacological agents with unavoidable off-target effects for assembly and lack the rapid kinetics, reversibility and spatial control afforded by the emerging optogenetic techniques discussed below.

4.1.2 Advantages of optogenetic phase separation models

As mentioned above, recent efforts in the development of optogenetic-based induction of intracellular phase transitions, such as our work outlined in Chapters 2 and 3, have begun to achieve some levels of control over this process that were previously unattainable in various *in vitro* and intracellular model systems. The first iterations of these models, presented by Shin, et al. in 2017 (Shin et al., 2017) and our group shown here in Chapter 2, utilized the light-responsive oligomerization (PHR) domain from the *Arabidopsis thaliana* Cryptochrome-2 (Cry2) protein to drive phase separation of IDR regions of various proteins or the TDP-43 PrLD and full-length TDP-43 respectively. The light-triggered oligomerization of this domain thus served as a rapidly inducible multivalent interaction domain able to promote homotypic IDR contacts responsible for driving droplet assembly upon light stimulation in these systems. In addition to rapid induction of phase separation, the reversibility and second-order kinetics of the Cry2 oligomerization domain has additionally provided a novel fine-tuning of protein phase behavior achieved through varying light dosage and activation intervals. This light-based tuning has importantly allowed for the direct intracellular testing of hypotheses arising from *in vitro* observations of droplet maturation and liquid-to-solid state transitions. For example, enhancement of the concentrations of the FUS (Shin

et al., 2017) or TDP-43 PrLDs (Chapter 2) within the dense phase of these droplets, due to either enhanced light intensity or chronic/repetitive activation, seemed to result in the arresting of droplet dynamics and formation of more solid-like structures. These liquid-to-solid state transitions seemed to be accelerated by ALS-linked mutations in the TDP-43 PrLD (Chapter 2), in a similar manner to that observed of the mutant FUS PrLD in purified reactions (Patel et al., 2015), suggesting that these *in vitro* observations may be relevant for the intracellular behavior of these proteins as well. These systems have similarly overcome technological limitations in the direct investigations of stress granule maturation, where similar intermittent activation protocols were used to test the effects of chronic and repetitive optogenetic stress granule (optoGranule) formation on cellular toxicity (Zhang et al., 2019a). Second generation models, such as Corelets system (originally described by Bracha, et al. in 2018 and adapted here in Chapter 3), PixELLs, and CasDrop systems, have further improved the temporal control and spatial patterning of these optogenetic phase separation models for various additional biological applications like genomic restructuring and analysis of spatial "memory" in intracellular condensate formation (Bracha et al., 2018; Dine et al., 2018; Shin et al., 2019).

In addition to the tight spatiotemporal control over biomolecular condensation demonstrated by these systems, the ability to perform these assays intracellularly also offers certain advantages over purified protein preparations. For example, while *in vitro* reconstitution of various protein self-assemblies can mimic intracellular conditions, many proteins have been shown to require a deviation from these conditions, for example through dropping salt concentration or temperature, to induce LLPS in these systems (Alberti et al., 2019). Furthermore, in many cases the proteins utilized in these *in vitro* assays are purified from bacterial cells that lack the enzymes responsible for normal post-translational modifications occurring within their native environments

(Alberti et al., 2018), which have been shown to drastically affect the phase behavior of proteins like TDP-43 and FUS (Hofweber and Dormann, 2019). The direct expression of these optogenetic tools in mammalian cells also ensures proper folding and chaperoning of proteins-of-interest, as many of these proteins are very aggregation prone during purification and often require the use of large solubility tags and/or denaturing agents to ensure solubility prior to phase separation assays.

The intracellular use of these tools also offers a unique opportunity to uncover endogenous regulatory mechanisms and functional outcomes of phase separation at work in the native cellular environment. In this sense, investigating the phase behavior of these proteins within relevant subcellular localizations may provide some novel clues regarding the propensity of proteins to undergo various phase transitions in the presence of different physiological interaction partners. Our observations here in Chapters 2 and 3, as well as other studies discussed below, that RNA ligands in a cell can act as an antagonist to aberrant TDP-43/FUS phase transitions illustrate this notion and may serve as an example for the different behavior of some these proteins *in vitro* and in cellular environments. Beyond RNA-based mechanisms, this strategy could also be utilized for other disease-linked proteins like tau or alpha-synuclein, which have both been recently shown to undergo LLPS *in vitro* and in cells (Ray et al., 2019; Wegmann et al., 2018). For example, tau is a microtubule-binding protein in neurons that has been shown to undergo complex coacervation with tubulin dimers *in vitro*, which seemed to promote microtubule assembly and growth in these purified reactions (Hernández-Vega et al., 2017). However, while tau droplet formation seemed to be enhanced by the presence of tubulin in these studies, it is unclear how interactions with microtubules within a cellular environment may affect the propensity for pathological aggregation observed in disease. This notion has also been hinted at in recent *in vitro* investigations of the phase behavior of the synaptic protein alpha-synuclein (Ray et al., 2019). Here, certain

environmental factors and interaction partners, such as metal ions and liposomes, typically associated with aggregation of the protein in disease were shown to promote LLPS and liquid-to-solid state transitions of alpha-synuclein *in vitro* (Ray et al., 2019). Thus, further models utilizing similar optogenetic strategies to control the phase behavior of these, as well as other disease-linked proteins, within the native intracellular environment could serve as a critical complement to interrogate the precise mechanisms controlling phase separation in the cell under normal and pathological conditions.

Along with the ability to uncover novel regulators of protein phase behavior, the spatiotemporal control afforded by these systems also allows for more precise investigations into the downstream effects of aberrant phase transitions in cellular and *in vivo* models. In this respect, the work described in Chapters 2 and 3 has demonstrated the direct testing of aberrant phase transitions of TDP-43 and FUS on cellular toxicity, which had been previously difficult to demarcate from other gain-of-function toxicity resulting from enhanced production of these proteins in various overexpression models (Hergesheimer et al., 2019). Although not included in this dissertation, future studies aimed at determining the downstream mechanisms underlying this assembly-specific toxicity have the potential to identify targetable pathways to antagonize neurodegeneration and slow disease progression in patients exhibiting aberrant phase transitions of these proteins. This optogenetic strategy has also been utilized successfully *in vivo* to determine the contribution of TDP-43 pathology to neurodegeneration, with observations of myofiber denervation and axonal shrinkage in zebrafish spinal motor neurons following light-induced TDP-43 oligomerization (Asakawa et al., 2020). Future *in vivo* models based upon this approach will also offer additional advantages over current overexpression models in the study of intercellular transmission and spreading of aggregate pathology. In this sense, the spatial and temporal control

of these systems should allow for the selective induction of pathology in particular regions of the nervous system and/or specific developmental time points to investigate the patterns and mechanisms of prion-like propagation observed of these aggregated proteins and may uncover novel therapeutic avenues to halt disease progression.

4.1.3 Limitations of optogenetic models and future directions

As is true of any other model in biological applications, these systems of course exhibit their own set of limitations that should be carefully considered in the design and interpretation of data resulting from these experiments. Perhaps the most obvious potential drawback of these strategies can be found in the artificial nature of condensate nucleation, where light-responsive molecules like Cry2 are responsible for the initial interactions driving phase separation of these proteins (Mann et al., 2019; Shin et al., 2017). However, the alterations in phase separation resulting from particular sequence modifications, for example aromatic- or disease-linked mutations (Chapter 2), that have been shown to affect phase behavior of these proteins in other models may suggest similar interaction modes giving rise to assembly of these structures in these Cry2-based systems. Nonetheless, second-generation models, such as the Corelets system, have begun to address this issue through the use of the iLID-SspB heterodimers (Bracha et al., 2018). Rather than inducing artificial initial protein oligomerization, as is observed with Cry2-based systems, here light activation results in the recruitment of proteins-of-interest to spherical core molecules, where resulting intra- and intermolecular interactions between IDR and other regions of these proteins are subsequently responsible for phase separation (Bracha et al., 2018). This strategy thus removes the potential contribution of Cry2 homotypic interactions to the formation and material state of light-induced condensates, presumably relying on more “natural” modes of

phase separation of these proteins. However, it should be recognized that all of these systems driving phase separation through light-responsive domains or modules may be "skipping" certain endogenous events that precede condensation of these proteins, such as post-translational modifications or interactions with specific binding partners, in physiological and pathological states. While this may be limiting in terms of mimicking exact pathological cascades preceding aberrant protein aggregation in disease, selective modulation of upstream pathways or interaction partners may result in alterations in the propensity for these proteins to undergo optogenetic phase transitions, as was the case for RNA in Chapters 2 and 3, and thus may provide a platform to identify novel modulators of this process.

Another potential limitation of these optogenetic modes of phase separation relates to the final conformation or structures of induced inclusions. A number of recent studies that have highlighted the role of distinct "strains" of aggregated proteins like TDP-43 and tau in differential patterns of spreading and toxicity observed across subtypes of these proteinopathies (Gibbons et al., 2019; Karikari et al., 2019; Laferrière et al., 2019). Unfortunately, in-depth structural comparisons of optogenetically-induced inclusions versus those observed in patient tissue have yet to be performed. It thus remains an open questions as to whether inclusions formed in these optogenetic systems, containing a number of artificial elements and fluorescent tags, result in pathologically-relevant aggregate species and, if so, which specific subtype(s) of these proteinopathies might be best recapitulated. However, it is important to note the similarities of inclusions formed through both Cry2- and iLID-based systems to those observed in patient tissue (Chapters 2 and 3), in terms of immunohistochemical and biochemical profiles, which may suggest a comparable cellular response to optogenetic inclusions as those at work in disease. Furthermore, while the conformations of these optogenetic aggregates are currently unknown, these systems do

provide an opportunity in future studies to screen for modulators of the formation of specific inclusion strains that may exhibit unique toxicity and/or spreading profiles, thus opening another potential therapeutic window.

Although current models have shown recruitment of endogenous or non-optogenetically active proteins into light-induced assemblies, another shortcoming of these models is the use of exogenous expression strategies to produce these light-responsive systems in cells. Thus, these current systems are generally limited to testing gain-of-function toxicity associated with inclusion formation, rather than the full disease state observed in postmortem tissue consisting of a combination of nuclear clearance and aberrant cytoplasmic aggregation of these proteins. To address these issues, hopefully future efforts will utilize recent technological advancements in the field of genetic editing to produce knock-in optogenetic models in various cellular and animal models of these proteinopathies. In this sense, the targeted insertion of these light-responsive modules into endogenous loci of various proteins of interest should allow for a full recapitulation of both loss- and gain-of-function mechanisms presumed to underlie TDP-43, FUS, and other proteinopathies. Similarly, expression of these fusion proteins from endogenous promoters would allow for native expression levels and regulation that may prove to be additionally relevant to disease pathogenesis.

Together, these new optogenetic tools have provided a number of new opportunities to investigate these biological phenomena in their native intracellular environment. These technological advancements have not only allowed for the direct intracellular testing of hypotheses gleaned from pioneering *in vitro* studies, but have also brought forth additional methods to interrogate and identify novel modulators of the phase behavior of these proteins that may be relevant to both physiology and disease. While these systems certainly exhibit their own inherent

limitations, recent and future efforts have already begun to address some of these issues and will hopefully work towards the generation of the most relevant, translatable models to recapitulate physiological and pathological phase transitions of these proteins in order to facilitate the development of novel therapeutics for neurodegenerative disease.

4.2 RNA as an antagonist of aberrant RBP phase transitions

4.2.1 RNA as an intracellular buffer system to prevent aberrant phase transitions of disease-linked RBPs

When considering the abundance of RNA-binding proteins that have been shown to undergo phase separation and incorporation into various MLOs around the cell, it is not surprising that many previous studies have investigated the role of RNA in modulating this process (Langdon and Gladfelter, 2018). Most observations from these studies have pointed to a general promotion of RBP phase separation by the presence of RNA ligands, presumably acting as additional multivalent scaffolds to enhance protein self-assembly and MLO formation (Langdon and Gladfelter, 2018). However, many of these experiments have utilized low RNA:protein molar ratios that may not represent physiological concentrations of these molecules, particularly in the native subcellular compartments where these proteins normally reside (Burke et al., 2015; Lin et al., 2015; Maharana et al., 2018). In fact, a few of these early investigations, as well as more recent reports, have shown that reversing this molar ratio to higher RNA concentrations seems to actually prevent phase separation of proteins like FUS and TDP-43 (Maharana et al., 2018; Mann et al., 2019) (see also Chapter 2). Thus, our work outlined in this dissertation and other recent

investigations have focused on directly investigating the effects of RNA on the propensity for these proteins to undergo aberrant phase transitions in a more physiological, intracellular environment (Maharana et al., 2018). Through the use of optogenetic tools described above and various deletion/mutagenesis studies, we and others have since proposed that the phase behavior of TDP-43, FUS and other PrLD-containing RBPs within a cell is strongly dependent upon their interaction with intracellular RNA (Maharana et al., 2018). Specifically, these experiments have shown that a loss of RNA interactions, through mutations or intracellular RNase injection, seems to promote phase separation and subsequent aggregation of these proteins into pathologically-relevant inclusions (Maharana et al., 2018). We have also shown here that intracellular addition of specific RNA substrates of these proteins can conversely prevent aggregation and, in some cases, actually reverse pre-formed inclusions in our optogenetic systems (Chapters 2 and 3). Further support for the role of RNA binding in antagonizing TDP-43 aggregation can be found in the recent discovery of novel ALS/FTD-linked mutations adjacent to the RRM regions of the protein (D169G/K181E/K263E) (Chen et al., 2019). Interestingly, two of these mutations (K181E/K263E) were shown to disrupt RNA binding and promote the intranuclear aggregation of TDP-43, while the D169G mutation neither affected RNA binding or intracellular aggregation of the protein (Chen et al., 2019).

Recent proteomic analysis of cell and tissue lysates subjected to RNase treatment has additionally demonstrated that this phenomenon may not be restricted to a small subset of disease-linked RBPs, as over 1300 individual proteins were shown to lose their solubility following cellular RNA degradation (Aarum et al., 2019). In addition to expected RBPs like TDP-43 and FUS, other disease-associated proteins not typically associated with RNA binding, such as Tau and Huntingtin, also became aggregated upon RNase digestion, which may suggest RNA dysregulation

as a common mechanism at work across these neurodegenerative disorders. Another key observation of this study was the over-representation of proteins associated with the Gene Ontology (GO) terms of “RNA binding” and “translation initiation” that became aggregated upon RNase treatment, which mirrors the major protein composition of stress granules as determined by similar proteomic analysis (Aarum et al., 2019; Markmiller et al., 2018). These results are especially interesting in light of recent work, including our observations in Chapter 2, that has begun to suggest a protective role for stress granules in the maintenance of TDP-43 and FUS solubility during periods of cellular stress (Gasset-Rosa et al., 2019; Hans et al., 2020; McGurk et al., 2018; Shelkovnikova et al., 2013b). Here, acute sequestration of proteins like TDP-43, FUS and others within these RNA-rich structures may actually prevent their aggregation during environmental conditions that could trigger protein misfolding or damage in a similar manner to that proposed for the yeast prion protein Sup35 during pH stress (Franzmann et al., 2018). In support of this notion, it has recently been demonstrated that osmotic stress conditions that are typically used to initiate stress granule assembly can directly trigger TDP-43 insolubility and ubiquitination independently of these structures, through use of pharmacological inhibitors of stress granule formation (Hans et al., 2020).

Thus, together these results suggest that intracellular RNA may exist as an endogenous buffering system evolved to maintain the solubility of proteins like TDP-43 and FUS under physiological conditions (Figure 33). In this sense, RNA could act in concert with other molecular chaperones that have been previously linked to the prevention of aberrant RBP aggregation, such as various heat-shock proteins (HSPs) and nuclear import receptors (Carlomagno et al., 2014; Chen et al., 2016; Guo et al., 2018). Interestingly, predictions of interactors for a number of HSPs in yeast have shown an enrichment for RNA binding proteins (Klus et al., 2015), and certain

mammalian HSPs like DNAJB2, HSP70, and HSP90 have been proposed to inhibit TDP-43 aggregation in different contexts (Carlomagno et al., 2014; Chen et al., 2016). While the mammalian disaggregase machinery is less understood, engineered versions of the yeast Hsp104 have been shown to disaggregate pre-formed TDP-43 and FUS fibrils in a similar manner to that previously shown by these proteins' cognate nuclear import receptors and short RNA oligonucleotides presented here in Chapter 3 (Guo et al., 2018; Tariq et al., 2019). Given the cytoplasmic roles of TDP-43 and FUS in the processes of mRNA transport and translational regulation (Birsa et al., 2020), which in involve dynamic RNA binding and release, it would not be surprising if other buffering systems have evolved to prevent aberrant aggregation of these proteins outside the RNA-rich nucleus. Direct evidence for this notion is admittedly lacking, but it is interesting to note that the nuclear import receptors for TDP-43 have been found in the post-synaptic density of rat hippocampal neurons (Thompson et al., 2004), where TDP-43 has also been reported to function along with FMRP in local translation (Chu et al., 2019). Thus, breakdown of any of these systems in pathological states, such as the disrupted interaction between ALS-linked mutant FUS and its nuclear import receptor Kapβ2 (Hofweber et al., 2018), thus may result in the deposition of insoluble inclusions of these proteins observed in disease (Figure 33).

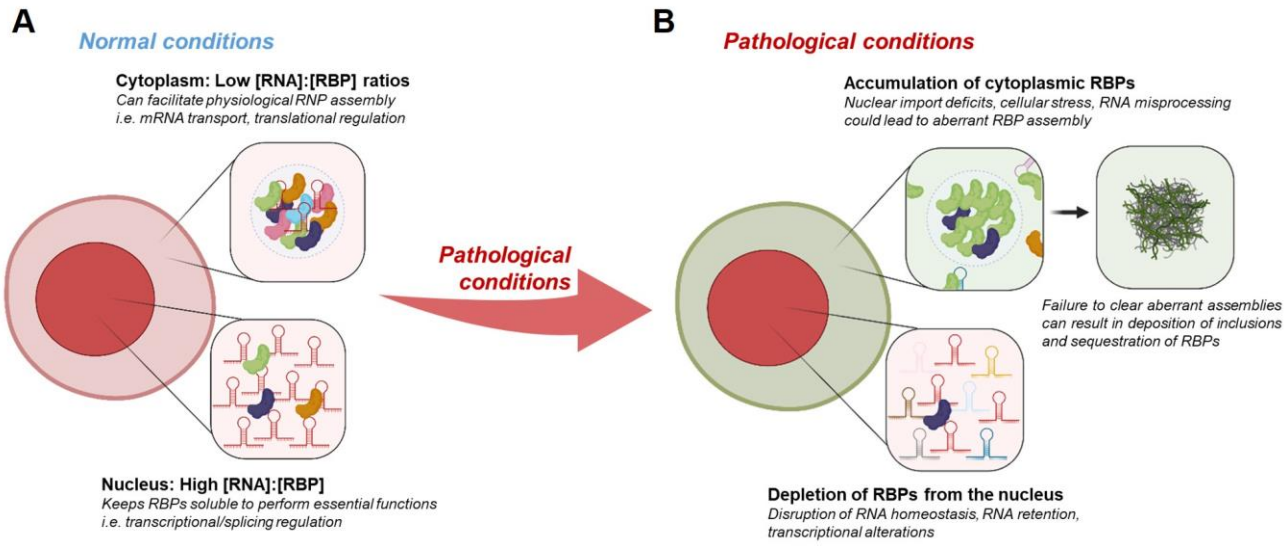

Figure 34. Possible breakdown of RNA buffering system resulting in pathological aggregation of RBPs.

(A) Under normal conditions, high concentrations of RNA within the nucleus may work to keep RBPs soluble to perform essential nuclear functions (i.e. regulation of alternative splicing, transcriptional regulation), whereas low concentrations of particular RNAs in the cytoplasm may facilitate physiological MLO assembly. (B) However, in certain pathological conditions observed in ALS/FTD (i.e. nuclear transport deficits, RNA misprocessing), the disruption of proper RBP:RNA interactions and/or molar ratios could lead to aberrant RBP assembly in the cytoplasm. Failure to clear these aberrant assemblies due to age- or mutation-related disruption of proteostasis may thus result in the deposition of pathological inclusions observed in disease and may further deplete RBPs from the nucleus.

4.2.2 Possible mechanisms of RNA-mediated antagonization of aberrant phase transitions

These recent intracellular and *in vitro* findings have shed new light on the complex regulatory role of RNA on the phase behavior of various RBPs. However, considering the variety of RNA species present within the intracellular environment and total RNA preparations used for many of these *in vitro* assays, it has been difficult to determine the specific RNA species that are particularly efficient inhibitors of aberrant phase transitions, as well as the mechanisms by which they may be exerting their effects. In a similar manner to RNAs promoting phase separation and

MLO incorporation, our work presented in this dissertation, as well as other recent investigations, have begun to highlight the importance of particular molecular characteristics like length and secondary structure in determining the inhibitory activities of these RNAs. These properties in turn have started to uncover potential mechanisms underlying the antagonization of RBP aggregation, which hopefully will prove beneficial in future efforts to develop RNA-based therapeutics targeting aberrant protein inclusions in disease.

Perhaps the most documented property of RNAs that seem able to prevent phase transitions of cognate RBPs has been overall RNA length. While direct comparisons between RNAs of differing length but similar valence and affinity are lacking, recent investigations of the buffering capacity of different types of RNAs (tRNA, NEAT1 lncRNA and rRNA) has shown an interesting, near-linear relationship between RNA length and antagonization of FUS phase separation (Maharana et al., 2018). Specifically, it was shown that the shorter RNA species (tRNA) were the most efficient solubilizers of FUS droplets, with the longer NEAT1 and rRNAs requiring much higher concentrations in solution for effective inhibition of FUS LLPS (Maharana et al., 2018). These short tRNA species were interestingly also shown to outcompete other, presumably longer RNAs to bind and prevent FUS assembly within stress granules (Maharana et al., 2018). Recent smFRET studies of FUS multimerization with polyU RNA of different lengths has echoed this notion, with longer polyU species allowing for FUS multimerization and dynamic FRET fluctuations potentially representative of condensate formation (Niaki et al., 2020). Conversely, shorter polyU tracts (U10-U30) seemed to only allow binding of single FUS monomers and did not promote FUS multimerization or dynamic RNA interactions in these assays (Niaki et al., 2020). This kind of 1:1 protein/RNA binding stoichiometry also seems important in the regulation of Pab1 phase behavior by polyA RNA, in which a 19-mer designed to promote monomeric Pab1 binding

was shown to antagonize thermally-induced phase transitions of Pab1 in a dose-dependent manner (Riback et al., 2017). In addition to our work presented here in Chapters 2 and 3, similar studies have also shown that TDP-43 self-assembly can be antagonized by short, specific RNA oligonucleotides (French et al., 2019; Maharana et al., 2018), but interestingly seems to be promoted in certain conditions by long RNAs like *NEAT1* lncRNA and *titin* mRNA that contain multiple binding sites for these proteins on single transcripts (Tollervey et al., 2011; Vogler et al., 2018). Thus, it may be the case that the ability of shorter oligonucleotides to inhibit higher-order assembly of these RBPs may be intrinsically linked to the low-occupancy binding capacity of these molecules, in contrast to longer multivalent RNA molecules that act as scaffolds for RBP multimerization and subsequent phase separation (Figure 35).

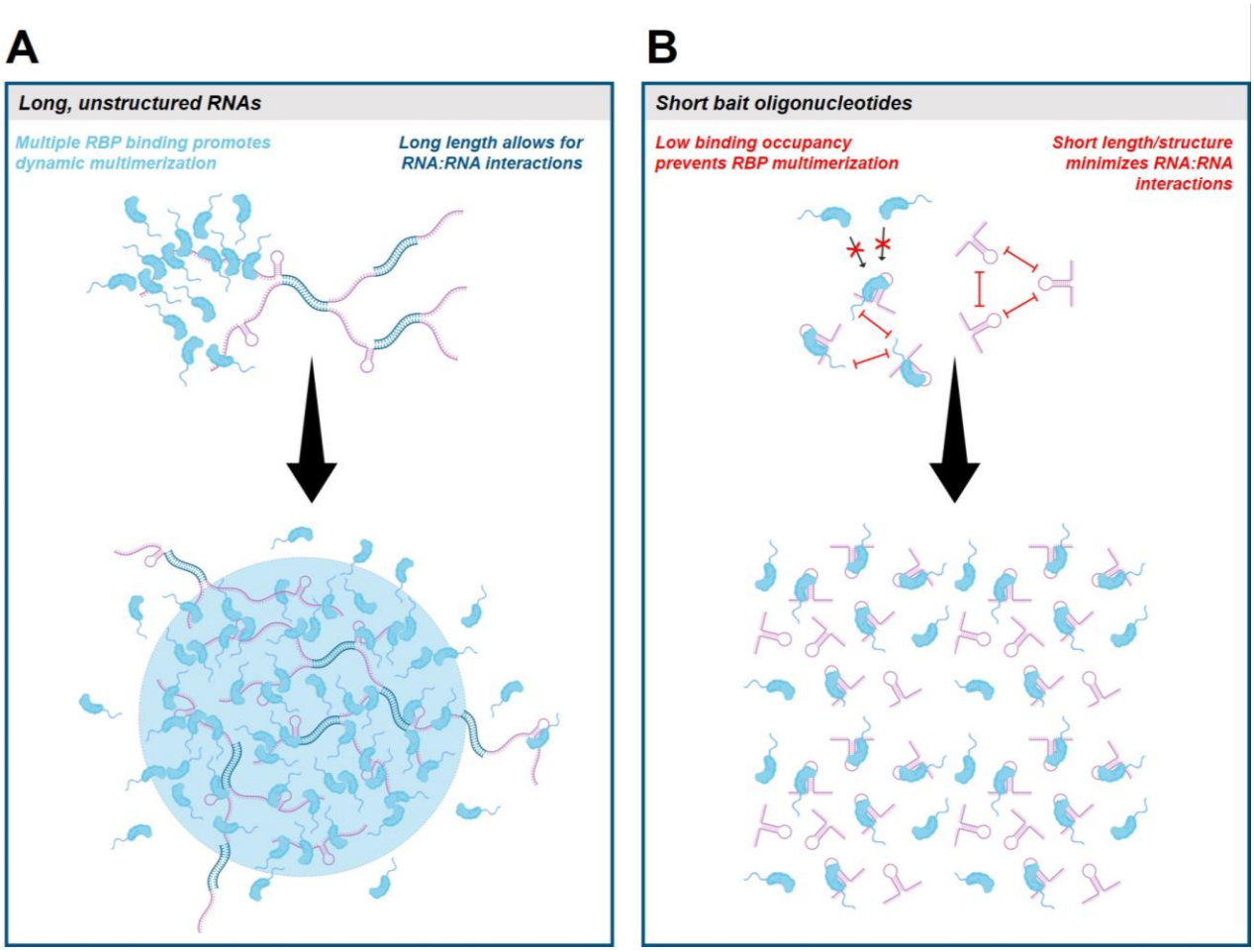

Figure 35. Differential effects of long RNAs and short oligonucleotides on RBP phase behavior.

(A) Longer RNAs may drive RBP phase separation and MLO assembly through a combination of mechanisms, including: 1) enhancement of RBP multimerization on single RNA molecules through the binding to multiple binding sites; and 2) increased potential for RNA:RNA interactions (i.e. complementary base-pairing) that may directly contribute to phase separation and/or aid in the formation of scaffolding networks for additional RBP recruitment to condensates. While some RBPs require structural elements for RNA binding, lower overall structure of these RNAs may increase the likelihood of RNA:RNA interactions and/or provide important flexibility to encourage dynamic RBP:RNA interactions to drive phase separation. (B) Conversely, short oligonucleotides may antagonize phase separation by limiting RBP binding occupany and multimerization that is required for phase separation. Structural elements of these oligonucleotides similarly might encourage single RBP binding and resist RNA remodeling and/or RNA:RNA interactions that contribute to the formation of these assemblies.

Our investigations described in Chapter 3 have also suggested a strong role for RNA secondary structure in this antagonization of protein phase transitions by short RNAs. In a similar manner to the smFRET studies described above, here the unstructured polyU50 RNA allowed for multiple FUS binding and subsequent LLPS, while the defined secondary structure of the S2 RNA inhibitor restricted binding to monomeric FUS and prevented this multimerization and phase separation. The importance of secondary structure has also been noted in the capacity of short synthetic oligonucleotides to solubilize protein aggregation induced by RNA digestion in whole cell lysate, with the most effective molecules containing single-stranded motifs like loops or bulges interspersed by double stranded regions (Aarum et al., 2019). Similar results have also been demonstrated following biotinylated isoxazole (b-isox) treatment in HeLa cell lysate, which has been shown to preferentially precipitate IDR-containing RBPs through currently unclear mechanisms (Han et al., 2012; Kato et al., 2012; Sanchez de Groot et al., 2019). Mass spectrometry analysis of aggregated proteins in this assay showed a preferential antagonization of aggregation following incubation with highly-structured RNAs, while low-structure RNAs seemed to produce results similar to background controls (Sanchez de Groot et al., 2019). These findings may seem relatively confusing when considering the importance of structural elements of certain RNAs shown to conversely promote phase separation and MLO assembly (Clemson et al., 2009; Maharana et al., 2018; Yamazaki et al., 2018), but it is important to consider the additional contribution of RNA length in determining the effects of these RNAs on RBP phase behavior. As the relative abundance of RNA structure has been shown to positively correlate with the number of protein interactions, and increased RNA length in turn seems to correlate with enhanced structure (Sanchez de Groot et al., 2019), it could be the case that these longer, structured RNAs drive multiple interactions with different RBPs to promote multimerization and RNP assembly.

On the other hand, the structural components in short RNAs may result in specific binding of a limited number of molecules to antagonize multimerization, as many RBPs have been shown to recognize RNAs through both sequence and structure-specific mechanisms (Dominguez et al., 2018).

It is also plausible that certain structural elements of these short RNAs may differentially engage various RNA binding regions of RBPs to exert their antagonizing effects through competitive inhibition of interactions important for driving phase separation. For example, while we did not observe binding of RNA inhibitors by the FUS PrLD, we did demonstrate strong contacts within both the FUS RRM and RGG-ZnF regions. This is consistent with a recent bipartite model of FUS RNA recognition, in which both structure-specific interactions by the RRM region and sequence-specific binding by the ZnF domain contribute to RNA binding, with additional RGG contacts providing further RNA interactions (Loughlin et al., 2019). A similar cooperative binding mechanism has been proposed for RRM1 and RRM2 to achieve the sequence-specific binding of TDP-43, but the exact contributions of each domain and role of structural specificity are still unclear (Flores et al., 2019; Furukawa et al., 2016; Zacco et al., 2018). Interestingly, while the RGG domains of FUS have been known to be major drivers of phase separation, via long-term cation-π interactions with the tyrosine-rich PrLD, the RRM regions of both FUS and TDP-43 have also been implicated in playing a role in the self-assembly of these proteins (Lu et al., 2017; Qamar et al., 2018; Wang et al., 2018b; Zacco et al., 2018). Specifically, it has been suggested that these regions may participate in solid-state aggregation of TDP-43 and FUS, as they have all been shown to homo-oligomerize and form amyloid fibrils *in vitro* (Agrawal et al., 2019; Lu et al., 2017; Shodai et al., 2013; Zacco et al., 2018). A similar mechanism has been proposed for Pab1, in which multimerization of the protein, which requires both the P domain and RRM region, seems to

actively compete with polyA RNA binding (Yao et al., 2007). Thus, it may be the case that the binding of RNA may directly compete with interactions involving these regions responsible for driving phase separation, thereby inhibiting liquid- or solid-state phase transitions of these proteins. This mode of antagonization would be quite analogous to that described in the buffering of aberrant FUS phase transitions by its nuclear import receptor, in which stable binding of Kapβ2 to the PY-NLS of FUS allows for weak, distributed contacts in other regions of the protein (PrLD, RRM, ZnF, and RGG domains) that result in the inhibition of these regions to drive phase separation (Guo et al., 2018; Yoshizawa et al., 2018). Hsp27 has also been recently shown to antagonize FUS phase transitions through a similar mechanism, involving weak contacts distributed throughout the FUS PrLD that resulted in a reduction of FUS assembly within stress granules and inhibition of FUS PrLD phase separation *in vitro* (Liu et al., 2020). Interestingly, stress-related phosphorylation or phosphomimetic substitutions in these studies led to co-phase separation of Hsp27 with FUS within stress granules and *in vitro* droplets and seemed to preserve the liquid-like state of these assemblies by discouraging subsequent fibrillization (Liu et al., 2020). This behavior is quite similar to that observed of weak RNA inhibitors in our studies (Chapter 3), which allowed for initial LLPS but antagonized FUS aggregation, and may suggest that some aspects of these buffer systems may have evolved to specifically discourage pathological aggregation of these proteins while not interfering with physiological LLPS.

In addition to competitive inhibition, these RNAs could also potentially exert their inhibitory effects on RBP phase transitions through allosteric modulation. In this sense, binding of RNA could induce or stabilize certain conformations of these proteins that prevent the interactions necessary to drive phase separation. RNA binding-induced conformational changes have been reported for FUS, which interestingly seems to be modulated by RNA properties like sequence

and length in a similar manner to the inhibitory efficiency of different RNAs in our studies (Hamad et al., 2020). Specifically, it was shown that conformational changes associated with binding shorter RNAs was highly sequence-specific, while both specific and non-specific sequences were capable of inducing these changes with longer RNAs (Hamad et al., 2020). Structure was also identified to be critical determinant of binding-induced conformational alterations for shorter oligonucleotides, echoing our arguments for the importance of structure in short RNA-mediated inhibition of FUS phase separation (Chapter 3). These kinds of conformational changes have also been reported for other RBPs like hnRNPA1 (Ding et al., 1999), HuR (Wang et al., 2013), UA1 (Leulliot and Varani, 2001) and PABP (Deo et al., 1999) upon binding of target RNA, suggesting that this may be a common mechanism across various proteins and RNA substrates. While in-depth investigations of possible TDP-43 conformational changes resulting from binding to different RNA species have yet to be reported, it has been suggested that the RRMs of TDP-43 in isolation do not significantly alter their conformation upon binding to short RNA oligonucleotides (Bhardwaj et al., 2013). However, similar investigations of the RRMs along with the N-terminal domain have shown that RNA molecules that promote the solubility of this truncated TDP-43 seem to stabilize the native conformation of the protein upon extended incubation (Zacco et al., 2019). Thus, it is possible that binding to RNA may promote and/or stabilize the functional conformation of TDP-43 required for things like splicing regulation, which has been proposed to involve "head-to-tail" oligomerization of the N-terminal domain (Afroz et al., 2017). Supporting this idea, the orientation of TDP-43 resulting from this mode of oligomerization is thought to antagonize its pathological aggregation by spatially separating the C-terminal PrLDs of adjacent molecules, as disruption of the N-terminal interaction interface disrupts splicing function and promotes inclusion formation (Afroz et al., 2017). However, another contrasting study has proposed a different model

in which N-terminal oligomerization encourages PrLD interactions, showing that alteration of this N-terminal interaction by phosphomimetic substitution interferes with polymerization, splicing function and phase separation of TDP-43 (Wang et al., 2018a). While these opposing models have yet to be resolved, it should be noted that phase separation of TDP-43 has recently been shown to be dispensable for proper splicing regulation (Schmidt et al., 2019). Thus, it is possible that the phosphomimetic mutation described above may disrupt oligomerization/splicing and LLPS of TDP-43 through independent mechanisms. However, the notions presented here are merely speculative, and future in-depth structural analyses will be needed to determine the exact mechanisms mediating the inhibition of TDP-43 and other RBP phase transitions by short RNA oligonucleotides.

4.2.3 The role of RNA binding in TDP-43-dependent neurotoxicity

While these recent observations have strongly suggested a role for intracellular RNA in the prevention of aberrant aggregation of proteins like TDP-43 and FUS, the implications of this concept on cellular toxicity associated with current models of ALS/FTD have proven slightly more complicated. For example, while mutations shown to disrupt the RNA binding efficiency of TDP-43 or FUS have been shown to result in nuclear aggregation of these proteins upon expression in cells (Cohen et al., 2015; Daigle et al., 2013; Flores et al., 2019) (see also Chapter 2), multiple groups have reported a reduction in overexpression toxicity associated with these RNA binding deficient mutants when compared to overexpression of wildtype proteins (Daigle et al., 2013; Elden et al., 2010; Flores et al., 2019; Ihara et al., 2013; Voigt et al., 2010). These results may seem paradoxical when considering the hypothesized relationship between aberrant protein aggregation and cell death in disease. However, these experiments highlight the importance for

careful consideration of the exact mechanisms of toxicity involved in various disease models, particularly in the extrapolation of results to complex pathological processes at work in disease. For example, a majority of TDP-43 overexpression models fail to reproduce key pathological hallmarks of these proteinopathies, such as nuclear depletion or cytoplasmic aggregation of the protein, yet still seem capable of driving cellular toxicity in most systems (Hergesheimer et al., 2019). Thus, it is possible that toxicity achieved in these systems may occur through separate mechanisms as those experienced in disease, such as gain-of-function RNA homeostasis changes associated with overproduction of these proteins. In support of this notion, one of these studies showed widespread RNA expression and splicing changes resulting from wildtype TDP-43 overexpression, which were largely not observed upon expression of RNA binding deficient mutant proteins associated with reduced toxicity (Flores et al., 2019). Another of these investigations reported that mutation of the TDP-43 nuclear localization signal (NLS) reduced toxicity to a similar degree as RNA binding mutations when compared to wildtype TDP-43 overexpression, which might similarly disrupt its ability to over-regulate target RNAs through nuclear depletion of the protein (Voigt et al., 2010). This idea is also supported by previous work that has identified knockdown of the lariat-debranching enzyme Dbr1 as a strong suppressor of TDP-43 overexpression toxicity, which was proposed to result from the accumulation of TDP-43-binding intronic lariats acting as "decoys" to buffer excess TDP-43 away from binding other essential cellular RNAs (Armakola et al., 2012).

Interestingly, various genetic manipulations of the TDP-43 homologue in *C. elegans*, TDP-1, has provided additional insight into the contrasting results associated with these overexpression models. In a similar manner to the observations mentioned above, overexpression of TDP-43 has proven to produce neurotoxicity and locomotor defects in *C. elegans* that can be reversed by

deletion of either RRM of the protein (Ash et al., 2010). However, CRISPR/Cas9-mediated mutagenesis of the endogenous TDP-1 protein to reduce RNA binding efficiency has recently shown an analogous phenotype, in terms of locomotor deficits, to that observed in TDP-1 knockout *C. elegans* (Flores et al., 2019). This mutation was also associated with a lack of RNA processing alterations induced by overexpression of wildtype TDP-43, further suggesting that the reduced toxicity of RRM mutants in overexpression models may be due to a diminished ability to exert toxic gain-of-function splicing changes (Flores et al., 2019).

This kind of widespread alteration in RNA splicing profiles has also been reported upon depletion of TDP-43, as well as in knock-in ALS-linked mutant models (Arnold et al., 2013; Fratta et al., 2018; Klim et al., 2019; Ling et al., 2015; Melamed et al., 2019), which may indicate that any alteration in TDP-43 expression can have profound effects on general RNA homeostasis. Direct comparison of splicing changes associated with TDP-43 loss- and gain-of-function mutations in mouse models has proposed opposing effects on RNA processing, specifically in the aberrant inclusion of "cryptic" exons in loss-of-function models and exclusion of "skiptic" exons corresponding to gain-of-function mutations (Fratta et al., 2018; Ling et al., 2015). However, while splicing changes associated with TDP-43 loss-of-function have been confirmed in sporadic and genetic forms of ALS-FTD associated with TDP-43 proteinopathy (Ling et al., 2015; Melamed et al., 2019), it is still unclear whether these gain-of-function effects can be detected in human patients harboring these mutations. Recent investigations directly comparing TDP-43-depleted human cell lines or iPSC neurons to cells harboring disease-linked mutations have interestingly shown RNA expression changes in both conditions, with a significant overlap between reduced and mutant TDP-43, suggesting some potential loss-of-function mechanisms resulting from these genetic forms of disease as well (Klim et al., 2019; Melamed et al., 2019). Other studies have

identified additional transcripts whose expression is normally sustained by TDP-43 but are downregulated in sporadic ALS postmortem tissue, specifically in inclusion-bearing motor neurons of these patients, pointing to a similar loss-of-function in the regulation of RNA stability resulting from aberrant aggregation of TDP-43 (Lagier-Tourenne et al., 2012). Supporting this notion, sequestration of endogenous TDP-43 within artificial TDP-43-12XQ/N inclusions seems to produce splicing changes that mimic RNAi-mediated depletion of the protein (De Conti et al., 2015). Thus, while it seems that alterations in RNA homeostasis caused by overexpression or reduction of functional TDP-43 can be toxic in many systems, it will be important moving forward to be mindful of the precise mechanisms at work in patients and focus research efforts on developing models to fully recapitulate human disease.

As mentioned above, our optogenetic efforts may represent initial efforts towards this end. However, while we have shown specific toxicity associated with aberrant phase transitions of TDP-43 and FUS in these systems, the exact mechanisms of toxicity in these models remain unknown. It is possible that splicing changes due to endogenous protein sequestration may play a role, as we have shown both recruitment of endogenous TDP-43/FUS and some preliminary evidence for altered TDP-43 regulation of the *CFTR* minigene following inclusion formation, but future in-depth investigations will be needed to truly determine whether these loss-of-function mechanisms may be exerting toxic effects. Other future efforts devoted to the development of knock-in and other models aimed at teasing apart the relative contribution of gain- and loss-of-function mechanisms resulting from aberrant TDP-43 and FUS inclusion formation will hopefully provide additional clarity into these outstanding questions in the field.

4.3 Final remarks

The study of biomolecular condensation and protein aggregation is a rapidly evolving field. Novel roles for phase separation are being defined all over the cell for a wide array of biological functions and have been accompanied by the emergence of cutting-edge tools to control and interrogate these assemblies. As our understanding of the regulatory mechanisms and molecular grammar governing this process has grown, so too has the recognition that RNA may be a key modulator of phase separation in physiology and disease. The work described in this dissertation represents efforts encompassing both these notions. In this sense, the development and intracellular use of optogenetic models to control phase separation has allowed for the discovery of the role for RNA in countering pathological phase transitions of disease-linked RBPs, in a similar manner to other recently proposed aggregation-buffering systems at work in the cell. Supporting this notion, observations of perturbed pathways in genetic and sporadic ALS/FTD has suggested that many upstream pathological mechanisms may converge on aberrant RBP aggregation, through dysregulation of these endogenous buffering or clearance systems, which may explain the common pathologies observed in these diseases (Ling et al., 2013). This work has also demonstrated that this buffering capacity of RNA could perhaps be harnessed through the use of short "bait" RNA oligonucleotides to directly antagonize aberrant RBP phase transitions and promote cellular survival, which may represent a novel therapeutic opportunity in the treatment of ALS/FTD and other disorders affected by pathological RBP aggregation. Support for the feasibility of this strategy can be found in the emergence of other short oligonucleotide-based therapeutics, most notably antisense oligonucleotides (ASOs), that have been recently developed for the treatment of a variety of neurological disorders (Rinaldi and Wood, 2018). Several of these ASO-mediated therapies have already been FDA-approved, with many more currently undergoing clinical trials,

and the continual evolution of these molecules to improve safety, delivery, and efficacy through this process may provide invaluable insight for the design and development of other oligonucleotide-based therapies for treatment of human disease (Rinaldi and Wood, 2018). While our work presented here may represent initial efforts towards this end, future *in vitro* and *in vivo* studies aimed at the identification of oligonucleotide properties and modifications that may enhance efficacy and specificity of these molecules in the disruption of pathological inclusions will be needed to truly determine the therapeutic potential of this strategy.

Appendix A

CW #	CW13-097	CW13-021	CW16-098
Age at death	62	78	60
Sex	F	M	M
Primary diagnosis	Familial ALS-FTLD (*C9ORF72*)	FTLD-TDP	Sporadic ALS
Sections examined	Hippocampus, Cervical spinal cord	Hippocampus	Cervical spinal cord
pTDP-43 inclusions	+	+	+
mRNA co-localization	-	-	-
G3BP1 co-localization	-	-	-
ATXN-2 co-localization	-	-	-

Appendix Table 1. ALS/FTD patient information and scoring, related to Chapter 2.

Appendix B

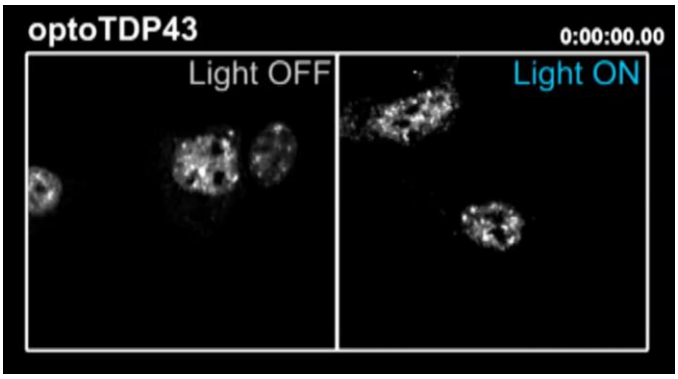

Appendix Video 1. **optoTDP43 Chronic Stimulation Longitudinal Imaging, Related to Figure 3**

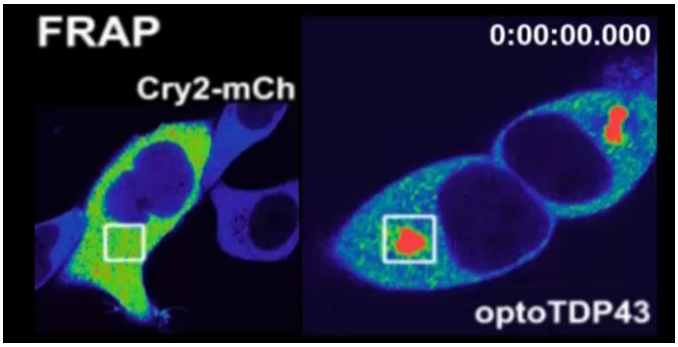

Appendix Video 2. **optoTDP43 Inclusion FRAP Analysis, Related to Figure 3**

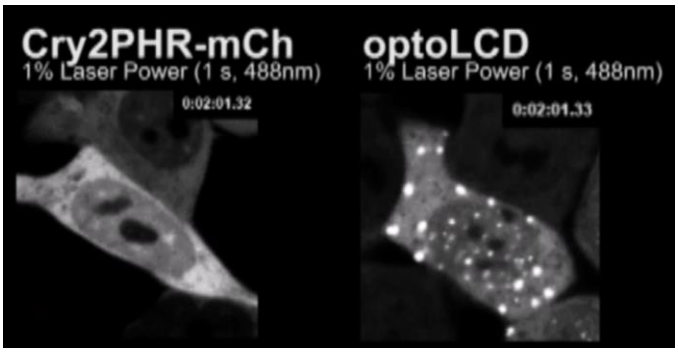

Appendix Video 3. **Cry2PHR versus optoLCD Light-Induced Phase Separation, Related to Figure 6**

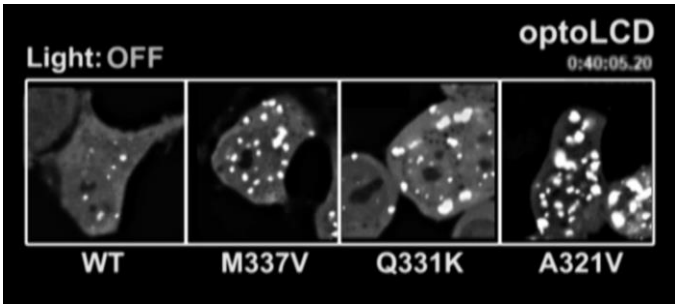

Appendix Video 4. **optoLCD versus optoLCDM377V, optoLCDQ331K, and optoLCDA321V Repetitive Light-Induced Phase Separation, Related to Figure 6**

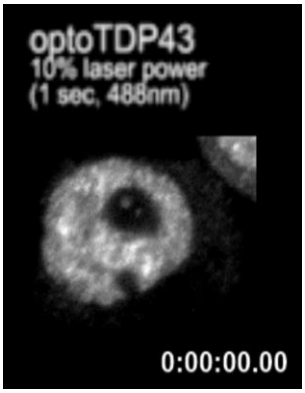

Appendix Video 5. **Lack of optoTDP43 Light-Induced Phase Separation, Related to Figure 7**

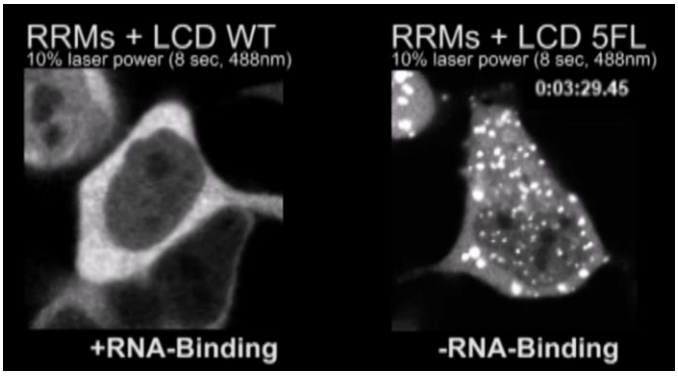

Appendix Video 6. **Cry2olig LCD RRMs and FUS RRM + LCD Light-Induced Phase Separation, Related to Figure 8**

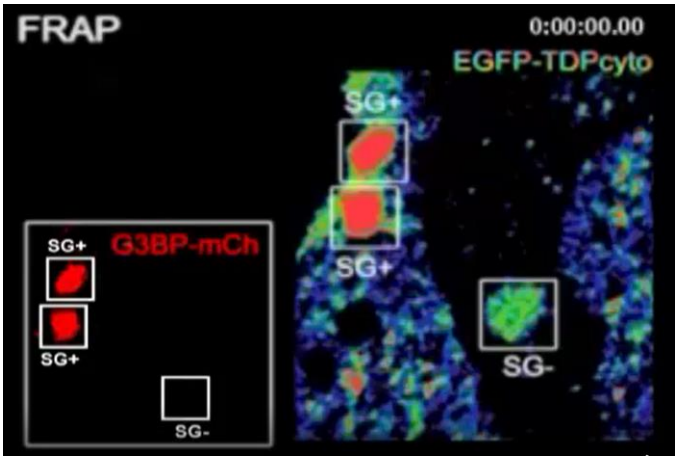

Appendix Video 7. [TDP-43 FRAP Within and Outside of G3BP+ Stress Granules, Related to Figure 13]

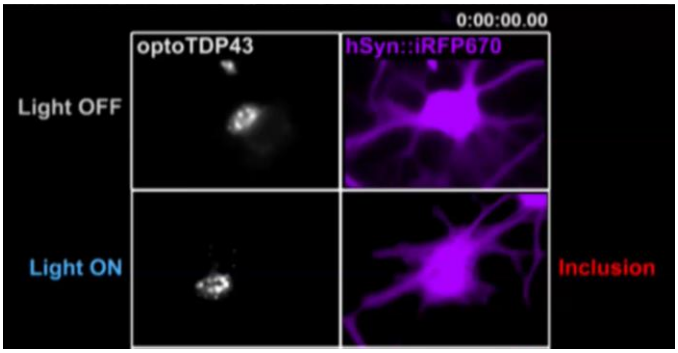

Appendix Video 8. [optoTDP43 Neuronal Survival Imaging, Related to Figure 15]

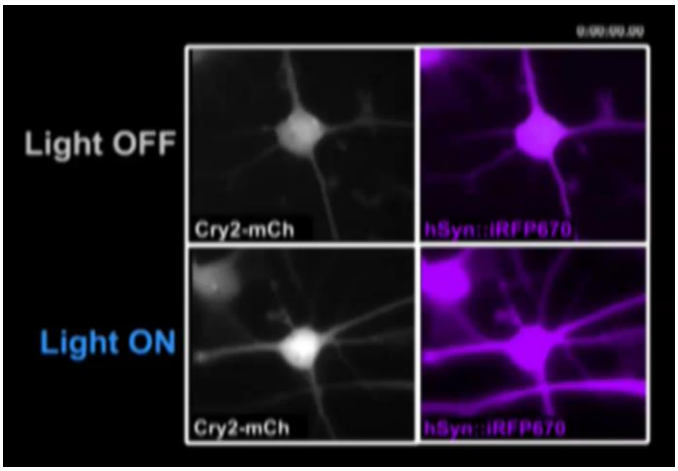

Appendix Video 9. [Cry2-mCh Neuronal Survival Imaging, Related to Figure 15]

Appendix C

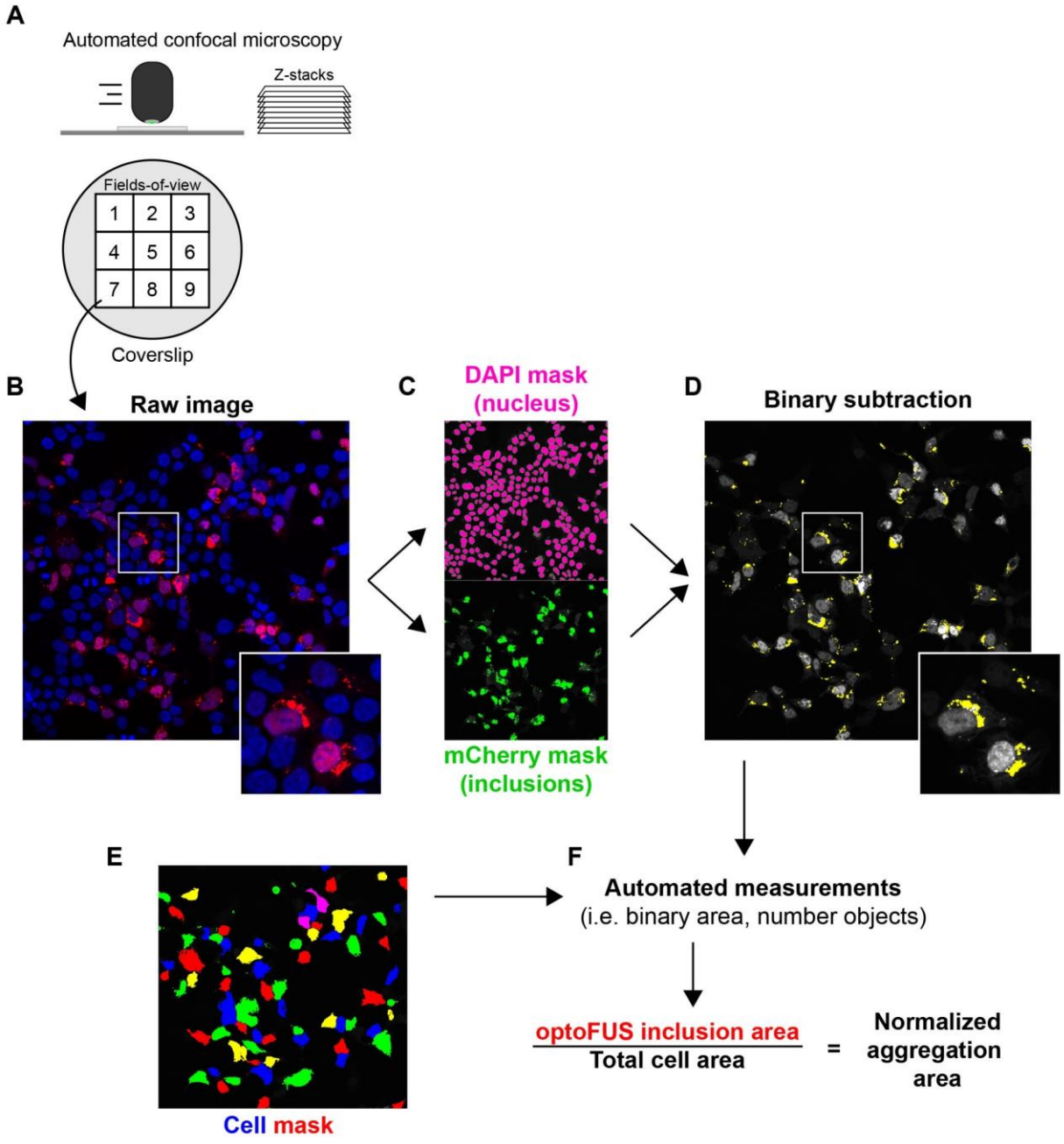

Appendix Figure 1. Workflow of automated optoFUS aggregation analysis, related to Chapter 3.

(A) Automated confocal microscopy was used to acquire z-stacks from at least nine fields-of-view of fixed cells mounted on coverslips. (B) Maximum intensity projections were generated from each field-of-view and (C) binaries

were applied based upon fluorescence intensity to define nuclear area (DAPI) and optoFUS inclusion area (mCherry). (D) Nuclear binaries were then subtracted from mCherry signal to remove confounding strong nuclear optoFUS signal. (E) Whole-cell masks were then used to (F) normalize optoFUS inclusion area to whole-cell area and calculate "normalized aggregation area" for each field-of-view.

Bibliography

Aarum, J., Cabrera, C., Jones, T., Rajendran, S., Adiutori, R., Giovannoni, G., Barnes, M., Malaspina, A., and Sheer, D. (2019). Enzymatic degradation of RNA causes widespread protein aggregation in cell and tissue lysates. BioRxiv.

Abramzon, Y.A., Fratta, P., Traynor, B.J., and Chia, R. (2020). The overlapping genetics of amyotrophic lateral sclerosis and frontotemporal dementia. Front. Neurosci. *14*, 42.

Achi, E.Y., and Rudnicki, S.A. (2012). ALS and Frontotemporal Dysfunction: A Review. Neurol Res Int *2012*, 806306.

Afroz, T., Hock, E.-M., Ernst, P., Foglieni, C., Jambeau, M., Gilhespy, L.A.B., Laferriere, F., Maniecka, Z., Plückthun, A., Mittl, P., et al. (2017). Functional and dynamic polymerization of the ALS-linked protein TDP-43 antagonizes its pathologic aggregation. Nat. Commun. *8*, 45.

Agrawal, S., Kuo, P.-H., Chu, L.-Y., Golzarroshan, B., Jain, M., and Yuan, H.S. (2019). RNA recognition motifs of disease-linked RNA-binding proteins contribute to amyloid formation. Sci. Rep. *9*, 6171.

Al-Husini, N., Tomares, D.T., Bitar, O., Childers, W.S., and Schrader, J.M. (2018). α-Proteobacterial RNA Degradosomes Assemble Liquid-Liquid Phase-Separated RNP Bodies. Mol. Cell *71*, 1027–1039.e14.

Al-Sarraj, S., King, A., Troakes, C., Smith, B., Maekawa, S., Bodi, I., Rogelj, B., Al-Chalabi, A., Hortobágyi, T., and Shaw, C.E. (2011). p62 positive, TDP-43 negative, neuronal cytoplasmic and intranuclear inclusions in the cerebellum and hippocampus define the pathology of C9orf72-linked FTLD and MND/ALS. Acta Neuropathol. *122*, 691–702.

Alami, N.H., Smith, R.B., Carrasco, M.A., Williams, L.A., Winborn, C.S., Han, S.S.W., Kiskinis, E., Winborn, B., Freibaum, B.D., Kanagaraj, A., et al. (2014). Axonal transport of TDP-43 mRNA granules is impaired by ALS-causing mutations. Neuron *81*, 536–543.

Alberti, S., and Hyman, A.A. (2016). Are aberrant phase transitions a driver of cellular aging? Bioessays *38*, 959–968.

Alberti, S., Mateju, D., Mediani, L., and Carra, S. (2017). Granulostasis: protein quality control of RNP granules. Front. Mol. Neurosci. *10*, 84.

Alberti, S., Saha, S., Woodruff, J.B., Franzmann, T.M., Wang, J., and Hyman, A.A. (2018). A User's Guide for Phase Separation Assays with Purified Proteins. J. Mol. Biol. *430*, 4806–4820.

Alberti, S., Gladfelter, A., and Mittag, T. (2019). Considerations and Challenges in Studying Liquid-Liquid Phase Separation and Biomolecular Condensates. Cell *176*, 419–434.

Amador-Ortiz, C., Lin, W.-L., Ahmed, Z., Personett, D., Davies, P., Duara, R., Graff-Radford, N.R., Hutton, M.L., and Dickson, D.W. (2007). TDP-43 immunoreactivity in hippocampal sclerosis and Alzheimer's disease. Ann. Neurol. *61*, 435–445.

Ambadipudi, S., Biernat, J., Riedel, D., Mandelkow, E., and Zweckstetter, M. (2017). Liquid-liquid phase separation of the microtubule-binding repeats of the Alzheimer-related protein Tau. Nat. Commun. *8*, 275.

An, H., Skelt, L., Notaro, A., Highley, J.R., Fox, A.H., La Bella, V., Buchman, V.L., and Shelkovnikova, T.A. (2019). ALS-linked FUS mutations confer loss and gain of function in the nucleus by promoting excessive formation of dysfunctional paraspeckles. Acta Neuropathol. Commun. *7*, 7.

Andersen, P.M., and Al-Chalabi, A. (2011). Clinical genetics of amyotrophic lateral sclerosis: what do we really know? Nat. Rev. Neurol. *7*, 603–615.

Anderson, P., and Kedersha, N. (2008). Stress granules: the Tao of RNA triage. Trends Biochem. Sci. *33*, 141–150.

Armakola, M., Higgins, M.J., Figley, M.D., Barmada, S.J., Scarborough, E.A., Diaz, Z., Fang, X., Shorter, J., Krogan, N.J., Finkbeiner, S., et al. (2012). Inhibition of RNA lariat debranching enzyme suppresses TDP-43 toxicity in ALS disease models. Nat. Genet. *44*, 1302–1309.

Arnold, E.S., Ling, S.-C., Huelga, S.C., Lagier-Tourenne, C., Polymenidou, M., Ditsworth, D., Kordasiewicz, H.B., McAlonis-Downes, M., Platoshyn, O., Parone, P.A., et al. (2013). ALS-linked TDP-43 mutations produce aberrant RNA splicing and adult-onset motor neuron disease without aggregation or loss of nuclear TDP-43. Proc. Natl. Acad. Sci. USA *110*, E736–45.

Arribas-Layton, M., Dennis, J., Bennett, E.J., Damgaard, C.K., and Lykke-Andersen, J. (2016). The C-Terminal RGG Domain of Human Lsm4 Promotes Processing Body Formation Stimulated by Arginine Dimethylation. Mol. Cell. Biol. *36*, 2226–2235.

Asakawa, K., Handa, H., and Kawakami, K. (2020). Optogenetic modulation of TDP-43 oligomerization accelerates ALS-related pathologies in the spinal motor neurons. Nat. Commun. *11*, 1004.

Ash, P.E.A., Zhang, Y.-J., Roberts, C.M., Saldi, T., Hutter, H., Buratti, E., Petrucelli, L., and Link, C.D. (2010). Neurotoxic effects of TDP-43 overexpression in C. elegans. Hum. Mol. Genet. *19*, 3206–3218.

Audas, T.E., Audas, D.E., Jacob, M.D., Ho, J.J.D., Khacho, M., Wang, M., Perera, J.K., Gardiner, C., Bennett, C.A., Head, T., et al. (2016). Adaptation to stressors by systemic protein amyloidogenesis. Dev. Cell *39*, 155–168.

Ayala, Y.M., Pagani, F., and Baralle, F.E. (2006). TDP43 depletion rescues aberrant CFTR exon 9 skipping. FEBS Lett. *580*, 1339–1344.

Ayala, Y.M., De Conti, L., Avendaño-Vázquez, S.E., Dhir, A., Romano, M., D'Ambrogio, A., Tollervey, J., Ule, J., Baralle, M., Buratti, E., et al. (2011). TDP-43 regulates its mRNA levels through a negative feedback loop. EMBO J. *30*, 277–288.

Babinchak, W.M., Haider, R., Dumm, B.K., Sarkar, P., Surewicz, K., Choi, J.-K., and Surewicz, W.K. (2019). The role of liquid-liquid phase separation in aggregation of the TDP-43 low-complexity domain. J. Biol. Chem. *294*, 6306–6317.

Baloh, R.H. (2011). TDP-43: the relationship between protein aggregation and neurodegeneration in amyotrophic lateral sclerosis and frontotemporal lobar degeneration. FEBS J. *278*, 3539–3549.

Banani, S.F., Rice, A.M., Peeples, W.B., Lin, Y., Jain, S., Parker, R., and Rosen, M.K. (2016). Compositional Control of Phase-Separated Cellular Bodies. Cell *166*, 651–663.

Barmada, S.J., Serio, A., Arjun, A., Bilican, B., Daub, A., Ando, D.M., Tsvetkov, A., Pleiss, M., Li, X., Peisach, D., et al. (2014). Autophagy induction enhances TDP43 turnover and survival in neuronal ALS models. Nat. Chem. Biol. *10*, 677–685.

Becker, L.A., Huang, B., Bieri, G., Ma, R., Knowles, D.A., Jafar-Nejad, P., Messing, J., Kim, H.J., Soriano, A., Auburger, G., et al. (2017). Therapeutic reduction of ataxin-2 extends lifespan and reduces pathology in TDP-43 mice. Nature *544*, 367–371.

Bennett, C.L., Dastidar, S.G., Ling, S.-C., Malik, B., Ashe, T., Wadhwa, M., Miller, D.B., Lee, C., Mitchell, M.B., van Es, M.A., et al. (2018). Senataxin mutations elicit motor neuron degeneration phenotypes and yield TDP-43 mislocalization in ALS4 mice and human patients. Acta Neuropathol. *136*, 425–443.

Bentmann, E., Neumann, M., Tahirovic, S., Rodde, R., Dormann, D., and Haass, C. (2012). Requirements for stress granule recruitment of fused in sarcoma (FUS) and TAR DNA-binding protein of 43 kDa (TDP-43). J. Biol. Chem. *287*, 23079–23094.

Berning, B.A., and Walker, A.K. (2019). The Pathobiology of TDP-43 C-Terminal Fragments in ALS and FTLD. Front. Neurosci. *13*, 335.

Berry, J., Weber, S.C., Vaidya, N., Haataja, M., and Brangwynne, C.P. (2015). RNA transcription modulates phase transition-driven nuclear body assembly. Proc. Natl. Acad. Sci. USA *112*, E5237–45.

Bhardwaj, A., Myers, M.P., Buratti, E., and Baralle, F.E. (2013). Characterizing TDP-43 interaction with its RNA targets. Nucleic Acids Res. *41*, 5062–5074.

Biamonti, G., and Vourc'h, C. (2010). Nuclear stress bodies. Cold Spring Harb. Perspect. Biol. *2*, a000695.

Birsa, N., Bentham, M.P., and Fratta, P. (2020). Cytoplasmic functions of TDP-43 and FUS and their role in ALS. Semin. Cell Dev. Biol. *99*, 193–201.

Blanc, R.S., and Richard, S. (2017). Arginine methylation: the coming of age. Mol. Cell *65*, 8–24.

Boeynaems, S., and Gitler, A.D. (2018). Pour Some Sugar on TDP(-43). Mol. Cell *71*, 649–651.

Boeynaems, S., Bogaert, E., Van Damme, P., and Van Den Bosch, L. (2016). Inside out: the role of nucleocytoplasmic transport in ALS and FTLD. Acta Neuropathol. *132*, 159–173.

Boeynaems, S., Alberti, S., Fawzi, N.L., Mittag, T., Polymenidou, M., Rousseau, F., Schymkowitz, J., Shorter, J., Wolozin, B., Van Den Bosch, L., et al. (2018). Protein phase separation: A new phase in cell biology. Trends Cell Biol. *28*, 420–435.

Bounedjah, O., Hamon, L., Savarin, P., Desforges, B., Curmi, P.A., and Pastré, D. (2012). Macromolecular crowding regulates assembly of mRNA stress granules after osmotic stress: new role for compatible osmolytes. J. Biol. Chem. *287*, 2446–2458.

Bounedjah, O., Desforges, B., Wu, T.-D., Pioche-Durieu, C., Marco, S., Hamon, L., Curmi, P.A., Guerquin-Kern, J.-L., Piétrement, O., and Pastré, D. (2014). Free mRNA in excess upon polysome dissociation is a scaffold for protein multimerization to form stress granules. Nucleic Acids Res. *42*, 8678–8691.

Bracha, D., Walls, M.T., Wei, M.-T., Zhu, L., Kurian, M., Avalos, J.L., Toettcher, J.E., and Brangwynne, C.P. (2018). Mapping Local and Global Liquid Phase Behavior in Living Cells Using Photo-Oligomerizable Seeds. Cell *175*, 1467–1480.e13.

Bracha, D., Walls, M.T., and Brangwynne, C.P. (2019). Probing and engineering liquid-phase organelles. Nat. Biotechnol. *37*, 1435–1445.

Brady, O.A., Meng, P., Zheng, Y., Mao, Y., and Hu, F. (2011). Regulation of TDP-43 aggregation by phosphorylation and p62/SQSTM1. J. Neurochem. *116*, 248–259.

Brangwynne, C., Tompa, P., and Pappu, R. (2015). Polymer physics of intracellular phase transitions. Nat. Phys. *11*, 899–904.

Brangwynne, C.P., Eckmann, C.R., Courson, D.S., Rybarska, A., Hoege, C., Gharakhani, J., Jülicher, F., and Hyman, A.A. (2009). Germline P granules are liquid droplets that localize by controlled dissolution/condensation. Science *324*, 1729–1732.

Brangwynne, C.P., Mitchison, T.J., and Hyman, A.A. (2011). Active liquid-like behavior of nucleoli determines their size and shape in Xenopus laevis oocytes. Proc. Natl. Acad. Sci. USA *108*, 4334–4339.

Brown, D.A., Kang, S.H., Gryaznov, S.M., DeDionisio, L., Heidenreich, O., Sullivan, S., Xu, X., and Nerenberg, M.I. (1994). Effect of phosphorothioate modification of oligodeoxynucleotides on specific protein binding. J. Biol. Chem. *269*, 26801–26805.

Buchan, J.R., and Parker, R. (2009). Eukaryotic stress granules: the ins and outs of translation. Mol. Cell *36*, 932–941.

Buratti, E., and Baralle, F.E. (2001). Characterization and functional implications of the RNA binding properties of nuclear factor TDP-43, a novel splicing regulator of CFTR exon 9. J. Biol. Chem. *276*, 36337–36343.

Burd, C.G., and Dreyfuss, G. (1994). Conserved structures and diversity of functions of RNA-binding proteins. Science *265*, 615–621.

Burke, K.A., Janke, A.M., Rhine, C.L., and Fawzi, N.L. (2015). Residue-by-Residue View of In Vitro FUS Granules that Bind the C-Terminal Domain of RNA Polymerase II. Mol. Cell *60*, 231–241.

Butti, Z., and Patten, S.A. (2018). RNA dysregulation in amyotrophic lateral sclerosis. Front. Genet. *9*, 712.

Cacciottolo, R., Ciantar, J., Lanfranco, M., Borg, R.M., Vassallo, N., Bordonné, R., and Cauchi, R.J. (2019). SMN complex member Gemin3 self-interacts and has a functional relationship with ALS-linked proteins TDP-43, FUS and Sod1. Sci. Rep. *9*, 18666.

Capitini, C., Conti, S., Perni, M., Guidi, F., Cascella, R., De Poli, A., Penco, A., Relini, A., Cecchi, C., and Chiti, F. (2014). TDP-43 inclusion bodies formed in bacteria are structurally amorphous, non-amyloid and inherently toxic to neuroblastoma cells. PLoS One *9*, e86720.

Caragounis, A., Price, K.A., Soon, C.P.W., Filiz, G., Masters, C.L., Li, Q.-X., Crouch, P.J., and White, A.R. (2010). Zinc induces depletion and aggregation of endogenous TDP-43. Free Radic. Biol. Med. *48*, 1152–1161.

Carlomagno, Y., Zhang, Y., Davis, M., Lin, W.-L., Cook, C., Dunmore, J., Tay, W., Menkosky, K., Cao, X., Petrucelli, L., et al. (2014). Casein kinase II induced polymerization of soluble TDP-43 into filaments is inhibited by heat shock proteins. PLoS One *9*, e90452.

Celetti, G., Paci, G., Caria, J., VanDelinder, V., Bachand, G., and Lemke, E.A. (2020). The liquid state of FG-nucleoporins mimics permeability barrier properties of nuclear pore complexes. J. Cell Biol. *219*.

Chang, C., Wu, T.-H., Wu, C.-Y., Chiang, M., Toh, E.K.-W., Hsu, Y.-C., Lin, K.-F., Liao, Y., Huang, T., and Huang, J.J.-T. (2012). The N-terminus of TDP-43 promotes its oligomerization and enhances DNA binding affinity. Biochem. Biophys. Res. Commun. *425*, 219–224.

Chen, H.-J., Mitchell, J.C., Novoselov, S., Miller, J., Nishimura, A.L., Scotter, E.L., Vance, C.A., Cheetham, M.E., and Shaw, C.E. (2016). The heat shock response plays an important role in TDP-43 clearance: evidence for dysfunction in amyotrophic lateral sclerosis. Brain *139*, 1417–1432.

Chen, H.-J., Topp, S.D., Hui, H.S., Zacco, E., Katarya, M., McLoughlin, C., King, A., Smith, B.N., Troakes, C., Pastore, A., et al. (2019). RRM adjacent TARDBP mutations disrupt RNA binding and enhance TDP-43 proteinopathy. Brain *142*, 3753–3770.

Chen, L., Wang, X.-L., Shi, T., Wu, T., Deng, Z., and Zhao, Y.-L. (2015). Theoretical study on the relationship between Rp-phosphorothioation and base-step in S-DNA: based on energetic and structural analysis. J. Phys. Chem. B *119*, 474–481.

Choksi, D.K., Roy, B., Chatterjee, S., Yusuff, T., Bakhoum, M.F., Sengupta, U., Ambegaokar, S., Kayed, R., and Jackson, G.R. (2014). TDP-43 Phosphorylation by casein kinase Iε promotes oligomerization and enhances toxicity in vivo. Hum. Mol. Genet. *23*, 1025–1035.

Chu, J.-F., Majumder, P., Chatterjee, B., Huang, S.-L., and Shen, C.-K.J. (2019). TDP-43 Regulates Coupled Dendritic mRNA Transport-Translation Processes in Co-operation with FMRP and Staufen1. Cell Rep. *29*, 3118–3133.e6.

Chujo, T., and Hirose, T. (2017). Nuclear bodies built on architectural long noncoding rnas: unifying principles of their construction and function. Mol. Cells *40*, 889–896.

Cid-Samper, F., Gelabert-Baldrich, M., Lang, B., Lorenzo-Gotor, N., Ponti, R.D., Severijnen, L.-A.W.F.M., Bolognesi, B., Gelpi, E., Hukema, R.K., Botta-Orfila, T., et al. (2018). An Integrative Study of Protein-RNA Condensates Identifies Scaffolding RNAs and Reveals Players in Fragile X-Associated Tremor/Ataxia Syndrome. Cell Rep. *25*, 3422–3434.e7.

Clemson, C.M., Hutchinson, J.N., Sara, S.A., Ensminger, A.W., Fox, A.H., Chess, A., and Lawrence, J.B. (2009). An architectural role for a nuclear noncoding RNA: NEAT1 RNA is essential for the structure of paraspeckles. Mol. Cell *33*, 717–726.

Cohen, T.J., Hwang, A.W., Restrepo, C.R., Yuan, C.-X., Trojanowski, J.Q., and Lee, V.M.Y. (2015). An acetylation switch controls TDP-43 function and aggregation propensity. Nat. Commun. *6*, 5845.

Colombrita, C., Zennaro, E., Fallini, C., Weber, M., Sommacal, A., Buratti, E., Silani, V., and Ratti, A. (2009). TDP-43 is recruited to stress granules in conditions of oxidative insult. J. Neurochem. *111*, 1051–1061.

Conicella, A.E., Zerze, G.H., Mittal, J., and Fawzi, N.L. (2016). ALS Mutations Disrupt Phase Separation Mediated by α-Helical Structure in the TDP-43 Low-Complexity C-Terminal Domain. Structure *24*, 1537–1549.

Conicella, A.E., Dignon, G.L., Zerze, G.H., Schmidt, H.B., D'Ordine, A.M., Kim, Y.C., Rohatgi, R., Ayala, Y.M., Mittal, J., and Fawzi, N.L. (2020). TDP-43 α-helical structure tunes liquid-liquid phase separation and function. Proc. Natl. Acad. Sci. USA.

De Conti, L., Akinyi, M.V., Mendoza-Maldonado, R., Romano, M., Baralle, M., and Buratti, E. (2015). TDP-43 affects splicing profiles and isoform production of genes involved in the apoptotic and mitotic cellular pathways. Nucleic Acids Res. *43*, 8990–9005.

Cortese, A., Plagnol, V., Brady, S., Simone, R., Lashley, T., Acevedo-Arozena, A., de Silva, R., Greensmith, L., Holton, J., Hanna, M.G., et al. (2014). Widespread RNA metabolism impairment in sporadic inclusion body myositis TDP43-proteinopathy. Neurobiol. Aging *35*, 1491–1498.

Couthouis, J., Hart, M.P., Shorter, J., DeJesus-Hernandez, M., Erion, R., Oristano, R., Liu, A.X., Ramos, D., Jethava, N., Hosangadi, D., et al. (2011). A yeast functional screen predicts new candidate ALS disease genes. Proc. Natl. Acad. Sci. USA *108*, 20881–20890.

Couthouis, J., Hart, M.P., Erion, R., King, O.D., Diaz, Z., Nakaya, T., Ibrahim, F., Kim, H.-J., Mojsilovic-Petrovic, J., Panossian, S., et al. (2012). Evaluating the role of the FUS/TLS-related gene EWSR1 in amyotrophic lateral sclerosis. Hum. Mol. Genet. *21*, 2899–2911.

Da Cruz, S., and Cleveland, D.W. (2011). Understanding the role of TDP-43 and FUS/TLS in ALS and beyond. Curr. Opin. Neurobiol. *21*, 904–919.

Daigle, J.G., Lanson, N.A., Smith, R.B., Casci, I., Maltare, A., Monaghan, J., Nichols, C.D., Kryndushkin, D., Shewmaker, F., and Pandey, U.B. (2013). RNA-binding ability of FUS regulates neurodegeneration, cytoplasmic mislocalization and incorporation into stress granules associated with FUS carrying ALS-linked mutations. Hum. Mol. Genet. *22*, 1193–1205.

Deo, R.C., Bonanno, J.B., Sonenberg, N., and Burley, S.K. (1999). Recognition of polyadenylate RNA by the poly(A)-binding protein. Cell *98*, 835–845.

Dewey, C.M., Cenik, B., Sephton, C.F., Johnson, B.A., Herz, J., and Yu, G. (2012). TDP-43 aggregation in neurodegeneration: are stress granules the key? Brain Res. *1462*, 16–25.

Dine, E., Gil, A.A., Uribe, G., Brangwynne, C.P., and Toettcher, J.E. (2018). Protein Phase Separation Provides Long-Term Memory of Transient Spatial Stimuli. Cell Syst. *6*, 655–663.e5.

Ding, J., Hayashi, M.K., Zhang, Y., Manche, L., Krainer, A.R., and Xu, R.M. (1999). Crystal structure of the two-RRM domain of hnRNP A1 (UP1) complexed with single-stranded telomeric DNA. Genes Dev. *13*, 1102–1115.

Ditlev, J.A., Case, L.B., and Rosen, M.K. (2018). Who's In and Who's Out-Compositional Control of Biomolecular Condensates. J. Mol. Biol. *430*, 4666–4684.

Doi, H., Okamura, K., Bauer, P.O., Furukawa, Y., Shimizu, H., Kurosawa, M., Machida, Y., Miyazaki, H., Mitsui, K., Kuroiwa, Y., et al. (2008). RNA-binding protein TLS is a major nuclear aggregate-interacting protein in huntingtin exon 1 with expanded polyglutamine-expressing cells. J. Biol. Chem. *283*, 6489–6500.

Dominguez, D., Freese, P., Alexis, M.S., Su, A., Hochman, M., Palden, T., Bazile, C., Lambert, N.J., Van Nostrand, E.L., Pratt, G.A., et al. (2018). Sequence, structure, and context preferences of human RNA binding proteins. Mol. Cell *70*, 854–867.e9.

Donato, R., Miljan, E.A., Hines, S.J., Aouabdi, S., Pollock, K., Patel, S., Edwards, F.A., and Sinden, J.D. (2007). Differential development of neuronal physiological responsiveness in two human neural stem cell lines. BMC Neurosci. *8*, 36.

Dormann, D., and Haass, C. (2011). TDP-43 and FUS: a nuclear affair. Trends Neurosci. *34*, 339–348.

Dormann, D., Rodde, R., Edbauer, D., Bentmann, E., Fischer, I., Hruscha, A., Than, M.E., Mackenzie, I.R.A., Capell, A., Schmid, B., et al. (2010). ALS-associated fused in sarcoma (FUS) mutations disrupt Transportin-mediated nuclear import. EMBO J. *29*, 2841–2857.

Drino, A., and Schaefer, M.R. (2018). RNAs, Phase Separation, and Membrane-Less Organelles: Are Post-Transcriptional Modifications Modulating Organelle Dynamics? Bioessays *40*, e1800085.

Ederle, H., Funk, C., Abou-Ajram, C., Hutten, S., Funk, E.B.E., Kehlenbach, R.H., Bailer, S.M., and Dormann, D. (2018). Nuclear egress of TDP-43 and FUS occurs independently of Exportin-1/CRM1. Sci. Rep. *8*, 7084.

Elbaum-Garfinkle, S., and Brangwynne, C.P. (2015). Liquids, fibers, and gels: the many phases of neurodegeneration. Dev. Cell *35*, 531–532.

Elbaum-Garfinkle, S., Kim, Y., Szczepaniak, K., Chen, C.C.-H., Eckmann, C.R., Myong, S., and Brangwynne, C.P. (2015). The disordered P granule protein LAF-1 drives phase separation into droplets with tunable viscosity and dynamics. Proc. Natl. Acad. Sci. USA *112*, 7189–7194.

Elden, A.C., Kim, H.-J., Hart, M.P., Chen-Plotkin, A.S., Johnson, B.S., Fang, X., Armakola, M., Geser, F., Greene, R., Lu, M.M., et al. (2010). Ataxin-2 intermediate-length polyglutamine expansions are associated with increased risk for ALS. Nature *466*, 1069–1075.

Falahati, H., Pelham-Webb, B., Blythe, S., and Wieschaus, E. (2016). Nucleation by rRNA Dictates the Precision of Nucleolus Assembly. Curr. Biol. *26*, 277–285.

Fang, M.Y., Markmiller, S., Vu, A.Q., Javaherian, A., Dowdle, W.E., Jolivet, P., Bushway, P.J., Castello, N.A., Baral, A., Chan, M.Y., et al. (2019). Small-Molecule Modulation of TDP-43 Recruitment to Stress Granules Prevents Persistent TDP-43 Accumulation in ALS/FTD. Neuron *103*, 802–819.e11.

Fang, Y.-S., Tsai, K.-J., Chang, Y.-J., Kao, P., Woods, R., Kuo, P.-H., Wu, C.-C., Liao, J.-Y., Chou, S.-C., Lin, V., et al. (2014). Full-length TDP-43 forms toxic amyloid oligomers that are present in frontotemporal lobar dementia-TDP patients. Nat. Commun. *5*, 4824.

Fay, M.M., and Anderson, P.J. (2018). The role of RNA in biological phase separations. J. Mol. Biol. *430*, 4685–4701.

Fay, M.M., Anderson, P.J., and Ivanov, P. (2017). ALS/FTD-Associated C9ORF72 Repeat RNA Promotes Phase Transitions In Vitro and in Cells. Cell Rep. *21*, 3573–3584.

Feric, M., Vaidya, N., Harmon, T.S., Mitrea, D.M., Zhu, L., Richardson, T.M., Kriwacki, R.W., Pappu, R.V., and Brangwynne, C.P. (2016). Coexisting liquid phases underlie nucleolar subcompartments. Cell *165*, 1686–1697.

Fernandes, N., Eshleman, N., and Buchan, J.R. (2018). Stress granules and ALS: A case of causation or correlation? Adv. Neurobiol. *20*, 173–212.

Ferrari, R., Kapogiannis, D., Huey, E.D., and Momeni, P. (2011). FTD and ALS: a tale of two diseases. Curr Alzheimer Res *8*, 273–294.

Flores, B.N., Li, X., Malik, A.M., Martinez, J., Beg, A.A., and Barmada, S.J. (2019). An Intramolecular Salt Bridge Linking TDP43 RNA Binding, Protein Stability, and TDP43-Dependent Neurodegeneration. Cell Rep. *27*, 1133–1150.e8.

Fox, A.H., Nakagawa, S., Hirose, T., and Bond, C.S. (2018). Paraspeckles: where long noncoding RNA meets phase separation. Trends Biochem. Sci. *43*, 124–135.

Franzmann, T.M., and Alberti, S. (2019). Prion-like low-complexity sequences: Key regulators of protein solubility and phase behavior. J. Biol. Chem. *294*, 7128–7136.

Franzmann, T.M., Jahnel, M., Pozniakovsky, A., Mahamid, J., Holehouse, A.S., Nüske, E., Richter, D., Baumeister, W., Grill, S.W., Pappu, R.V., et al. (2018). Phase separation of a yeast prion protein promotes cellular fitness. Science *359*.

Fratta, P., Sivakumar, P., Humphrey, J., Lo, K., Ricketts, T., Oliveira, H., Brito-Armas, J.M., Kalmar, B., Ule, A., Yu, Y., et al. (2018). Mice with endogenous TDP-43 mutations exhibit gain of splicing function and characteristics of amyotrophic lateral sclerosis. EMBO J. *37*.

Freibaum, B.D., Lu, Y., Lopez-Gonzalez, R., Kim, N.C., Almeida, S., Lee, K.-H., Badders, N., Valentine, M., Miller, B.L., Wong, P.C., et al. (2015). GGGGCC repeat expansion in C9orf72 compromises nucleocytoplasmic transport. Nature *525*, 129–133.

French, R.L., Grese, Z.R., Aligireddy, H., Dhavale, D.D., Reeb, A.N., Kedia, N., Kotzbauer, P.T., Bieschke, J., and Ayala, Y.M. (2019). Detection of TAR DNA-binding protein 43 (TDP-43) oligomers as initial intermediate species during aggregate formation. J. Biol. Chem. *294*, 6696–6709.

Furukawa, Y., Suzuki, Y., Fukuoka, M., Nagasawa, K., Nakagome, K., Shimizu, H., Mukaiyama, A., and Akiyama, S. (2016). A molecular mechanism realizing sequence-specific recognition of nucleic acids by TDP-43. Sci. Rep. *6*, 20576.

Garnier, C., Devred, F., Byrne, D., Puppo, R., Roman, A.Y., Malesinski, S., Golovin, A.V., Lebrun, R., Ninkina, N.N., and Tsvetkov, P.O. (2017). Zinc binding to RNA recognition motif of TDP-43 induces the formation of amyloid-like aggregates. Sci. Rep. *7*, 6812.

Gasset-Rosa, F., Lu, S., Yu, H., Chen, C., Melamed, Z., Guo, L., Shorter, J., Da Cruz, S., and Cleveland, D.W. (2019). Cytoplasmic TDP-43 De-mixing Independent of Stress Granules

Drives Inhibition of Nuclear Import, Loss of Nuclear TDP-43, and Cell Death. Neuron *102*, 339–357.e7.

Gibbons, G.S., Lee, V.M.Y., and Trojanowski, J.Q. (2019). Mechanisms of Cell-to-Cell Transmission of Pathological Tau: A Review. JAMA Neurol. *76*, 101–108.

De Giorgio, F., Maduro, C., Fisher, E.M.C., and Acevedo-Arozena, A. (2019). Transgenic and physiological mouse models give insights into different aspects of amyotrophic lateral sclerosis. Dis. Model. Mech. *12*.

Gitler, A.D., and Shorter, J. (2011). RNA-binding proteins with prion-like domains in ALS and FTLD-U. Prion *5*, 179–187.

Gittings, L.M., Foti, S.C., Benson, B.C., Gami-Patel, P., Isaacs, A.M., and Lashley, T. (2019). Heterogeneous nuclear ribonucleoproteins R and Q accumulate in pathological inclusions in FTLD-FUS. Acta Neuropathol. Commun. *7*, 18.

Gomes, E., and Shorter, J. (2019). The molecular language of membraneless organelles. J. Biol. Chem. *294*, 7115–7127.

Gopal, P.P., Nirschl, J.J., Klinman, E., and Holzbaur, E.L.F. (2017). Amyotrophic lateral sclerosis-linked mutations increase the viscosity of liquid-like TDP-43 RNP granules in neurons. Proc. Natl. Acad. Sci. USA *114*, E2466–E2475.

Götz, J., Halliday, G., and Nisbet, R.M. (2019). Molecular pathogenesis of the tauopathies. Annu. Rev. Pathol. *14*, 239–261.

Grabow, W.W., and Jaeger, L. (2014). RNA self-assembly and RNA nanotechnology. Acc. Chem. Res. *47*, 1871–1880.

Greaves, C.V., and Rohrer, J.D. (2019). An update on genetic frontotemporal dementia. J. Neurol. *266*, 2075–2086.

Guenther, E.L., Cao, Q., Trinh, H., Lu, J., Sawaya, M.R., Cascio, D., Boyer, D.R., Rodriguez, J.A., Hughes, M.P., and Eisenberg, D.S. (2018a). Atomic structures of TDP-43 LCD segments and insights into reversible or pathogenic aggregation. Nat. Struct. Mol. Biol. *25*, 463–471.

Guenther, E.L., Ge, P., Trinh, H., Sawaya, M.R., Cascio, D., Boyer, D.R., Gonen, T., Zhou, Z.H., and Eisenberg, D.S. (2018b). Atomic-level evidence for packing and positional amyloid polymorphism by segment from TDP-43 RRM2. Nat. Struct. Mol. Biol. *25*, 311–319.

Guo, L., Kim, H.J., Wang, H., Monaghan, J., Freyermuth, F., Sung, J.C., O'Donovan, K., Fare, C.M., Diaz, Z., Singh, N., et al. (2018). Nuclear-Import Receptors Reverse Aberrant Phase Transitions of RNA-Binding Proteins with Prion-like Domains. Cell *173*, 677–692.e20.

Guo, W., Fumagalli, L., Prior, R., and Van Den Bosch, L. (2017). Current advances and limitations in modeling ALS/FTD in a dish using induced pluripotent stem cells. Front. Neurosci. *11*, 671.

Hamad, N., Mashima, T., Yamaoki, Y., Kondo, K., Yoneda, R., Oyoshi, T., Kurokawa, R., Nagata, T., and Katahira, M. (2020). RNA sequence and length contribute to RNA-induced conformational change of TLS/FUS. Sci. Rep. *10*, 2629.

Han, T.W., Kato, M., Xie, S., Wu, L.C., Mirzaei, H., Pei, J., Chen, M., Xie, Y., Allen, J., Xiao, G., et al. (2012). Cell-free formation of RNA granules: bound RNAs identify features and components of cellular assemblies. Cell *149*, 768–779.

Hans, F., Glasebach, H., and Kahle, P.J. (2020). Multiple distinct pathways lead to hyperubiquitylated insoluble TDP-43 protein independent of its translocation into stress granules. J. Biol. Chem. *295*, 673–689.

Harrison, A.F., and Shorter, J. (2017). RNA-binding proteins with prion-like domains in health and disease. Biochem. J. *474*, 1417–1438.

Hazelett, D.J., Chang, J.-C., Lakeland, D.L., and Morton, D.B. (2012). Comparison of parallel high-throughput RNA sequencing between knockout of TDP-43 and its overexpression reveals primarily nonreciprocal and nonoverlapping gene expression changes in the central nervous system of Drosophila. G3 (Bethesda) *2*, 789–802.

Heinz, S., Benner, C., Spann, N., Bertolino, E., Lin, Y.C., Laslo, P., Cheng, J.X., Murre, C., Singh, H., and Glass, C.K. (2010). Simple combinations of lineage-determining transcription factors prime cis-regulatory elements required for macrophage and B cell identities. Mol. Cell *38*, 576–589.

Hergesheimer, R.C., Chami, A.A., de Assis, D.R., Vourc'h, P., Andres, C.R., Corcia, P., Lanznaster, D., and Blasco, H. (2019). The debated toxic role of aggregated TDP-43 in amyotrophic lateral sclerosis: a resolution in sight? Brain *142*, 1176–1194.

Hernández-Vega, A., Braun, M., Scharrel, L., Jahnel, M., Wegmann, S., Hyman, B.T., Alberti, S., Diez, S., and Hyman, A.A. (2017). Local Nucleation of Microtubule Bundles through Tubulin Concentration into a Condensed Tau Phase. Cell Rep. *20*, 2304–2312.

Hicks, D.A., Cross, L.L., Williamson, R., and Rattray, M. (2019). Endoplasmic Reticulum Stress Signalling Induces Casein Kinase 1-Dependent Formation of Cytosolic TDP-43 Inclusions in Motor Neuron-Like Cells. Neurochem. Res.

Hipp, M.S., Kasturi, P., and Hartl, F.U. (2019). The proteostasis network and its decline in ageing. Nat. Rev. Mol. Cell Biol. *20*, 421–435.

Hirsch-Reinshagen, V., Pottier, C., Nicholson, A.M., Baker, M., Hsiung, G.-Y.R., Krieger, C., Sengdy, P., Boylan, K.B., Dickson, D.W., Mesulam, M., et al. (2017). Clinical and neuropathological features of ALS/FTD with TIA1 mutations. Acta Neuropathol. Commun. *5*, 96.

Hock, E.-M., Maniecka, Z., Hruska-Plochan, M., Reber, S., Laferrière, F., Sahadevan M K, S., Ederle, H., Gittings, L., Pelkmans, L., Dupuis, L., et al. (2018). Hypertonic stress causes

cytoplasmic translocation of neuronal, but not astrocytic, FUS due to impaired transportin function. Cell Rep. *24*, 987–1000.e7.

Hoell, J.I., Larsson, E., Runge, S., Nusbaum, J.D., Duggimpudi, S., Farazi, T.A., Hafner, M., Borkhardt, A., Sander, C., and Tuschl, T. (2011). RNA targets of wild-type and mutant FET family proteins. Nat. Struct. Mol. Biol. *18*, 1428–1431.

Hofweber, M., and Dormann, D. (2019). Friend or foe-Post-translational modifications as regulators of phase separation and RNP granule dynamics. J. Biol. Chem. *294*, 7137–7150.

Hofweber, M., Hutten, S., Bourgeois, B., Spreitzer, E., Niedner-Boblenz, A., Schifferer, M., Ruepp, M.-D., Simons, M., Niessing, D., Madl, T., et al. (2018). Phase separation of FUS is suppressed by its nuclear import receptor and arginine methylation. Cell *173*, 706–719.e13.

Hughes, M.P., Sawaya, M.R., Boyer, D.R., Goldschmidt, L., Rodriguez, J.A., Cascio, D., Chong, L., Gonen, T., and Eisenberg, D.S. (2018). Atomic structures of low-complexity protein segments reveal kinked β sheets that assemble networks. Science *359*, 698–701.

Hülsmann, B.B., Labokha, A.A., and Görlich, D. (2012). The permeability of reconstituted nuclear pores provides direct evidence for the selective phase model. Cell *150*, 738–751.

Hyman, A.A., Weber, C.A., and Jülicher, F. (2014). Liquid-liquid phase separation in biology. Annu. Rev. Cell Dev. Biol. *30*, 39–58.

Ibstedt, S., Sideri, T.C., Grant, C.M., and Tamás, M.J. (2014). Global analysis of protein aggregation in yeast during physiological conditions and arsenite stress. Biol. Open *3*, 913–923.

Ihara, R., Matsukawa, K., Nagata, Y., Kunugi, H., Tsuji, S., Chihara, T., Kuranaga, E., Miura, M., Wakabayashi, T., Hashimoto, T., et al. (2013). RNA binding mediates neurotoxicity in the transgenic Drosophila model of TDP-43 proteinopathy. Hum. Mol. Genet. *22*, 4474–4484.

Ishigaki, S., Masuda, A., Fujioka, Y., Iguchi, Y., Katsuno, M., Shibata, A., Urano, F., Sobue, G., and Ohno, K. (2012). Position-dependent FUS-RNA interactions regulate alternative splicing events and transcriptions. Sci. Rep. *2*, 529.

Ishiguro, T., Sato, N., Ueyama, M., Fujikake, N., Sellier, C., Kanegami, A., Tokuda, E., Zamiri, B., Gall-Duncan, T., Mirceta, M., et al. (2017). Regulatory Role of RNA Chaperone TDP-43 for RNA Misfolding and Repeat-Associated Translation in SCA31. Neuron *94*, 108–124.e7.

Ito, D., Seki, M., Tsunoda, Y., Uchiyama, H., and Suzuki, N. (2011). Nuclear transport impairment of amyotrophic lateral sclerosis-linked mutations in FUS/TLS. Ann. Neurol. *69*, 152–162.

Jain, A., and Vale, R.D. (2017). RNA phase transitions in repeat expansion disorders. Nature *546*, 243–247.

Jambhekar, A., and Derisi, J.L. (2007). Cis-acting determinants of asymmetric, cytoplasmic RNA transport. RNA *13*, 625–642.

Janssens, J., and Van Broeckhoven, C. (2013). Pathological mechanisms underlying TDP-43 driven neurodegeneration in FTLD-ALS spectrum disorders. Hum. Mol. Genet. *22*, R77–87.

Johnson, B.S., McCaffery, J.M., Lindquist, S., and Gitler, A.D. (2008). A yeast TDP-43 proteinopathy model: Exploring the molecular determinants of TDP-43 aggregation and cellular toxicity. Proc. Natl. Acad. Sci. USA *105*, 6439–6444.

Johnson, B.S., Snead, D., Lee, J.J., McCaffery, J.M., Shorter, J., and Gitler, A.D. (2009). TDP-43 is intrinsically aggregation-prone, and amyotrophic lateral sclerosis-linked mutations accelerate aggregation and increase toxicity. J. Biol. Chem. *284*, 20329–20339.

Kaiser, T.E., Intine, R.V., and Dundr, M. (2008). De novo formation of a subnuclear body. Science *322*, 1713–1717.

Kang, J., Lim, L., Lu, Y., and Song, J. (2019). A unified mechanism for LLPS of ALS/FTLD-causing FUS as well as its modulation by ATP and oligonucleic acids. PLoS Biol. *17*, e3000327.

Karikari, T.K., Nagel, D.A., Grainger, A., Clarke-Bland, C., Crowe, J., Hill, E.J., and Moffat, K.G. (2019). Distinct conformations, aggregation and cellular internalization of different tau strains. Front. Cell Neurosci. *13*, 296.

Kato, M., Han, T.W., Xie, S., Shi, K., Du, X., Wu, L.C., Mirzaei, H., Goldsmith, E.J., Longgood, J., Pei, J., et al. (2012). Cell-free formation of RNA granules: low complexity sequence domains form dynamic fibers within hydrogels. Cell *149*, 753–767.

Kaushik, S., and Cuervo, A.M. (2015). Proteostasis and aging. Nat. Med. *21*, 1406–1415.

Kawakami, I., Arai, T., and Hasegawa, M. (2019). The basis of clinicopathological heterogeneity in TDP-43 proteinopathy. Acta Neuropathol. *138*, 751–770.

Khong, A., Matheny, T., Jain, S., Mitchell, S.F., Wheeler, J.R., and Parker, R. (2017). The Stress Granule Transcriptome Reveals Principles of mRNA Accumulation in Stress Granules. Mol. Cell *68*, 808–820.e5.

Khvorova, A., and Watts, J.K. (2017). The chemical evolution of oligonucleotide therapies of clinical utility. Nat. Biotechnol. *35*, 238–248.

Kim, H.J., and Taylor, J.P. (2017). Lost in transportation: nucleocytoplasmic transport defects in ALS and other neurodegenerative diseases. Neuron *96*, 285–297.

Kim, Y., and Myong, S. (2016). RNA remodeling activity of DEAD box proteins tuned by protein concentration, RNA length, and ATP. Mol. Cell *63*, 865–876.

Kim, H.J., Kim, N.C., Wang, Y.-D., Scarborough, E.A., Moore, J., Diaz, Z., MacLea, K.S., Freibaum, B., Li, S., Molliex, A., et al. (2013). Mutations in prion-like domains in hnRNPA2B1 and hnRNPA1 cause multisystem proteinopathy and ALS. Nature *495*, 467–473.

Kim, H.-J., Raphael, A.R., LaDow, E.S., McGurk, L., Weber, R.A., Trojanowski, J.Q., Lee, V.M.-Y., Finkbeiner, S., Gitler, A.D., and Bonini, N.M. (2014). Therapeutic modulation of eIF2α phosphorylation rescues TDP-43 toxicity in amyotrophic lateral sclerosis disease models. Nat. Genet. *46*, 152–160.

King, O.D., Gitler, A.D., and Shorter, J. (2012). The tip of the iceberg: RNA-binding proteins with prion-like domains in neurodegenerative disease. Brain Res. *1462*, 61–80.

Kitamura, A., Nakayama, Y., Shibasaki, A., Taki, A., Yuno, S., Takeda, K., Yahara, M., Tanabe, N., and Kinjo, M. (2016). Interaction of RNA with a C-terminal fragment of the amyotrophic lateral sclerosis-associated TDP43 reduces cytotoxicity. Sci. Rep. *6*, 19230.

Klim, J.R., Williams, L.A., Limone, F., Guerra San Juan, I., Davis-Dusenbery, B.N., Mordes, D.A., Burberry, A., Steinbaugh, M.J., Gamage, K.K., Kirchner, R., et al. (2019). ALS-implicated protein TDP-43 sustains levels of STMN2, a mediator of motor neuron growth and repair. Nat. Neurosci. *22*, 167–179.

Klus, P., Ponti, R.D., Livi, C.M., and Tartaglia, G.G. (2015). Protein aggregation, structural disorder and RNA-binding ability: a new approach for physico-chemical and gene ontology classification of multiple datasets. BMC Genomics *16*, 1071.

Köhler, A., and Hurt, E. (2007). Exporting RNA from the nucleus to the cytoplasm. Nat. Rev. Mol. Cell Biol. *8*, 761–773.

Kraemer, B.C., Schuck, T., Wheeler, J.M., Robinson, L.C., Trojanowski, J.Q., Lee, V.M.Y., and Schellenberg, G.D. (2010). Loss of murine TDP-43 disrupts motor function and plays an essential role in embryogenesis. Acta Neuropathol. *119*, 409–419.

Kuo, P.-H., Doudeva, L.G., Wang, Y.-T., Shen, C.-K.J., and Yuan, H.S. (2009). Structural insights into TDP-43 in nucleic-acid binding and domain interactions. Nucleic Acids Res. *37*, 1799–1808.

Kurtishi, A., Rosen, B., Patil, K.S., Alves, G.W., and Møller, S.G. (2019). Cellular proteostasis in neurodegeneration. Mol. Neurobiol. *56*, 3676–3689.

Labokha, A.A., Gradmann, S., Frey, S., Hülsmann, B.B., Urlaub, H., Baldus, M., and Görlich, D. (2013). Systematic analysis of barrier-forming FG hydrogels from Xenopus nuclear pore complexes. EMBO J. *32*, 204–218.

Laferrière, F., Maniecka, Z., Pérez-Berlanga, M., Hruska-Plochan, M., Gilhespy, L., Hock, E.-M., Wagner, U., Afroz, T., Boersema, P.J., Barmettler, G., et al. (2019). TDP-43 extracted from frontotemporal lobar degeneration subject brains displays distinct aggregate assemblies and neurotoxic effects reflecting disease progression rates. Nat. Neurosci. *22*, 65–77.

Lagier-Tourenne, C., Polymenidou, M., and Cleveland, D.W. (2010). TDP-43 and FUS/TLS: emerging roles in RNA processing and neurodegeneration. Hum. Mol. Genet. *19*, R46–64.

Lagier-Tourenne, C., Polymenidou, M., Hutt, K.R., Vu, A.Q., Baughn, M., Huelga, S.C., Clutario, K.M., Ling, S.-C., Liang, T.Y., Mazur, C., et al. (2012). Divergent roles of ALS-linked proteins FUS/TLS and TDP-43 intersect in processing long pre-mRNAs. Nat. Neurosci. *15*, 1488–1497.

Lamark, T., and Johansen, T. (2012). Aggrephagy: selective disposal of protein aggregates by macroautophagy. Int. J. Cell Biol. *2012*, 736905.

Langdon, E.M., and Gladfelter, A.S. (2018). A New Lens for RNA Localization: Liquid-Liquid Phase Separation. Annu. Rev. Microbiol. *72*, 255–271.

Langdon, E.M., Qiu, Y., Ghanbari Niaki, A., McLaughlin, G.A., Weidmann, C.A., Gerbich, T.M., Smith, J.A., Crutchley, J.M., Termini, C.M., Weeks, K.M., et al. (2018). mRNA structure determines specificity of a polyQ-driven phase separation. Science *360*, 922–927.

Langmead, B., Trapnell, C., Pop, M., and Salzberg, S.L. (2009). Ultrafast and memory-efficient alignment of short DNA sequences to the human genome. Genome Biol. *10*, R25.

Lee, S., and Huang, E.J. (2017). Modeling ALS and FTD with iPSC-derived neurons. Brain Res. *1656*, 88–97.

Leigh, P.N., Whitwell, H., Garofalo, O., Buller, J., Swash, M., Martin, J.E., Gallo, J.M., Weller, R.O., and Anderton, B.H. (1991). Ubiquitin-immunoreactive intraneuronal inclusions in amyotrophic lateral sclerosis. Morphology, distribution, and specificity. Brain *114 (Pt 2)*, 775–788.

Lerga, A., Hallier, M., Delva, L., Orvain, C., Gallais, I., Marie, J., and Moreau-Gachelin, F. (2001). Identification of an RNA binding specificity for the potential splicing factor TLS. J. Biol. Chem. *276*, 6807–6816.

Leulliot, N., and Varani, G. (2001). Current Topics in RNA−Protein Recognition: Control of Specificity and Biological Function through Induced Fit and Conformational Capture†. Biochemistry *40*, 7947–7956.

Li, C., Goryaynov, A., and Yang, W. (2016). The selective permeability barrier in the nuclear pore complex. Nucleus *7*, 430–446.

Li, H.-R., Chiang, W.-C., Chou, P.-C., Wang, W.-J., and Huang, J.-R. (2018). TAR DNA-binding protein 43 (TDP-43) liquid-liquid phase separation is mediated by just a few aromatic residues. J. Biol. Chem. *293*, 6090–6098.

Li, H.-Y., Yeh, P.-A., Chiu, H.-C., Tang, C.-Y., and Tu, B.P. (2011). Hyperphosphorylation as a defense mechanism to reduce TDP-43 aggregation. PLoS One *6*, e23075.

Li, Y.R., King, O.D., Shorter, J., and Gitler, A.D. (2013). Stress granules as crucibles of ALS pathogenesis. J. Cell Biol. *201*, 361–372.

Liachko, N.F., Guthrie, C.R., and Kraemer, B.C. (2010). Phosphorylation promotes neurotoxicity in a Caenorhabditis elegans model of TDP-43 proteinopathy. J. Neurosci. *30*, 16208–16219.

Lin, Y., Protter, D.S.W., Rosen, M.K., and Parker, R. (2015). Formation and Maturation of Phase-Separated Liquid Droplets by RNA-Binding Proteins. Mol. Cell *60*, 208–219.

Lin, Y., Currie, S.L., and Rosen, M.K. (2017). Intrinsically disordered sequences enable modulation of protein phase separation through distributed tyrosine motifs. J. Biol. Chem. *292*, 19110–19120.

Ling, J.P., Pletnikova, O., Troncoso, J.C., and Wong, P.C. (2015). TDP-43 repression of nonconserved cryptic exons is compromised in ALS-FTD. Science *349*, 650–655.

Ling, S.-C., Polymenidou, M., and Cleveland, D.W. (2013). Converging mechanisms in ALS and FTD: disrupted RNA and protein homeostasis. Neuron *79*, 416–438.

Lippa, C.F., Heiman-Patterson, T., Gambetti, P., Croul, S., and Koffler, S. (2001). Ubiquitinated Inclusions Link Amyotrophic Lateral Sclerosis with Frontotemporal Dementia. In Contemporary Neuropsychiatry, K. Miyoshi, C.M. Shapiro, M. Gaviria, and Y. Morita, eds. (Tokyo: Springer Japan), pp. 164–170.

Liu, X., Niu, C., Ren, J., Zhang, J., Xie, X., Zhu, H., Feng, W., and Gong, W. (2013). The RRM domain of human fused in sarcoma protein reveals a non-canonical nucleic acid binding site. Biochim. Biophys. Acta *1832*, 375–385.

Liu, Z., Zhang, S., Gu, J., Tong, Y., Li, Y., Gui, X., Long, H., Wang, C., Zhao, C., Lu, J., et al. (2020). Hsp27 chaperones FUS phase separation under the modulation of stress-induced phosphorylation. Nat. Struct. Mol. Biol.

Liu-Yesucevitz, L., Lin, A.Y., Ebata, A., Boon, J.Y., Reid, W., Xu, Y.-F., Kobrin, K., Murphy, G.J., Petrucelli, L., and Wolozin, B. (2014). ALS-linked mutations enlarge TDP-43-enriched neuronal RNA granules in the dendritic arbor. J. Neurosci. *34*, 4167–4174.

Loganathan, S., Lehmkuhl, E.M., Eck, R.J., and Zarnescu, D.C. (2019). To Be or Not To Be…Toxic-Is RNA Association With TDP-43 Complexes Deleterious or Protective in Neurodegeneration? Front. Mol. Biosci. *6*, 154.

Loughlin, F.E., Lukavsky, P.J., Kazeeva, T., Reber, S., Hock, E.-M., Colombo, M., Von Schroetter, C., Pauli, P., Cléry, A., Mühlemann, O., et al. (2019). The Solution Structure of FUS Bound to RNA Reveals a Bipartite Mode of RNA Recognition with Both Sequence and Shape Specificity. Mol. Cell *73*, 490–504.e6.

Lu, Y., Lim, L., and Song, J. (2017). RRM domain of ALS/FTD-causing FUS characteristic of irreversible unfolding spontaneously self-assembles into amyloid fibrils. Sci. Rep. *7*, 1043.

Mackenzie, I.R., Rademakers, R., and Neumann, M. (2010). TDP-43 and FUS in amyotrophic lateral sclerosis and frontotemporal dementia. Lancet Neurol. *9*, 995–1007.

Mackenzie, I.R., Arzberger, T., Kremmer, E., Troost, D., Lorenzl, S., Mori, K., Weng, S.-M., Haass, C., Kretzschmar, H.A., Edbauer, D., et al. (2013). Dipeptide repeat protein pathology in C9ORF72 mutation cases: clinico-pathological correlations. Acta Neuropathol. *126*, 859–879.

Mackenzie, I.R., Nicholson, A.M., Sarkar, M., Messing, J., Purice, M.D., Pottier, C., Annu, K., Baker, M., Perkerson, R.B., Kurti, A., et al. (2017). TIA1 mutations in amyotrophic lateral sclerosis and frontotemporal dementia promote phase separation and alter stress granule dynamics. Neuron *95*, 808–816.e9.

Mackenzie, I.R.A., Ansorge, O., Strong, M., Bilbao, J., Zinman, L., Ang, L.-C., Baker, M., Stewart, H., Eisen, A., Rademakers, R., et al. (2011). Pathological heterogeneity in amyotrophic lateral sclerosis with FUS mutations: two distinct patterns correlating with disease severity and mutation. Acta Neuropathol. *122*, 87–98.

Maharana, S., Wang, J., Papadopoulos, D.K., Richter, D., Pozniakovsky, A., Poser, I., Bickle, M., Rizk, S., Guillén-Boixet, J., Franzmann, T.M., et al. (2018). RNA buffers the phase separation behavior of prion-like RNA binding proteins. Science *360*, 918–921.

Majlessi, M., Nelson, N.C., and Becker, M.M. (1998). Advantages of 2'-O-methyl oligoribonucleotide probes for detecting RNA targets. Nucleic Acids Res. *26*, 2224–2229.

Malik, A.M., Miguez, R.A., Li, X., Ho, Y.-S., Feldman, E.L., and Barmada, S.J. (2018). Matrin 3-dependent neurotoxicity is modified by nucleic acid binding and nucleocytoplasmic localization. Elife *7*.

Mandrioli, J., Mediani, L., Alberti, S., and Carra, S. (2020). ALS and FTD: Where RNA metabolism meets protein quality control. Semin. Cell Dev. Biol. *99*, 183–192.

Mann, J.R., Gleixner, A.M., Mauna, J.C., Gomes, E., DeChellis-Marks, M.R., Needham, P.G., Copley, K.E., Hurtle, B., Portz, B., Pyles, N.J., et al. (2019). RNA Binding Antagonizes Neurotoxic Phase Transitions of TDP-43. Neuron *102*, 321–338.e8.

Markmiller, S., Soltanieh, S., Server, K.L., Mak, R., Jin, W., Fang, M.Y., Luo, E.-C., Krach, F., Yang, D., Sen, A., et al. (2018). Context-Dependent and Disease-Specific Diversity in Protein Interactions within Stress Granules. Cell *172*, 590–604.e13.

Marrone, L., Drexler, H.C.A., Wang, J., Tripathi, P., Distler, T., Heisterkamp, P., Anderson, E.N., Kour, S., Moraiti, A., Maharana, S., et al. (2019). FUS pathology in ALS is linked to alterations in multiple ALS-associated proteins and rescued by drugs stimulating autophagy. Acta Neuropathol. *138*, 67–84.

McCord, M.C., and Aizenman, E. (2014). The role of intracellular zinc release in aging, oxidative stress, and Alzheimer's disease. Front. Aging Neurosci. *6*, 77.

McGurk, L., Gomes, E., Guo, L., Mojsilovic-Petrovic, J., Tran, V., Kalb, R.G., Shorter, J., and Bonini, N.M. (2018). Poly(ADP-Ribose) Prevents Pathological Phase Separation of TDP-43 by Promoting Liquid Demixing and Stress Granule Localization. Mol. Cell *71*, 703–717.e9.

McKee, A.C., Gavett, B.E., Stern, R.A., Nowinski, C.J., Cantu, R.C., Kowall, N.W., Perl, D.P., Hedley-Whyte, E.T., Price, B., Sullivan, C., et al. (2010). TDP-43 proteinopathy and motor neuron disease in chronic traumatic encephalopathy. J. Neuropathol. Exp. Neurol. *69*, 918–929.

Mejzini, R., Flynn, L.L., Pitout, I.L., Fletcher, S., Wilton, S.D., and Akkari, P.A. (2019). ALS genetics, mechanisms, and therapeutics: where are we now? Front. Neurosci. *13*, 1310.

Melamed, Z., López-Erauskin, J., Baughn, M.W., Zhang, O., Drenner, K., Sun, Y., Freyermuth, F., McMahon, M.A., Beccari, M.S., Artates, J.W., et al. (2019). Premature polyadenylation-mediated loss of stathmin-2 is a hallmark of TDP-43-dependent neurodegeneration. Nat. Neurosci. *22*, 180–190.

Metz, A., Soret, J., Vourc'h, C., Tazi, J., and Jolly, C. (2004). A key role for stress-induced satellite III transcripts in the relocalization of splicing factors into nuclear stress granules. J. Cell Sci. *117*, 4551–4558.

Mimura, M., Tomita, S., Shinkai, Y., Shiraki, K., and Kurita, R. (2020). Quadruplex Folding of DNA Promotes the Condensation of Linker Histones via Liquid-Liquid Phase Separation.

Mitrea, D.M., Cika, J.A., Guy, C.S., Ban, D., Banerjee, P.R., Stanley, C.B., Nourse, A., Deniz, A.A., and Kriwacki, R.W. (2016). Nucleophosmin integrates within the nucleolus via multi-modal interactions with proteins displaying R-rich linear motifs and rRNA. Elife *5*.

Modic, M., Grosch, M., Rot, G., Schirge, S., Lepko, T., Yamazaki, T., Lee, F.C.Y., Rusha, E., Shaposhnikov, D., Palo, M., et al. (2019). Cross-Regulation between TDP-43 and Paraspeckles Promotes Pluripotency-Differentiation Transition. Mol. Cell *74*, 951–965.e13.

Molliex, A., Temirov, J., Lee, J., Coughlin, M., Kanagaraj, A.P., Kim, H.J., Mittag, T., and Taylor, J.P. (2015). Phase separation by low complexity domains promotes stress granule assembly and drives pathological fibrillization. Cell *163*, 123–133.

Mompeán, M., Romano, V., Pantoja-Uceda, D., Stuani, C., Baralle, F.E., Buratti, E., and Laurents, D.V. (2017). Point mutations in the N-terminal domain of transactive response DNA-binding protein 43 kDa (TDP-43) compromise its stability, dimerization, and functions. J. Biol. Chem. *292*, 11992–12006.

Monahan, Z., Shewmaker, F., and Pandey, U.B. (2016). Stress granules at the intersection of autophagy and ALS. Brain Res. *1649*, 189–200.

Monahan, Z., Ryan, V.H., Janke, A.M., Burke, K.A., Rhoads, S.N., Zerze, G.H., O'Meally, R., Dignon, G.L., Conicella, A.E., Zheng, W., et al. (2017). Phosphorylation of the FUS low-

complexity domain disrupts phase separation, aggregation, and toxicity. EMBO J. *36*, 2951–2967.

Murakami, T., Qamar, S., Lin, J.Q., Schierle, G.S.K., Rees, E., Miyashita, A., Costa, A.R., Dodd, R.B., Chan, F.T.S., Michel, C.H., et al. (2015). ALS/FTD Mutation-Induced Phase Transition of FUS Liquid Droplets and Reversible Hydrogels into Irreversible Hydrogels Impairs RNP Granule Function. Neuron *88*, 678–690.

Murray, D.T., Kato, M., Lin, Y., Thurber, K.R., Hung, I., McKnight, S.L., and Tycko, R. (2017). Structure of FUS Protein Fibrils and Its Relevance to Self-Assembly and Phase Separation of Low-Complexity Domains. Cell *171*, 615–627.e16.

Murthy, A.C., Dignon, G.L., Kan, Y., Zerze, G.H., Parekh, S.H., Mittal, J., and Fawzi, N.L. (2019). Molecular interactions underlying liquid-liquid phase separation of the FUS low-complexity domain. Nat. Struct. Mol. Biol. *26*, 637–648.

Naganuma, T., Nakagawa, S., Tanigawa, A., Sasaki, Y.F., Goshima, N., and Hirose, T. (2012). Alternative 3'-end processing of long noncoding RNA initiates construction of nuclear paraspeckles. EMBO J. *31*, 4020–4034.

Nakamura, H., Lee, A.A., Afshar, A.S., Watanabe, S., Rho, E., Razavi, S., Suarez, A., Lin, Y.-C., Tanigawa, M., Huang, B., et al. (2018). Intracellular production of hydrogels and synthetic RNA granules by multivalent molecular interactions. Nat. Mater. *17*, 79–89.

Nakaya, T., Alexiou, P., Maragkakis, M., Chang, A., and Mourelatos, Z. (2013). FUS regulates genes coding for RNA-binding proteins in neurons by binding to their highly conserved introns. RNA *19*, 498–509.

Namkoong, S., Ho, A., Woo, Y.M., Kwak, H., and Lee, J.H. (2018). Systematic Characterization of Stress-Induced RNA Granulation. Mol. Cell *70*, 175–187.e8.

Narayanaswamy, R., Levy, M., Tsechansky, M., Stovall, G.M., O'Connell, J.D., Mirrielees, J., Ellington, A.D., and Marcotte, E.M. (2009). Widespread reorganization of metabolic enzymes into reversible assemblies upon nutrient starvation. Proc. Natl. Acad. Sci. USA *106*, 10147–10152.

Neumann, M., Sampathu, D.M., Kwong, L.K., Truax, A.C., Micsenyi, M.C., Chou, T.T., Bruce, J., Schuck, T., Grossman, M., Clark, C.M., et al. (2006). Ubiquitinated TDP-43 in frontotemporal lobar degeneration and amyotrophic lateral sclerosis. Science *314*, 130–133.

Neumann, M., Kwong, L.K., Truax, A.C., Vanmassenhove, B., Kretzschmar, H.A., Van Deerlin, V.M., Clark, C.M., Grossman, M., Miller, B.L., Trojanowski, J.Q., et al. (2007). TDP-43-positive white matter pathology in frontotemporal lobar degeneration with ubiquitin-positive inclusions. J. Neuropathol. Exp. Neurol. *66*, 177–183.

Neumann, M., Bentmann, E., Dormann, D., Jawaid, A., DeJesus-Hernandez, M., Ansorge, O., Roeber, S., Kretzschmar, H.A., Munoz, D.G., Kusaka, H., et al. (2011). FET proteins

TAF15 and EWS are selective markers that distinguish FTLD with FUS pathology from amyotrophic lateral sclerosis with FUS mutations. Brain *134*, 2595–2609.

Neumann, M., Valori, C.F., Ansorge, O., Kretzschmar, H.A., Munoz, D.G., Kusaka, H., Yokota, O., Ishihara, K., Ang, L.-C., Bilbao, J.M., et al. (2012). Transportin 1 accumulates specifically with FET proteins but no other transportin cargos in FTLD-FUS and is absent in FUS inclusions in ALS with FUS mutations. Acta Neuropathol. *124*, 705–716.

Nguemaha, V., and Zhou, H.-X. (2018). Liquid-Liquid Phase Separation of Patchy Particles Illuminates Diverse Effects of Regulatory Components on Protein Droplet Formation. Sci. Rep. *8*, 6728.

Nguyen, H.P., Van Broeckhoven, C., and van der Zee, J. (2018). ALS Genes in the Genomic Era and their Implications for FTD. Trends Genet. *34*, 404–423.

Niaki, A.G., Sarkar, J., Cai, X., Rhine, K., Vidaurre, V., Guy, B., Hurst, M., Lee, J.C., Koh, H.R., Guo, L., et al. (2020). Loss of Dynamic RNA Interaction and Aberrant Phase Separation Induced by Two Distinct Types of ALS/FTD-Linked FUS Mutations. Mol. Cell *77*, 82–94.e4.

Ninomiya, K., Adachi, S., Natsume, T., Iwakiri, J., Terai, G., Asai, K., and Hirose, T. (2020). LncRNA-dependent nuclear stress bodies promote intron retention through SR protein phosphorylation. EMBO J. *39*, e102729.

Nolan, M., Talbot, K., and Ansorge, O. (2016). Pathogenesis of FUS-associated ALS and FTD: insights from rodent models. Acta Neuropathol. Commun. *4*, 99.

Nonaka, T., Suzuki, G., Tanaka, Y., Kametani, F., Hirai, S., Okado, H., Miyashita, T., Saitoe, M., Akiyama, H., Masai, H., et al. (2016). Phosphorylation of TAR DNA-binding Protein of 43 kDa (TDP-43) by Truncated Casein Kinase 1δ Triggers Mislocalization and Accumulation of TDP-43. J. Biol. Chem. *291*, 5473–5483.

Nott, T.J., Petsalaki, E., Farber, P., Jervis, D., Fussner, E., Plochowietz, A., Craggs, T.D., Bazett-Jones, D.P., Pawson, T., Forman-Kay, J.D., et al. (2015). Phase transition of a disordered nuage protein generates environmentally responsive membraneless organelles. Mol. Cell *57*, 936–947.

Nussbacher, J.K., Tabet, R., Yeo, G.W., and Lagier-Tourenne, C. (2019). Disruption of RNA metabolism in neurological diseases and emerging therapeutic interventions. Neuron *102*, 294–320.

Oueslati, A. (2016). Implication of Alpha-Synuclein Phosphorylation at S129 in Synucleinopathies: What Have We Learned in the Last Decade? J. Parkinsons. Dis. *6*, 39–51.

Ozdilek, B.A., Thompson, V.F., Ahmed, N.S., White, C.I., Batey, R.T., and Schwartz, J.C. (2017). Intrinsically disordered RGG/RG domains mediate degenerate specificity in RNA binding. Nucleic Acids Res. *45*, 7984–7996.

Pagani, F., Buratti, E., Stuani, C., Romano, M., Zuccato, E., Niksic, M., Giglio, L., Faraguna, D., and Baralle, F.E. (2000). Splicing factors induce cystic fibrosis transmembrane regulator exon 9 skipping through a nonevolutionary conserved intronic element. J. Biol. Chem. *275*, 21041–21047.

Patel, A., Lee, H.O., Jawerth, L., Maharana, S., Jahnel, M., Hein, M.Y., Stoynov, S., Mahamid, J., Saha, S., Franzmann, T.M., et al. (2015). A Liquid-to-Solid Phase Transition of the ALS Protein FUS Accelerated by Disease Mutation. Cell *162*, 1066–1077.

Patel, S.S., Belmont, B.J., Sante, J.M., and Rexach, M.F. (2007). Natively unfolded nucleoporins gate protein diffusion across the nuclear pore complex. Cell *129*, 83–96.

Philips, T., and Rothstein, J.D. (2015). Rodent models of amyotrophic lateral sclerosis. Curr. Protoc. Pharmacol. *69*, 5.67.1–21.

Pinarbasi, E.S., Cağatay, T., Fung, H.Y.J., Li, Y.C., Chook, Y.M., and Thomas, P.J. (2018). Active nuclear import and passive nuclear export are the primary determinants of TDP-43 localization. Sci. Rep. *8*, 7083.

Polymenidou, M., Lagier-Tourenne, C., Hutt, K.R., Bennett, C.F., Cleveland, D.W., and Yeo, G.W. (2012). Misregulated RNA processing in amyotrophic lateral sclerosis. Brain Res. *1462*, 3–15.

Porta, S., Xu, Y., Restrepo, C.R., Kwong, L.K., Zhang, B., Brown, H.J., Lee, E.B., Trojanowski, J.Q., and Lee, V.M.-Y. (2018). Patient-derived frontotemporal lobar degeneration brain extracts induce formation and spreading of TDP-43 pathology in vivo. Nat. Commun. *9*, 4220.

Posey, A.E., Holehouse, A.S., and Pappu, R.V. (2018). Phase separation of intrinsically disordered proteins. Meth. Enzymol. *611*, 1–30.

Prasad, A., Bharathi, V., Sivalingam, V., Girdhar, A., and Patel, B.K. (2019). Molecular Mechanisms of TDP-43 Misfolding and Pathology in Amyotrophic Lateral Sclerosis. Front. Mol. Neurosci. *12*, 25.

Prasad, D.D., Ouchida, M., Lee, L., Rao, V.N., and Reddy, E.S. (1994). TLS/FUS fusion domain of TLS/FUS-erg chimeric protein resulting from the t(16;21) chromosomal translocation in human myeloid leukemia functions as a transcriptional activation domain. Oncogene *9*, 3717–3729.

Protter, D.S.W., and Parker, R. (2016). Principles and properties of stress granules. Trends Cell Biol. *26*, 668–679.

Prpar Mihevc, S., Baralle, M., Buratti, E., and Rogelj, B. (2016). TDP-43 aggregation mirrors TDP-43 knockdown, affecting the expression levels of a common set of proteins. Sci. Rep. *6*, 33996.

Purice, M.D., and Taylor, J.P. (2018). Linking hnRNP Function to ALS and FTD Pathology. Front. Neurosci. *12*, 326.

Qamar, S., Wang, G., Randle, S.J., Ruggeri, F.S., Varela, J.A., Lin, J.Q., Phillips, E.C., Miyashita, A., Williams, D., Ströhl, F., et al. (2018). FUS Phase Separation Is Modulated by a Molecular Chaperone and Methylation of Arginine Cation-π Interactions. Cell *173*, 720–734.e15.

Qiu, H., Lee, S., Shang, Y., Wang, W.-Y., Au, K.F., Kamiya, S., Barmada, S.J., Finkbeiner, S., Lui, H., Carlton, C.E., et al. (2014). ALS-associated mutation FUS-R521C causes DNA damage and RNA splicing defects. J. Clin. Invest. *124*, 981–999.

Ratti, A., and Buratti, E. (2016). Physiological functions and pathobiology of TDP-43 and FUS/TLS proteins. J. Neurochem. *138 Suppl 1*, 95–111.

Ray, S., Singh, N., Pandey, S., Kumar, R., Gadhe, L., Datta, D., Patel, K., Mahato, J., Navalkar, A., Panigrahi, R., et al. (2019). Liquid-liquid phase separation and liquid-to-solid transition mediate α-synuclein amyloid fibril containing hydrogel formation. BioRxiv.

Rayman, J.B., Karl, K.A., and Kandel, E.R. (2018). TIA-1 Self-Multimerization, Phase Separation, and Recruitment into Stress Granules Are Dynamically Regulated by Zn2. Cell Rep. *22*, 59–71.

Rentzeperis, D., Jonsson, T., and Sauer, R.T. (1999). Acceleration of the refolding of Arc repressor by nucleic acids and other polyanions. Nat. Struct. Biol. *6*, 569–573.

Riback, J.A., Katanski, C.D., Kear-Scott, J.L., Pilipenko, E.V., Rojek, A.E., Sosnick, T.R., and Drummond, D.A. (2017). Stress-Triggered Phase Separation Is an Adaptive, Evolutionarily Tuned Response. Cell *168*, 1028–1040.e19.

Ries, R.J., Zaccara, S., Klein, P., Olarerin-George, A., Namkoong, S., Pickering, B.F., Patil, D.P., Kwak, H., Lee, J.H., and Jaffrey, S.R. (2019). m6A enhances the phase separation potential of mRNA. Nature *571*, 424–428.

Rinaldi, C., and Wood, M.J.A. (2018). Antisense oligonucleotides: the next frontier for treatment of neurological disorders. Nat. Rev. Neurol. *14*, 9–21.

Ringholz, G.M., Appel, S.H., Bradshaw, M., Cooke, N.A., Mosnik, D.M., and Schulz, P.E. (2005). Prevalence and patterns of cognitive impairment in sporadic ALS. Neurology *65*, 586–590.

Ross, W.N. (2012). Understanding calcium waves and sparks in central neurons. Nat. Rev. Neurosci. *13*, 157–168.

Ryan, V.H., Dignon, G.L., Zerze, G.H., Chabata, C.V., Silva, R., Conicella, A.E., Amaya, J., Burke, K.A., Mittal, J., and Fawzi, N.L. (2018). Mechanistic View of hnRNPA2 Low-Complexity Domain Structure, Interactions, and Phase Separation Altered by Mutation and Arginine Methylation. Mol. Cell *69*, 465–479.e7.

Ryan, V.H., Perdikari, T.M., Naik, M.T., Saueressig, C.F., Lins, J., Dignon, G.L., Mittal, J., Hart, A.C., and Fawzi, N.L. (2020). Tyrosine phosphorylation regulates hnRNPA2 granule protein partitioning & reduces neurodegeneration. BioRxiv.

Saha, S., Weber, C.A., Nousch, M., Adame-Arana, O., Hoege, C., Hein, M.Y., Osborne-Nishimura, E., Mahamid, J., Jahnel, M., Jawerth, L., et al. (2016). Polar Positioning of Phase-Separated Liquid Compartments in Cells Regulated by an mRNA Competition Mechanism. Cell *166*, 1572–1584.e16.

Sama, R.R.K., Ward, C.L., Kaushansky, L.J., Lemay, N., Ishigaki, S., Urano, F., and Bosco, D.A. (2013). FUS/TLS assembles into stress granules and is a prosurvival factor during hyperosmolar stress. J. Cell Physiol. *228*, 2222–2231.

Sanchez de Groot, N., Armaos, A., Graña-Montes, R., Alriquet, M., Calloni, G., Vabulas, R.M., and Tartaglia, G.G. (2019). RNA structure drives interaction with proteins. Nat. Commun. *10*, 3246.

Schmidt, H.B., and Görlich, D. (2015). Nup98 FG domains from diverse species spontaneously phase-separate into particles with nuclear pore-like permselectivity. Elife *4*.

Schmidt, H.B., and Görlich, D. (2016). Transport selectivity of nuclear pores, phase separation, and membraneless organelles. Trends Biochem. Sci. *41*, 46–61.

Schmidt, H.B., and Rohatgi, R. (2016). In Vivo Formation of Vacuolated Multi-phase Compartments Lacking Membranes. Cell Rep. *16*, 1228–1236.

Schmidt, H.B., Barreau, A., and Rohatgi, R. (2019). Phase separation-deficient TDP43 remains functional in splicing. Nat. Commun. *10*, 4890.

Schwartz, J.C., Wang, X., Podell, E.R., and Cech, T.R. (2013). RNA seeds higher-order assembly of FUS protein. Cell Rep. *5*, 918–925.

Scotter, E.L., Vance, C., Nishimura, A.L., Lee, Y.-B., Chen, H.-J., Urwin, H., Sardone, V., Mitchell, J.C., Rogelj, B., Rubinsztein, D.C., et al. (2014). Differential roles of the ubiquitin proteasome system and autophagy in the clearance of soluble and aggregated TDP-43 species. J. Cell Sci. *127*, 1263–1278.

Scotter, E.L., Chen, H.-J., and Shaw, C.E. (2015). TDP-43 Proteinopathy and ALS: Insights into Disease Mechanisms and Therapeutic Targets. Neurotherapeutics *12*, 352–363.

Seilhean, D., Cazeneuve, C., Thuriès, V., Russaouen, O., Millecamps, S., Salachas, F., Meininger, V., Leguern, E., and Duyckaerts, C. (2009). Accumulation of TDP-43 and alpha-actin in an amyotrophic lateral sclerosis patient with the K17I ANG mutation. Acta Neuropathol. *118*, 561–573.

Sephton, C.F., Cenik, C., Kucukural, A., Dammer, E.B., Cenik, B., Han, Y., Dewey, C.M., Roth, F.P., Herz, J., Peng, J., et al. (2011). Identification of neuronal RNA targets of TDP-43-containing ribonucleoprotein complexes. J. Biol. Chem. *286*, 1204–1215.

Serio, T.R., Cashikar, A.G., Kowal, A.S., Sawicki, G.J., Moslehi, J.J., Serpell, L., Arnsdorf, M.F., and Lindquist, S.L. (2000). Nucleated conformational conversion and the replication of conformational information by a prion determinant. Science *289*, 1317–1321.

Shahheydari, H., Ragagnin, A., Walker, A.K., Toth, R.P., Vidal, M., Jagaraj, C.J., Perri, E.R., Konopka, A., Sultana, J.M., and Atkin, J.D. (2017). Protein quality control and the amyotrophic lateral sclerosis/frontotemporal dementia continuum. Front. Mol. Neurosci. *10*, 119.

Shelkovnikova, T.A., Peters, O.M., Deykin, A.V., Connor-Robson, N., Robinson, H., Ustyugov, A.A., Bachurin, S.O., Ermolkevich, T.G., Goldman, I.L., Sadchikova, E.R., et al. (2013a). Fused in sarcoma (FUS) protein lacking nuclear localization signal (NLS) and major RNA binding motifs triggers proteinopathy and severe motor phenotype in transgenic mice. J. Biol. Chem. *288*, 25266–25274.

Shelkovnikova, T.A., Robinson, H.K., Connor-Robson, N., and Buchman, V.L. (2013b). Recruitment into stress granules prevents irreversible aggregation of FUS protein mislocalized to the cytoplasm. Cell Cycle *12*, 3194–3202.

Shevtsov, S.P., and Dundr, M. (2011). Nucleation of nuclear bodies by RNA. Nat. Cell Biol. *13*, 167–173.

Shiihashi, G., Ito, D., Yagi, T., Nihei, Y., Ebine, T., and Suzuki, N. (2016). Mislocated FUS is sufficient for gain-of-toxic-function amyotrophic lateral sclerosis phenotypes in mice. Brain *139*, 2380–2394.

Shimonaka, S., Nonaka, T., Suzuki, G., Hisanaga, S.-I., and Hasegawa, M. (2016). Templated Aggregation of TAR DNA-binding Protein of 43 kDa (TDP-43) by Seeding with TDP-43 Peptide Fibrils. J. Biol. Chem. *291*, 8896–8907.

Shin, Y., and Brangwynne, C.P. (2017). Liquid phase condensation in cell physiology and disease. Science *357*.

Shin, Y., Berry, J., Pannucci, N., Haataja, M.P., Toettcher, J.E., and Brangwynne, C.P. (2017). Spatiotemporal Control of Intracellular Phase Transitions Using Light-Activated optoDroplets. Cell *168*, 159–171.e14.

Shin, Y., Chang, Y.-C., Lee, D.S.W., Berry, J., Sanders, D.W., Ronceray, P., Wingreen, N.S., Haataja, M., and Brangwynne, C.P. (2019). Liquid nuclear condensates mechanically sense and restructure the genome. Cell *176*, 1518.

Shodai, A., Morimura, T., Ido, A., Uchida, T., Ayaki, T., Takahashi, R., Kitazawa, S., Suzuki, S., Shirouzu, M., Kigawa, T., et al. (2013). Aberrant assembly of RNA recognition motif 1 links to pathogenic conversion of TAR DNA-binding protein of 43 kDa (TDP-43). J. Biol. Chem. *288*, 14886–14905.

Smethurst, P., Newcombe, J., Troakes, C., Simone, R., Chen, Y.-R., Patani, R., and Sidle, K. (2016). In vitro prion-like behaviour of TDP-43 in ALS. Neurobiol. Dis. *96*, 236–247.

Smith, J.S., and Nikonowicz, E.P. (2000). Phosphorothioate substitution can substantially alter RNA conformation†. Biochemistry *39*, 5642–5652.

Sugiyama, K., Aida, T., Nomura, M., Takayanagi, R., Zeilhofer, H.U., and Tanaka, K. (2017). Calpain-Dependent Degradation of Nucleoporins Contributes to Motor Neuron Death in a Mouse Model of Chronic Excitotoxicity. J. Neurosci. *37*, 8830–8844.

Sun, Y., and Chakrabartty, A. (2017). Phase to Phase with TDP-43. Biochemistry *56*, 809–823.

Sun, Y., Arslan, P.E., Won, A., Yip, C.M., and Chakrabartty, A. (2014). Binding of TDP-43 to the 3'UTR of its cognate mRNA enhances its solubility. Biochemistry *53*, 5885–5894.

Sun, Z., Diaz, Z., Fang, X., Hart, M.P., Chesi, A., Shorter, J., and Gitler, A.D. (2011). Molecular determinants and genetic modifiers of aggregation and toxicity for the ALS disease protein FUS/TLS. PLoS Biol. *9*, e1000614.

Svetoni, F., Frisone, P., and Paronetto, M.P. (2016). Role of FET proteins in neurodegenerative disorders. RNA Biol. *13*, 1089–1102.

Tank, E.M., Figueroa-Romero, C., Hinder, L.M., Bedi, K., Archbold, H.C., Li, X., Weskamp, K., Safren, N., Paez-Colasante, X., Pacut, C., et al. (2018). Abnormal RNA stability in amyotrophic lateral sclerosis. Nat. Commun. *9*, 2845.

Tariq, A., Lin, J., Jackrel, M.E., Hesketh, C.D., Carman, P.J., Mack, K.L., Weitzman, R., Gambogi, C., Hernandez Murillo, O.A., Sweeny, E.A., et al. (2019). Mining Disaggregase Sequence Space to Safely Counter TDP-43, FUS, and α-Synuclein Proteotoxicity. Cell Rep. *28*, 2080–2095.e6.

Taslimi, A., Vrana, J.D., Chen, D., Borinskaya, S., Mayer, B.J., Kennedy, M.J., and Tucker, C.L. (2014). An optimized optogenetic clustering tool for probing protein interaction and function. Nat. Commun. *5*, 4925.

Taylor, J.P., Hardy, J., and Fischbeck, K.H. (2002). Toxic proteins in neurodegenerative disease. Science *296*, 1991–1995.

Taylor, J.P., Brown, R.H., and Cleveland, D.W. (2016). Decoding ALS: from genes to mechanism. Nature *539*, 197–206.

Teixeira, D., Sheth, U., Valencia-Sanchez, M.A., Brengues, M., and Parker, R. (2005). Processing bodies require RNA for assembly and contain nontranslating mRNAs. RNA *11*, 371–382.

Terry, L.J., and Wente, S.R. (2009). Flexible gates: dynamic topologies and functions for FG nucleoporins in nucleocytoplasmic transport. Eukaryotic Cell *8*, 1814–1827.

Theillet, F.-X., Kalmar, L., Tompa, P., Han, K.-H., Selenko, P., Dunker, A.K., Daughdrill, G.W., and Uversky, V.N. (2013). The alphabet of intrinsic disorder. Intrinsically Disord Proteins *1*, e24360.

Thompson, K.R., Otis, K.O., Chen, D.Y., Zhao, Y., O'Dell, T.J., and Martin, K.C. (2004). Synapse to nucleus signaling during long-term synaptic plasticity; a role for the classical active nuclear import pathway. Neuron *44*, 997–1009.

Tischbein, M., Baron, D.M., Lin, Y.-C., Gall, K.V., Landers, J.E., Fallini, C., and Bosco, D.A. (2019). The RNA-binding protein FUS/TLS undergoes calcium-mediated nuclear egress during excitotoxic stress and is required for GRIA2 mRNA processing. J. Biol. Chem. *294*, 10194–10210.

Tollervey, J.R., Curk, T., Rogelj, B., Briese, M., Cereda, M., Kayikci, M., König, J., Hortobágyi, T., Nishimura, A.L., Zupunski, V., et al. (2011). Characterizing the RNA targets and position-dependent splicing regulation by TDP-43. Nat. Neurosci. *14*, 452–458.

Van Treeck, B., and Parker, R. (2018). Emerging Roles for Intermolecular RNA-RNA Interactions in RNP Assemblies. Cell *174*, 791–802.

Van Treeck, B., Protter, D.S.W., Matheny, T., Khong, A., Link, C.D., and Parker, R. (2018). RNA self-assembly contributes to stress granule formation and defining the stress granule transcriptome. Proc. Natl. Acad. Sci. USA *115*, 2734–2739.

Tüű-Szabó, B., Kóczy, L.T., and Fuxreiter, M. (2018). Simulations of Higher-Order Protein Organizations Using a Fuzzy Framework. Complexity *2018*, 1–10.

van der Lee, R., Buljan, M., Lang, B., Weatheritt, R.J., Daughdrill, G.W., Dunker, A.K., Fuxreiter, M., Gough, J., Gsponer, J., Jones, D.T., et al. (2014). Classification of intrinsically disordered regions and proteins. Chem. Rev. *114*, 6589–6631.

van Eersel, J., Ke, Y.D., Gladbach, A., Bi, M., Götz, J., Kril, J.J., and Ittner, L.M. (2011). Cytoplasmic accumulation and aggregation of TDP-43 upon proteasome inhibition in cultured neurons. PLoS One *6*, e22850.

Vance, C., Scotter, E.L., Nishimura, A.L., Troakes, C., Mitchell, J.C., Kathe, C., Urwin, H., Manser, C., Miller, C.C., Hortobágyi, T., et al. (2013). ALS mutant FUS disrupts nuclear localization and sequesters wild-type FUS within cytoplasmic stress granules. Hum. Mol. Genet. *22*, 2676–2688.

Vanden Broeck, L., Callaerts, P., and Dermaut, B. (2014). TDP-43-mediated neurodegeneration: towards a loss-of-function hypothesis? Trends Mol. Med. *20*, 66–71.

Verdile, V., De Paola, E., and Paronetto, M.P. (2019). Aberrant phase transitions: side effects and novel therapeutic strategies in human disease. Front. Genet. *10*, 173.

Vogler, T.O., Wheeler, J.R., Nguyen, E.D., Hughes, M.P., Britson, K.A., Lester, E., Rao, B., Betta, N.D., Whitney, O.N., Ewachiw, T.E., et al. (2018). TDP-43 and RNA form amyloid-like myo-granules in regenerating muscle. Nature *563*, 508–513.

Voigt, A., Herholz, D., Fiesel, F.C., Kaur, K., Müller, D., Karsten, P., Weber, S.S., Kahle, P.J., Marquardt, T., and Schulz, J.B. (2010). TDP-43-mediated neuron loss in vivo requires RNA-binding activity. PLoS One *5*, e12247.

Walker, A.K., Spiller, K.J., Ge, G., Zheng, A., Xu, Y., Zhou, M., Tripathy, K., Kwong, L.K., Trojanowski, J.Q., and Lee, V.M.-Y. (2015). Functional recovery in new mouse models of ALS/FTLD after clearance of pathological cytoplasmic TDP-43. Acta Neuropathol. *130*, 643–660.

Wallace, E.W.J., Kear-Scott, J.L., Pilipenko, E.V., Schwartz, M.H., Laskowski, P.R., Rojek, A.E., Katanski, C.D., Riback, J.A., Dion, M.F., Franks, A.M., et al. (2015). Reversible, Specific, Active Aggregates of Endogenous Proteins Assemble upon Heat Stress. Cell *162*, 1286–1298.

Wan, W.B., Migawa, M.T., Vasquez, G., Murray, H.M., Nichols, J.G., Gaus, H., Berdeja, A., Lee, S., Hart, C.E., Lima, W.F., et al. (2014). Synthesis, biophysical properties and biological activity of second generation antisense oligonucleotides containing chiral phosphorothioate linkages. Nucleic Acids Res. *42*, 13456–13468.

Wang, A., Conicella, A.E., Schmidt, H.B., Martin, E.W., Rhoads, S.N., Reeb, A.N., Nourse, A., Ramirez Montero, D., Ryan, V.H., Rohatgi, R., et al. (2018a). A single N-terminal phosphomimic disrupts TDP-43 polymerization, phase separation, and RNA splicing. EMBO J. *37*.

Wang, C., Duan, Y., Duan, G., Ma, Z., Zhang, K., Deng, X., Qian, B., Gu, J., Wang, Q., Zhang, S., et al. (2019). Stress induces cytoprotective TDP-43 nuclear bodies through lncRNA NEAT1-promoted phase separation. BioRxiv.

Wang, H., Zeng, F., Liu, Q., Liu, H., Liu, Z., Niu, L., Teng, M., and Li, X. (2013). The structure of the ARE-binding domains of Hu antigen R (HuR) undergoes conformational changes during RNA binding. Acta Crystallogr. Sect. D, Biol. Crystallogr. *69*, 373–380.

Wang, J., Choi, J.-M., Holehouse, A.S., Lee, H.O., Zhang, X., Jahnel, M., Maharana, S., Lemaitre, R., Pozniakovsky, A., Drechsel, D., et al. (2018b). A Molecular Grammar Governing the Driving Forces for Phase Separation of Prion-like RNA Binding Proteins. Cell *174*, 688–699.e16.

Wang, J., Wang, L., Diao, J., Shi, Y.G., Shi, Y., Ma, H., and Shen, H. (2020). Binding to m6A RNA promotes YTHDF2-mediated phase separation. Protein Cell *11*, 304–307.

Wang, M., Tao, X., Jacob, M.D., Bennett, C.A., Ho, J.J.D., Gonzalgo, M.L., Audas, T.E., and Lee, S. (2018c). Stress-Induced Low Complexity RNA Activates Physiological Amyloidogenesis. Cell Rep. *24*, 1713–1721.e4.

Wang, X., Schwartz, J.C., and Cech, T.R. (2015). Nucleic acid-binding specificity of human FUS protein. Nucleic Acids Res. *43*, 7535–7543.

Wegmann, S., Eftekharzadeh, B., Tepper, K., Zoltowska, K.M., Bennett, R.E., Dujardin, S., Laskowski, P.R., MacKenzie, D., Kamath, T., Commins, C., et al. (2018). Tau protein liquid-liquid phase separation can initiate tau aggregation. EMBO J. *37*.

Wegorzewska, I., and Baloh, R.H. (2011). TDP-43-based animal models of neurodegeneration: new insights into ALS pathology and pathophysiology. Neurodegener Dis *8*, 262–274.

Weskamp, K., Tank, E.M., Miguez, R., McBride, J.P., Gómez, N.B., White, M., Lin, Z., Gonzalez, C.M., Serio, A., Sreedharan, J., et al. (2020). Shortened TDP43 isoforms upregulated by neuronal hyperactivity drive TDP43 pathology in ALS. J. Clin. Invest.

Williamson, J.R. (2000). Induced fit in RNA-protein recognition. Nat. Struct. Biol. *7*, 834–837.

Wilson, A.C., Dugger, B.N., Dickson, D.W., and Wang, D.-S. (2011). TDP-43 in aging and Alzheimer's disease - a review. Int J Clin Exp Pathol *4*, 147–155.

Winton, M.J., Igaz, L.M., Wong, M.M., Kwong, L.K., Trojanowski, J.Q., and Lee, V.M.-Y. (2008). Disturbance of nuclear and cytoplasmic TAR DNA-binding protein (TDP-43) induces disease-like redistribution, sequestration, and aggregate formation. J. Biol. Chem. *283*, 13302–13309.

Wolozin, B., and Ivanov, P. (2019). Stress granules and neurodegeneration. Nat. Rev. Neurosci. *20*, 649–666.

Wu, L.-S., Cheng, W.-C., Chen, C.-Y., Wu, M.-C., Wang, Y.-C., Tseng, Y.-H., Chuang, T.-J., and Shen, C.-K.J. (2019). Transcriptomopathies of pre- and post-symptomatic frontotemporal dementia-like mice with TDP-43 depletion in forebrain neurons. Acta Neuropathol. Commun. *7*, 50.

Xu, Z.-S. (2012). Does a loss of TDP-43 function cause neurodegeneration? Mol. Neurodegener. *7*, 27.

Xu, Z., and Yang, C. (2014). TDP-43-The key to understanding amyotrophic lateral sclerosis. Rare Dis. *2*, e944443.

Yamazaki, T., Souquere, S., Chujo, T., Kobelke, S., Chong, Y.S., Fox, A.H., Bond, C.S., Nakagawa, S., Pierron, G., and Hirose, T. (2018). Functional Domains of NEAT1 Architectural lncRNA Induce Paraspeckle Assembly through Phase Separation. Mol. Cell *70*, 1038–1053.e7.

Yao, G., Chiang, Y.-C., Zhang, C., Lee, D.J., Laue, T.M., and Denis, C.L. (2007). PAB1 self-association precludes its binding to poly(A), thereby accelerating CCR4 deadenylation in vivo. Mol. Cell. Biol. *27*, 6243–6253.

Yoo, H., Triandafillou, C., and Drummond, D.A. (2019). Cellular sensing by phase separation: Using the process, not just the products. J. Biol. Chem. *294*, 7151–7159.

Yoshizawa, T., Ali, R., Jiou, J., Fung, H.Y.J., Burke, K.A., Kim, S.J., Lin, Y., Peeples, W.B., Saltzberg, D., Soniat, M., et al. (2018). Nuclear Import Receptor Inhibits Phase Separation of FUS through Binding to Multiple Sites. Cell *173*, 693–705.e22.

Youmans, K.L., and Wolozin, B. (2012). TDP-43: a new player on the AD field? Exp. Neurol. *237*, 90–95.

Yu, Y., Chi, B., Xia, W., Gangopadhyay, J., Yamazaki, T., Winkelbauer-Hurt, M.E., Yin, S., Eliasse, Y., Adams, E., Shaw, C.E., et al. (2015). U1 snRNP is mislocalized in ALS patient fibroblasts bearing NLS mutations in FUS and is required for motor neuron outgrowth in zebrafish. Nucleic Acids Res. *43*, 3208–3218.

Zacco, E., Martin, S.R., Thorogate, R., and Pastore, A. (2018). The RNA-Recognition Motifs of TAR DNA-Binding Protein 43 May Play a Role in the Aberrant Self-Assembly of the Protein. Front. Mol. Neurosci. *11*, 372.

Zacco, E., Graña-Montes, R., Martin, S.R., de Groot, N.S., Alfano, C., Tartaglia, G.G., and Pastore, A. (2019). RNA as a key factor in driving or preventing self-assembly of the TAR DNA-binding protein 43. J. Mol. Biol. *431*, 1671–1688.

Zarei, S., Carr, K., Reiley, L., Diaz, K., Guerra, O., Altamirano, P.F., Pagani, W., Lodin, D., Orozco, G., and Chinea, A. (2015). A comprehensive review of amyotrophic lateral sclerosis. Surg Neurol Int *6*, 171.

Zhang, H., Elbaum-Garfinkle, S., Langdon, E.M., Taylor, N., Occhipinti, P., Bridges, A.A., Brangwynne, C.P., and Gladfelter, A.S. (2015a). RNA controls polyq protein phase transitions. Mol. Cell *60*, 220–230.

Zhang, K., Donnelly, C.J., Haeusler, A.R., Grima, J.C., Machamer, J.B., Steinwald, P., Daley, E.L., Miller, S.J., Cunningham, K.M., Vidensky, S., et al. (2015b). The C9orf72 repeat expansion disrupts nucleocytoplasmic transport. Nature *525*, 56–61.

Zhang, K., Daigle, J.G., Cunningham, K.M., Coyne, A.N., Ruan, K., Grima, J.C., Bowen, K.E., Wadhwa, H., Yang, P., Rigo, F., et al. (2018). Stress granule assembly disrupts nucleocytoplasmic transport. Cell *173*, 958–971.e17.

Zhang, P., Fan, B., Yang, P., Temirov, J., Messing, J., Kim, H.J., and Taylor, J.P. (2019a). Chronic optogenetic induction of stress granules is cytotoxic and reveals the evolution of ALS-FTD pathology. Elife *8*.

Zhang, Y., Yang, M., Duncan, S., Yang, X., Abdelhamid, M.A.S., Huang, L., Zhang, H., Benfey, P.N., Waller, Z.A.E., and Ding, Y. (2019b). G-quadruplex structures trigger RNA phase separation. Nucleic Acids Res. *47*, 11746–11754.

Zhang, Y.-J., Xu, Y.-F., Cook, C., Gendron, T.F., Roettges, P., Link, C.D., Lin, W.-L., Tong, J., Castanedes-Casey, M., Ash, P., et al. (2009). Aberrant cleavage of TDP-43 enhances aggregation and cellular toxicity. Proc. Natl. Acad. Sci. USA *106*, 7607–7612.